Linear Spectral Model of Tropical Mesoscale Systems

by
Maria Faus Silva Dias

Department of Atmospheric Science
Colorado State University
Fort Collins, Colorado

Colorado State University

Department of Atmospheric Science

Paper No. 311

LINEAR SPECTRAL MODEL OF TROPICAL MESOSCALE SYSTEMS

by

Maria Faus Silva Dias

Research Report supported by
The Global Atmospheric Research Program,
National Science Foundation and the
GATE Project Office, NOAA under grants
ATM 78-05743 and ATM 77-15369

Department of Atmospheric Science
Colorado State University
Fort Collins, Colorado
80523

June, 1979.

Atmospheric Science Paper No. 311

ABSTRACT

LINEAR SPECTRAL MODEL OF TROPICAL MESOSCALE SYSTEMS

The sensitivity of mesoscale features with respect to large scale tropical profiles of wind and temperature and to small scale parameterizations is investigated through a linear, spectral, non-hydrostatic model. The cumulus heating parameterization is the so-called Wave-CISK parameterization, defined by an idealized moisture budget. The momentum mixing parameterization is as developed by Schneider and Lindzen (1976). It is found that the growth rates of different scales of motion are very sensitive to small scale parameters, such as top of moist layer, mean mixing ratio in moist layer and level of maximum heating rate. The speed of propagation and the mode of maximum growth rate are not very sensitive to small scale parameterization. The feature of the basic state wind that most seriously influences the selection of a most unstable mode is the direction and the speed of the upper level jet. Features in the basic state winds can effectively determine that the East Atlantic region has, in the mean, a most unstable mode that falls in the mesoscale length scale, while the West Pacific shows no preferred mode in the mesoscale length scale. Differences in wind hodographs between different categories of a composited easterly wave in the East Atlantic lead to the conclusion that the categories that precede the trough clearly define a preferred mode in the mesoscale, while the categories after the trough do not.

The time evolution of an initial disturbance shows that for a small scale initial condition (20-50 km), an initial line of convergence

evolves into a convective line whose vertical extent reaches the whole troposphere. The squall lines assume a curvature comparable to the ones reported by Houze (1977). An initial condition of larger scale (100 km) has very small growth and does not evolve into a convective line.

ACKNOWLEDGMENTS

I would like to thank Drs. Alan K. Betts and Duane E. Stevens for their kind guidance and encouragement throughout this work. I also greatly benefited from discussions with Drs. William R. Cotton, Wayne H. Schubert, Pedro L. Silva Dias and David A. Krueger.

This research was done while on leave from the Departamento de Meteorologia of the Instituto Astronômico e Geofísico of the Universidade de São Paulo, Brazil. The Conselho Nacional de Desenvolvimento Científico e Tecnológico - CNPq provided the scholarship.

Many thanks go to Polly Cletcher who typed the manuscript and to Mark Howes who drafted the figures.

Acknowledgment is made to the National Center for Atmospheric Research, which is sponsored by the National Science Foundation, for the computing time used in this research.

This research was supported by the National Science Foundation under Grants ATM 78-05743 and ATM 77-15369.

TABLE OF CONTENTS

	Page
Abstract	iii
Acknowledgments	v
Table of Contents	vi
List of Tables	ix
List of Figures	x
List of Symbols	xix
I. Introduction	1
II. Background	7
2.1 Observational features	7
2.1.1 Convective line features	8
2.1.2 Mesoscale vortices	11
2.1.3 Summary	11
2.2 Previous modelling results	12
2.2.1 Cumulonimbus scale	12
2.2.2 Mesoscale	14
2.2.3 Wave-CISK and mesoscale modelling	15
2.2.4 Summary	16
III. Model Description and Assumptions	17
3.1 Governing equations	18
a) Basic state	23
b) Final set of equations	25
3.1.1 Finite difference scheme	26
3.1.2 Boundary conditions	29
3.1.3 Method of solution	31
3.1.4 Final computations	35
3.2 Test of model without parameterizations	36
3.2.1 Speed of internal gravity waves	36
3.2.2 Instability of stratified sheared flow	37
3.3 Parameterization of small-scale processes	42
3.3.1 Cumulus heating	43
3.3.2 Momentum mixing	46
3.3.3 Cloud scale downdraft	52
3.4 Summary	54

Table of Contents (Continued) Page

IV. Model Sensitivity Tests. 55
4.1 Sensitivity to small-scale parameterization 56
a) Model structure and basic state. 57
4.1.1 Sensitivity with respect to cumulus heating parameters 57
a) Heating parameters 60
b) Eigenvalues. 62
c) Vertical structure 74
d) Effect of top boundary condition 86
4.1.2 Sensitivity with respect to momentum mixing parameters. 88
a) Cumulus heating and momentum mixing parameters 88
b) Eigenvalues. 92
c) Vertical structures. 97
4.1.3 Sensitivity with respect to cloud-scale downdraft parameters 102
a) Cumulus heating, momentum mixing and cloud-scale parameters 102
b) Eigenvalues. 102
c) Vertical structure 105
4.1.4 Summary of recommended parameters. 105
4.2 Sensitivity with respect to basic state 105
a) Model structure and small-scale parameters 106
4.2.1 Effect of wind speed 107
a) Basic state wind and temperature 107
b) Eigenvalues. 109
4.2.2 Effect of potential temperature. 111
a) Basic state wind and temperature 118
b) Eigenvalues. 118
4.2.3 Effect of directional shear of the wind. . . . 122
a) Basic state wind and temperature 122
b) Eigenvalues. 122
4.2.4 Summary of important basic state characteristics. 126

V. Model Results. 128
5.1 Differences in tropical regimes 128
5.1.1 East Atlantic vs West Pacific. 129
a) Eigenvalues. 129
5.1.2 Easterly wave categories 132
a) Eigenvalues. 133
5.1.3 Day 248. 139
a) Eigenvalues. 144
5.1.4 Summary. 146

Table of Contents (Continued) Page

5.2 Evolution of initial disturbance. 146
a) Basic state and small scale parameters . . 148
b) Truncation in the Fourier summation. . . . 148
c) Analytical expression for the initial condition and its Fourier transform. . . . 148
5.2.1 Narrow initial condition: convective line. . . 152
a) Horizontal structure at lowest level . . . 156
b) Vertical structure along a zonal plane . . 170
c) Horizontal structure at higher levels. . . 175
d) Fluxes 178
e) Summary. 180
5.2.2 Wider initial disturbance: a = b = 50 km . . . 181
a) Horizontal structure at lowest level . . . 181
b) Vertical structure in a zonal plane. . . . 187
c) Fluxes 190
d) Summary. 190
5.2.3 Still winder initial disturbance: a = b = 100 km 190
a) Horizontal structure at lowest level . . . 197
b) Vertical structure in a zonal plane. . . . 197
c) Summary. 197
5.2.4 Summary of main points 197

VI. Conclusions and Recommendations for Future Work. 199

References 203

Appendix A 1 209

Appendix A 2 212

LIST OF TABLES

Table		Page
1a	Phase velocities given by the 3-layer model and by equation (3.38) for different horizontal and vertical wavelengths. H is 9 km and $(g/\theta_o)\, d\theta_o/dz$ is 3.11 x $10^{-4}s^{-2}$, $(k_y=0)$, Δ_z = 3km.	38
1b	Same as Table 1a, but for 9-layer model, Δ_z = 1km.	38
2	Summary of sensitivity with respect to basic state wind speed	110
3	Summary of Figs. 4.44, 5.2, 5.3 and 5.4.	138
4	Summary of Figs. 5.6, 5.7 and 5.8.	144

LIST OF FIGURES

Figure		Page
1.1	Full disc IR satellite picture (SMS-1) taken at 1230 GMT on 5 Sept 1974 during the GATE.	2
1.2	Radar composited picture from the C-band radars on the ships Oceanographer (7°45'N, 22°12'W), Researcher (7°N,23°20'W), Quadra (9°N, 22°40'W) and Gillis (9°15'N, 24°48'W) at 1200 GMT on 5 Sept 1974. (from GATE International Meteorological Radar Atlas, 1977). . .	3
1.3	Streamline analysis of surface winds from the ship array and from a low level (0.5 km) flight of the UK 130 airplane. The observations are representative of 1200 GMT on 5 Sept 1974	4
3.1	The vertical structure of the model showing distribution of variables; solid lines (i+½) indicate the levels dividing the layers; dashed lines (integer i) indicate levels within layers at which the indicated variables are carried	27
3.2	Non dimensional growth rate as a function of non-dimensional wavenumber for Richardson number J=0.125; a) 5-layer model b) 10-layer model; c) 15-layer model; d) same as c except for the use of a 4th order differencing scheme to calculate basic state derivatives; ⊖ results from Hazel (1971)	40
4.1	Wind hodographs for GATE B-scale (E. Atlantic) from Thompson et al., (1979) and for KEP triangle (W. Pacific) from Reed and Recker (1971).	58
4.2	Potential temperature for GATE B-scale (E. Atlantic) from Thompson et al., (1979); for KEP triangle (W. Pacific) from Reed and Recker (1971) and for a mean between the temperature soundings in the ships DALLAS and OCEANOGRAPHER on 5 Sept 1974 at 900 GMT (Day 248) during the GATE	59
4.3	Eigenvalues of most unstable mode for model run with only the cumulus heating paramterization (parameters in Table 1). (a) real part of ω; (b) imaginary part of ω, or growth rate. Dashed lines in Fig. 4.3(a) denote regions of relative maximum and minimum, respectively, in the growth rate.	63

LIST OF FIGURES CONTINUED

Figure		Page
4.4	Eigenvalues for model run with only cumulus heating parameterization; parameters in Table 1 except for z_{ML} = 3 km. (cf. Fig. 4.3 for details).	67
4.5	Eigenvalues for model run with only cumulus heating parameterization; parameters in Table 1 except for z_{ML} = 4 km. (cf. Fig. 4.3).	68
4.6	Eigenvalues for model run with only cumulus heating parameterization; parameters in Table 1 except for z_{ML} = 5 km (cf. Fig. 4.3)	69
4.7	Eigenvalues for model run with only cumulus heating parameterization; parameters in Table 1 except for z_{MH} = 4.5 km.	70
4.8	Eigenvalues for model run with only cumulus heating parameterization; parameters in Table 1 except for z_{MH} = 6 km.	71
4.9	Eigenvalues for model run with only cumulus heating parameterization; parameters in Table 1 except for z_{MH} = 9 km.	72
4.10	Horizontal cross section at z = 0.5 km showing the field of the horizontal velocity vector for wavenumber (2, 1.3) (cf. Fig. 4.3) for cumulus heating parameters in Table 1.	76
4.11	Vertical cross section at x = 0 (meridional plane) showing the field of vector(v',w') for wavenumber (2, 1.3) (cf. Fig. 4.3) for cumulus heating parameters in Table 1.	77
4.12	Isolines of mesoscale potential temperature in the meridional plane at x = 0; wavenumber (2, 1.3) (cf. Fig. 4.3) for cumulus heating parameters in Table 1 . . .	78
4.13	Isolines of mesoscale vertical velocity in the meridional plane at x = 0; wavenumber (2, 1.3) (cf. Fig. 4.3) for cumulus heating parameters in Table 1.	79
4.14	Vertical structure of (A) $\overline{u'w'}$; (B) $\overline{v'w'}$; (C) $\overline{p'w'}$; (D) $\overline{\theta'w'}$. (cf. Appendix A1, A2). For wavenumber (2, 1.3) and with cumulus heating parameters in Table 1	80

LIST OF FIGURES CONTINUED

Figure		Page
4.15	Vertical cross section at x = 0 (meridional plane) showing the field of vector (v',w') for wavenumber (2, 1.3) (cf. Fig. 4.8) for cumulus heating parameters in Table 1 except for z_{MH} = 6 km.	81
4.16	Vertical cross section of x = 0 (meridional plane) showing the field of vector (v', w') for wavenumber (2, 1.3) (cf. Fig. 4.9) for cumulus heating parameters in Table 1 except for z_{MH} = 9 km.	82
4.17	Vertical structure of (A) $\overline{u'w'}$; (B) $\overline{v'w'}$; (C) $\overline{p'w'}$; (D) $\overline{\theta'w'}$. For wavenumber (2, 1.3) and with cumulus heating parameters in Table 1, except for z_{MH} = 6 km. . . .	83
4.18	Vertical structure of (A) $\overline{u'w'}$; (B) $\overline{v'w'}$; (C) $\overline{p'w'}$; (D) $\overline{\theta'w'}$. For wavenumber (2, 1.3) and with cumulus heating parameters in Table 1 except for z_{MH} = 9 km	84
4.19	Vertical structure of the amplitude of $\hat{w}$ for the wavenumber (2, 1.3) and cumulus heating parameters in Table 1: (a) Radiation condition at the top boundary, (b) top boundary condition of zero vertical velocity. . . .	87
4.20	Cumulus mass flux: (a) large scale, from Yanai et al., (1973); (b) mesoscale for q_o = 12g.kg^{-1} (cf. equation 3.54)	89
4.21	Optimal profile of basic state vertical mass flux (2 x 10^{-2} kg . m^{-2} . s^{-1} = 7 mb . hr^{-1})	90
4.22	A plot of the vertical profile of the terms in equation (3.53a) for an optimal profile of w_o, and the residual in the same equation.	91
4.23	Eigenvalues for model run with cumulus heating parameterization (Table 1) and momentum mixing by cumulus clouds (Fig. 4.20). Basic state wind and temperature "East Atlantic"	94
4.24	Eigenvalues for model run with cumulus heating parameterization (Table 1, except for z_{ML} = 3 km) and momentum mixing by cumulus clouds (Fig. 4.20)	95
4.25	Eigenvalues for model run with cumulus heating parameterization (Table 1, except for z_{ML} = 4 km) and momentum mixing by cumulus clouds (Fig. 4.20)	96

LIST OF FIGURES CONTINUED

Figure		Page
4.26	Isolines of mesoscale vertical velocity in the meridional plane at x = 0; wavenumber (2, 1.3) (cf. Fig. 4.23) for cumulus heating parameters in Table 1 and momentum mixing parameterization (Fig. 4.20). (cf. Fig. 4.13)	98
4.27	Vertical structure of (A) $\overline{u'w'}$; (B) $\overline{v'w'}$; (C) $\overline{p'w'}$; (D) $\overline{\theta'w'}$. For wavenumber (2, 1.3) and with cumulus heating (Table 1) and momentum mixing parameterization (Fig. 4.20) (cf. Fig. 4.14)	99
4.28	Isolines of mesoscale vertical velocity in the meridional plane at x = 0; wavenumber (10,2) (cf. Fig. 4.23). Cumulus heating parameters in Table 1 and momentum mixing parameter profiles in Fig. 4.20. (cf. Fig. 4.26)	100
4.29	Vertical structure of (A) $\overline{u'w'}$; (B) $\overline{v'w'}$; (C) $\overline{p'w'}$; (D) $\overline{\theta'w'}$. For wavenumber (10, 2). Cumulus heating parameters in Table 1 and momentum mixing parameter in Fig. 4.20. (cf. Fig. 4.27)	101
4.30	Eigenvalues for model run with cumulus heating (Table 1), momentum mixing (Fig. 4.20) and cloud-scale downdraft (downdraft initiation at 2.5 km) parameterizations	103
4.31	Eigenvalues for model run with cumulus heating (Table 1), momentum mixing (Fig. 4.20) and cloud-scale downdraft (downdraft initiation at 3.5 km) parameterizations	104
4.32	Wind speed for different levels and intensities of upper lower level jets	108
4.33	Eigenvalues for basic state wind 1A and temperature "Day 248"	112
4.34	Eigenvalues for basic state wind 1B and temperature "Day 248"	113
4.35	Eigenvalues for basic state wind 1C and temperature "Day 248"	114
4.36	Eigenvalues for basic state wind 3B (or 2B) and temperature "Day 248"	115

LIST OF FIGURES CONTINUED

Figure		Page
4.37	Eigenvalues for basic state wind 3A and temperature "Day 248".	116
4.38	Eigenvalues for basic state wind 2A and temperature "Day 248".	117
4.39	Eigenvalues for basic state wind 4B and temperature "Day 248".	119
4.40	Eigenvalues for basic state wind 4B and temperature "West Pacific"	120
4.41	Eigenvalues for basic state wind 4B and temperature "East Atlantic".	121
4.42	Wind hodographs for categories 1, 3, 5 and 7 in Thompson et al., (1979) composited large scale easterly wave. . .	123
4.43	Eigenvalues for basic state wind speeds of "Category 1" without directional shear and basic state temperature "East Atlantic".	124
4.44	Eigenvalues for basic state wind speeds of "Category 1" with directional shear and basic state temperature "East Atlantic".	125
5.1	Eigenvalues for basic state wind speeds of "West Pacific" and basic state temperature "West Pacific"	130
5.2	Eigenvalues for basic state wind speeds of "Category 3" and basic state temperature "East Atlantic".	134
5.3	Eigenvalues for basic state wind speeds of "Category 5" and basic state temperature "East Atlantic".	135
5.4	Eigenvalues for basic state wind speeds of "Category 7" and basic state temperature "East Atlantic".	136
5.5	Wind hodographs for soundings in ships Prof. Vize (8.5°N, 23.5°W) and Vanguard (10°N, 23.5°W) and for the mean between the two soundings. This data corresponds to 600 GMT on 5 Sept 1974 (Day 248) during GATE. .	140
5.6	Eigenvalues for basic state winds from ship Vanguard and basic state temperature of "Day 248"	141
5.7	Eigenvalues for basic state winds from ship Prof. Vize and basic state temperature of "Day 248".	142

LIST OF FIGURES CONTINUED

Figure		Page
5.8	Eigenvalues for basic state winds which are a mean between the winds at Vanguard and Prof. Vize; basic state temperature of "Day 248".	143
5.9	Isolines of $(a^2bk_x^2 + ab^2k_y^2) \exp(-k_x^2 a^2/4 - k_y^2 b^2/4)$ for different values of a,b. The circle denotes the most unstable mode in Fig. 4.24	151
5.10	Vertical cross sections of mesoscale vertical velocity (a) along z = 0 (east-west plane); (b) along y = 0 (north-south plane) at time t = 0. (Initial condition: a = b = 20 km).	154
5.11	Horizontal cross-section of the mesoscale horizontal wind vector (u',v') at z = 500 m and t = 0. Dashed lines denote axis of convergence (Initial condition: a = b = 20 km).	155
5.12	Horizontal cross section of the mesoscale horizontal wind vector (u',v') at z = 500 m and t = 500 seconds. (Initial condition: a = b = 20 km).	157
5.13	Horizontal cross section of the mesoscale horizontal wind vector (u',v') at z = 500 m and t = 1000 seconds. (Initial condition: a = b = 20 km).	158
5.14	Horizontal cross section of the mesoscale horizontal wind vector (u',v') at z = 500 m and t = 1500 seconds. (Initial condition: a = b = 20 km).	159
5.15	Horizontal cross section of the mesoscale horizontal wind vector (u',v') at z = 500 m and t = 2000 seconds. (Initial condition: a = b = 20 km).	160
5.16	Horizontal cross section of the mesoscale horizontal wind vector (u',v') at z = 500 m and t = 2500 seconds. (Initial condition: a = b = 20 km).	161
5.17	Horizontal cross section of the mesoscale horizontal wind vector (u',v') at z = 500 and t = 3000 seconds. Note the change in scale from previous figures. (Initial condition: a = b = 20 km)	162
5.18	Horizontal cross section of the mesoscale horizontal wind vector (u',v') at z = 500 m and t = 4500 seconds. (Initial condition: a = b = 20 km).	163

LIST OF FIGURES CONTINUED

Figure		Page
5.19	Horizontal cross section of the mesoscale horizontal wind vector (u',v') at z = 500 m and t = 6000 seconds. (Initial condition: a = b = 20 km).	164
5.20	Isolines of mesoscale potential temperature θ' at z = 500 m and t = 3000 seconds. (Initial condition: a = b = 20 km).	165
5.21	Isolines of mesoscale pressure p' at z = 500 m and t = 3000 seconds (Initial condition: a = b = 20 km) . . .	166
5.22	Time sequence of the position of the leading edge of the two convective lines shown in Figures 5.11 to 5.19. The numbers denote time steps in 1000 seconds	169
5.23	Vertical cross sections along y = 0 (zonal plane) of mesoscale vertical velocity (a) at t = 500 seconds; (b) at t = 1000 sec. (Initial condition: a = b = 20 km). .	171
5.24	Vertical cross sections along y = 0 (zonal plane) of mesoscale vertical velocity. (z) at t = 1500 seconds; (b) at t = 2000 sec. (Initial condition: a = b = 20 km).	172
5.25	Vertical cross sections along y = 0 (zonal plane) at mesoscale vertical velocity. (z) at t = 2500 seconds; (b) at t = 3000 sec. Note difference in scales between (a) and (b). (Initial condition: a = b = 20 km)	173
5.26	Vertical cross sections along y = 0 (zonal plane) of mesoscale vertical velocity. (a) at t = 4500 seconds; (b) at t = 6000 sec. (Initial condition: a = b = 20 km). .	174
5.27	Horizontal cross section of the mesoscale horizontal wind vector (u',v') at z = 6.5 km and t = 2500 sec. (cf. Figure 5.15). (Initial condition: a = b = 20 km). . .	176
5.28	Horizontal cross section of the mesoscale horizontal wind vector (u',v') at z = 13.5 km at t = 2500 sec. (cf. Figures 5.15 and 5.23). (Initial condition: a = b = 20 km).	177
5.29	Vertical structure of: (A) $\rho_o\overline{u'w'}$; (B) $\rho_o\ \overline{v'w'}$; (C) $\overline{p'w'}$; (D) $\rho_o\ \overline{\theta'w'}$ at time t = 3000 seconds. (Initial condition: a = b = 20 km)	179

LIST OF FIGURES CONTINUED

Figure		Page
5.30	Horizontal cross section of mesoscale horizontal wind vector (u',v') at z = 500 m and t = 0. (Initial condition: a = b = 50 km).	182
5.31	Horizontal cross section of mesoscale horizontal wind vector (u',v') at z = 500 m and t = 1500 seconds. (Initial condition: a = b = 50 km).	183
5.32	Horizontal cross section of mesoscale horizontal wind vector (u',v') at z = 500 m and t = 3000 sec. (Initial condition: a = b = 50 km)	184
5.33	Horizontal cross section of mesoscale horizontal wind vector (u',v') at z = 500 m and t = 4500 sec. (Initial condition: a = b = 50 km)	185
5.34	Horizontal cross section of mesoscale horizontal wind vector (u',v') at z = 500 m and t = 14400 sec. (Initial condition: a = b = 50 km)	186
5.35	Vertical cross sections of mesoscale vertical velocity along a zonal plane at y = 0. (a) at time t = 0; (b) at time t = 4500 sec. (Initial condition: a = b = 50 km).	188
5.36	Vertical structure of: (A) $\rho_o\overline{u'w'}$; (B) $\rho_o\overline{v'w'}$; (C) $\overline{p'w'}$; (D) $\rho_o\theta'w'$; at time t = 4500 sec. (Initial condition: a = b = 50 km).	189
5.37	Horizontal cross section of mesoscale horizontal wind vector (u',v') at z = 500 m and t = 0. (Initial condition: a = b = 100 km)	191
5.38	Horizontal cross section of mesoscale horizontal wind vector (u',v') at z = 500 m and t = 1500 seconds. (Initial condition: a = b = 100 km).	192
5.39	Horizontal cross section of mesoscale horizontal wind vector (u',v') at z = 500 m and t = 3000 seconds. (Initial condition: a = b = 100 km).	193
5.40	Horizontal cross section of mesoscale horizontal wind vector (u',v') at z = 500 m and t = 4500 seconds. (Initial condition: a = b = 100 km).	194

LIST OF FIGURES CONTINUED

Figure		Page
5.41	Horizontal cross section of mesoscale horizontal wind vector (u',v') at z = 500 m and t = 6000 seconds. (Initial condition: a = b = 100 km).	195
5.42	Vertical cross sections of mesoscale vertical velocity in a zonal plane at y = 0. (a) at time t = 0; (b) at time t = 6000 seconds. (Initial condition: a = b = 100 km).	196

LIST OF SYMBOLS

Symbol	
$\mathbf{v}$	$= u\hat{i} + v\hat{j} + w\hat{k}$ - velocity vector with components in the east-west ($\hat{i}$), north-south ($\hat{j}$) and vertical directions
f	Coriolis parameter
g	gravity acceleration
ρ	density
p	pressure
θ	potential temperature
ψ_x, ψ_y, ψ_z	small scale terms in the mesoscale equations of motion
ψ_θ	small scale terms in the mesoscale thermodynamic equation
Q	diabatic heating
$\mathbf{k}$	$= k_x\hat{i} + k_y\hat{j}$ - wavenumber vector
ω	$= \omega_r + i\omega_i$ - frequency
c	$= \omega/(k_x^2 + k_y^2)$
H	= density scale height
v_k	$= \mathbf{v}_o \cdot \mathbf{k}/\lvert\mathbf{k}\rvert$ - component of basic state wind along the wavenumber vector
z_{ML}	top of moist layer
z_{MH}	level of maximum heating rate
q_o	mean mixing ratio in the moist layer
M_c	cloud mass flux
z_c	cloud base
z_T	cloud top
$\Gamma_w^{\theta E}$	potential temperature lapse rate along a moist adiabat

I. INTRODUCTION

The range of predictability of large scale models or general circulation models of the atmosphere is highly dependent on the amount of physics specified and on the accuracy of the boundary conditions, as well as the problems related to initialization and discretization schemes. To improve the range of reliability of weather forecasts it has long been recognized that the tropical regions have to be properly modeled. In this context the last 10 or 15 years have seen an increasing number of scientists studying the weather in the tropics. Several observations and experiments have been designed and executed in lower latitudes to provide a framework upon which theories can be developed and models initialized or tested.

The resolution of large-scale models and general circulation models ranges from about 150 km to 500 km, so that important tropical phenomena such as cloud clusters and squall lines may fall in the subgrid scale of these models or be allowed two or three grid points at the most. Fig. 1.1 shows a satellite picture of a well developed double cloud cluster taken during the GARP Atlantic Tropical Experiment (GATE) on 5 Sept. 1974 at 1230 GMT. Each of the cloud clusters has a horizontal dimension of about 3° latitude. As seen from an IR sensor, the two clusters appear as homogeneous blobs of cloudiness. The pattern of precipitation and winds is not, however, homogeneous, but shows a considerable amount of organization as may be seen in Figs. 1.2 and 1.3. Fig. 1.2 is a radar composite made at 1200 GMT on the same day during the GATE. Clearly defined lines of heavy precipitation may be seen which are associated with the squall lines described

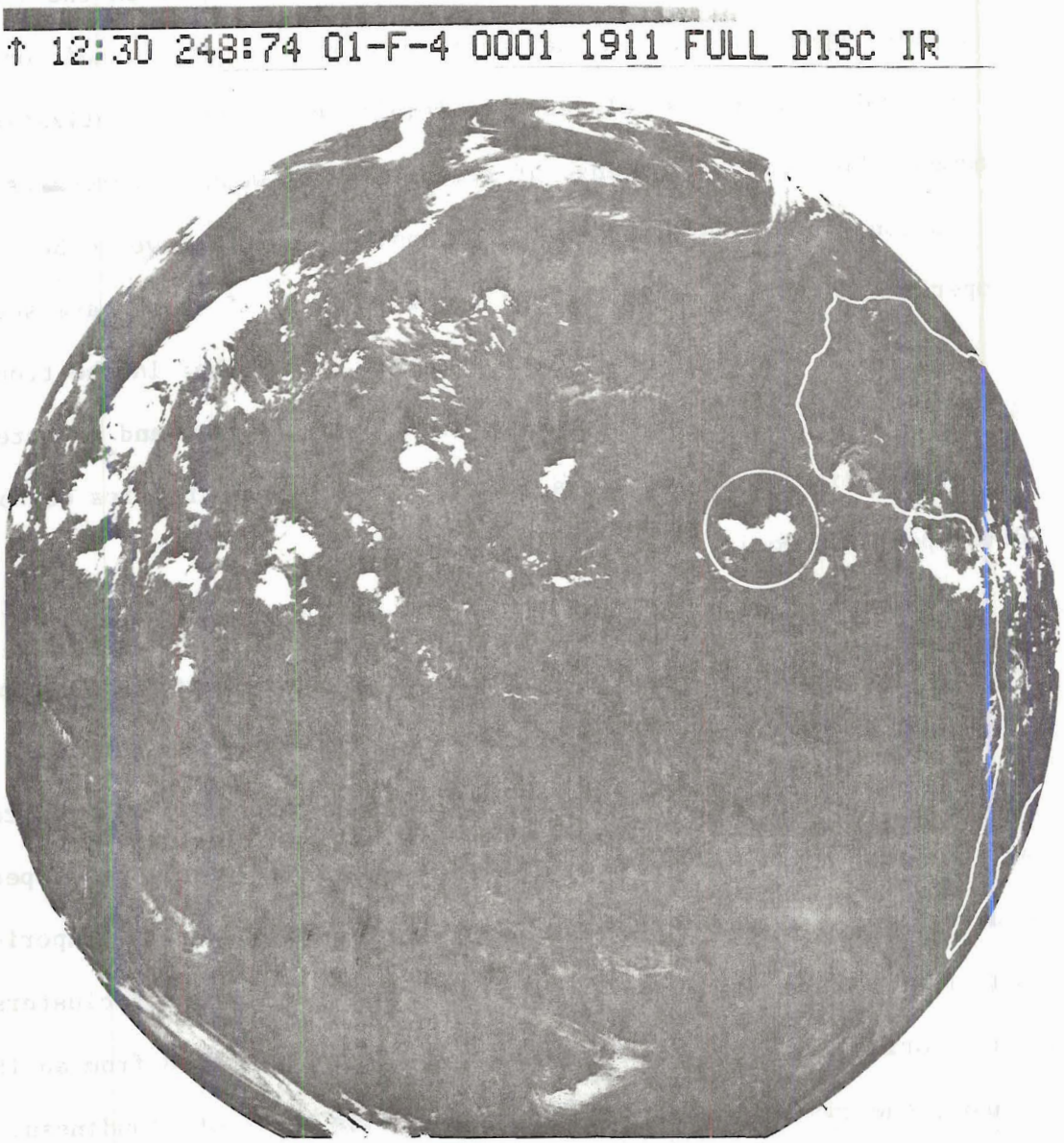

Figure 1.1 Full disc IR satellite picture (SMS-1) taken at 1230 GMT on 5 Sept 1974 during the GATE.

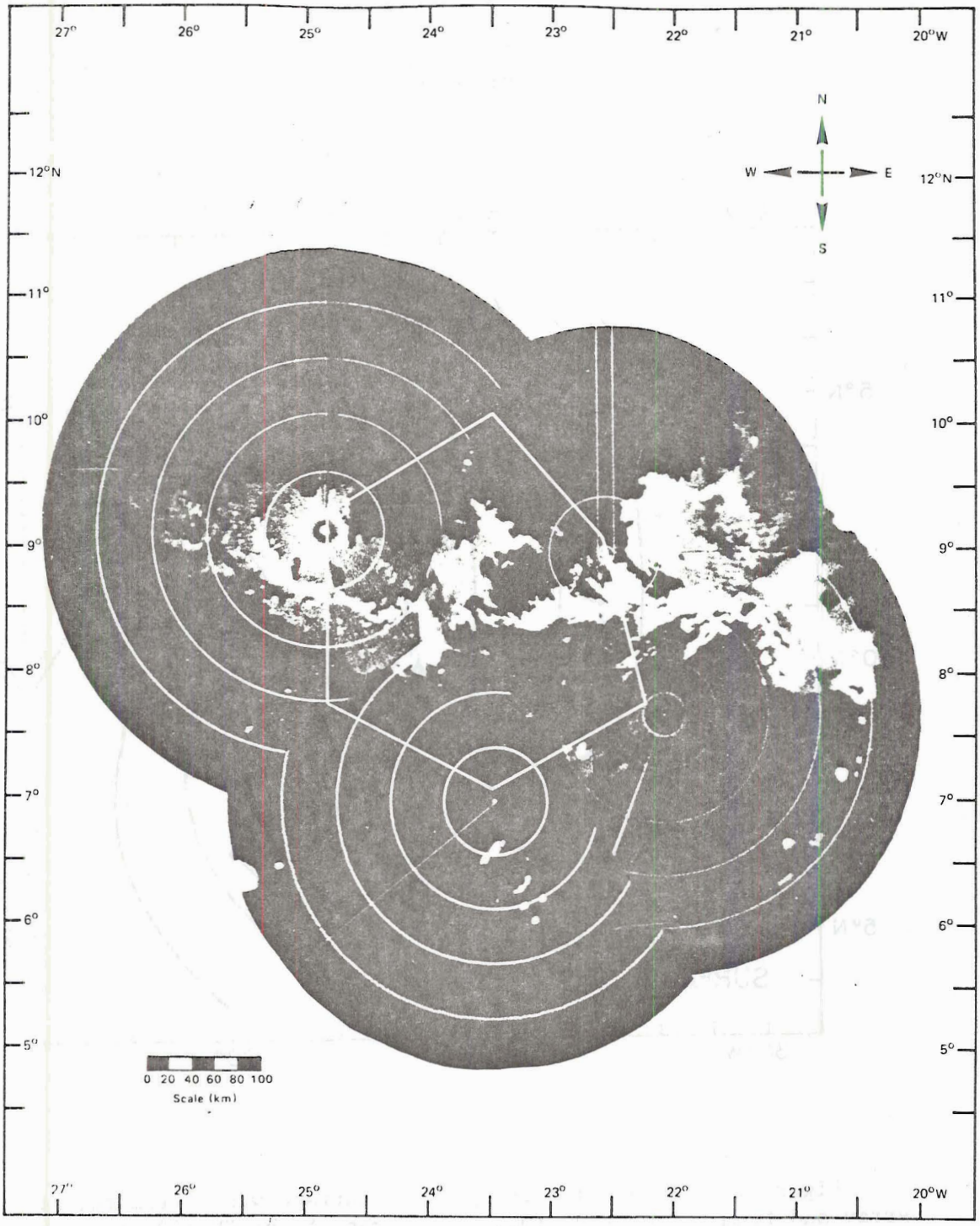

September 5, 1974 (Julian day 248), 1200 GMT.

Figure 1.2 Radar composited picture from the C-band radars on the ships Oceanographer (7°45'N, 22°12'W), Researcher (7°N, 23°30'W) Quadra (9°N, 22°40'W) and Gillis (9°15'N, 24°48'W) at 1200 GMT on 5 Sept 1974. (from GATE International Meteorological Radar Atlas, 1977)

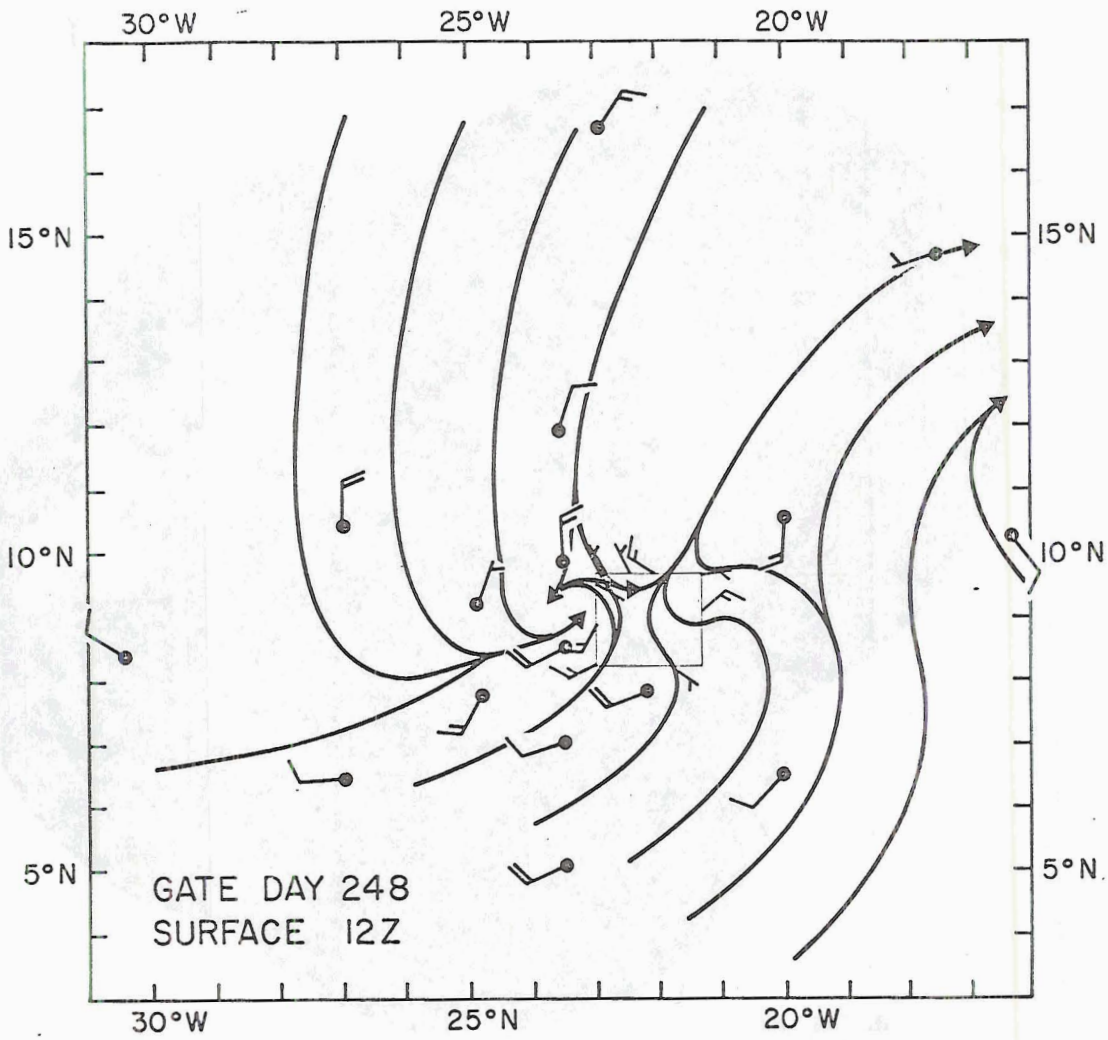

Figure 1.3 Streamline analysis of surface winds from the ship array and from a low level (0.5 km) flight of the UK 130 airplane. The observations are representative of 1200 GMT on 5 Sept 1974.

by Houze (1977). Fig. 1.3 shows a surface streamline analysis representative of 1200 GMT on the same day. This figure shows a highly organized mesoscale wind pattern with a cyclonic vortex centered at 9°N, 23.5^{o}W, just north of the line of cloudiness seen in Fig. 1.2.

The inclusion of subgrid scale processes in large scale models requires the parameterization of momentum and heat transports by small scale and mesoscale systems. Observational studies which describe mesoscale disturbances (Zipser 1969, 1977; Zipser and Gauthier, 1978; Smith et al., 1975 a,b; Houze, 1977) have attempted to determine points in common between different systems and to develop some understanding of why the different manifestations of mesoscale organization occur. This approach is mainly descriptive and cannot by itself provide a consistent parameterization scheme unless perhaps a huge amount of observations is processed and catalogued. A second approach has been to numerically model single clouds (Liu and Orville, 1969; Takeda, 1971, and Moncrieff and Miller, 1976, among others) and determine the transports. This approach, however, may be considerably underestimating the transports that can be generated by an organized set of clouds. The assessment of the transports of heat and momentum by mesoscale systems has to be done through a mesoscale model. Though several mesoscale models have been developed (Cotton and Pielke, 1977; Pielke and Mahrer, 1978; Frisch, 1978; Brown, 1979), a simple parameterization scheme suitable for use in large-scale models has not been developed.

This thesis will approach the question of how the mesoscale features depend on large scale characteristics by using a relatively simple model. Although we may still have years to go to achieve the goal of

a comprehensive parameterization scheme that will successfully represent the mesoscale contribution to the large scale picture of atmospheric motions, the work to be presented will attempt to shed some light on this problem.

The following chapters present: a review of mesoscale features that have been identified throughout the literature; the model assumptions, governing equations and parameterization of small scale processes; the sensitivity of model results to the parameterization and to basic state features; the development of initial perturbations and differences in tropical regimes.

II. BACKGROUND

The study of mesoscale systems has received attention from the past of observation and modelling research. Experimental programs have been designed for the special purpose of understanding and classification of mesoscale systems; several models have been designed for the simulation of these systems. This chapter reviews the results in these two distint areas of atmospheric research in order to provide some background information for the following chapters.

2.1 Observational Features

Several studies based on GATE data agree that the onset of deep convection is preceded by a maximum in upward vertical velocity. According to one school of thought (Reed et al.,1977; Thompson et al, 1979; Burpee, 1972), this maximum is associated with the passage of an easterly wave trough, with organized convection occurring preferentially just ahead of the 700 mb trough (Payne and McGarry, 1977). According to others (Gray, 1968; Frank, 1977; Dean and Smith, 1977), the structure of the cyclonic disturbances which appear in GATE is complicated and non-steady and therefore not likely to be accurately forced by a single steady sinusoidal wave. One way or the other, the profiles of wind (or divergence and vorticity) ahead of the trough in the Reed et al. (1977) composited easterly wave are very similar to those in Frank's (1977) deep convection category.

As reported in the above studies, the strongest surface convergence is found close to the maximum in convective activity. Gray (1977) reports that the strongest convergence goes up to about 800 mb.

In Reed et al., (1977) composited wave, the total wind ahead of the trough shows southwesterlies at the surface, northeasterlies at 700 mb and southeasterlies at 200 mb. The wave moves at a speed of approximately $8ms^{-1}$ with a typical wavelength of 2500 km.

The wind profiles associated with squall-line events show strong vertical shear in upper levels. Middle and low-level shear do not seem to be essential. Mower (1977) reported an almost unsheared environment below 300 mb on the 2 September convective line. Zipser (1977) in a case study of a Barbados mesoscale disturbance also reports a lack of middle level shear. The GATE area, however, had in the mean wind for Phase III a low-level easterly jet just above 700 mb and an upper-level easterly jet at around 200 mb (see GATE Workshop Report, 1977; or Thompson et al., 1979). Directional shear was also present in the mean wind of Phase III; around 800 mb the wind shifted from south-southwesterlies below that level to easterlies above.

2.1.1 Convective Line Features

Aspliden et al., (1976) tabulated all squall line cases occurring during GATE. Phase III, which is known to be the most disturbed period during the whole experiment, had eight squall lines identified over the ocean according to the criteria that they have cloud tops around 15 km, attain a $2^{o} \times 2^{o}$ size during their lifetime and be active for a minimum of 6 hours. The squalls had a mean speed of 11.4 $m.s^{-1}$, extended over a distance of more than 500 km long and lasted for 14 hours. In 65% of the cases, the time of generation was between 0300 and 1200 GMT, as was pointed out also by Gray (1977).

Of the eight cases during Phase III of GATE, two are of particular interest: the 2 September and the 4-5 September cases. The former has

been described by Kelley (1977) and Mower (1977) and the latter by Houze (1977), Dean and Smith (1977), among others. Zipser (1977) gives a description of a tropical squall line event during the Barbados experiment.

According to Kelley and Mower the 2 September convective line was oriented in the northwest-southeast direction, being 300 km long and 20-30 km wide; it progressed over the GATE array during its lifetime from 1200 to 1800 GMT, with a speed of $6ms^{-1}$; by around 1500 GMT, the surface streamlines revealed a low-level mesoscale circulation which persisted through 1800 GMT. With the appearance of this mesoscale vortex motion, the convective bands became less defined.

The 5 September disturbance showed similar features. Houze (1977) reports that the observed squall had a step-wise motion as new cumulonimbus (Cb) elements formed well ahead of the existing line while old squall lines elements weakened toward the rear, their rainfall became stratiform and they blended into the trailing anvil region. The squall was located along the leading edge of a mesoscale downdraft which formed and spread out in the middle and lower troposphere below the anvil cloud. According to Dean and Smith (1977), by 1200 GMT a mesoscale cyclone developed which extended from the surface to 400 mb and was located on the western edge of the cloud mass. Further to the west, another cyclone developed. The pair of cyclones persisted up to 1800 GMT when the cloud region began to decay.

According to Zipser (1977) a mesohigh is often observed shortly after squall passage, with a mesolow frequently observed some hours later, in both tropical and mid-latitude squall systems. Fujita (1963)

and Williams (1963) had already noted the occasional presence of a mesoscale low pressure area some distance behind squall lines, persisting for 4-6 hours.

As has been reported by many investigators since the early work of Byers and Braham (1949) based on data obtained during the Thunderstorm Project, the downdraft plays a very important tole in the propagation of squall lines. Miller and Betts (1977) and Zipser (1977) identify two types of downdrafts: a cloud downdraft which is nearly saturated and an unsaturated mesoscale downdraft. Zipser (1977) suggests that the cloud scale downdrafts originate around 650 mb but do not penetrate the lowest 150 m. The mesoscale downdraft would originate around 800 mb below the raining anvil. There is a difference in scale between the two downdrafts. Using a numerical model, Miller and Betts (1977) show that the mesoscale downdraft is dynamically rather than evaporatively driven as stated by Zipser (1969, 1977), and Brown (1979).

Betts et al., (1976) in a study of tropical squall lines over Venezuela observed marked changes in the dynamic and thermodynamic structure of the atmosphere after a squall line passage. Basically, the boundary layer air is transported into high levels and replaced by air from mid-levels. Except in the lowest 150 mb where a large cooling occurs and at high levels, this change in equivalent potential temperature (Θ_E) is dominated by a mixing ratio change. In the wind field there is significant increase of easterly momentum in lower levels and westerly momentum is increased in upper levels.

2.1.2 Mesoscale Vortices

Mesoscale cyclonic vortices are also observed without being related to convective lines as reported by Zipser and Gautier (1978) and Smith et al., (1975a,b).

According to Smith et al., (1975a), the main characteristic that differentiates the mesoscale vortex from the squall line is the lack of organization in the cumulonimbus downdrafts. On the other hand, Zipser and Gautier (1978) report that mesoscale downdrafts existed as evidenced by mesoscale divergence of low-level winds. According to Zipser and Gautier the downdrafts in the 15 July 1974 mesoscale vortex observed in the GATE area did not change the thermodynamic properties of the subcloud layer in a significant way.

In both cases the wind field showed a closed circulation of about 2° - 4° in diameter and a lifetime of about 12 hours.

Smith et al., (1975a) report the speed of the vortex observed in the BOMEX area on 26 July 1979 to be of 8.2 $m \cdot s^{-1}$ from the northwest.

2.1.3 Summary

This section has described some overall characteristics of propagating convective lines and mesoscale vortices. Although the model results will not be able to reproduce the total picture of either phenomena, it will attempt to clarify the properties of propagating convective lines and the sensitivity of these properties with respect to large-scale atmospheric conditions.

2.2 Previous Modelling Results

Previous attempts to model mesoscale motions fall in two main categories: one is the modelling of the cumulonimbus scale dealing with horizontal dimensions up to about 30 km; the other deals with horizontal scales up to 1000 km. The basic difference between these two areas is in the parameterization of different physical processes. The following subsections review a few models in the cumulonimbus scale and on the larger mesoscale. A review on previous work using the Wave-CISK parameterization scheme for mesoscale modelling will also be presented.

2.2.1 Cumulonimbus Scale

The models of the cumulonimbus scale close the system of equations by parameterizing microphysical and sometimes turbulent processes. Although this type of model is restricted to scales up to 20 or 30 km, some results are extrapolated and used to explain features of convective lines in the mesoscale. The main assumption involved in this extrapolation is that a convective line is composed by a set of cumulonimbus clouds. Interaction between the several components of the convective line is assumed to be of secondary importance. This type of approach is not able to explain the structure of curved convective lines nor the extension of mesoscale downdrafts; however, very interesting results have been obtained. The models described below are all three-dimensional.

Moncrieff and Miller (1976) presented theoretical and numerical models of cumulonimbus convection and succeeded in determining quite well the propagation speed of squall lines based on a convective available potential energy. Betts et al., (1976) compared Moncrieff

and Miller's (1976) results to observations of squall lines over Venezuela. They concluded that the propagation speeds and transport properties determined by the model are similar to the observed.

The experiments presented by Klemp and Wilhelmson (1978a,b) were directed to examine convective storms and their dependence on the environmental wind shear. Splitting of the original storm into right and left moving storms was sensitive to low-level environmental wind shear. They also found out that if the wind hodograph turned clockwise with height, a single right-moving storm evolved from the splitting processes. Conversely, counterclockwise turning of the hodograph favored development of the left-moving storm. The horizontal scale of this storm was of about 10 km, so that they fall in the borderline between mesoscale and small-scale processes. Thorpe and Miller (1978) also show that the splitting process is highly dependent on the environmental wind shear.

Cotton and Tripoli (1978) verified the ability of a simulation to predict observed liquid water content. Again, the environmental wind shear was found to play a major role in the accuracy of this determination. They conclude that unless one or two-dimensional models include the parameterization of cloud interaction with shear flow in some realistic manner, they are not likely to successfully predict cloud liquid water content as well as cloud top height.

In summary, the environmental wind shear seems to be extremely important in determining the properties of small scale systems. The propagation of these systems compares fairly well with the propagation of squall lines.

2.2.2 Mesoscale

The models described below are hydrostatic non-linear models with a constant Coriolis parameter; their resolution in the horizontal is around 20 km while the vertical resolution is between 0.5 km and 1 km; the governing equations include conservation of momentum, energy and moisture. They all use sophisticated parameterization schemes that account for cloud base, cloud top, updraft thermodynamics, microphysics, entrainment effects; subsidence and its effects on the environment; precipitation, collection and evaporation of liquid water. The parameterization used by Kreitzberg and Perkey (1976,1977) as well as the one presented by Fritsch(1978) take into account cloud lifetimes as opposed to Brown (1979) that makes the quasi-equilibrium assumption (Arakawa and Schubert, 1974).

Kreitzberg and Perkey (1977) used a two-dimensional model with small-scale convection parameterized through a lagrangian cloud model developed and tested by Kreitzberg and Perkey (1976). The objective of Kreitzberg and Perkey (1977) was to examine scale interactions; the results of their simulation showed that at the initial stages, the motions are dominated by the small-scale convective heating, while after 6 hrs, the motions are dominated by the hydrostatic mesoscale updraft that develops in response to diabatic heating from the earlier convection. Mesoscale updraft produces stratiform precipitation that exceeds the earlier convective precipitation. In this simulation, there is no vertical shear in the initial wind field.

Fritsch's (1978) three-dimensional model successfully simulated the development of squall lines, mesoscale downdrafts and mesohighs produced by mesoscale compensating subsidence. The vertical structure of

the squall lines, as in the case simulated by Kreitzberg and Perkey (1977), is not tilted as opposed to the observations of Zipser (1977), Sanders and Emanuel (1977), and Houze (1977).

Brown (1979) showed with a two-dimensional model that the growth of mesoscale disturbances is highly sensitive to the amount of heating imposed through the small-scale parameterization. Through a series of experiments, Brown showed that the shear of the environmental wind and the evaporation of rain are essential for obtaining a structure comparable to Zipser (1969, 1977) and Houze (1977) observations.

The models described above are complex in the sense that they include as many effects as possible. The resulting experiments show strong resemblance to observed systems; however, they do not help much the process of understanding the physics of these systems. For that matter, there is clearly a need for simple models.

2.2.3 Wave-CISK and Mesoscale Modelling

The Wave-CISK parameterization scheme (c.f. subsection 3.3.1) was first used in mesoscale modelling by Raymond (1975, 1976). Its previous use by Yamasaki (1969), Hayashi (1970) and Lindzen (1974) was directed to the modelling of large-scale waves.

Raymond's model is linear, spectral and three-dimensional; the Coriolis parameter is set to zero. The cumulus heating as in the previous Wave-CISK studies has a given vertical distribution and is modulated by the vertical velocity at cloud base. The results of Raymond's simulation compare fairly well wtih propagation of severe storms; the shear of the mean wind is shown to have a very important role in the splitting process, a conclusion which has been confirmed by Klemp and Wilhelmson (1978) in a much more complicated model.

Raymond (1976), however, only investigated the propagation of a region of surface convergence. No attempt was made to compare modeled vertical structure with observations; the scale of the region of convergence was of 10 km, i.e., in the borderline between the small scale and the mesoscale.

2.2.4 Summary

A conclusion to be drawn from the above mentioned results is that the current state of mesoscale modelling has reached a considerable degree of sophistication: the results compare fairly well with observed features. However, the understanding of the physics governing the mesoscale motions is lagging behind the ability to model. For the purpose of understanding the different processes involved, there is a need of simple models that may be able to separate distinct physical mechanisms. The model used by Raymond (1976) is simple enough to be used as a learning tool and it can be improved in certain aspects and generalized in others. This will be the subject of chapter 3.

III. MODEL DESCRIPTION AND ASSUMPTIONS

The model to be described in the following sections may be considered as a generalized version of the one proposed by Raymond (1975, 1976) in the sense that the method of solution (which has been used previously by Yamasaki (1969) among others) is not dependent on the particular type of parameterization chosen to represent small scale processes; and also in the use of a more general initial condition.

A one sentence description of the model would be; it is a linear, spectral, non-hydrostatic model with a horizontally homogeneous basic state on a non rotating plane; cumulus heating is parameterized through the so-called Wave-CISK scheme (Yamasaki, 1969; Hayashi, 1970; Lindzen, 1974, among others) and momentum mixing by cumulus clouds is parameterized through the scheme proposed by Schneider and Lindzen (1976).

Several advantages exist in using a linear spectral model. Spectral models are especially convenient for theoretical studies where it is important to determine the contribution of each mode to the overall picture, as well as the structure of each mode separately. Furthermore, the major part of numerical problems involving finite difference approximations are avoided.

In comparison to three dimensional mesoscale numerical models (e.g. Moncrieff and Miller, 1976; Cotton and Tripoli, 1978; Brown, 1979), the linear spectral model has the advantage of providing useful information such as structure and growth of most unstable mode and sensitivity to model structure and externally specified parameters (c.f. chapter 4) without need of extensive computer time.

The validity of a linear model is restricted to the initial development of a disturbance when the non-linear terms in the governing equations may be considered small enough to be neglected. This may appear as a disadvantage; but, indeed, much can be learned about the linear behavior of the atmosphere under different circumstances, and the mathematical simplicity of a linear model as opposed to a non-linear one is especially appealing. Considering the present state of mesoscale modelling, an assessment of the importance of basic state characteristics and small scale processes, at least for the initial growth stage, is particularly desirable.

The next sections will describe the governing equations and the method of solution; test a simplified version of the model against theoretical results; and present the parameterization schemes.

3.1 Governing Equations

The governing equations are the equations of motion, thermodynamics and continuity of mass:

$$\frac{\partial \mathbf{v}}{\partial t} + \mathbf{v} \cdot \nabla \mathbf{v} + f\hat{k} \times \mathbf{v} + \frac{1}{\rho} \nabla p + g\hat{k} = 0 \tag{3.1}$$

$$\frac{\partial \theta}{\partial t} + \mathbf{v} \cdot \nabla \theta = Q \tag{3.2}$$

$$\frac{\partial \rho}{\partial t} + \nabla \cdot (\rho \mathbf{v}) = 0 \tag{3.3}$$

The symbols have the usual meanings and their definitions may be found in the List of Symbols.

The governing equations will undergo averaging, linearization and Fourier decomposition procedures. Three scales will be identified as basic state or large-scale, mesoscale and small scale. The basic state will be specified, the small scale contribution will be parameterized and the model equations solved for the mesoscale variables.

It has been found convenient to use height as the vertical coordinate rather than pressure or log-pressure due to the fact that the hydrostatic approximation is not made. Although making the model suitable for inclusion in a coarser resolution large-scale model, the use of pressure coordinates for a non-hydrostatic problem involves several approximations and does not render the problem more tractable.

First of all, denote basic state by subscript zero and the deviations from it by primes. The basic state has to obey the governing equations (3.1) - (3.3), as also does the <u>sum</u> of the basic state and deviation quantities which is represented by the non-subscripted, non-primed variables of equations (3.1) - (3.3). Subtraction of the latter set of equations from the former provides a set of equations for the primed variables. A non-rotating plane is assumed and consequently the third term on the LHS of equation (3.1) is set to zero. The neglect of the earth's rotation in a mesoscale model is indeed a valid first approximation, especially near the equator where the Coriolis parameter tends to zero and consequently the Rossby number becomes much greater than unity.

The continuity equation (3.3) is replaced by its anelastic form (equation 3.7 below) as introduced by Ogura and Phillips (1962), who

show that this form has the convenient property of filtering sound waves. Dutton and Fichtl (1969) show that the anelastic form of the continuity equation is appropriate to the modelling of deep convection. Poisson's equation, in its linearized form, will be used to eliminate the dependence of the above equations on a perturbation density.

$$\frac{\theta'}{\theta_o} = \frac{\rho'}{\rho_o} + \frac{c_v}{c_p}\frac{p'}{p_o} \tag{3.4}$$

The assumptions made so far may be summarized as

1) Separation of scales between basic state or large-scale and deviations from it which contain mesoscale and small-scale contributions;

2) Model imbedded in a non-rotating plane, or f=0;

3) Individual changes of perturbation density may be neglected in the continuity equation.

A fourth assumption is introduced in the vertical component of the momentum equation: the term $\frac{p'}{p_o} g \left(H \frac{d \ln \rho_o}{dz} - \frac{c_v}{c_p}\right)$, where H is the local scale height, is at least one order of magnitude smaller than the term $\frac{\theta'}{\theta_o} g$ and therefore may be neglected. This assumption is consistent with the anelastic approximation (Charney and Eliassen, 1964).

With the above assumptions the perturbation equations, which are obtained after subtraction from equations (3.1) - (3.3) of the corresponding equations for the basic state, may be written as

$$\frac{\partial \mathbf{v}'}{\partial t} + \mathbf{v}_o \cdot \nabla \mathbf{v}' + \mathbf{v}' \cdot \nabla \mathbf{v}_o + \nabla \frac{p'}{\rho_o} - \frac{\theta'}{\theta_o} g \hat{k} = \psi \tag{3.5}$$

$$\frac{\partial \theta'}{\partial t} + \mathbf{v}_o \cdot \nabla\theta' + \mathbf{v}' \nabla\theta_o = Q' - \psi_\theta \tag{3.6}$$

$$\nabla \cdot (\rho_o \mathbf{v}') = 0 \tag{3.7}$$

where

$$-\psi = \mathbf{v}' \cdot \nabla \mathbf{v}' + \frac{\rho'}{\rho_o^2} \nabla p', \quad \psi_\theta = \mathbf{v}' \cdot \nabla \theta' \tag{3.8}$$

Note that the non-linear terms are still present in the right hand side of Eqs. (3.5) and (3.6) through the term $\psi = (\psi_x, \psi_y, \psi_z)$ and ψ_θ defined in Eq. (3.8).

Equations (3.5) - (3.7) are five equations (equation 3.5 represents the vector form of the momentum equation) into five unknowns $\mathbf{v}'$ (u', v', w'), p' and θ', and are similar to the ones used by Raymond (1975). In the derivation of Eqs. (3.5) - (3.7) it has been assumed that the atmospheric motions can be separated into a basic state and the deviations from it. A step further is taken now when the deviations from the basic state variables are broken into mesoscale variables and small scale variables. Mathematically this separation of scales requires a simple averaging technique. Physically, however, there is no certainty that this is possible or even reasonable since very little is known about scale interaction from the observational point of view. A justification for the widespread use of this technique is that different physical mechanisms govern the motions in each scale: for example, turbulence may play a minor role in long atmospheric waves and mesoscale motions, but be important in cumulus scale processes. On the assumption that different physical mechanisms govern the motion of each scale, the separation of mesoscale from small scale variables will be performed here.

To separate the mesoscale from the smaller scale phenomena a horizontally running average is defined as

$$\langle \mathbf{v}'(x,y,z,t)\rangle = \frac{1}{\Delta x \Delta y}\int_{x-\frac{\Delta x}{2}}^{x+\frac{\Delta x}{2}}\int_{y-\frac{\Delta x}{2}}^{y+\frac{\Delta y}{2}} \mathbf{v}'(r,s,z,t)\,dr\,ds \qquad (3.9)$$

so that the perturbation fields may be written as

$$\mathbf{v}' = \langle \mathbf{v}'\rangle + \mathbf{v}'' \qquad (3.10)$$

where the two primes refer to the residual after the running average is performed and correspond to the small-scale contribution.

The linearity assumption is made now. Equation (3.8) may undergo a smoothing by the running average defined above and be written as

$$\langle -\psi\rangle = \langle \mathbf{v}'\rangle \cdot \nabla\langle \mathbf{v}'\rangle + \langle \frac{\rho'}{\rho_o^2}\rangle \nabla\langle p'\rangle + \langle \mathbf{v}'' \cdot \nabla \mathbf{v}''\rangle + \langle \frac{\rho''}{\rho_o^2}\nabla p''\rangle$$

$$\langle -\psi_\theta\rangle = \langle \mathbf{v}'\rangle \cdot \nabla\langle \theta'\rangle + \langle \mathbf{v}'' \cdot \nabla\theta''\rangle \qquad (3.11)$$

The linearity assumption consists in neglecting the correlation between mesoscale quantities in equations (3.11). The transports by small-scale processes as defined in equations (3.11) are subsequently parameterized (section 3.3). This assumption will only be valid in the initial growth stage where the mesoscale perturbation quantities are still small and so their products may be neglected in equations (3.11).

a) Basic State

Examining equations (3.5) - (3.7) it may be seen that there is no explicit dependence in the specified coefficients, or basic state variables, on space variables or time. Choosing a basic state with vertical structure but horizontally homogeneous and steady makes the Fourier decomposition of the mesoscale variables a particularly useful mathematical tool since in this case there is no coupling between horizontal, vertical and time derivatives. The mesoscale velocity field may be represented by the integral

$$\langle \mathbf{v}'(x,y,z,t)\rangle = \iint_{-\infty}^{+\infty} \hat{\mathbf{v}}(k,z) \exp i(\mathbf{k}.\mathbf{r} - \omega t)\, dk_x dk_y \qquad (3.12)$$

and analogously for the other variables.

If the basic state variables depended upon all three space dimensions, the perturbation equations would either have to be solved by finite difference techniques or involve the solution of an eigenvalue problem for four dimensional matrices with the consequent problems of storage and extensive computer time in both cases. On the other hand, a three dimensional basic state would allow vorticity and divergence on this scale. However, the observed large-scale fields may already have the contribution of mesoscale systems (e.g. $\langle \mathbf{v}' \cdot \nabla \mathbf{v}' \rangle$) so that the consistent specification of the basic state would involve several assumptions and approximations.

The specification of a more realistic basic state will be left as a subject of future work. Here the basic state quantities will be assumed to be dependent on height only. Note, however, that the profile

$$-i\ (\omega - \mathbf{k}.\mathbf{v}_o)\ \hat{u} + \frac{du_o}{dz}\ \hat{w} + i\frac{k_x}{\rho_o}\ \hat{p} = \psi_x \tag{3.13}$$

$$-i\ (\omega - \mathbf{k}.\mathbf{v}_o)\ \hat{v} + \frac{dv_o}{dz}\ \hat{w} + i\frac{k_y}{\rho_o}\ \hat{p} = \psi_y \tag{3.14}$$

$$-i\ (\omega - \mathbf{k}.\mathbf{v}_o)\ \hat{w} + \frac{d}{dz}\frac{\hat{p}}{\rho_o} - \frac{g}{\theta_o}\ \hat{\theta} = \psi_z \tag{3.15}$$

$$-i\ (\omega - \mathbf{k}.\mathbf{v}_o)\ \hat{\theta} + \frac{d\theta_o}{dz}\ \hat{w} = Q - \psi_\theta \tag{3.16}$$

$$i\ \mathbf{k}.\hat{\mathbf{v}} + \frac{1}{\rho_o}\frac{d}{dz}\ (\rho_o\ \hat{w}) = 0 \tag{3.17}$$

The solution of the above system for the variables with hat, as will be seen in the following sections, consists in finding, for each value of wavenumber $\mathbf{k} = k_x\mathbf{i} + k_y\mathbf{j}$, the values of frequency ω for which the above equations have a solution. This is a so-called eigenvalue problem where ω is the eigenvalue and $\hat{u},\hat{v},\hat{w},\hat{p},\hat{\theta}$ are the corresponding eigenfunctions. Clearly, for a fixed $\mathbf{k}$ several ω may be found. Also, ω may be a complex number: the real part of ω is related to phase speed c_r

$$\omega = \omega_r + i\ \omega_i = (c_r + i\ c_i)(k_x^2 + k_y^2)^{\frac{1}{2}} = c(k_x^2 + k_y^2)^{\frac{1}{2}} \tag{3.18}$$

and the imaginary part, to the exponential growth. The exponential in equation (3.12) may be rewritten as

$$\exp\left[i\ (\mathbf{k}\cdot\mathbf{r} - \omega_r t) + \omega_i t\right] \tag{3.19}$$

of wind may have directional shear since both zonal and meridional components of the basic state wind will be specified.

If small scale processes are neglected, a consistent basic state with only vertical shear of the horizontal wind contains no vertical motion. However, the parameterization of ψ_x, ψ_y, which will be done in section 3.3.2, will involve adding an extra term to the right hand side of the basic state equations in which case a consistent set of equations requires a basic state with vertical velocity. As will be seen in section 3.3.2, an optimum profile of basic state vertical velocity can be found to have approximately constant mass flux and consequently to be almost non-divergent. The horizontal components of the wind may then remain as functions of height only.

The basic state density will be specified as having an exponential decay with height, with density scale height equal to $R\ T_o\ (z=0)/g$.

As it is, the problem consists of specifying the basic state quantities, define a parameterization scheme that will give the terms in equation (3.11) and solve the equations for the mesoscale variables.

b) Final Set of Equations

The assumptions and approximations discussed above are applied to the perturbation equations (3.5) - (3.7). The equations are then averaged according to the running average defined in equation (3.9) and Fourier decomposed according to equation (3.12). Due to the linearity assumption the term under the integral sign in equation (3.12) will be a solution of the equations for all wave number $\mathbf{k}$. In this way, the governing equations will be written as

A positive ω_r means propagation in the same direction as the wavenumber vector $|k = k_x |i + k_y j|$ while negative ω_r (or c_r) means propagation in the opposite sense as the one defined by $|k$. A positive ω_i (or c_i) means exponential growth and a mode for which ω_i is positive is called an unstable mode. A neutral mode is one for which ω_i is zero and a decaying (or stable) mode is associated with negative ω_i.

3.1.1 Finite Difference Scheme

To solve the system of equations (3.13) - (3.17), a vertical differencing scheme has to be defined since the vertical derivatives are not analytical and the large-scale fields depend on height. Following the scheme proposed by Arakawa and Lamb (1977), the atmosphere has been divided into N layers by N-1 levels of constant z. The layers are identified by integer index and carry the horizontal components of velocity $\hat{u}$ and $\hat{v}$, the potential temperature $\hat{\theta}$ and pressure $\hat{p}$. The levels which divide the layers are identified with half indices and carry the vertical velocity $\hat{w}$. Figure 3.1 shows the vertical structure of the model. This scheme conserves integral properties of atmospheric parameters (cf. Arakawa and Lamb, 1977).

$$-i\,(\omega - |k \cdot |v_o^{\,i})\,\hat{u}_i + \frac{1}{2}\left(\frac{du_o}{dz}^{\,i+\frac{1}{2}}\,\hat{w}_{i+\frac{1}{2}} + \frac{du_o}{dz}^{\,i-\frac{1}{2}}\,\hat{w}_{i-\frac{1}{2}}\right) -$$

$$+\, i\,\frac{k_x}{\rho_o^{\,i}}\,\hat{p}_i - \hat{\psi}_{x_i} = 0 \qquad (3.20)$$

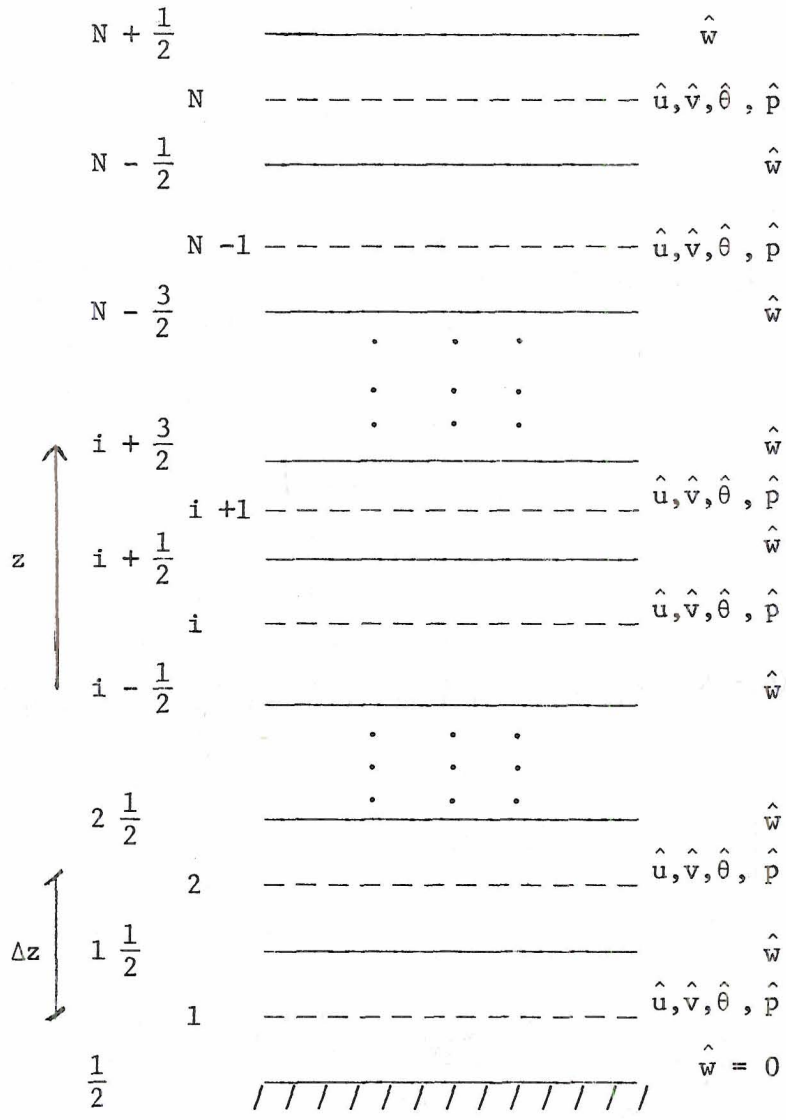

Figure 3.1. The vertical structure of the model showing distribution of variables; solid lines ($i+\frac{1}{2}$) indicate the levels dividing the layers; dashed lines (integer i) indicate levels within layers at which the indicated variables are carried.

$$-i\ (\omega - \mathbb{k}\ .\ \mathbb{v}_o^{\ i})\ \hat{v}_i + \frac{1}{2}\left(\frac{dv_o}{dz}^{i+\frac{1}{2}}\ \hat{w}_{i+\frac{1}{2}} + \frac{dv_o}{dz}^{i-\frac{1}{2}}\ \hat{w}_{i-\frac{1}{2}}\right) +$$

$$+\ i\ \frac{k_y}{\rho_o^{\ i}}\ \hat{p}_i - \hat{\psi}_{y_i} = 0 \tag{3.21}$$

$$-i\left[\omega - \mathbb{k}.\ \frac{1}{2}\ (\mathbb{v}_o^{\ i+1} + \mathbb{v}_o^{\ i})\right]\ \hat{w}_{i+\frac{1}{2}} + \frac{1}{\Delta z}\left(\frac{\hat{p}_{i+1}}{\rho_o^{\ i+1}} - \frac{\hat{p}_i}{\rho_o^{\ i}}\right)$$

$$-\ \frac{g}{2}\left(\frac{\hat{\theta}_{i+1}}{\theta_o^{i+1}} + \frac{\hat{\theta}_i}{\theta_o^{i}}\right) - \hat{\psi}_{z_i} = 0 \tag{3.22}$$

$$-i\ (\omega - \mathbb{k}\ .\ \mathbb{v}_o^{\ i})\ \hat{\theta}_i + \frac{1}{2}\left(\frac{d\theta_o}{dz}^{i+\frac{1}{2}}\ \hat{w}_{i+\frac{1}{2}} + \frac{d\theta_o}{dz}^{i-\frac{1}{2}}\ \hat{w}_{i-\frac{1}{2}}\right)$$

$$-\hat{Q}_i\ -\hat{\psi}_{\theta_i} = 0 \tag{3.23}$$

$$i\ \mathbb{k}\ .\ \hat{\mathbb{v}}_i + \frac{1}{\rho_o^{\ i}}\ \frac{\rho_o^{\ i+\frac{1}{2}}\ \hat{w}_{i+\frac{1}{2}} - \rho_o^{\ i-\frac{1}{2}}\ \hat{w}_{i-\frac{1}{2}}}{\Delta z} = 0 \tag{3.24}$$

Equation (3.24) may, indeed, be used to eliminate one of the components of the horizontal velocity vector, and this has been done here since it reduces the computer storage needed; but the formalism is the same and will not be presented.

3.1.2 Boundary Conditions

The boundary condition at the surface is that of no vertical velocity. A rigid boundary condition at the top of the model has the error of reflecting the waves back into the model domain, thus introducing non-realistic oscillations. Klemp and Lilly (1978) examined the problem of reflection by the upper boundary and concluded that any locally specified boundary condition does trap wave energy instead of allowing it to radiate away. They imposed a viscous layer beneath the upper boundary designed to remove the upward propagating wave energy before it can be reflected. Equations (3.16), (3.17) and (3.18) would then have an additional term $\nu \frac{d^2 w}{dz^2}$, with ν increasing gradually from zero at the bottom of the viscous layer to some value ν_T at the top. A problem with this scheme is that, to be effective, it needs a considerable amount of grid points inside the viscous layer. Due to computer storage limitations, this is not convenient for the model described here since this artificial viscous layer would occupy most of the model atmosphere. The radiation-type boundary condition presents another alternative. As introduced by Eliassen and Palm (1960) it consists of imposing, as the solution in the uppermost layer, an expression for the vertical velocity which allows tropospheric energy to be radiated away to upper levels. The procedure followed by Eliassen and Palm (1960) was to apply a vertical structure equation, to layers of constant temperature and wind.

Following the same procedure as Eliassen and Palm (1960), we examine the vertical structure equation. According to Raymond (1975), the vertical structure equation corresponding to the system (3.13) -

(3.17) without eddy terms is

$$\frac{d^2\rho_o^{\frac{1}{2}}\hat{w}}{dz} + \left[\frac{g\ d\ \ln\ \theta_o/dz}{(c-v_k)^2} - \frac{1}{(c-v_k)}\left(\frac{1}{H}\frac{dv_k}{dz} + \frac{d^2v_k}{dz^2}\right) - \frac{1}{4H^2} - |k|^2\right]\rho_o^{\frac{1}{2}}w = 0 \tag{3.25}$$

where v_k is $\mathbf{v}_o \cdot \mathbf{k}/|\mathbf{k}|$ and c is $\omega/|\mathbf{k}|$.

In the uppermost layer, the coefficient in equation (3.25) is assumed constant with $d\mathbf{v}_o/dz = 0$, so that the solution is

$$\rho_o^{\frac{1}{2}}\hat{w} = A\ e^{i\lambda z} + B\ e^{-i\lambda z}\ , \tag{3.26}$$

where

$$\lambda^2 = \frac{g\ d\ln\ \theta_o/dz}{(c-v_k)^2} - |k|^2 - \frac{1}{4H^2} \tag{3.27}$$

The radiation condition consists in the elimination of one of the solutions of equation (3.26), namely, the one corresponding to downward energy flux. Eliassen and Palm (1960), Charney and Pedlosky (1963), and Lindzen (1974) discuss the choice of the solution. It may be seen from equation (3.27) that the imaginary parts of c and λ have opposite signs so that in the case of growth ($c_i>0$), the imaginary part of λ is negative. The requirement that unstable waves decay with height implies

that the solution to be retained in equation (3.26) is the one with the negative sign in the exponential.

The equation for the vertical velocity at the uppermost layer may be written as

$$\left(c - v_k\right)\frac{d}{dz}(\rho_o^{\frac{1}{2}}\,\hat{w}) + i\left[g\,\frac{d\,\ln\theta_o}{dz} - (|k^2| + \frac{1}{4H^2})\,(c - v_k)^2\right]^{\frac{1}{2}}\rho_o^{\frac{1}{2}}\,\hat{w} = 0 \tag{3.28}$$

Equation (3.28) shows that except for the term in $|k^2 - 1/4H^2$ inside the brackets this expression is linear in c (or ω), and consequently consistent with the eigenvalue problem to be posed in the next section. For an isothermal layer at about 15 km the first term is of the order of $5 \times 10^{-3}\,s^{-2}$, while the second term in brackets, for a short wavelength of about 10 km is two orders of magnitude smaller ($\sim 5 \times 10^{-5}\,s^{-2}$) so that it can be neglected. With that the finite difference form of equation (3.28) is

$$\frac{1}{|k|}\left(\omega - |k\,.\,v_o^N\right)\frac{\rho_o^{\frac{1}{2}N+\frac{1}{2}}\,\hat{w}_{N+\frac{1}{2}} - \rho_o^{\frac{1}{2}N-\frac{1}{2}}\,\hat{w}_{N-\frac{1}{2}}}{\Delta z} + i\left[g\left(\frac{d\,\ln\theta_o}{dz}\right)^N\right]^{\frac{1}{2}}\frac{1}{2}\left(\rho_o^{\frac{1}{2}N+\frac{1}{2}}\,\hat{w}_{N+\frac{1}{2}} + \rho_o^{\frac{1}{2}N-\frac{1}{2}}\,\hat{w}_{N-\frac{1}{2}}\right) = 0 \tag{3.29}$$

3.1.3 Method of Solution

Equations (3.20) - (3.24) form a linear homogeneous system of equations provided the parameterizations of heating and eddy momentum

transports are linear function of the dependent variables. In this case, the mentioned system may be written as

$$(A - \omega B)\, \hat{\underset{\sim}{Z}} = 0 \tag{3.30}$$

where

$$\hat{\underset{\sim}{Z}} = \Big(\hat{u}_1, \hat{v}_1, \hat{p}_1, \hat{\theta}_1, \hat{w}_{1\frac{1}{2}}, \hat{u}_2, \hat{v}_2, \ldots\ldots \\ \hat{u}_{N-1}, \hat{v}_{N-1}, \hat{p}_{N-1}, \hat{\theta}_{N-1}, \hat{w}_{N-\frac{1}{2}}, \hat{u}_N, \hat{v}_N, \hat{p}_N, \hat{\theta}_N, \hat{w}_N\Big) \tag{3.31}$$

and A and B are MxM matrices of the coeficients defined by equations (3.20) - (3.24). With a rigid upper boundary condition, M is 5 N-1 and $\hat{Z}$ does not have the term $\hat{w}_N$. With the radiation condition $\hat{w}_N$ is allowed to vary and so with the introduction of equation (3.29) the dimensions of A and B are increased by 1 (M = 5N).

Equation (3.30) is the representation of a complex generalized eigenvalue problem, where the frequency ω is the eigenvalue and $\hat{Z}$ is the corresponding eigenvector. For each fixed $|k$, equation (3.30) defines several eigenvalues and eigenvectors. Pedlosky (1964) studied the problem of completeness in the set of eigenfunctions. His reasoning shows that if the initial condition is wavelike in the horizontal plane with a certain wavenumber K and the vertical structure is arbitrary, it is necessary to include the continuous spectrum to describe an arbitrary condition. Koss (1976) also refers to the impossibility of describing arbitrary initial conditions with a non-complete set of eigenfunctions. Raymond (1976) defined the initial condition at the surface only and let the vertical structure be determined by the

eigenfunctions of interest, namely, the ones corresponding to the most unstable modes. The surface initial condition may then be reproduced if enough wavenumbers are considered. The procedure to be followed here will be, basically, a generalization of Raymond's approach. The evolution from the initial condition will be obtained with a particular sub-set of eigenvectors. Since this particular sub-set is not complete, only the projection of the initial condition will be reproduced and only the evolution of this part will be obtained. However, if the initial perturbation is given at the surface only, as in Raymond (1976), again the surface initial condition will be reproduced and the vertical structure will be determined by the eigenfunctions. This approach permits giving the initial condition at any level and any combination of variables. For each wavenumber $|k$, several unstable modes exist. In some cases, the most unstable mode has growth rate much greater than the second most unstable mode; in other cases, the two or three most unstable modes have comparable growth rates, in which case the resulting structure will be a combination of these modes. The usual approach (e.g. Raymond, 1975) is to consider, for each wavenumber $|k$, only the contribution of the most unstable mode. In the case of having several modes with comparable growth, this may lead to very different results. The procedure to be followed here will allow for the use of as many unstable modes, for each $|k$, as considered necessary. It may be regarded as a generalization of Raymond's approach in this aspect too.

The mathematical procedure is the following. Equation (3.12) may be rewritten for all variables in the following vector form

$$\underset{\sim}{Z}\ (x,y,t) = \underset{\sim}{Z}_o + \iint_{-\infty}^{+\infty} \hat{\underset{\sim}{Z}}\ (|k\ ,\ t)\ \ e^{i\,|k.|r}\ dk_x dk_y \tag{3.32}$$

where

$$\begin{aligned}\underset{\sim}{Z}\ (x,y,t) = \Big(&u_1(x,y,t),\ v_1(x,y,t,),\ p_1(x,y,t),\ \theta_1(x,y,t),\\ &w_{1\frac{1}{2}}\ (x,y,t),\ u_2(x,y,t),\ldots,u_N(x,y,t),v_N(x,y,t),\\ &p_N(x,y,t),\ \theta_N(x,y,t),\ w_{N+\frac{1}{2}}(x,y,t)\Big)\end{aligned} \tag{3.33}$$

and

$$\left(\underset{\sim}{Z}_o = u_o^1,\ v_o^1,\ p_o^1,\ \theta_o^1,\ w_o^{1+\frac{1}{2}},\ u_o^2,\ldots,\ u_o^N,\ v_o^N,\ p_o^N,\ \theta_o^N,\ w_o^{N+\frac{1}{2}}\right) \tag{3.34}$$

At the initial time equation (3.32) gives the value of $\hat{\underset{\sim}{Z}}(|k,0)$ as

$$\hat{\underset{\sim}{Z}}\ (|k\ ,o) = \frac{1}{(2\pi)^2} \iint_{-\infty}^{+\infty} \left(\underset{\sim}{Z}(x,y,o) - \underset{\sim}{Z}_o\right) e^{-i\,|k.|r}\ dxdy \tag{3.35}$$

The evolution in time, based on a particular sub-set of unstable modes for each wavenumber $|k$, will be obtained if we define

$$\hat{\underset{\sim}{Z}}\ (|k,\ t) \underset{\sim}{\sim} \sum_m C\ (|k,m)\ \ \hat{\underset{\sim}{Z}}\ (|k,m)\ e^{-i\omega(|k,m)\ t} \tag{3.36}$$

The sub-set of eigenvectors may be orthonormalized without loss of generality so that

$$C\ (|k,m) = \left(\hat{\underset{\sim}{Z}}\ (|k,o)\ \ ,\ \hat{\underset{\sim}{Z}}\ (|k,m)\right) \tag{3.37}$$

which follows from the substitution of equation (3.36) into equation (3.32) evaluated at the initial time. The parenthesis in equation (3.37) refers to the inner product between two vector quantities.

In the way it has been defined, equation (3.36) defines the projection of the initial condition onto the particular sub-set of eigenfunctions chosen.

3.1.4 Final Computations

Evaluation of the integrals in equations (3.32) and (3.35) requires discretization so that the integrals are replaced by sums. The wavenumber may be chosen to be an inverse multiple of a horizontal dimension ($n_x\ 2\pi/L_x$, $n_y\ 2\pi/L_y$). In this case the initial condition will be periodic with period L_x in the x- direction and L_y in the y-direction. If L_x and L_y are large enough, the initial development of the disturbance will be free from interference from neighboring periodic solutions. On the other hand, a large value of L_x and L_y requires a large number of k_x and k_y's for which the eigenvalue problem has to be evaluated with the consequent need of extensive computer time. A compromise has been found using $L_x = L_y = 300$ km and n_x, $n_y = -29...-1, 0, 1...29$ so that the highest mode has a wavelength of 10.5 km. Looking into an area of 200 km length and width centered in the proximity of the disturbance increases the time for which the solution is free from interference from the periodic boundary conditions of the solution. The integral in equation (3.35) may be evaluated analytically by giving an analytical form of the initial disturbance. The particular form used will be given in the next chapter.

Two computer programs have been developed to simulate the model. The first resolves the eigenvalue problem subject to imposed basic state profiles of temperature and wind and stores the eigenvalues and eigenvectors for further use. The second program defines an initial condition and computes the time evolution of any desired field. The measure of reliability of the second program is seen in its ability to reproduce the initial condition by calculating equation (3.33) at the initial time. This will be discussed in the next chapter of model results. The accuracy of the algorithm that calculates the eigenvalues and eigenvectors will be examined in the following two sections.

3.2 Test of the Model without Parameterizations

Before going further into the details of parameterization schemes, it was found necessary to check the computer program which finds the solution to the eigenvalue problem against theoretical studies. In this section, an upper boundary with no vertical velocity will be used as boundary condition since this is the boundary condition used in the studies that will be referred to below.

3.2.1 Speed of Internal Gravity Waves

With the appropriate basic state the model should be able to reproduce the speed of internal gravity waves. According to Haltiner (1971), the phase speed of internal gravity waves in a non-rotating flow with no basic state velocity and isothermal atmosphere is

$$c_x = \frac{\omega}{k_x} = \pm \frac{k_x}{k_x^2 + k_z^2} \left(\frac{g}{\theta_o} \frac{d\theta_o}{dz} \right)^{\frac{1}{2}} \tag{3.38}$$

where k_z is the vertical wavelength. In this case, the phase speed c_x is real since the atmosphere is stably stratified. k_y is set to zero in this test.

A 3-layer model produced the results of Table 1. Increasing the vertical resolution to a 9-layer model provided better approximation to the theoretical phase velocity. For the longer vertical wavelengths, the error is only 10% in the 3-layer model decreasing to 1% in the 9-layer model. As the vertical wavelength decreases it becomes less well resolved by the vertical grid and the error increases. This emphasizes a need for good vertical resolution. The phase velocity in this case is a real number and no instability is observed (the profile of θ_o is stable and there is no mechanism to generate instability.

3.2.2 Instability of Stratified Sheared Flows

The inclusion of a sheared basic state wind field makes the theoretical problem a bit more complicated. With no rotation and no small-scale processes, and making the incompressibility assumption, the system of equations (3.13) - (3.17) can be combined into a single equation for $\hat{w}$ (assume $k_y = 0$, $v_o(z) = 0$).

$$\frac{d^2w}{dz^2} + \left\{ \frac{N^2(z)}{u_o(z)-c^2} - \frac{d^2u_o/dz^2}{u_o(z)-c} - k_x^2 \right\} \hat{w}(z) = 0 \tag{3.39}$$

Table 1. Phase velocities given by the 3-layer model and by equation (3.38) for different horizontal and vertical wavelengths. H is 9 km and $(g/\theta_o)\, d\theta_o/dz$ is $3.11 \times 10^{-4}\ s^{-2}$, ($k_y = 0$), $\Delta z = 3$km.

L_z (km)	k_x (km^{-1})	c-model ($m.s^{-1}$)	c - Eq(3.38) ($m.s^{-1}$)
2H	0.1	43.5	48.6
	0.4	29.5	33.2
2H/3	0.1	15.0	16.8
	0.4	12.5	15.7

Table 2. Same as Table 1, but for 9-layer model, $\Delta z = 1$km.

L_z (km)	k_x (km^{-1})	c-model ($m.s^{-1}$)	c - Eq(3.38) ($m.s^{-1}$)
2H	0.1	48.1	48.6
	0.4	32.8	33.2
H	0.1	24.0	25.0
	0.4	20.9	21.9
2H/3	0.1	15.2	16.8
	0.4	14.2	15.7
H/2	0.1	10.5	12.6
	0.4	10.0	12.1
4H/9	0.1	7.4	11.2
	0.4	7.2	10.9
H/3	0.1	5.1	8.4
	0.4	4.9	8.3
2H/9	0.1	3.2	5.6
	0.4	3.1	5.6

This is the so-called Taylor-Goldstein equation, where

$$N^2(z) = -g \frac{d \ln \rho_o}{dz} \tag{3.40}$$

is the Burnt-Vaisälä frequency. Equation (3.39) has been studied extensively in fluid mechanics (e.g. Howard, 1961, Hazel, 1971 among others) and therefore the solutions may be compared easily with the present model. In order to make this comparison, equation (3.16) has been replaced by the corresponding one for a compressible fluid

$$-i\ (\omega - \mathbf{k}.\mathbf{v}_o)\ \hat{\rho} + \hat{w} \frac{d \rho_o}{dz} = 0 \tag{3.41}$$

Hazel (1971) uses the incompressible form of the continuity equation to derive equation 3.39 and so it will be used here also. In equation (3.13) the last left-hand-side term is substituted using equation (3.4).

The method of solution of equation (3.41) is to impose boundary conditions and find the eigenvalues c as a function of k_x. Note that if the hydrostatic approximation is made, the equation becomes

$$\frac{d^2\hat{w}}{dz^2} + \left\{ \frac{N^2(z)}{\left(u_o(z)-c\right)^2} - \frac{d^2u_o/dz^2}{u_o(z)-c} \right\} \hat{w}(z) = 0 \tag{3.42}$$

and it can be seen that the eigenvalue c is independent of k_x. The computer program was run making the hydrostatic approximation with arbitrary wind and temperature profiles and it was confirmed that $c = \omega/k_x$ is not a function of k_x. Equation (3.42) shows that the hydrostatic

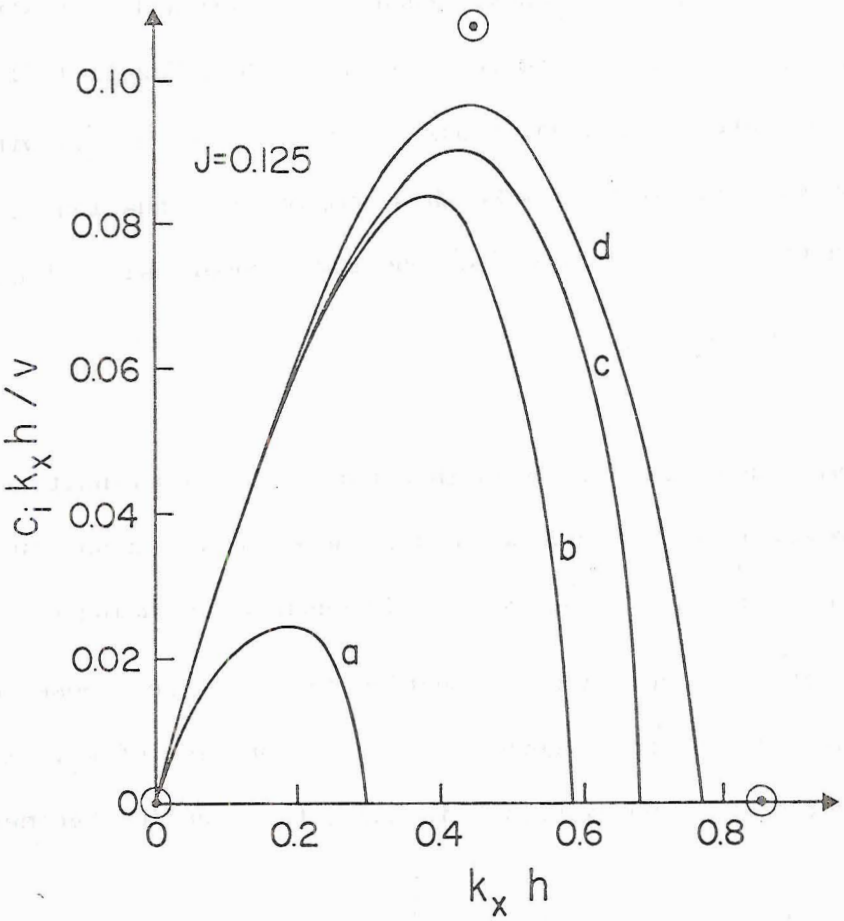

Figure 3.2 Non dimensional growth rate as a function of non-dimensional wavenumber for Richardson number J=0.125: a) 5-layer model b) 10-layer model; c) 15-layer model; d) same as c except for the use of a 4th order differencing scheme to calculate basic state derivatives; ⊙ results from Hazel (1971).

assumption is justified for long wavelengths where k_x^2 can be neglected in equation (3.39).

Hazel (1971) solved equation (3.39) subject to the boundary conditions of no vertical velocity at the top and bottom of the model. In one of his cases, the profiles of wind and density were given by

$$u_o(z) = V \tanh \frac{z-z_o}{h} \tag{3.43a}$$

$$\frac{1}{\rho_o} \frac{d\rho_o}{dz} = \sigma \tanh \frac{z-z_o}{h} \tag{3.43b}$$

where V is a typical velocity, z_o is H/2, σ is a typical density measure and h is the depth of the shear layer. The results were given in terms of a Richardson number defined as

$$J = \sigma g h / V^2 \tag{3.44}$$

Figure 3.2 shows the growth rate nondimensionalized as in Hazel (1971) as a function of nondimensional wavenumber, obtained with J = 0.125 for different vertical resolutions. Hazel (1971) gives, for each J, the value of maximum growth rate and the associated wavenumber and also the wavenumber where the stability is neutral. These three points are plotted as circles in Figure 3.2 for comparison. The other curves were run with a 1 km shear layer in the basic state, the depth of the atmosphere being 9 km; it can be seen that with increased resolution of the shear layer the results tend to the theoretical ones.

In order to describe the basic state derivatives in a more precise way, a fourth order finite difference scheme was introduced: curve d of Figure 3.2 indicate the improved results. This is a rather extreme case since it is not common in the atmosphere to have such shallow shear layers, except perhaps in billow clouds, but it emphasizes the need for vertical resolution in order to accurately describe the instability characteristics.

3.3 Parameterization of Small-scale Processes

Questions on the validity of the attempts to parameterize small-scale atmospheric processes are raised by many atmospheric scientists nowadays on the basis that very little is known about the physics of small-scale processes, in general, and of the scale interactions, in particular. The modellers, on the other hand, feel the need to include phenomena of scales smaller than the ones under study but are constrained by computing limitations. The solution for modellers is always to close the system of equations, at some point, with the introduction of a parameterization theory. Between the observationlists claiming that it is too soon to parameterize and the modellers saying that they will do it anyway with the available techniques, very little work has been done to prove, disprove or improve the validity of current parameterization schemes either theoretically or from data analysis.

The model described in this thesis is intended for mesoscale analysis and with this purpose will look into scales from ten to a few hundred kilometers. The cumulus scale falls into the smaller scale and obviously plays a very important role in the description and

understanding of mesoscale motions; thus we parameterize the cumulus scale. This is a crucial step, however, since very little is known of the interaction of cumulus scale and mesoscale motions. But, as modellers always do, we still want to try, and see what we get...

It should be stressed here that the chosen parameterization schemes do not include all small-scale physical processes that can be considered as influencing the mesoscale motions, but rather those processes that are believed more important and already have a developed parametric theory.

3.3.1 Cumulus Heating

The diabatic heating in the cumulus scale affects the mesoscale temperature fields through the term ψ_θ on the right hand side of equation (3.16). The horizontal advection of temperature by the small scale in ψ_θ will be neglected under the assumption that the diabatic heating rate offers a bigger contribution. A future revision of this model should attempt to include these terms perhaps through the so-called pseudoviscosity concept used to parameterize turbulent transports (see Cotton, 1975). Q is the mesoscale diabatic heating and is neglected here since there is no moisture in the present model. All the moisture is in the cumulus scale processes.

The CISK (Conditional Instability of the Second Kind) mechanism as envisioned by Charney and Eliassen (1964), Ooyama (1963) and very well described by Ooyama (1969), is based on the idea that cumulus clouds and large-scale tropical systems support each other, the cumulus cell by supplying the heat energy for driving the depression and the depression by providing low-level convergence of moisture into the

cumulus cell. The mid tropospheric air in the tropics is not convectively unstable so that moist convection depends critically on the high values of moist static energy in the boundary layer. In order to support organized convective activity for a period much longer than the time scale of individual convective clouds it is apparently necessary for the boundary layer flow to converge so that unstable air will be continuously supplied to convective clouds. Clouds then provide the lifting of air parcels; i.e., they generate potential energy that is released in compensating downward motions that will adiabatically warm the environment of clouds; this warming enhances the depression and therefore also the low-level convergence. This physical mechanism may be used to explain interaction between the cumulus scale and the mesoscale as well, or perhaps in a better way, even if the time scale of mesoscale events is not as large as that of large-scale systems, because the convergence supplied by mesoscale systems may be one or two orders of magnitude larger than that provided by the large-scale ones.

The classical way (e.g. Ooyama, 1969) to parameterize the CISK concepts has been to add a diabatic heating term in the thermodynamic equation (3.2) of the form

$$-\psi_\theta = \eta(z)\ w^* = \langle w'' \frac{\partial \theta''}{\partial z} \rangle \qquad (3.45)$$

where w^* is the vertical velocity at the top of the boundary layer and η is a function of height. This term would supposedly cancel the adiabatic cooling due to lifting of air parcels. Several criticisms

have been raised to that form of parameterization. First of all, w* should be a characteristic mean updraft vertical velocity and is, indeed, a mean between up and down motions and so it may not balance the adiabatic cooling. This criticism applies mainly to the earlier versions of CISK which were regarded as representing Ekman layer pumping. The second and most serious criticism is that the results are sensitive to the specified heating profile such that one can obtain any desired result by simply tuning the heating profile. Chang (1976) studied the sensitivity of the eigenvalues of the vertical structure equation to different intensities and shapes of the heating function. His computations show that the real part of the eigenvalues are little affected by the intensity of the heating rate or by variations in the level of maximum heating rate while the imaginary part of the eigenvalue is highly sensitive to both. This means that a sound physical reason for choosing the heating rate profile must be given to justify the use of this parameterization.

The parameterization to be used here will be the one used by Stevens and Lindzen (1978) and described in what follows. Stevens and Lindzen (1978) defined the intensity of the heating rate from a budget point of view, i.e., the integrated heating in a column has to equal the net condensation minus evaporation which equals the precipitation at the surface P

$$\int_0^\infty c_p' \frac{T_o}{\theta_o} \psi_\theta \rho \, dz = L_v P \tag{3.46}$$

where P is given by

$$P = \int_0^\infty \nabla.(\rho_o q_o \mathbf{v})\, dz \simeq q_o \rho_{o_{ML}}\, w_{ML} \tag{3.47}$$

which assumes that the main moisture source is from a so-called moist layer (sub) ML) with mean mixing ratio equal to q_o. w_{ML} is the vertical velocity at the top of the moist layer. Now, if the shape of the heating profile is given by

$$\eta(z) = \begin{cases} \alpha \dfrac{\theta_o}{T_o} \exp(bz) \sin \dfrac{\pi(z-z_c)}{z_T-z_c} & z_c \leq z \leq z_T \\ 0 & z \leq z_c \quad \text{and} \quad z \geq z_T \end{cases} \tag{3.48}$$

The magnitude of the heating rate is given by

$$\alpha = \frac{L_v\, q_o \exp\,(-z_{ML}/H)\,(z_T-z_c)\left[(b-1/H)^2 + \pi/(z_T-z_c)^2\right]}{\pi\, c_p \left\{\exp\left[(b-1/H)z_T + (b-1/H)\, z_c\right]\right\}} \tag{3.49}$$

Equations (3.48) and (3.49) allow for different levels of maximum heating with the same integrated value of the heating rate, which is basically dependent on the mean mixing ratio in the moist layer. Note that the eigenvalue condition is given by $w_{ML} = w'(z_{ML})$.

3.3.2 Momentum Mixing

Observational studies (e.g., Houze, 1973) have shown that vertical momentum transport by cumulus may be of the same order of magnitude as

the large-scale vertical momentum transport. The mesoscale contribution is, however, mixed up with the cumulus scale contribution, so that no real assessment of the former has been done. In modeling the mesoscale motions, the cumulus scale transports also play an important role. Schneider and Lindzen (1976) parameterized the momentum exchange by cumulus convection for use in large-scale models of the tropical atmosphere. The main assumption involved is that the fractional area covered by convective clouds is much less than one. Though this assumption will be only marginally valid in the case of mesoscale circulations, this parameterization will be used here for lack of a more suitable one. The terms ψ_x, ψ_y, ψ_z in equations (3.13) - (3.15) contain (c.f. equation (3.11)) the transports of momentum by the small scale and the correlation of small scale pressure gradient and density. Cloud modellers regard the non-hydrostatic pressure perturbation as a very important term in the equations. Holton (1973) presented a theory to parameterize the non-hydrostatic perturbation pressure. In the present model, however, the mesoscale motions are assumed to be non-hydrostatic and so the small scale pressure perturbation is a deviation about a field that already contains significant vertical accelerations. The theory presented by Holton was intended to correct the assumption that the pressure inside the cloud equals the environmental pressure which was hydrostatic. It is not certain that Holton's scheme is appropriate to the present model. This is certainly an example of lack of understanding of the physics of scale interaction and separation. In the present work, the correlation between density perturbation and pressure gradient in the small scale will be neglected.

The remaining part of ψ_x, ψ_y, ψ_z contains vertical and horizontal transports by small-scale processes. The horizontal transports or horizontal advection of velocity are in this scale smaller than the vertical transports since the horizontal transports are more likely to average out. Only the vertical advection of horizontal momentum will be parameterized. The vertical advection of vertical momentum will also be neglected here. Justification for the neglect of horizontal advection and of vertical advection of vertical momentum in the cumulus scale may be found in the observational work of Lenschow (1970), and Pennel and LeMone (1974) among others.

According to the scheme developed by Schneider and Lindzen (1976), the parameterized vertical advection of horizontal momentum may be expressed as

$$\frac{1}{\rho_o} \frac{d}{dz} \left[M_c \left(\mathbb{v}_H - \mathbb{v}_H^{\,c} \right) \right] \tag{3.50}$$

where M_c is the cloud mass flux and $\mathbb{v}_H^{\,c}$ is a horizontal velocity vector characteristic of cumulus clouds. Stevens et al (1977) constrain the integral of equation (3.50) to be zero on the assumption that clouds do not generate momentum but only transport it from one level to another. This assumption is satisfied if $\mathbb{v}_H^{\,c}$ is the horizontal velocity vector at cloud base. The constraint on the integral of the cumulus friction allows for an acceleration of westerlies at the lower atmosphere and easterlies in the upper atmosphere as observed after a passage of a squall line (e.g. Betts et al 1976) and obtained in theoretical models (Moncrieff and Miller, 1976). The validity of this

assumption that clouds do not generate net momentum may be questioned on the basis that there is work done by the non-hydrostatic pressure field as shown by Moncrieff and Miller (1976), but, the results of their model still show that the above mentioned constraint is valid at least as a first approximation.

Applying the averaging and smoothing techniques mentioned in the beginning of this chapter with

$$M_c = M_{c_o}(z) + M_c'(x,y,z,t) \tag{3.51}$$

the term in ψ_H in equation (3.5) becomes

$$\psi_H = M_{c_o}(w' - w'^c) + M_c'(w_o - w_o^c) + \left[M_c'(w' - w'^c) - \overline{M_c'(w' - w'^c)}\right] \tag{3.52}$$

while the basic state equations are

$$w_o \frac{du_o}{dz} = \frac{1}{\rho_o} \frac{d}{dz}\left[M_{c_o}(u_o - \bar{u}_o^c)\right] \tag{3.53a}$$

$$w_o \frac{dv_o}{dz} = \frac{1}{\rho_o} \frac{d}{dz}\left[M_{c_o}(v_o - \bar{v}_o^c)\right] \tag{3.53b}$$

$$\frac{dw_o}{dz} - \frac{w_o}{H} = 0 \tag{3.53c}$$

plus the thermodynamic and hydrostatic equations. Eddy interaction terms have been neglected in the dynamics of the basic state. $\bar{M}_c$ is the cloud

mass flux into the large-scale and may be specified as the one obtained by Yanai et al (1973). Note that the basic state has to allow for a vertical velocity in order to satisfy the governing equations.

M_c' is the cloud mass flux into the mesoscale and, as shown by Stevens and Lindzen (1978), has to be consistent with the observed heating in the following form

$$\int_{z_c}^{z_T} M_c' \frac{T_o}{\theta_o} \frac{d\theta_o}{dz} dz = \int_o^{\infty} \rho_o c_p \frac{T_o}{\theta_o} Q' \, dz \tag{3.54}$$

so that M_c' may be defined as

$$M_c' = f(z) \rho_{o_{ML}} w'_{ML} \tag{3.55}$$

according to equations (3.42) and (3.43). The function f(z) in equation (3.50) has been chosen to be

$$f(z) = e^{az} \sin (\pi z / z_{TM}) \tag{3.56}$$

with "a" found from equation (3.54). As defined above, the cloud mass flux is zero at the surface and at $z_{TM} = (N-\frac{1}{2})\Delta z$, but non zero at cloud base. As shown by Stevens et al., (1977) the appropriate boundary condition at the top (due to the introduction of one more vertical derivatives) is that

$$\frac{d}{dz}\left[M_c\ (\mathbb{v} - \mathbb{v}_c)\right] = \frac{dM_c}{dz}\ (\mathbb{v} - \mathbb{v}_c) \tag{3.57}$$

which has the effect of removing a singularity from the fourth order differential equation into which the system of equations can, after some simplifications, be combined.

In order to correctly apply the radiation condition at the top of the model, M_c' has to be zero at that height. On the other hand, (3.57) has to be applied at the top of the model (Stevens et al., (1977). The cloud top defined in the cumulus heating parameterization has to be lower than model top in order to apply the radiation condition. The way to integrate all these details has been to define cloud top at a certain level below model top, or tropopause in this case, and let $\overline{M}_c$ and M_c' go to zero right below model top so that, indeed, some overshoooting is allowed in the momentum parameterization. The boundary conditions may then be applied without any further complication.

The third term on the right of equation (3.52) is non-linear and has to be neglected in a linear theory even though its magnitude may be comparable to or even greater than the other terms.

With the introduction of momentum mixing by cumulus convection it is seen in equation (3.53) that the basic state has vertical velocity associated with it. Since the objective of this study is to specify u_o, v_o, and also since the observed profile of $\overline{M}_c$ is well known (Yanai et al., 1973), equation (3.53) may be solved, as an overdetermined system of equations, for an optimal profile of w_o. The residual in equation (3.53) may be attributed to the fact that there is some

divergence in the basic state contrary to the initial assumption. It should be noted that with the introduction of w_o, equations (3.13) - (3.16) contain an extra term, namely $w_o\, d\hat{u}/dz$, $w_o\, d\hat{v}/dz$, $w_o\, d\hat{w}/dz + \hat{w} d\, w_o/dz$, and $w_o\, d\hat{\theta}/dz$, respectively.

The finite difference scheme for the vertical derivatives of $\hat{u}$, $\hat{v}$, $\hat{w}$ and $\hat{\theta}$ consists of centered differences except at the lower and upper boundaries where backward and forward differencing techniques are applied.

3.3.3 Cloud Scale Downdraft

As mentioned in Chapter 2, Miller and Betts (1977) and Zipser (1977) have identified a cloud scale saturated downdraft and a meso-scale unsaturated downdraft. Betts and Silva Dias (1979) developed a parameterization of the thermodynamic characteristics of cumulonimbus downdrafts based on data collected during VIMHEX II and on a simple one dimensional model of rainfall evaporation developed by Kamburova and Ludlam (1966). In the case of a saturated downdraft, it was shown that the asymptotic solution

$$\left(\frac{\partial\theta}{\partial z}\right)_{\text{downdraft}} = \Gamma_W^{\theta_E} \tag{3.58}$$

is valid, where $\Gamma_W^{\theta_E}$ is the lapse rate along a moist adiabat (or along constant θ_E). Zipser (1977) shows that a characteristic value of θ_E inside the cloud scale downdraft is 341°K. The level of initiation, according to Miller and Betts (1977) is anywhere from 650 mb to 800 mb.

To introduce the cloud scale downdraft in the present model the following term

$$\Gamma_W^{\theta E} w_D \tag{3.59}$$

was added to the left hand side of the thermodynamic equation (3.5), where w_D is the vertical velocity at a certain level, just above which the downdraft is assumed to initiate. The term in equation (3.59) is introduced only below the level of initiation of the downdraft. As in the case of cumulus heating the cloud scale downdraft parameterization is unconditional, i.e., equation (3.59) is used whether w_D is positive or negative. The argument used to justify the negative cumulus heating in the literature, (e.g., Lindzen, 1974) has been that it is a perturbation over the large scale value of diabatic heating which includes the mean effect of cumulus in the large scale plus radiation effects. In fact w_D cannot represent the actual speed of the downdraft, it merely shows a mean between updraft and downdraft in the cloud scale so that the introduction of equation (3.59) may be seen as a mean effect that takes into account the upward and downward moving parts of the cumulus cells. It should be noted that Betts and Silva Dias (1979) developed the above mentioned downdraft parameterization based on the effect of squall lines as a whole on the thermodynamic structure of the subcloud layer, coherent with a mesoscale downdraft; the cloud scale downdraft as a saturated flow was actually detected in a few cases for which equation (3.59) is fairly accurate.

3.4 Summary

The main aspects of the model described in this chapter are the following

a) It is a linear non-hydrostatic spectral model in z-coordinates with a horizontally homogeneous basic state on a non-rotating plane. The fields of wind velocity, temperature and pressure are obtained by Fourier summations over all spectral components.

b) The model, without small scale parameterizations, is able to reproduce the speed of internal gravity waves and instability characteristics of waves produced by shear instability in stratified flows.

c) The cumulus heating parameterization is the so-called Wave-CISK parameterization, defined by an idealized moisture budget.

d) The momentum mixing parameterization is as developed by Schneider and Lindzen (1976).

e) A tentative inclusion of a cloud scale downdraft parameterization as defined by Betts and Silva Dias (1979) is presented.

IV. MODEL SENSITIVITY TESTS

The model described in Chapter III has two distinct stages: the first is the eigenmode decomposition through the solution of equation (3.30); the second stage is the definition of an initial condition and consequent Fourier summation over the unstable eigenmodes as stated by equations (3.32) - (3.37). The main part of this chapter will be devoted to investigating the sensitivity of the eigenvalues to different parameters related to small scale processes and to basic state structure. The significance of this analysis is, however, closely linked to the final part, the time and space evolution of an initial condition. In dealing with spectral models, it is very common to have a preconceived idea that the most unstable mode will be the predominant term in the Fourier summation after some time. This is true in principle, but depending on the initial condition, it may take so long for the most unstable mode to predominate that other assumptions, the linearity for example, are no longer valid. Suppose, for example, that the most unstable mode has a wavelength of 25 km and growth rate of $(2\ \mathrm{hr})^{-1}$, and the mode with 100 km wavelength has growth rate of $(12\ \mathrm{hr})^{-1}$. Depending on the Fourier transform of the initial condition represented by $C(\mathbb{k},m)$ in equation (3.37), the difference in growth rate may or may not be important. An initial condition showing a region of convergence with scale of 100 km will have a Fourier transform $\left(C(\mathbb{k},m)\right)$ with a peak around wavelength of 100 km. The value of $C(\mathbb{k},m)$ at wavelength 100 km may be five or six orders of magnitude larger than at wavelength 25 km, in which case it would take one or two days for the most unstable mode to predominate; by that time, the linearity assumption would certainly

not be valid for reasonable amplitudes of initial conditions. On the other hand, observations of mesoscale disturbances indicate typical time scales of less than a day.

It should be kept in mind throughout this chapter that the selection of a particular mode is not solely determined by the solution of the eigenvalue problem, but also by the particular atmospheric situation chosen as initial condition. Although the most unstable mode will be subject to closer scrutiny in this chapter, some attention will be given also to other modes whose wavelengths are important from the point of view of initialization.

The first part of Chapter IV will be devoted to studying the model sensitivity to the small scale parameterization; the second part will show how the eigenvalues are dependent on particular features of the basic state wind and temperature profiles. A few examples of how the vertical structure of these modes is modified will also be shown.

4.1 Sensitivity to Small-scale Parameterization

Three parameterization schemes have been defined in Chapter III, namely, cumulus heating, momentum mixing by cumulus clouds and cloud scale downdraft parameterizations. Several parameters are involved in the definition of these schemes and the way chosen to test the sensitivity of the eigenmodes is the following: the cumulus heating is introduced in the model and its parameters tested (section 4.1.1); the cumulus heating parameters are fixed and the momentum mixing parameterization introduced and its parameters tested (section 4.1.2); finally, the cloud scale downdraft parameterization is introduced,

with the two other schemes fixed, and the involved parameters are tested (section 4.1.3).

a) Model Structure and Basic State

The top boundary is set at the tropopause or 16 km. After a few tests on how much resolution was needed, the spacing between levels (cf. Fig. 3.1) was set at 1 km so that there are 16 levels in the vertical. Increasing the resolution to 890 m (18 levels) or 800 m (20 levels) did not change the resulting eigenvalues by more than 5%. However, changing the resolution from 2 km (8 levels) to 1 km (16 levels) produced eigenvalues that differ by as much as 50%.

The radiation condition is applied right below the tropopause.

The basic state throughout section 4.1 will be chosen as the mean state during the GATE as computed by Thompson et al., (1979). Fig. 4.1 shows the wind hodograph labeled East Atlantic which was obtained by averaging the winds in the B-scale during GATE. It may be noted that there is considerable directional shear of the winds from the surface up to 700 mb. Above that level, the winds are basically from the east. Fig. 4.2 shows the potential temperature labeled East Atlantic for the same period. The stability ($d\theta_o/dz$) is greater between the surface and 8 km than between 8 and 13 km. Above 13 km, the stability is increased as the isothermal layer (or lower stratosphere) is reached.

4.1.1 Sensitivity with Respect to Cumulus Heating Parameters

Several parameters are involved in the cumulus heating parameterization as defined by equations 3.45, 3.48, 3.49, namely, the level of maximum heating rate, the top of the moist layer, cloud base and cloud

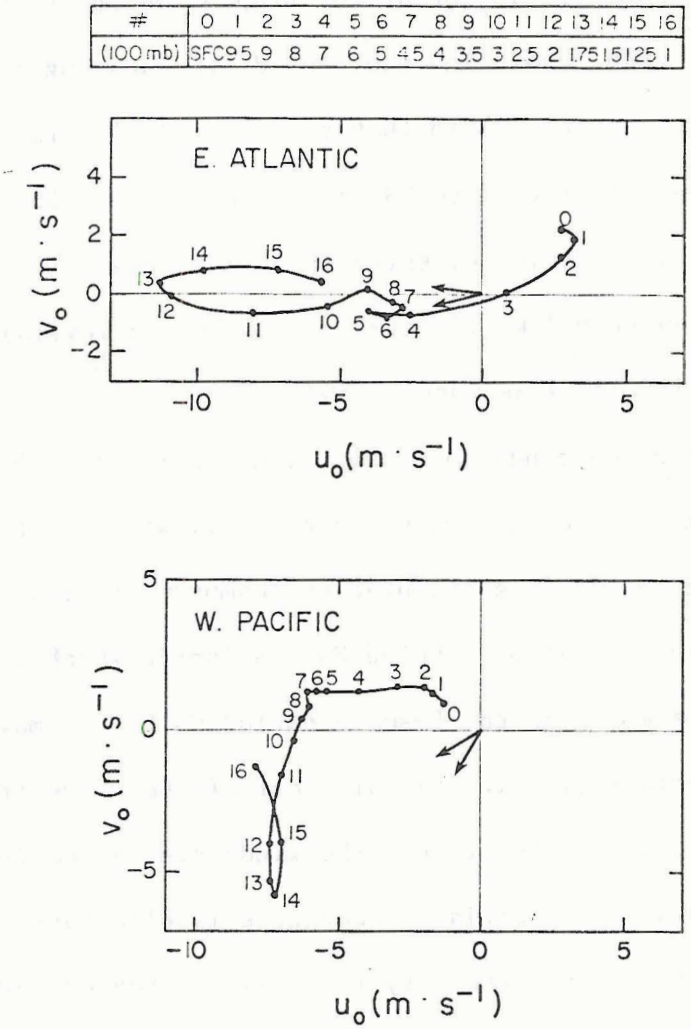

Figure 4.1. Wind hodographs for GATE B-scale (E. Atlantic) from Thompson et al., (1979) and for KEP triangle (W. Pacific) from Reed and Recker (1971).

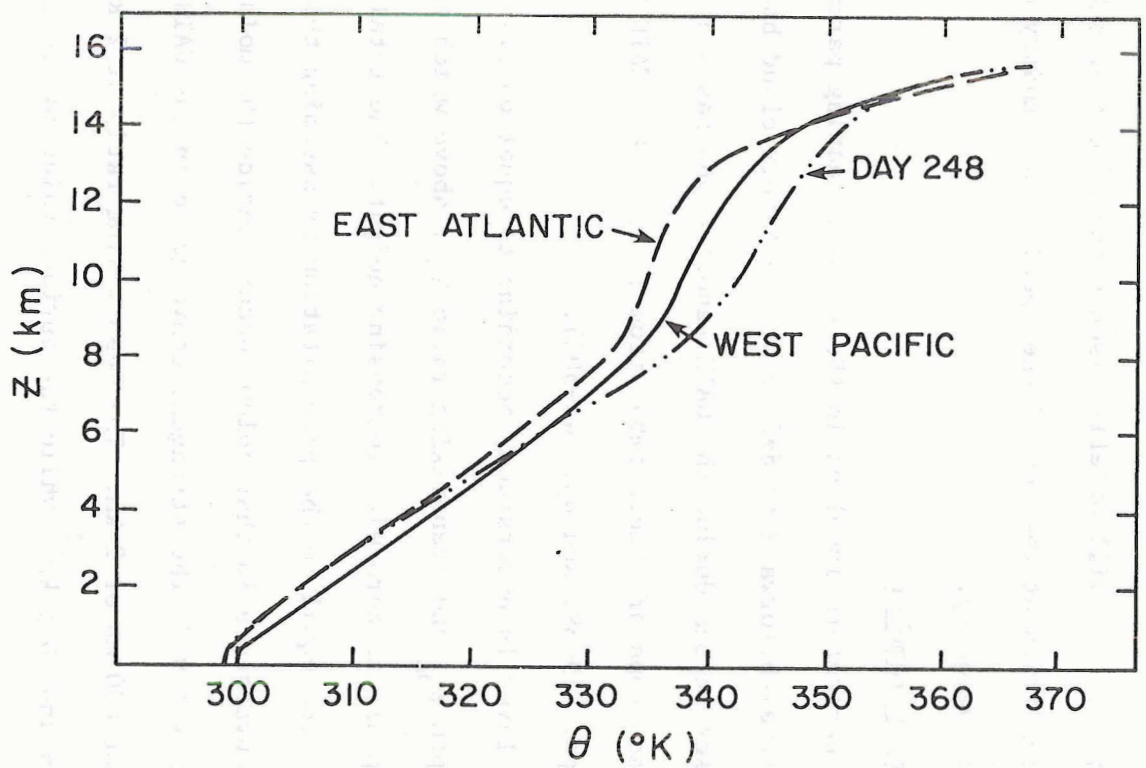

Figure 4.2. Potential temperature for GATE B-scale (E. Atlantic) from Thompson et al.,(1979); for KEP triangle (W. Pacific) from Reed and Recker (1971) and for a mean between the temperature soundings in the ships DALLAS and OCEANOGRAPHER on 5 Sept. 1974 at 900 GMT (Day 248) during the GATE.

top, mixing ratio in the moist layer. In part (a) below, the physical basis for assigning a particular value to these parameters will be discussed as well as the expected variability of the assigned values; part (b) will look to the effect of varying these parameters on the eigenvalues; part (c) will present and discuss the vertical structure of a few modes; part (d) will briefly discuss the effect of substituting the radiation condition at the top of the model by a boundary condition of zero vertical velocity.

a) Heating parameters

Among the parameters involved in the cumulus heating parameterization the most straightforward to define are certainly cloud base and cloud top. Observations during the GATE report cloud bases between 400 and 600 m and tops of cumulonimbus from 10 to 15 km (GATE Workshop Report, 1977, pp. 289-397 and pp. 441-503).

The moist layer is understood, according to equation 3.47, as a layer, with depth z_{ML} and mean mixing ratio q_o , above which the mixing ratio falls rapidly to zero with increasing height. The total heating in a column is made equal to the precipitation by assuming that most of the moisture convergence in that column occurs inside the moist layer. According to Gray (1977) the strongest convergence in the GATE systems goes up to about 800 mb or 2 km. The mean mixing ratio at 2 km has a value between 6 and 10 $g \cdot kg^{-1}$ while the surface value is about 16 or 17 $g \cdot kg^{-1}$ so that a mean value for a 2 km layer is about 12 $g \cdot kg^{-1}$. The mixing ratio at 2 km is already decreasing rapidly with increasing height but still some contribution to precipitation by advection of moisture may be coming from above 2 km, up to perhaps 4 or 5 km.

The most controversial of the parameters involved in the cumulus heating parameterization is the level of maximum heating rate. The difficulty in specifying this parameter is that observational studies have concentrated in calculating the profiles of heating rate in large-scale budgets. Nitta (1977) for example, shows the results of large-scale budgets during three periods of varying mesoscale activity. The resulting profiles of heating rate are, then, the combined result of mesoscale and small scale heating rates. The present model, however, requires a profile of heating rate that represents the effect of the cumulus scale on the mesoscale, and it is not known whether the maximum heating rate level is the same as the one obtained in large-scale budgets. Another complication is that large-scale studies have found great variability in the level of maximum heating rate, probably due to different types of mesoscale and small scale processes. Yanai et al., (1973) and Nitta (1977) agree with a level of maximum heating rate (z_{MH}) at about 400 mb or 7.5 km. Thompson et al., (1979) finds the maximum heating rate at about 4.5 km. Williams and Gray (1973) report this level at about 8.5 km. Johnson (1978) reports that z_{MH} is between 6 and 8 km. It is not known if the variability encountered is due to the mesoscale or to the small scale contribution, so that for lack of more specific information it will be assumed that the same range of variability in the level of maximum heating rate found in large scale budgets applies to the present case.

In summary, the cumulus heating parameters assume the values in Table 1, except when stated otherwise in the text.

Table 1. Values of Cumulus Heating Parameters

z_C	z_T	z_{ML}	q_o	z_{MH}
0.5 km	12 km	2 km	$12g \cdot k_g^{-1}$	7.5 km

b) Eigenvalues

With the introduction of the cumulus parameterization and the parameters listed in Table 1, the model was run for different wavenumbers n_x and n_y ($k_x = 2\pi n_x/200$ km, $k_y = 2\pi n_y/200$ km). For each pair of (n_x, n_y) the solution of equation (3.30) produces a set of eigenvalues, the most unstable one being the one with greatest imaginary part ω_i (cf. equation 3.19) or fastest growth rate. Fig. 4.3 shows the most unstable eigenvalues for $n_x = -24, \ldots, 0, \ldots, 24$ and $n_y = 0, \ldots, 24$. The part of the diagram corresponding to $n_y = -24, \ldots, 0$ is not shown since it is equal to the one shown (obtained by rotational symmetry around the origin). It is easily verified from equations (3.13) - (3.17) that if ω is a solution for wavenumber (n_x, n_y) then $-\omega^*$ (* denoting complex conjugate) is a solution for wavenumber $(-n_x, -n_y)$, so that the real part of ω changes sign and the imaginary part still corresponds to an unstable mode. The two solutions correspond, indeed, to a single physical solution obtained by adding the two complex conjugate pairs into a single real quantity. Fig. 4.3(a) shows isolines of ω_r, and Fig. 4.3(b), isolines of ω_i. For wavenumber (-10, 10) corresponding to a wavelength of 14 km the

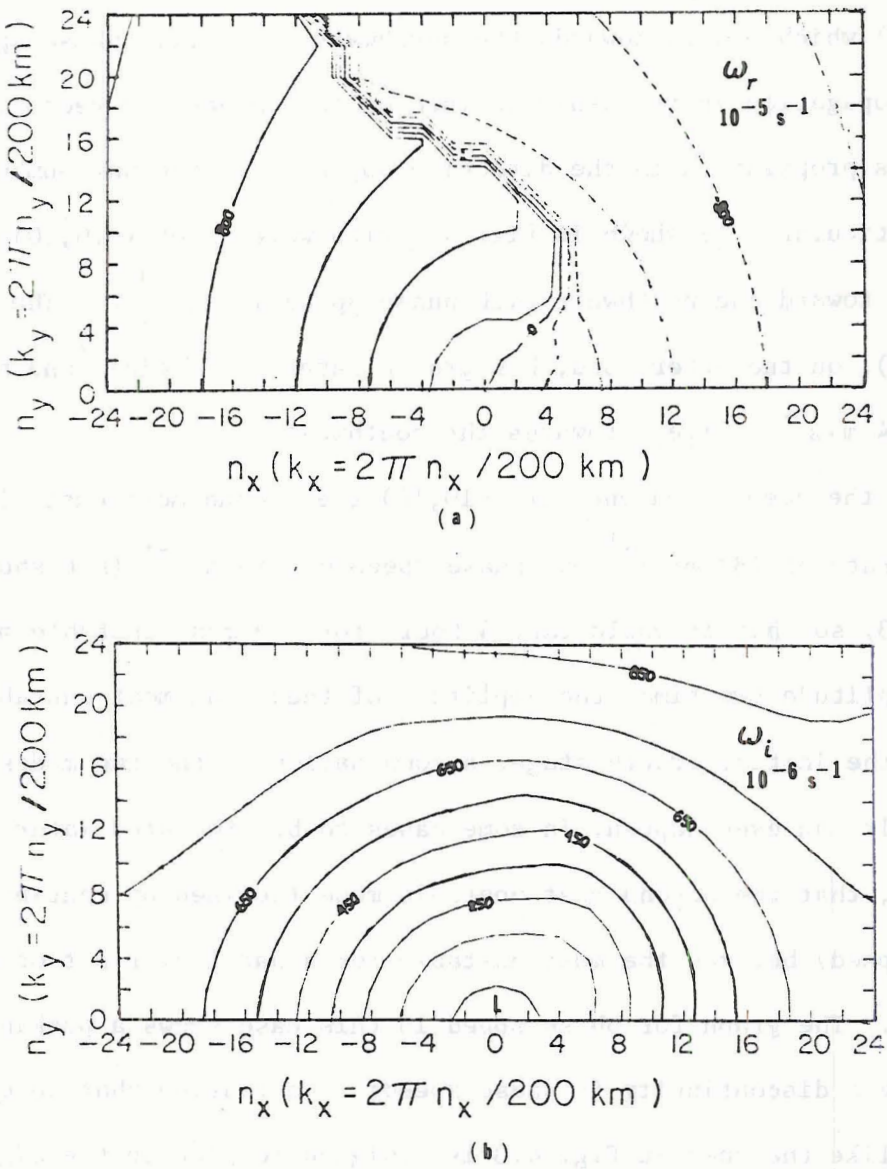

Figure 4.3. Eigenvalues of most unstable mode for model run with only the cumulus heating parameterization (parameters in Table 1). (a) real part of ω; (b) imaginary part of ω, or growth rate. Dashed lines in Fig. 4.3(a) denote negative values of phase speed. Symbol H and L denote regions of relative maximum and minimum, respectively, in the growth rate.

growth rate is $0.544 \times 10^{-3} s^{-1}$ or $(31 \text{ min})^{-1}$ with ω_r equal to $0.62 \times 10^{-2} s^{-1}$ or phase speed c_r (cf. equation 3.18) of 14 $m.s^{-1}$. The direction of propagation of this particular mode is along the wavenumber vector (-10,10) which points towards the northwest. Positive phase speed means wave propagation in the sense defined by the wavenumber vector. Negative c_r means propagation in the direction opposite to the wavenumber vector. The particular mode shown in Fig. 4.3 with wavenumber (-10,10), then, travels toward the northwest with phase speed 14 $m.s^{-1}$. The wavenumber (10, 10), on the other hand, has growth rate of $(34 \text{ min})^{-1}$ and phase speed of -14.4 $m \cdot s^{-1}$, i.e. towards the southwest.

In the case of wavenumber (-10,10) the second most unstable mode has growth rate of $(33 \text{ min})^{-1}$ and phase speed of -10 $m.s^{-1}$ (not shown in Fig. 4.3) so that it would take 4 hours for the most unstable mode to have amplitude two times the amplitude of the second most unstable mode. During the initial growth stage, a combination of the two modes may be seen. It can even happen, in some cases to be presented later in this chapter, that the second most unstable mode (defined by continuity in phase speed) becomes the most unstable for a particular set of wavenumbers. The graph for phase speed in this case shows a packing of lines denoting a discontinuity in phase speed; the routine that generates graphs like the ones in Fig. 4.3 is designed to pick up the eigenvalues with greater value of ω_i, so that, sudden shifts in ω_r just mean that different modes, with quite different ω_r, become the most unstable mode at particular sets of wavenumbers.

Fig. 4.3(b) shows the growth rate steadily increasing from the lower center of the figure, or wavenumber (0,0), towards the higher

wavenumbers. The highest growth rates are found at progressively higher wavenumbers or smaller wavelengths so that no preferred scale can be defined in terms of maximum growth rate. This result is similar to previous wave-CISK studies, (e.g. Hayashi, 1970). For n_x, n_y greater than about 20 the wavelengths fall in the cumulus scale and should not be considered.

At this point it is useful to discuss the concept of group velocity. Group velocity as defined in neutral wave studies (zero growth rate) is the velocity at which a packet of waves with different wavelengths will propagate. The mathematical experession for this concept is related to the derivatives of phase speed (Bretherton, 1969).

$$\mathbb{C}_g(k_x, k_y) = \frac{\partial \omega_r}{\partial k_x} \mathbb{i} + \frac{\partial \omega_r}{\partial k_y} \mathbb{j} \tag{4.1}$$

It can be argued that this expression may be approximately valid at the very initial stage of growth, but, as time goes on and a particular wave with higher growth rate starts to predominate, the propagation speed tends to the phase speed of this particular unstable mode. The theoretical basis of the above argument should be subject to further study; the results in chapter 5 show that indeed there is a tendency for the propagation speed to go from an initial value to the phase speed of a particular mode. The initial value, however, is not quite the one obtained by equation 4.1, but then, this equation does not take into account the existence of several unstable modes for the same wavenumber.

The sensitivity of the eigenvalues with respect to cloud base and cloud top is minimal. Changing cloud base from 400 m to 600 m and cloud top from 10 km to 15 km had the effect of changing the phase speed and

growth rate by less than 10% while keeping the overall dependence on wavenumber as in Fig. 4.3.

The effect of changing the heating amplitude has been discussed by Chang (1976), and his result is confirmed here. The growth rate linearly increases with increasing q_o while the phase speed remains constant. An increase or decrease in q_o is related to an increase or decrease in the integrated value of heating and to the precipitation, according to equation 3.47. This value can be externally specified in accordance wtih observations. Furthermore, the relationship between growth rate and heating amplitude is expected, i.e., the most unstable waves, which have increasing values of vertical velocities , being well correlated to high precipitation.

The effect of changing the top of the moist layer is not so straightforward and is very much model dependent due to the particular vertical stratification and vertical extent of the model, which tends to force waves of a particular vertical wavelength. Figs. 4.4, 4.5, and 4.6 show the same plot as in Fig. 4.3 except for the top of moist layer which is at 3 km, 4 km and 5 km respectively, as opposed to 2 km in Fig. 4.3. The main effects of an upward displacement of the top of the moist layer is reduction of the value of growth rate and the appearance of more discontinuities in the ω_r diagrams (Figs. 4.4a, 4.5a, 4.6a), denoting the appearance of unstable modes that have quite different phase velocities than for neighboring values of wavenumber. When the top of the moist layer is changed, the vertical velocity that is used in the cumulus heating parameterization is also changed (cf. equation 3.45 and 3.47) so that depending on the structure of the eigenvectors, the total value of

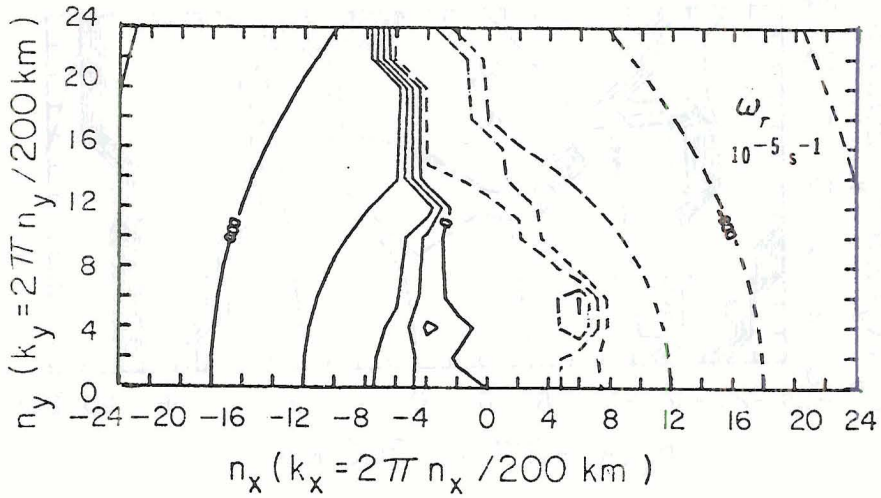

(a)

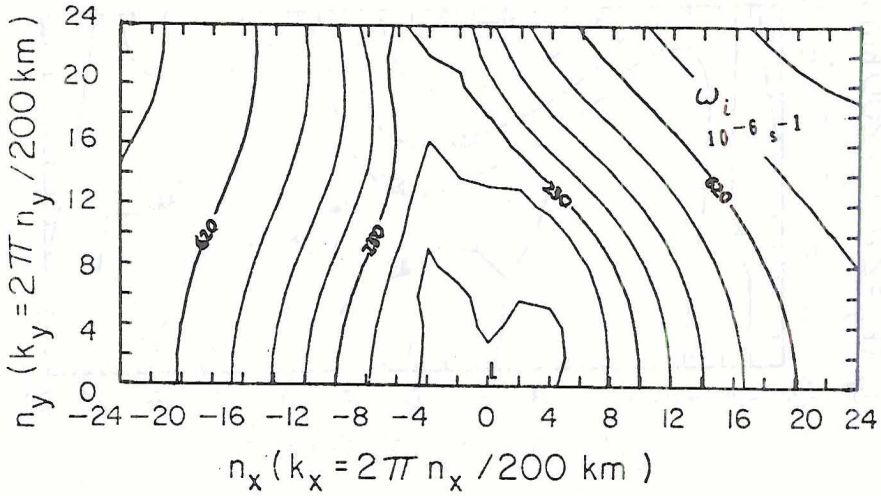

(b)

Figure 4.4. Eigenvalues for model run with only cumulus heating parameterization; parameters in Table 1 except for z_{ML} = 3 km. (cf. Fig. 4.3 for details).

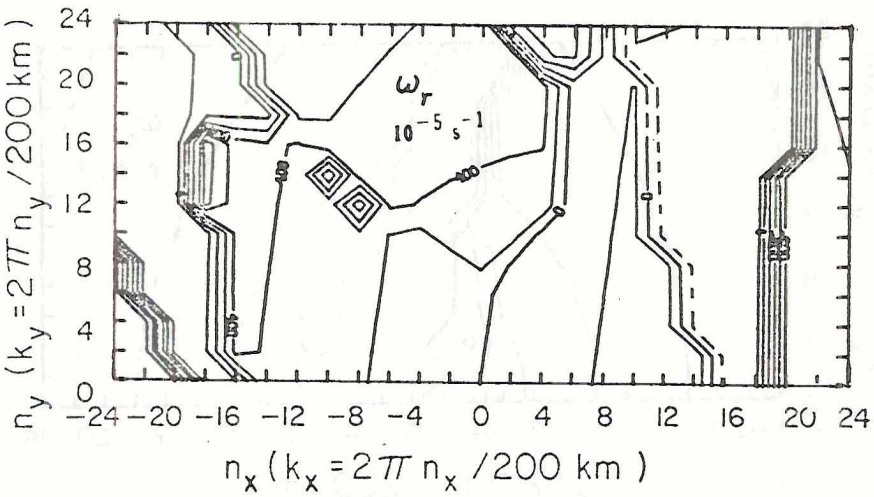

(a)

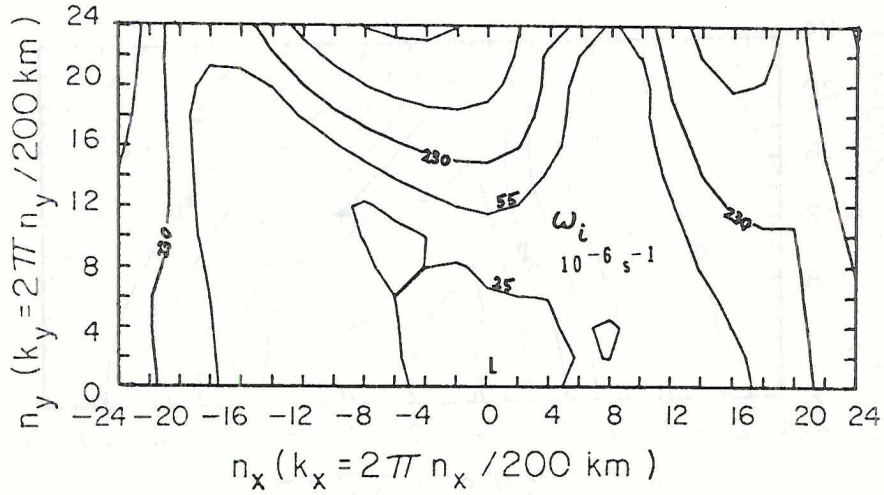

(b)

Figure 4.5. Eigenvalues for model run with only cumulus heating parameterization; parameters in Table 1 except for z_{ML} = 4 km. (cf. Fig. 4.3).

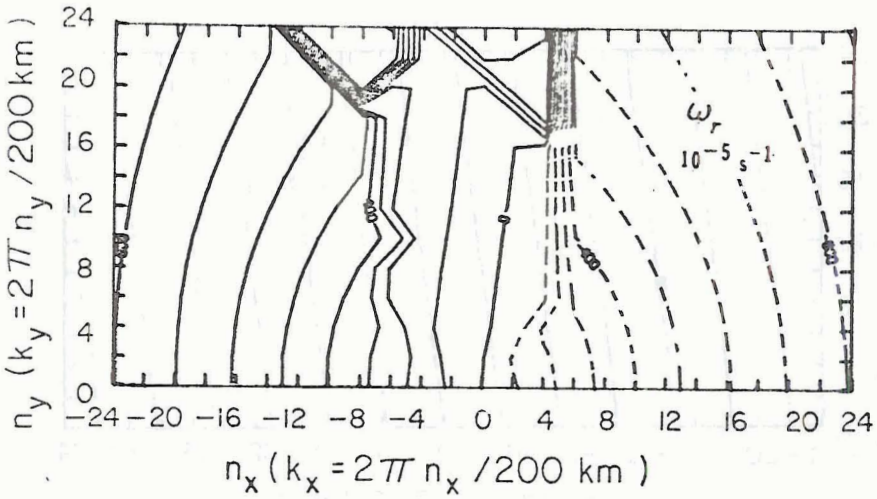

(a)

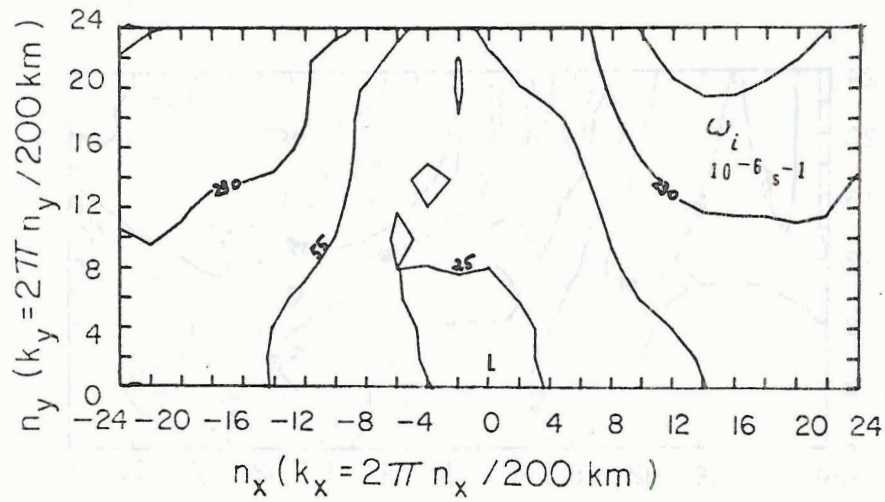

(b)

Figure 4.6. Eigenvalues for model run with only cumulus heating parameterization; parameters in Table 1 except for z_{ML} = 5 km. (cf. Fig. 4.3).

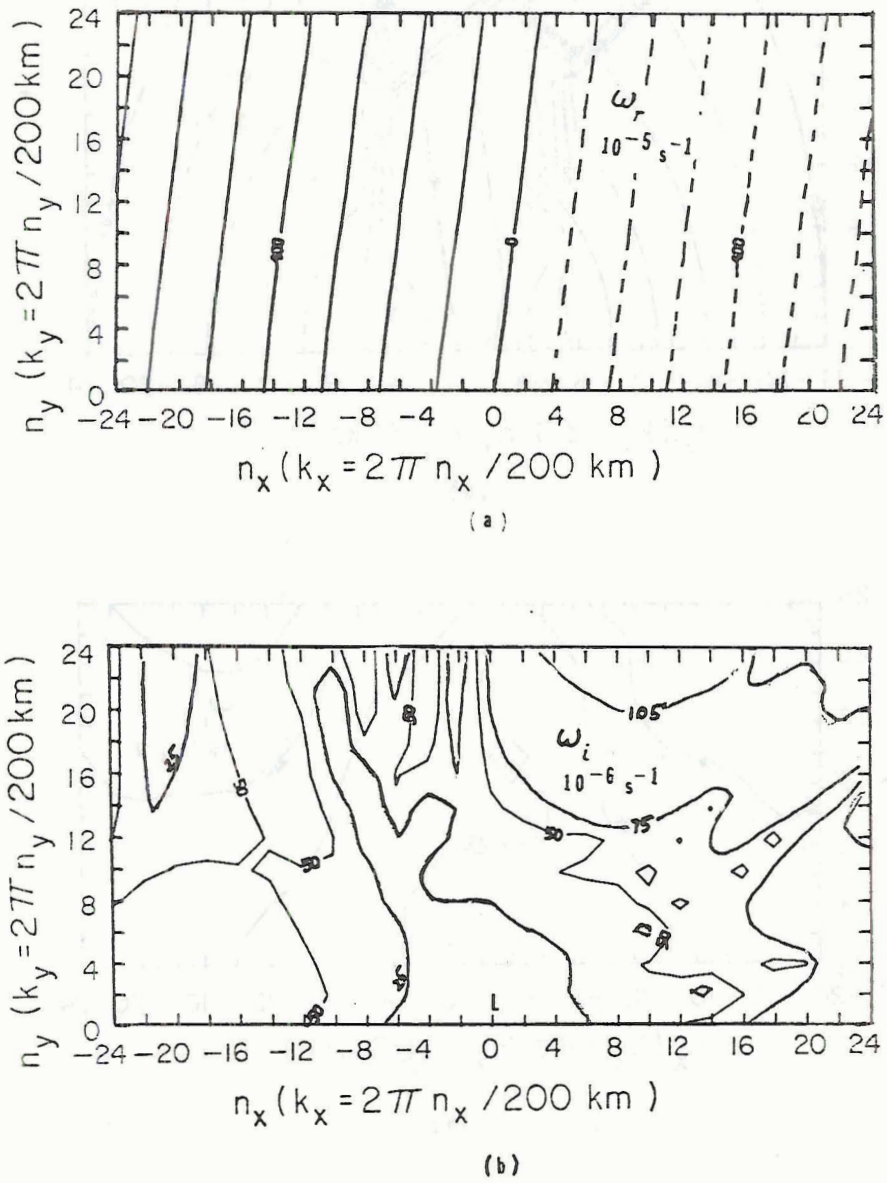

Figure 4.7. Eigenvalues for model run with only cumulus heating parameterization; parameters in Table 1 except for z_{MH} = 4.5 km.

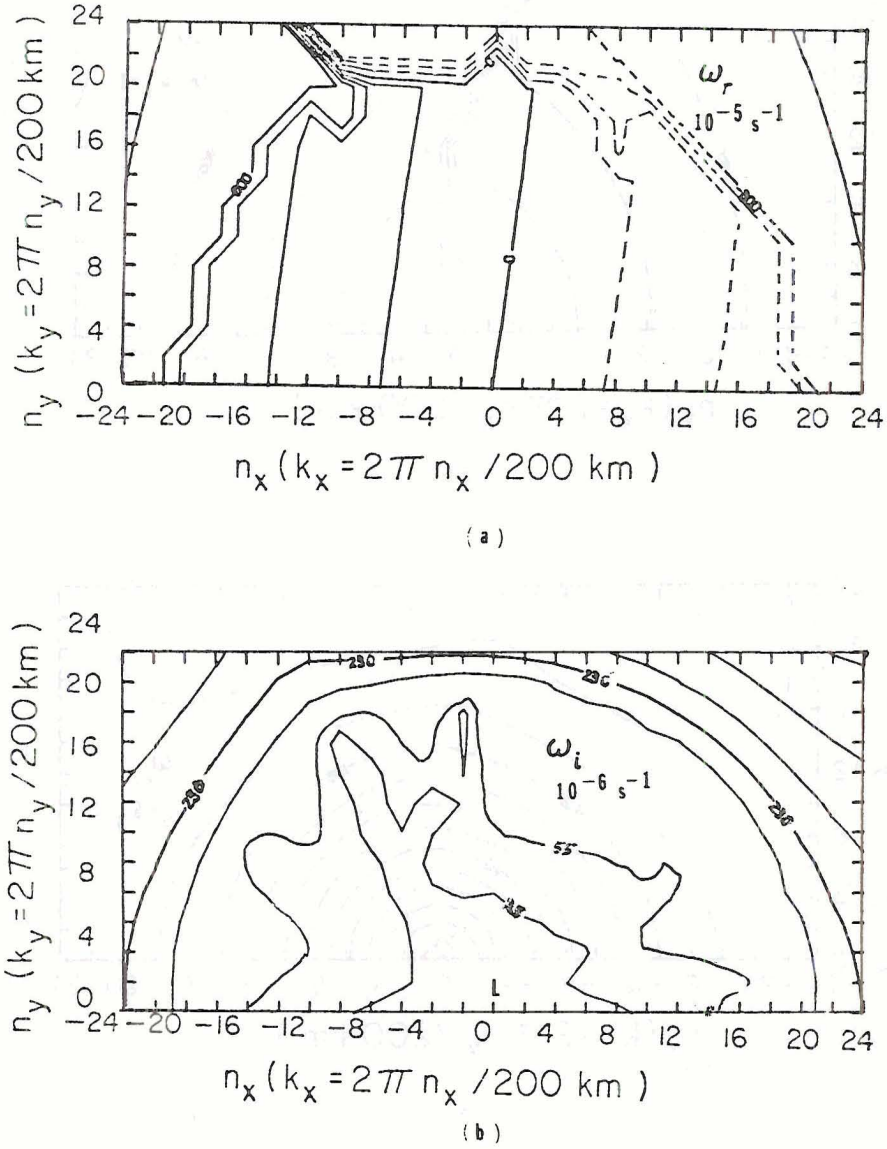

Figure 4.8. Eigenvalues for model run with only cumulus heating parameterization; parameters in Table 1 except for z_{MH} = 6 km.

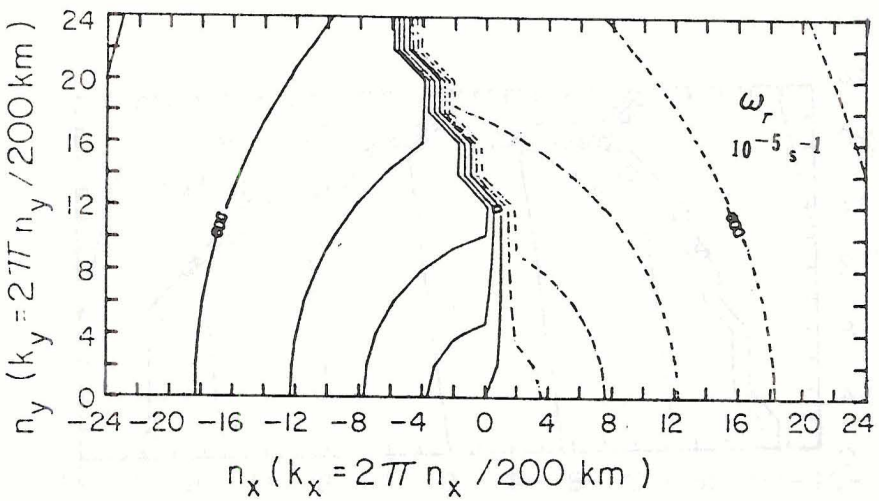

(a)

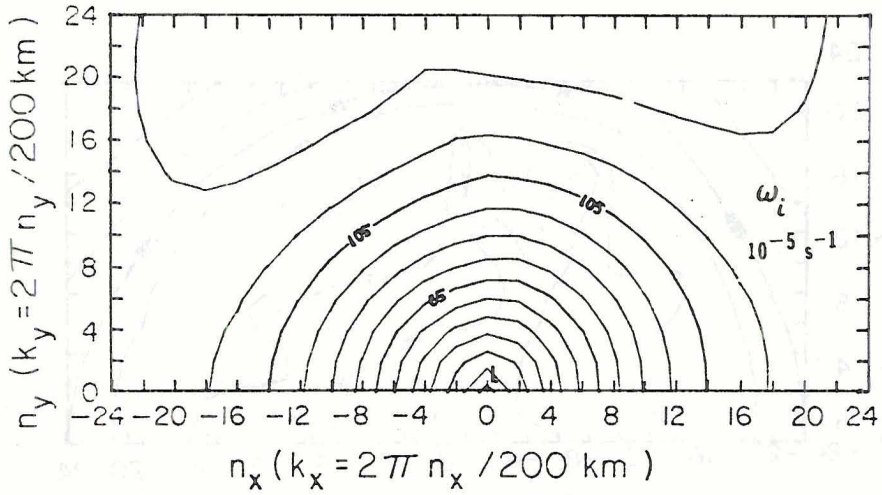

(b)

Figure 4.9. Eigenvalues for model run with only cumulus heating parameterization; parameters in Table 1 except for z_{MH} = 9 km.

heating is increased or decreased. This will be discussed again in the next section on the vertical structure.

The sensitivity with respect to the level of maximum heating rate may be seen in Figs. 4.7, 4.8, 4.9 for which z_{MH} is 4.5 km, 6 km and 9 km, respectively. Fig. 4.3 had a level of maximum heating rate at 7.5 km. A transition may be observed from low to high values of growth rate while z_{MH} changes from 4.5 to 9 km. Figs. 4.3 and 4.9 are particularly similar, except for the value of growth rate increasing about 60% for an increase of 20% in z_{MH} (from 7.5 km to 9 km). The change in growth rate from Fig. 4.7 (z_{MH} = 4.5 km) to Fig. 4.8 (z_{MH} = 6 km) is very small. In fact for z_{MH} at 4.5 km and 6 km, there is a factor of 80 between ω_r and ω_i so that the waves are almost neutral. This is in accordance with Hayashi (1970) which found out that the heating in upper troposphere should be greater than in lower troposphere as a condition for instability. From Fig. 4.8 to Fig. 4.3 (z_{MH} = 7.5 km) there is a big change in growth rates again of about one order of magnitude. Chang (1976) reported a linear increase in growth rate with the increase of z_{MH}, but he looked into level of maximum heating rates higher than 7.5 km. For z_{MH} greater than 7.5 km the results obtained here agree with Chang's (1976).

There are two noteworthy aspects on the variability encountered in the eigenvalues as a result of varying the top of the moist layer and the level of maximum heating rate: the strong dependence of the value of growth rate on z_{ML} and z_{MH} so that the model can be "tuned" to give a specific growth rate; however, the overall shape of the isolines of growth rate is not modified for sufficiently high z_{MH} and sufficiently low z_{ML}), i.e., all modes have their growth rate increased by the same

amount. This means that if a given mode is the most unstable mode for certain z_{MH} and z_{ML}, it will remain the most unstable mode for varying values of z_{MH} and z_{ML}. The phase speed is not very sensitive to z_{MH}, z_{ML} except for high wavenumbers, or short wavelengths, where the discontinuities tend to appear.

c) Vertical Structure

The study of the vertical structure of a particular mode may be done in two ways. One of them is to just plot the vertical profile of the eigenvectors $\hat{u}$, $\hat{v}$, $\hat{p}$, $\hat{\theta}$, $\hat{w}$. Since the eigenvectors are complex numbers, either the real and imaginary parts are plotted separately or the amplitude and phase are plotted. Although the procedure is indeed very simple, the interpretation of the different profiles is not straightforward since it requires a considerable degree of imagination on the part of the reader. This can be certainly avoided by plotting instead of the eigenvectors, the actual mesoscale fields of velocity pressure and potential temperature in vertical cross sections. Equations (3.32)-(3.37) are used in a simplified manner. A particular wavenumber $\mathbb{k}$ is chosen and for this wavenumber, the mode m of highest instability is selected. In equation (3.36), the summation is eliminated and the coefficient $\mathbb{C}(\mathbb{k},m)$ is set equal to 1 and the calculation is carried for t=0. At later times, the structure is the same due to lack of interaction with other modes; the amplitudes grow exponentially, but this does not modify the shape of the cross sections. From equation (3.32) the integral is eliminated and $\underset{\sim}{Z}'(x,y,0) = \underset{\sim}{Z}(x,y,0) - \underset{\sim}{Z}_o$ may be calculated.

The structure of wavenumber (2, 1.3) wavelength (100 km, 150 km) in Fig. 4.3 corresponding to the cumulus heating parameters in Table 1 may be seen in Figs. 4.10 - 4.13. Fig. 4.10 shows a plot of the horizontal velocity vector at the first vertical level, i.e., 0.5 km. This is a typical wave with regions of convergence and divergence separated by 42 km (wavelength of 84 km) traveling in the direction ENE - WSW with phase speed 9.6 $m.s^{-1}$ and growth rate of $(6 \text{ hr } 15 \text{ min})^{-1}$. Fig. 4.11 shows a vertical cross section of the vector (v', w') for the north-south plane along $x = 0$. Fig. 4.12 shows a plot in the same plane of θ' and Fig. 4.13 of w'. Note that the vertical coordinate is stretched. The main feature in these figures is the vertical tilting that may be observed mainly in cross sections of θ' and of w' (Figs. 4.12 and 4.13, respectively). There are basically two cells in the vertical. For $y = 45$ km, the vertical velocity is small and negative up to 2 km; at 9 km, there is a maximum in upward vertical velocity and a secondary maximum around 3.5 km. The potential temperature vertical cross section presents a more complicated structure and a steeper tilting of the transition lines between positive and negative values of θ'. In Appendix A1, the energy equation for the present model is derived and it may be seen that the term $w'\theta'$ is related to the conversion of potential energy to kinetic energy. A positive value of $w'\theta'$ (up-warm, down-cold) decreases the value of potential energy and increases the kinetic energy of vertical motions. A positive mean value of $w'\theta'$ over the wavelength corresponds to a net increase of the mean kinetic energy of vertical motions. Appendix A2 shows how the terms $\overline{u'w'}$, $\overline{v'w'}$, $\overline{p'w'}$ and $\overline{\theta'w'}$, where bar denotes the mean over a wavelength, may be calculated from the eigenvalues and eigenvectors of equation (3.30). Fig.

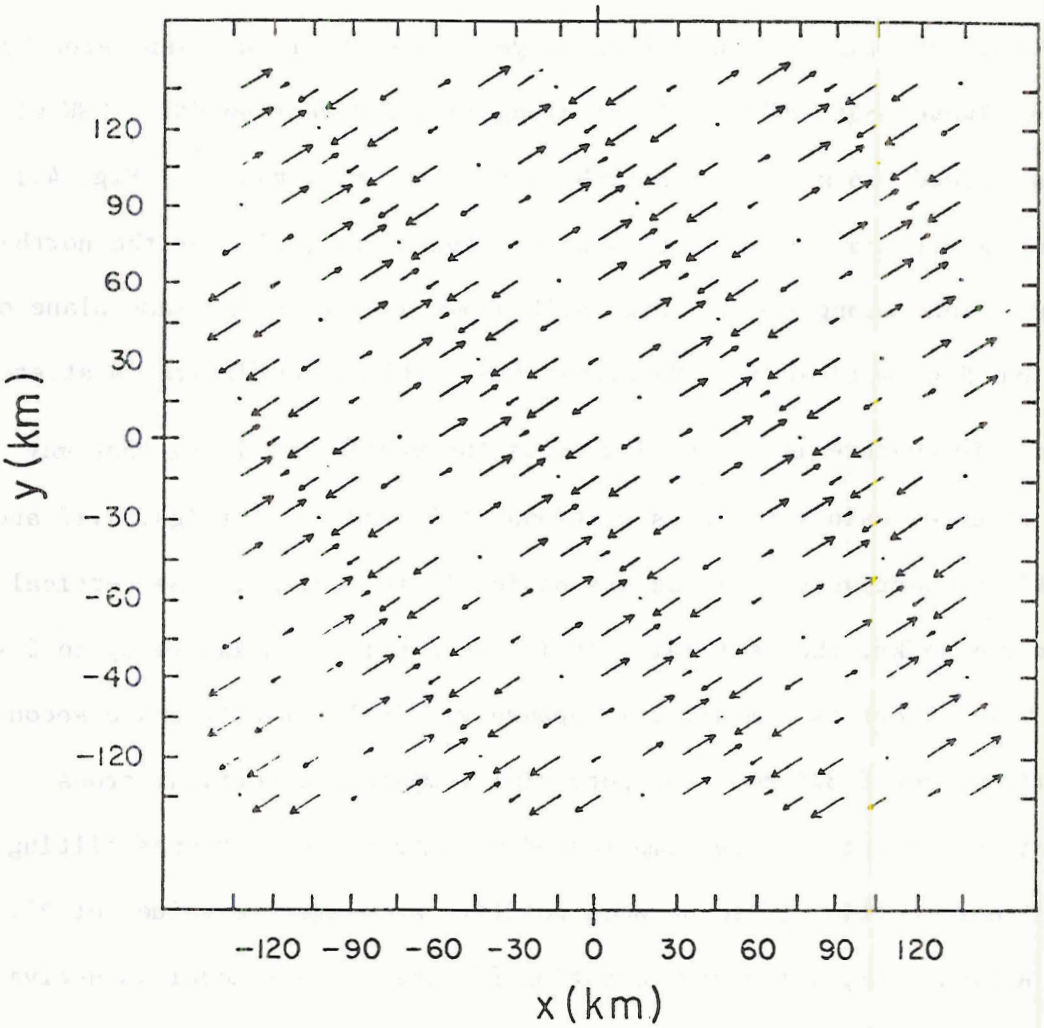

Figure 4.10. Horizontal cross section at z = 0.5 km showing the field of the horizontal velocity vector for wavenumber (2, 1.3) (cf. Fig. 4.3) for cumulus heating parameters in Table 1.

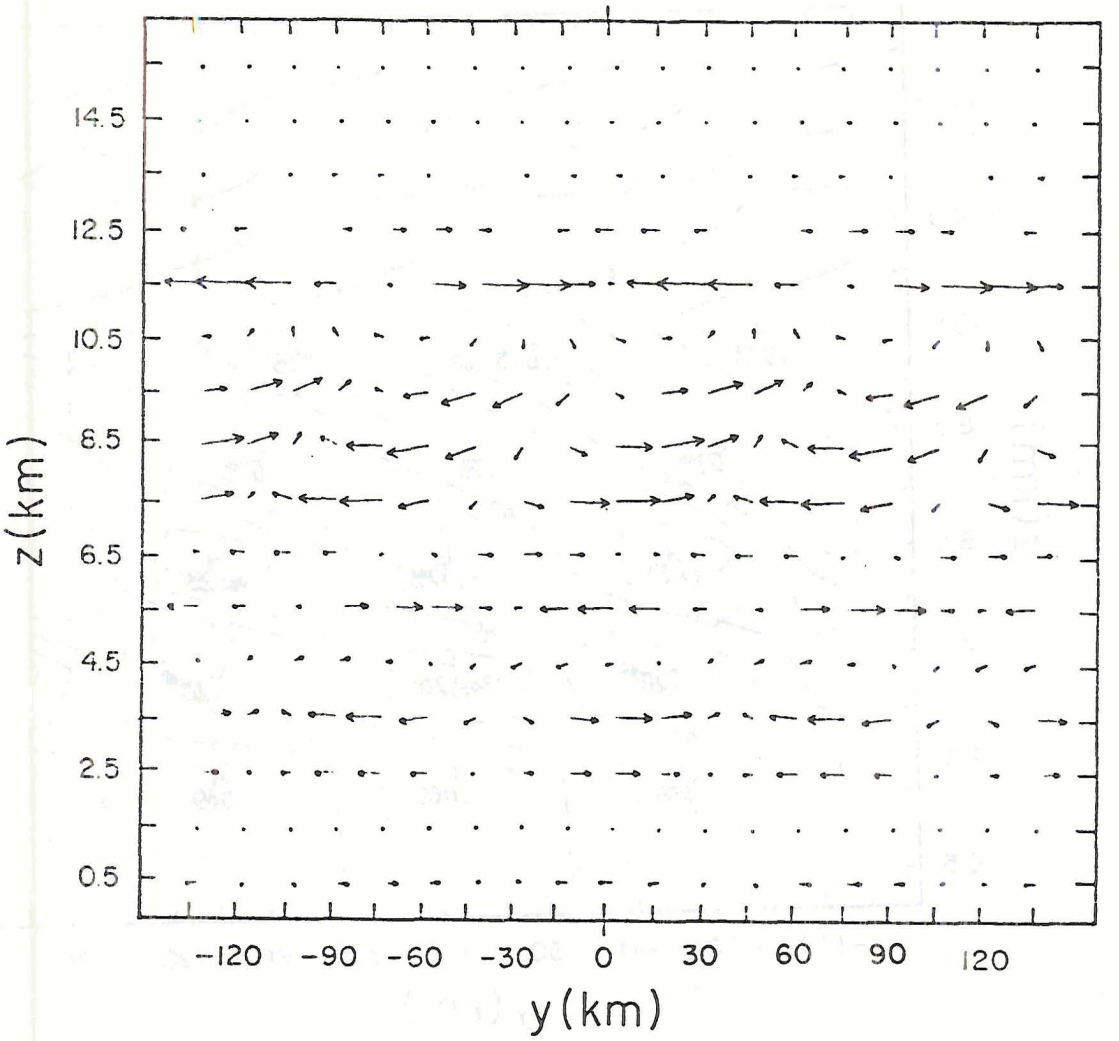

Figure 4.11. Vertical cross section at x = 0 (meridional plane) showing the field of vector (v',w') for wavenumber (2,1.3) (cf. Fig. 4.3) for cumulus heating parameters in Table 1.

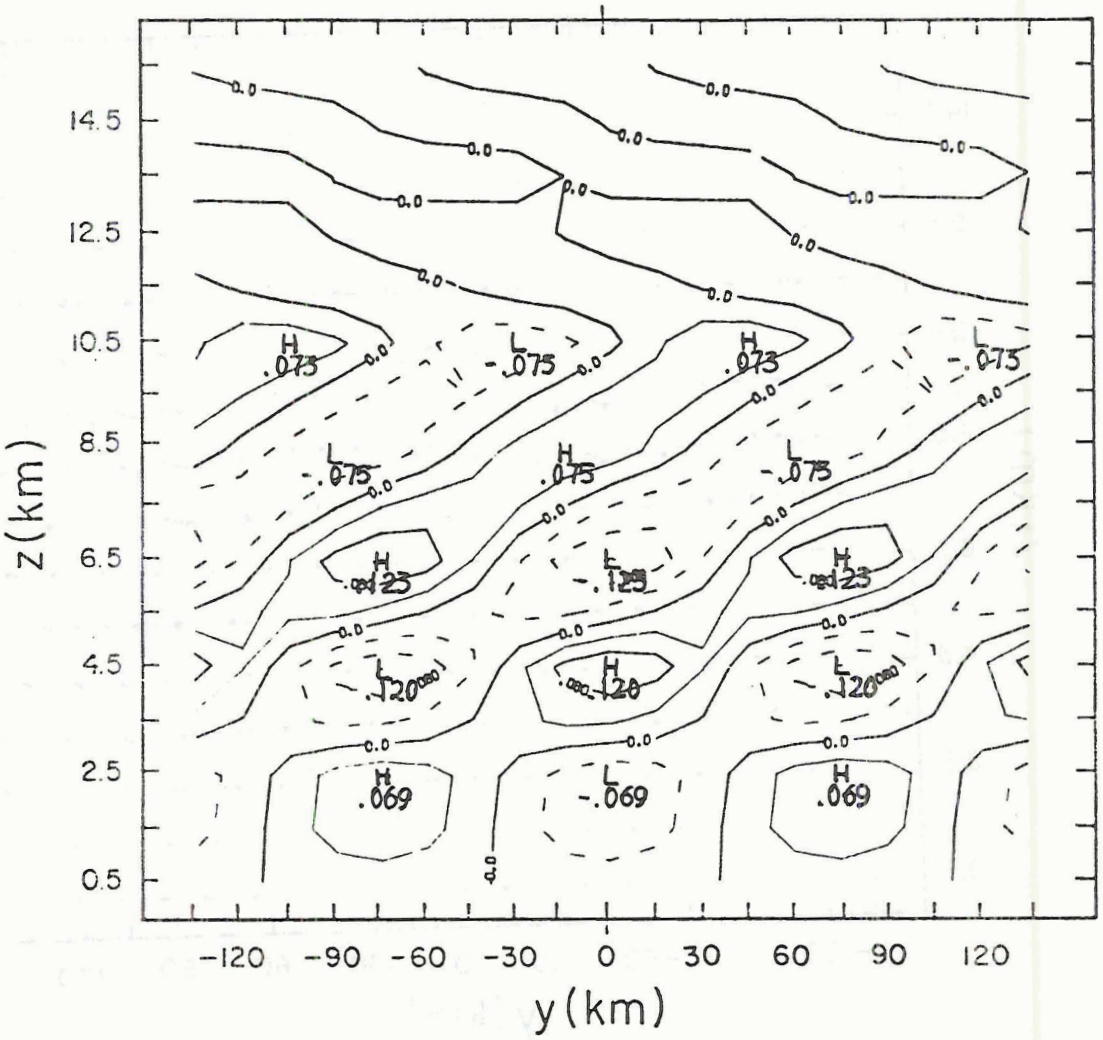

Figure 4.12. Isolines of mesoscale potential temperature in the meridional plane at x = 0; wavenumber (2,1.3) (cf. Fig. 4.3) for cumulus heating parameters in Table 1.

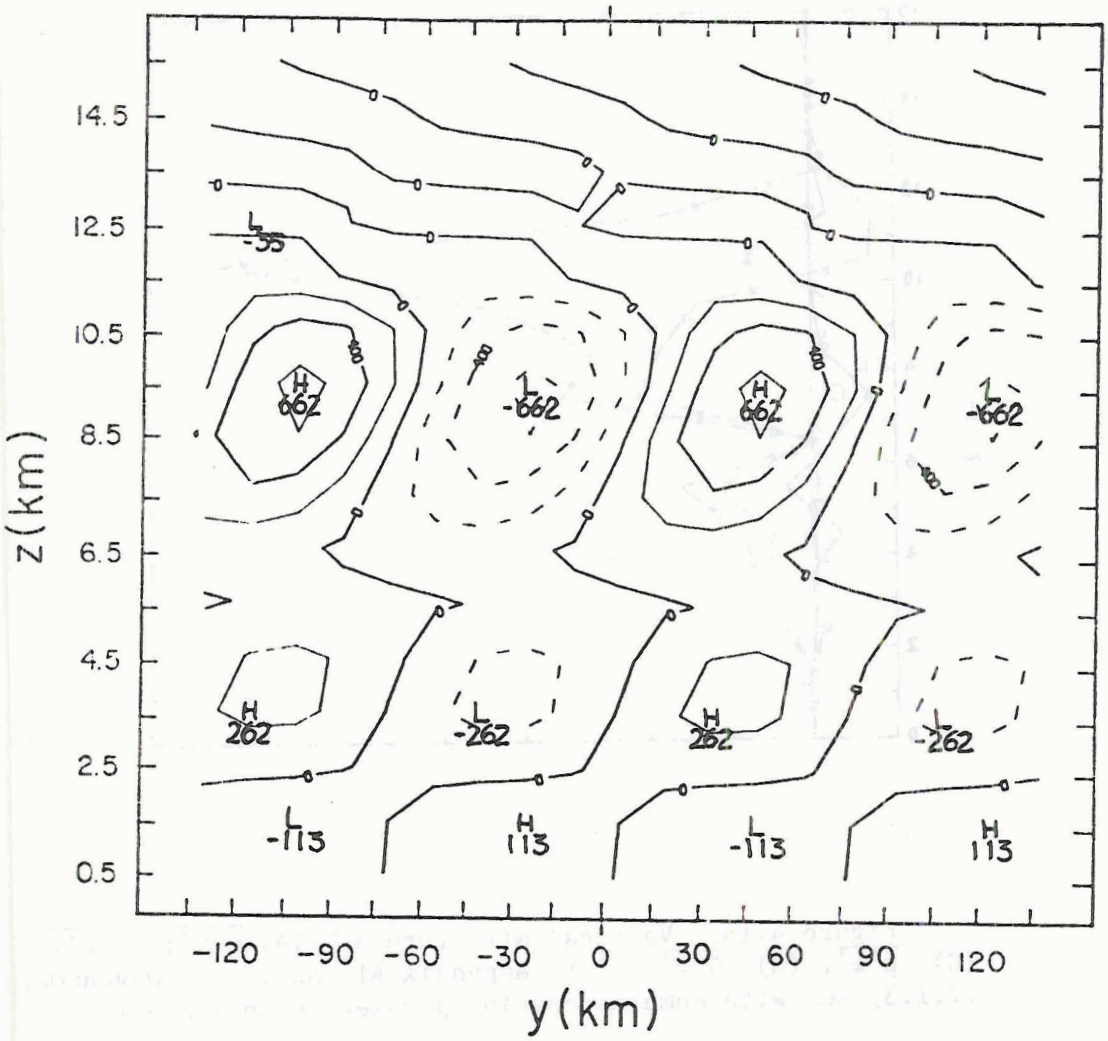

Figure 4.13. Isolines of mesoscale vertical velocity in the meridional plane at x = 0; wavenumber (2, 1.3) (cf. Fig. 4.3) for cumulus heating parameters in Table 1.

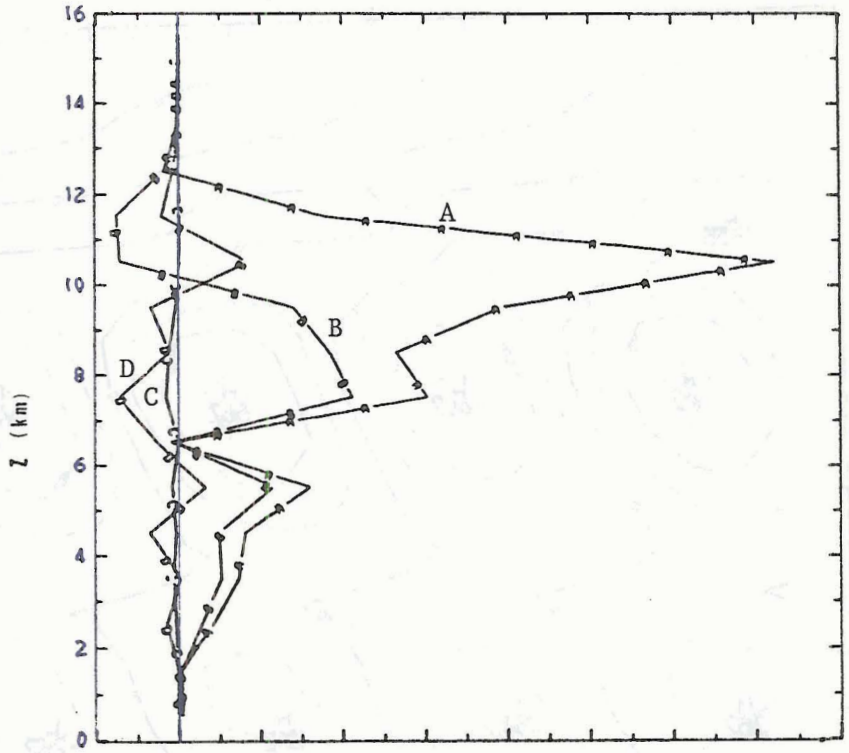

Figure 4.14. Vertical structure of (A) $\overline{u'w'}$;(B) $\overline{v'w'}$; (C) $\overline{p'w'}$; (D) $\overline{\theta'w'}$. (cf. Appendix A1, A2). For wavenumber (2,1.3) and with cumulus heating parameters in Table 1.

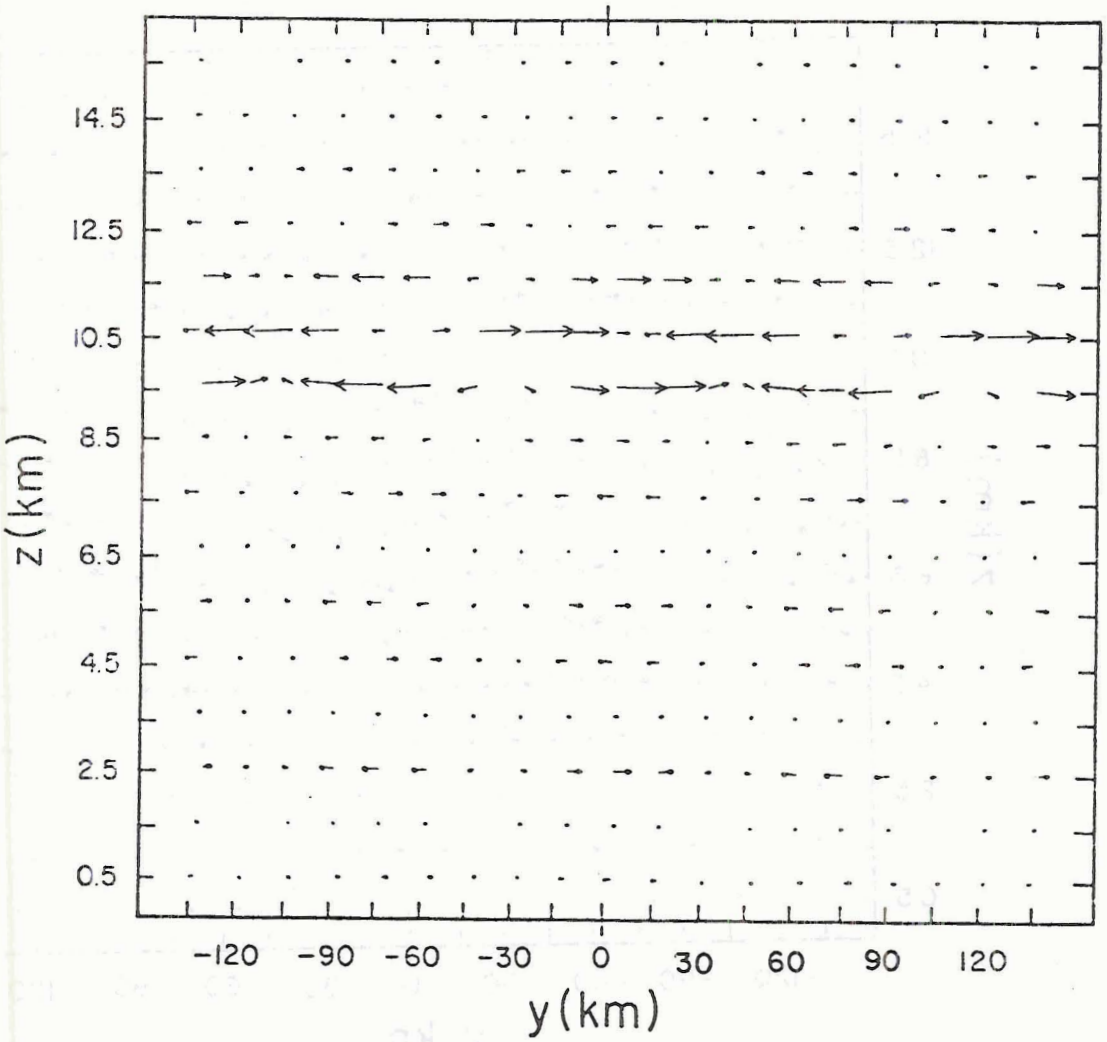

Figure 4.15. Vertical cross section at x = 0 (meridional plane) showing the field of vector (v',w') for wavenumber (2,1.3) (cf. Fig. 4.8) for cumulus heating parameters in Table 1 except for z_{MH} = 6 km.

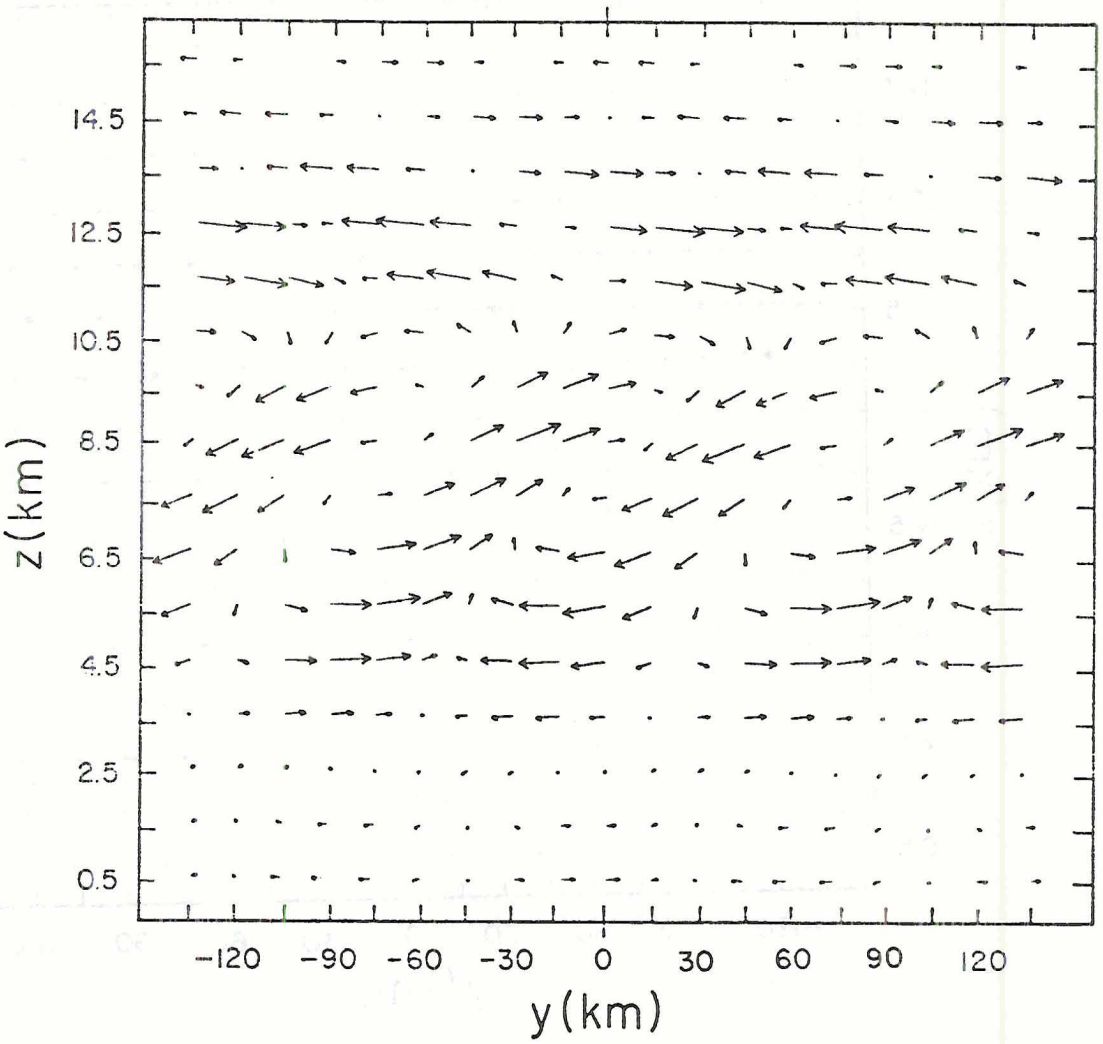

Figure 4.16. Vertical cross section of x = 0 (meridional plane) showing the field of vector (v',w') for wavenumber (2,1.3) (cf. Fig. 4.9) for cumulus heating parameters in Table 1 except for z_{MH} = 9 km.

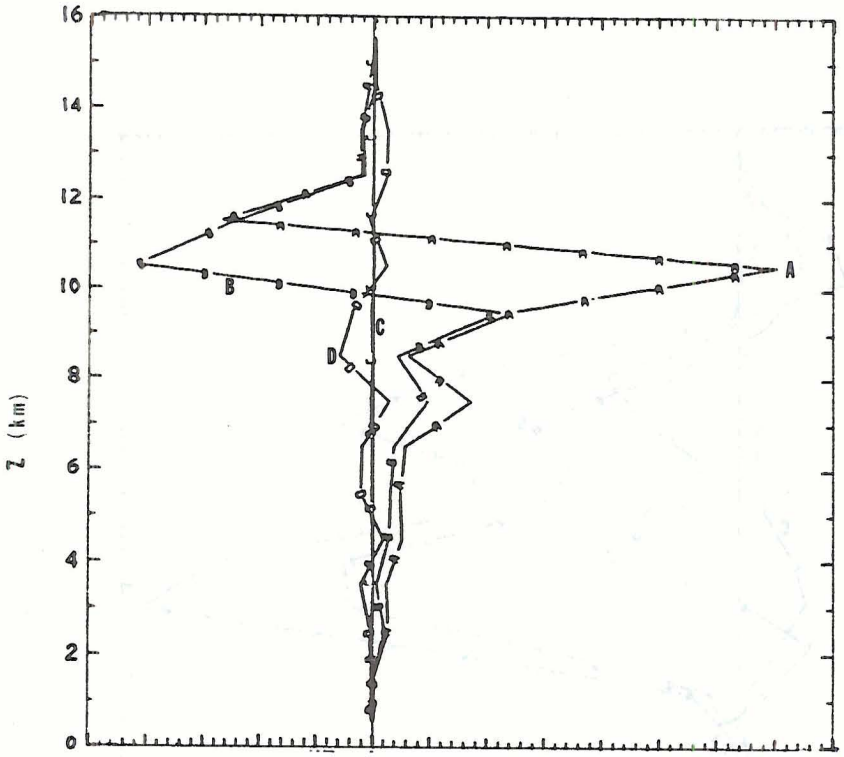

Figure 4.17. Vertical structure of (A) $\overline{u'w'}$; (B) $\overline{v'w'}$; (C) $\overline{p'w'}$; (D) $\overline{\theta'w'}$. For wavenumber (2,1.3) and with cumulus heating parameters in Table 1, except for z_{MH} = 6 km.

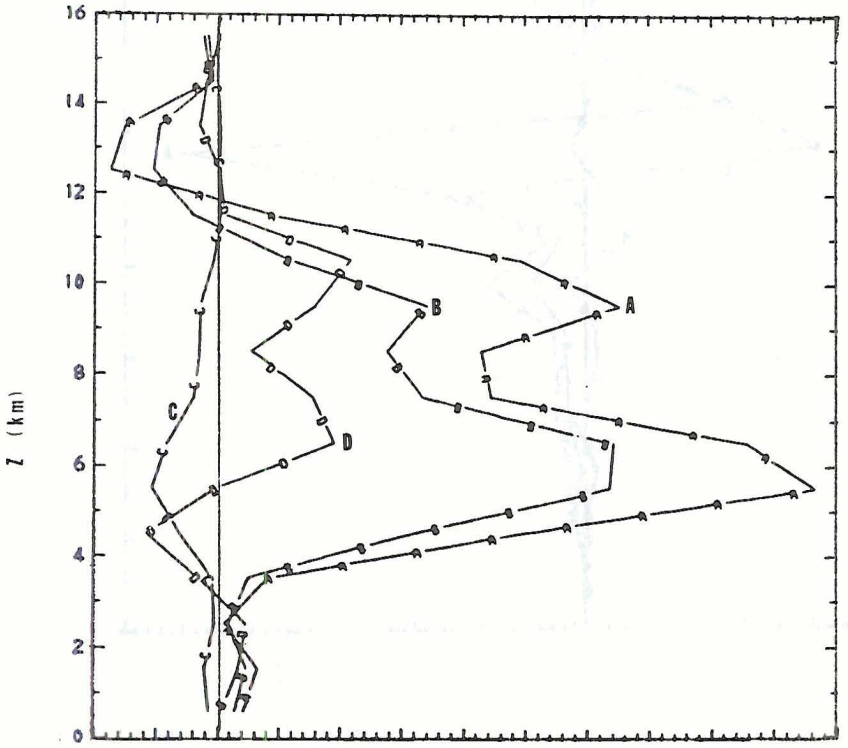

Figure 4.18. Vertical structure of (A) $\overline{u'w'}$; (B) $\overline{v'w'}$; (C) $\overline{p'w'}$; (D) $\overline{\theta'w'}$. For wavenumber (2,1.3) and with cumulus heating parameters in Table 1 except for z_{MH} = 9 km.

4.14 shows a plot of $\overline{u'w'}$, $\overline{v'w'}$, $\overline{p'w'}$, $\overline{\theta'w'}$ as a function of the vertical coordinate. From Appendix A 1, it is seen that a positive value of $\overline{u'w'}\ du_o/dz$ decreases the total energy of the disturbance. Fig. 4.14A shows a positive value of $u'w'$ from the surface up to 12.5 km while Fig. 4.1 shows that the zonal wind shear for the East Atlantic hodograph is negative almost all the way from 950 mb to 175 mb with negative values from 600 mb to 450 mb so that $\overline{u'w'}\ du_o/dz$ is negative for almost the whole troposphere denoting an increase in total energy in the form of horizontal kinetic energy. The meridional wind shear is smaller than the zonal wind shear in the East Atlantic hodograph of Fig. 4.1. The correlation $\overline{v'w'}$ is also smaller than $\overline{u'w'}$. The term $\overline{v'w'}\ dv_o/dz$ is negative up to 6.5 km then positive up to 10 km. A negative value of $\overline{u'w'}\ du_o/dz$ or $\overline{v'w'}\ dv_o/dz$ is also referred to as downgradient momentum transport (e.g. Dutton, 1976) and according to Eliassen and Palm (1960), the wave extracts energy from the mean flow (cf. Appendix A 1). The term $d\ \overline{w'p'}/dz$ according to Eliassen and Palm (1960) corresponds to the energy divergence associated with the perturbation pressure field; in Appendix A 1, it is seen that a positive vertical derivative of $\overline{p'w'}$ decreases the total energy. Fig. 4.1 C does not show a predominant sign for $d\ \overline{p'w'}/dz$.

Figs. 4.15 and 4.16 show the vertical cross section along $x = 0$ of the vector (v',w') for level of maximum heating at 6 km and 9 km, respectively. For z_{MH} equal to 6 km the structure is mostly horizontal with vertical velocities very small when compared to horizontal velocities. For z_{MH} at 9 km, on the other hand, a single cell in the middle troposphere is clearly dominant with about the same tilting as in

Fig. 4.11 for z_{MH} at 7.5 km. Figs. 4.17 and 4.18 show the vertical structure of the fluxes for z_{MH} at 6 km and 9 km respectively. For z_{MH} at 6 km, the same features already discussed concerning Fig. 4.14 for z_{MH} at 7.5 km still hold. For z_{MH} at 9 km, however, Fig. 4.18 D shows the plot of $\overline{\theta' w'}$ with the positive values from 5.5 km to 12.5 km corresponding to an increase of kinetic energy of vertical motions. The term $d\,\overline{p'w'}/dz$ is negative from the surface up to 5.5 km, and then positive up to 12 km corresponding to an increase of wave energy in the lower troposphere and a decrease of wave energy in the middle troposphere.

Changes in the top of the moist layer from 2 km to 4 km, although affecting the growth rate as seen in the previous subsection, do not significantly affect the vertical structure, which is not shown here.

The main effect of varying the level of maximum heating rate is on the intensity of the vertical velocity; the sign of the transports of momentum are not affected by the change in z_{MH}, while the region of conversion of potential into kinetic energy are well defined for z_{MH} at 9 km, while for z_{MH} at 6 km and 7.5 km, there are successive regions, in the vertical, of increase and decrease of kinetic energy.

d) Effect of Top Boundary Condition

The effect of imposing an upper boundary condition of zero vertical velocity will be briefly discussed in what follows. The growth rate is about 30% higher with a top boundary condition of no vertical velocity than with the radiation condition. The phase speed is only a few percent different. In the vertical, the imposition of a rigid lid has the effect of producing a slight change in the eigenvectors as may be seen in Fig. 4.19 for the amplitude of $\hat{w}$.

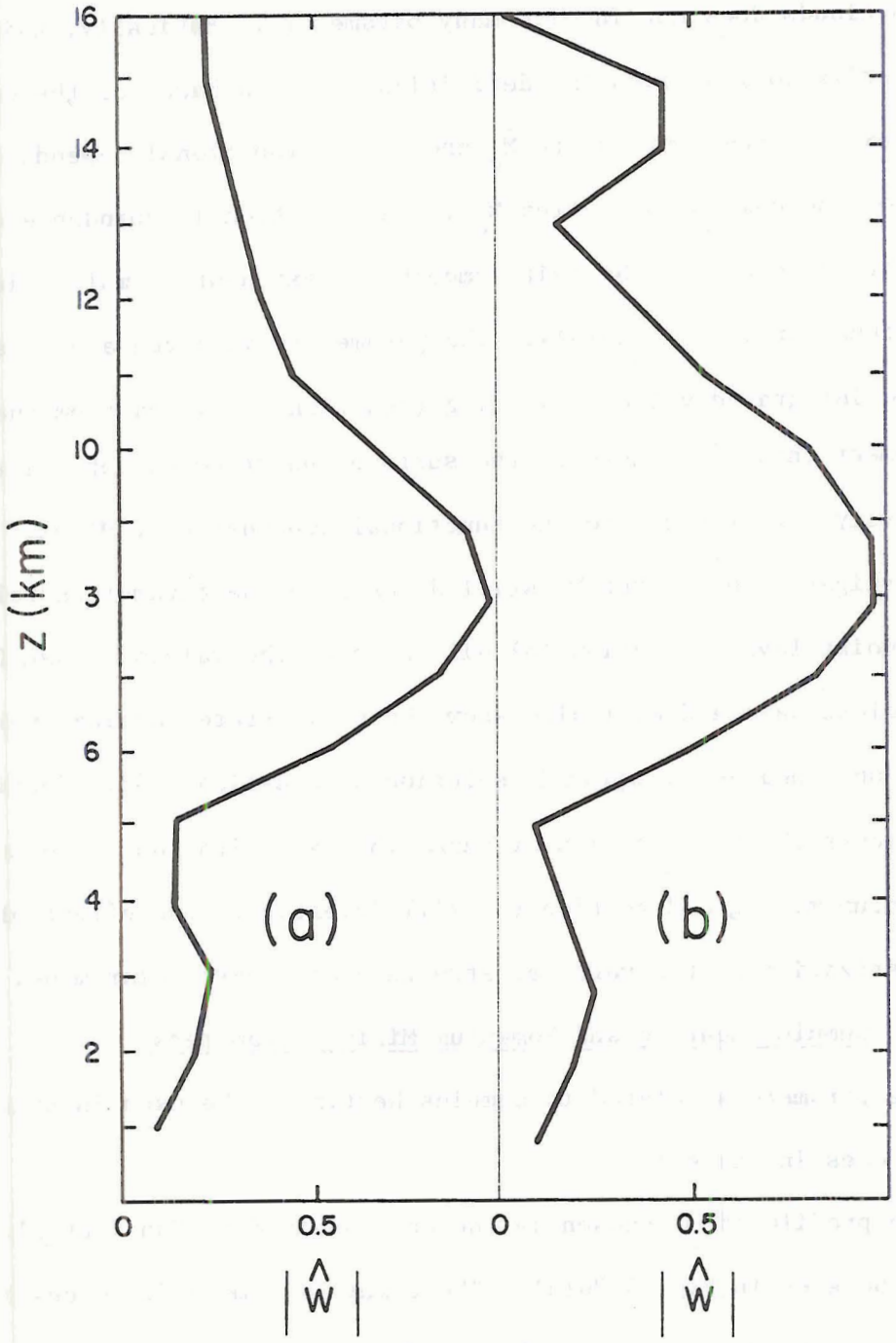

Figure 4.19. Vertical structure of the amplitude of $\hat{w}$ for the wavenumber (2,1.3) and cumulus heating parameters in Table 1: (a) Radiation condition at the top boundary, (b) top boundary condition of zero vertical velocity.

4.1.2 Sensitivity with Respect to Momentum Mixing Parameters

The definition of the parameterization of momentum mixing by cumulus clouds does not involve many parameters. Basically, this parameterization involves the definition of cloud base, of the cumulus mass flux of the basic state $\overline{M}_c$ and of the functional dependence on height of the cumulus mass flux M'_c . The functional dependence of M'_c on height was chosen to be quite smooth, an exponential multiplied by a sine function (Fig. 4.20(b)). The parameters involved are determined from the integrated value of heating (equation 3.54) and from the requirement that M'_c be zero at the surface and at model top. The sensitivity with respect to the functional dependence of M'_c will not be investigated here. But M'_c still depends on the parameters related to the moist layer. Section (a) will present the values chosen for $\overline{M}_c$ and cloud base and will also show the basic state vertical velocity profile obtained as an optimal solution of equation 3.53. Section (b) will discuss the modification of Figs. 4.3 - 4.9 with the introduction of momentum mixing and section (c) will investigate the effect of this parameterization on the vertical structure of a particular mode.

a) Cumulus Heating and Momentum Mixing Parameters

The parameters related to cumulus heating to be used in this section are the ones in Table 1.

The profile of $\overline{M}_c$ chosen is the one obtained by Yanai et al.,(1973) and may be seen in Fig. 4.20(a). There may be some differences in the shape of this curve for different data sets and budgets, but the order of magnitude does not change a lot. As a sensitivity test, the model will be run for $\overline{M}_c$ equal to one order of magnitude smaller and one order of magnitude larger than the profile in Fig. 4.20(a).

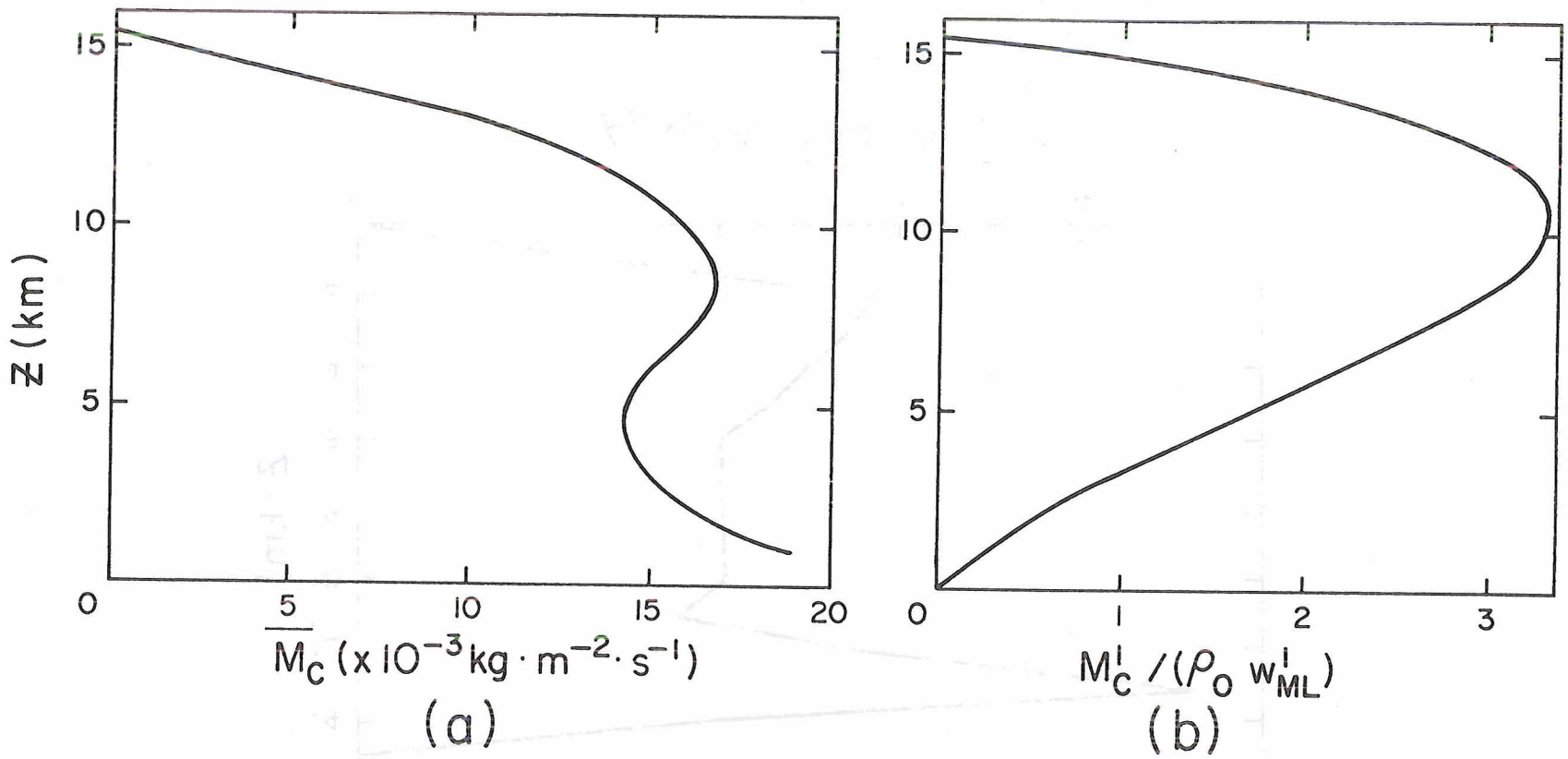

Figure 4.20. Cumulus mass flux: (a) large scale, from Yanai et al., (1973); (b) mesoscale for $q_o = 12 g.kg^{-1}$ (cf. equation 3.54).

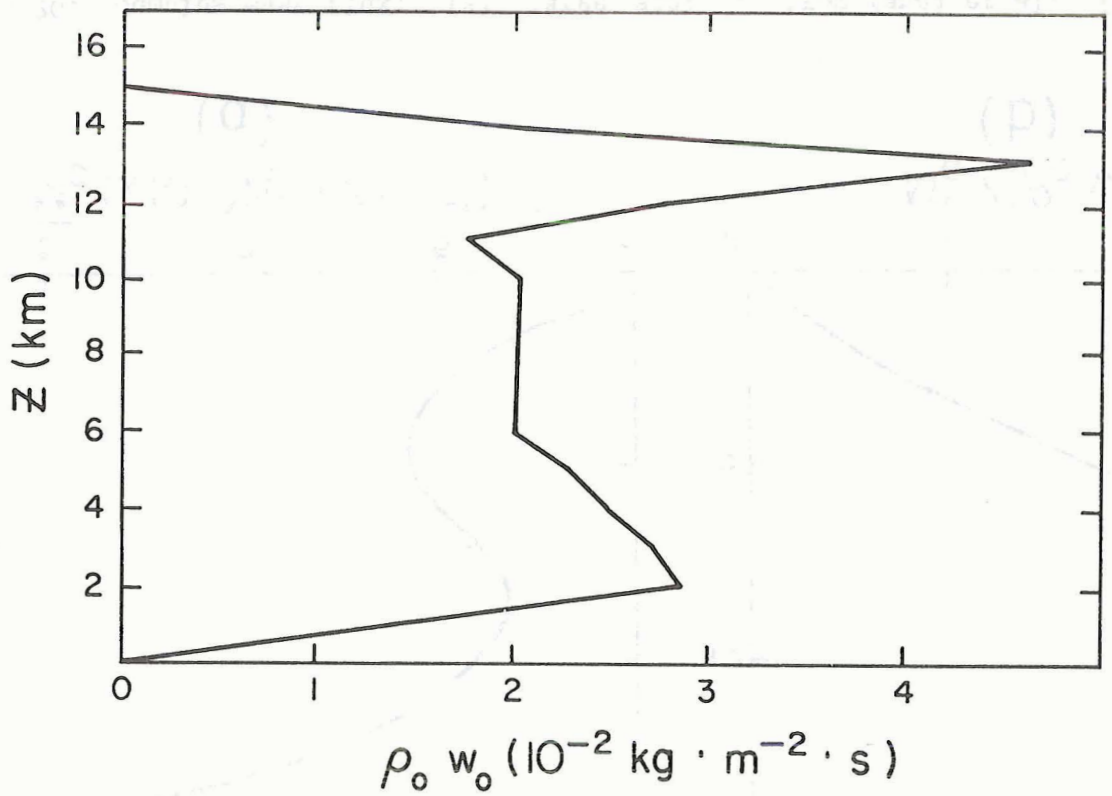

Figure 4.21. Optimal profile of basic state vertical mass flux (2×10^{-2} kg . m^{-2} . s^{-1} = 7 mb . hr^{-1}).

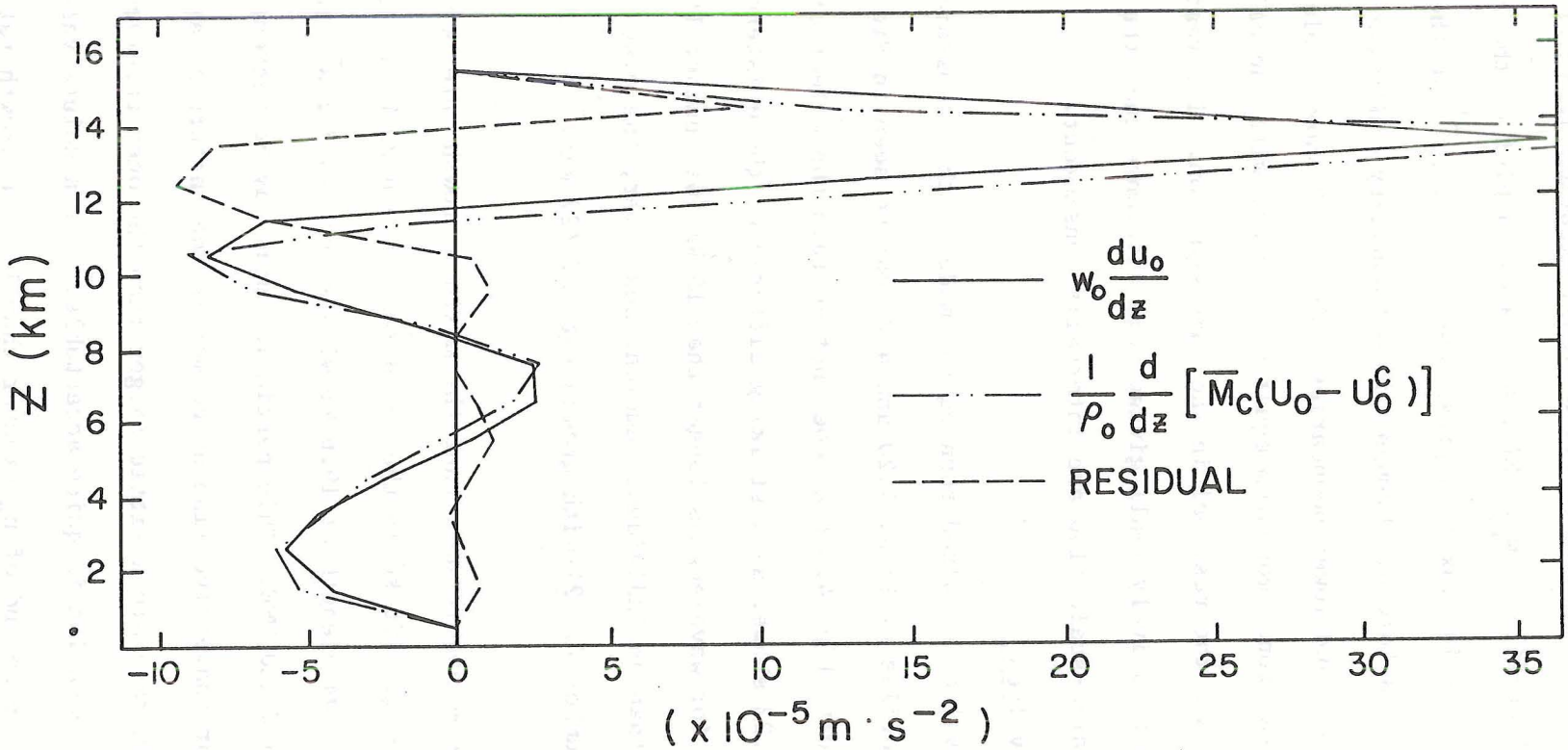

Figure 4.22. A plot of the vertical profile of the terms in equation (3.53a) for an optimal profile of w_o , and the residual in the same equation.

With the $\overline{M}_c$ profile of Fig. 4.20(a) and the basic state wind and temperature already defined (section 4.1a), equation 3.53 may be solved for an optimal profile of w_o. Fig. 4.21 shows a plot of the basic state mass flux $\rho_o w_o$. This flux is approximately 7 mb . hr^{-1} in the middle troposphere and is forced, through imposed boundary conditions, to be zero at the upper and lower boundaries. Fig. 4.22 shows a plot of the terms of the mean zonal momentum equation (3.53a), with the calculated profile of w_o, and the residual in the same equation. The residual at all heights is relatively small giving some assurance that the assumptions on the large-scale flow are internally consistent.

b) Eigenvalues

The eigenvalues obtained running the model with the parameters of Table 1 and profiles of Figs. 4.20 and 4.21 may be seen in Fig. 4.23. In comparison with Fig. 4.3 that does not contain the effect of momentum mixing, Fig. 4.23 shows, as a striking difference, the existence of a preferred mode for wavelengths longer than 15 km (wavenumber 14). For scales larger than an individual cumulonimbus tower, the most unstable mode has wavenumber (10,2) with growth rate of $(27\ \text{min})^{-1}$ and phase speed $-18.7\ \text{m.s}^{-1}$.

It is interesting to note that the maximum growth rate occurs for a wave of wavelength 100 km in the y direction and 20 km in the x direction, i.e., wavelength of 19.6 km with speed $-18.7\ \text{m.s}^{-1}$ towards 257° or between W and WSW. This particular mode may be representing a squall line or convective line so common in the Eastern Atlantic; speed and growth rate are a little larger than the ones observed, but direction of propagation is quite acceptable. For absolute value of n_x greater than 16 and of n_y greater than 14, the growth rate

starts to increase again, as in the inviscid case. In the upper right of Fig. 3.24(a), there is again a packing of isolines denoting a discontinuity in phase speed due to the fact that a mode with quite different value of phase velocity becomes more unstable than the most unstable mode for neighboring values of wavenumber.

These curves are not sensitive to variations in $\overline{M}_c$ and in w_o. Changing $\overline{M}_c$ by as much as one order of magnitude had the effect of changing the values of phase speed by 0.5% and the growth speed by 0.2%. The results of imposing a basic state with no vertical velocity at all produced the same variation as above.

The sensitivity of the eigenvalues to the moist layer parameters is somewhat modified with the inclusion of momentum mixing. The value of growth rate still increases for increasing mean moist layer mixing ratio q_o, but much less. With only the cumulus heating parameterization, a 20% variation in q_o would produce a 20% variation in growth rate. For the same variation of q_o, the growth rate varies only 5% after the inclusion of momentum mixing.

Increasing the value of z_{ML}, the top of the moist layer, to 3 km and to 4 km, had the effect, as may be seen in Figs. 4.24 and 4.25 respectively, of diminishing the growth rates of modes with high wavenumber or short wavelength. This makes the peak in growth at (10,2) more pronounced. Again, the wavenumber of maximum growth rate is not modified by variations in z_{ML}. The actual value of growth rate for the most unstable wave is $(26\ \text{min})^{-1}$ for z_{ML} equal to 3 km, and $(32\ \text{min})^{-1}$ for z_{ML} at 4 km. For z_{ML} = 2 km, this value was $(27\ \text{min})^{-1}$. The phase speed for mode (10,2) is not modified (less than 1% change) by variations of z_{ML}.

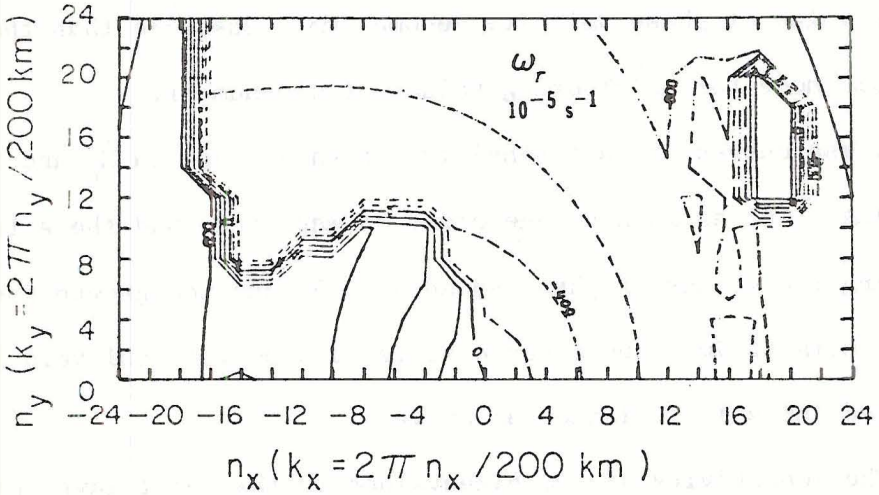

(a)

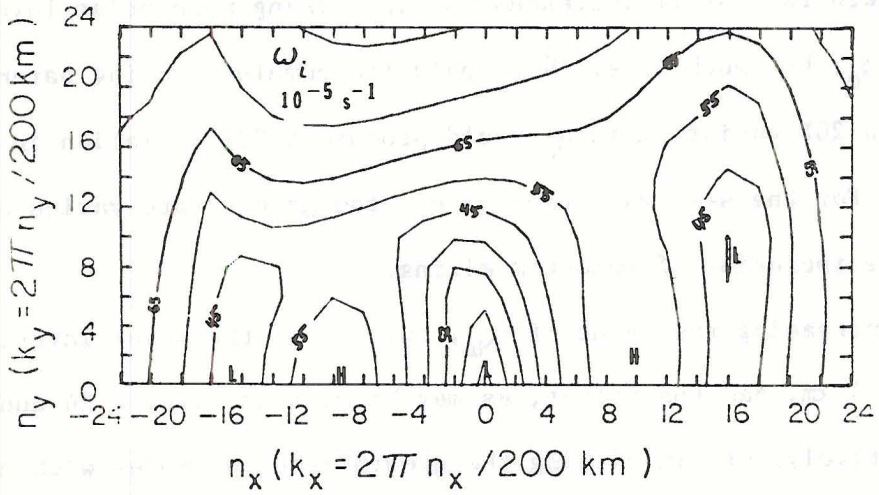

(b)

Figure 4.23. Eigenvalues for model run with cumulus heating parameterization (Table 1) and momentum mixing by cumulus clouds (Fig. 4.20). Basic state wind and temperature "East Atlantic".

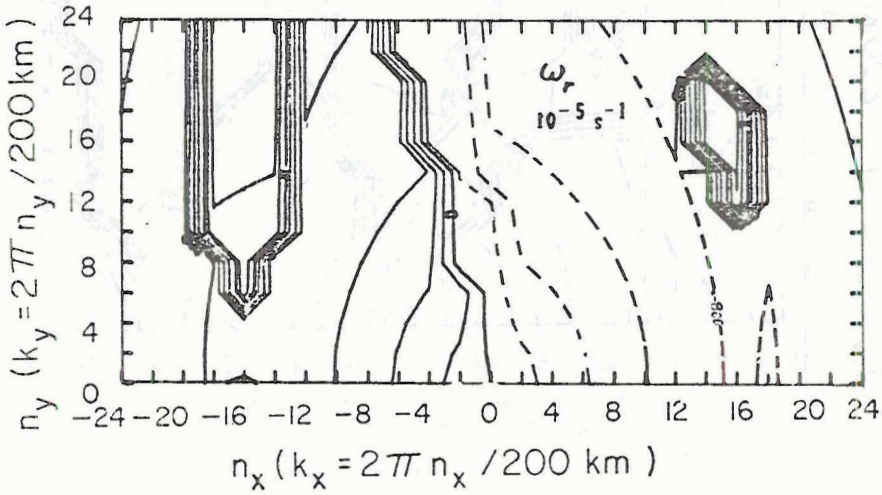

(a)

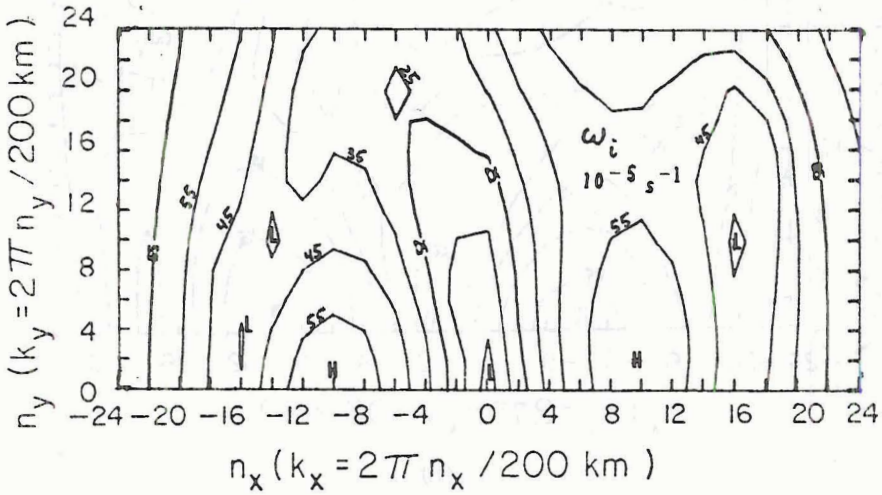

(b)

Figure 4.24. Eigenvalues for model run with cumulus heating parameterization (Table 1, except for z_{ML} = 3 km) and momentum mixing by cumulus clouds (Fig. 4.20).

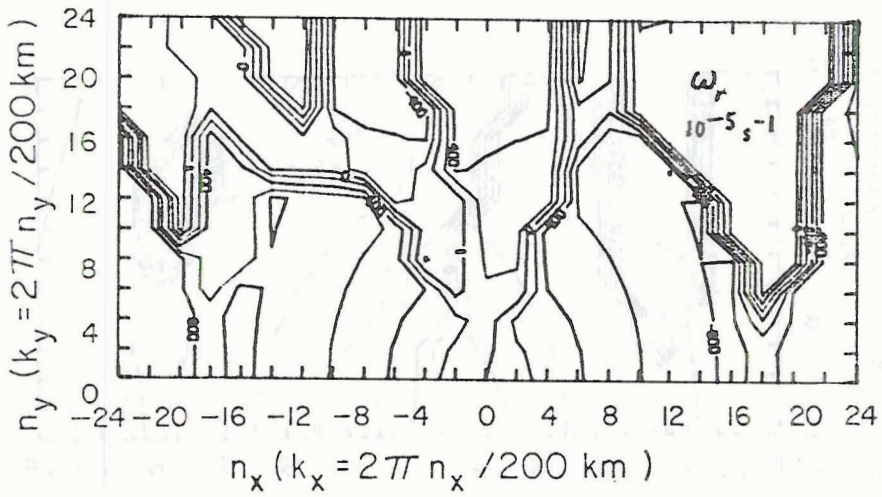

(a)

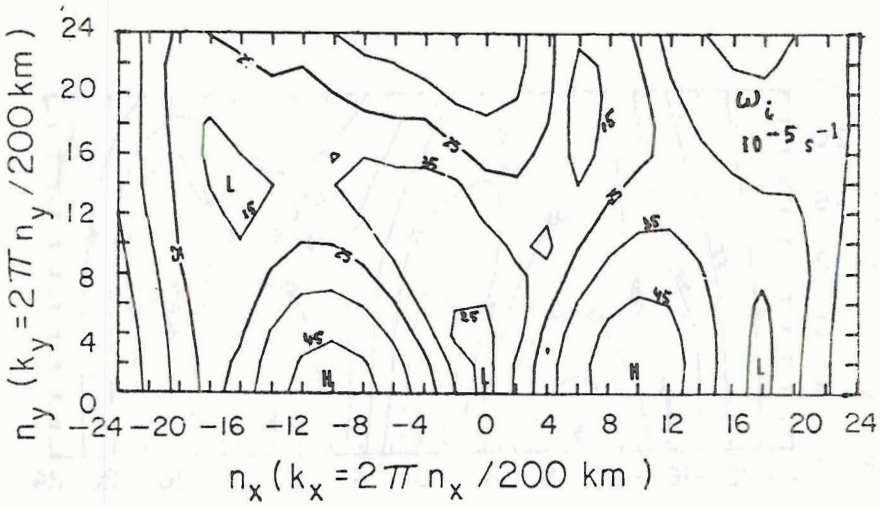

(b)

Figure 4.25. Eigenvalues for model run with cumulus heating parameterization (Table 1, except for z_{ML} = 4 km) and momentum mixing by cumulus clouds (Fig. 4.20).

c) Vertical Structure

The effect of inclusion of momentum mixing parameterization on the mode already studied in section 4.1.1b (2,1.3) may be seen in Figs. 4.26 and 4.27 which the isolines of vertical velocity in the plane x = 0 and the fluxes, respectively. Fig. 4.26 may be compared to Fig. 4.13 to show a clearly defined single cell structure throughout the middle and higher troposphere; again, low values of w' are seen in the lower troposphere. Fig. 4.27 may be compared to Fig. 4.14. The main differences may be listed as: curve A ($\overline{u'w'}$) does not approach zero for the whole middle troposphere for Fig. 4.27; curve B ($\overline{v'w'}$) goes negative in Fig. 4.14 above 10 km and in Fig. 4.27, $\overline{v'w'}$ is negative between 11 and 12 km and is positive from 12 to 14 km.

The main effects of introducing the momentum mixing parameterization are a change in the momentum field and consequently in the transports of momentum.

The structure of the most unstable mode in Fig. 4.23, i.e., wavenumber (10,2) may be seen in Figs. 4.28 and 4.29 for the isolines of vertical velocity and the fluxes, respectively. The vertical velocity again shows a single cell structure in the middle troposphere; note that the horizontal wavelength is shorter in Fig. 4.28 than in Fig. 4.26. The main difference between Figs. 4.29 and 4.27 is in more conversion of potential to kinetic energy above 10 km denoted by the negative sign of $\overline{\theta'w'}$ (curve D); $\overline{v'w'}$ has negative sign between 10 and 14 km in Fig. 4.29.

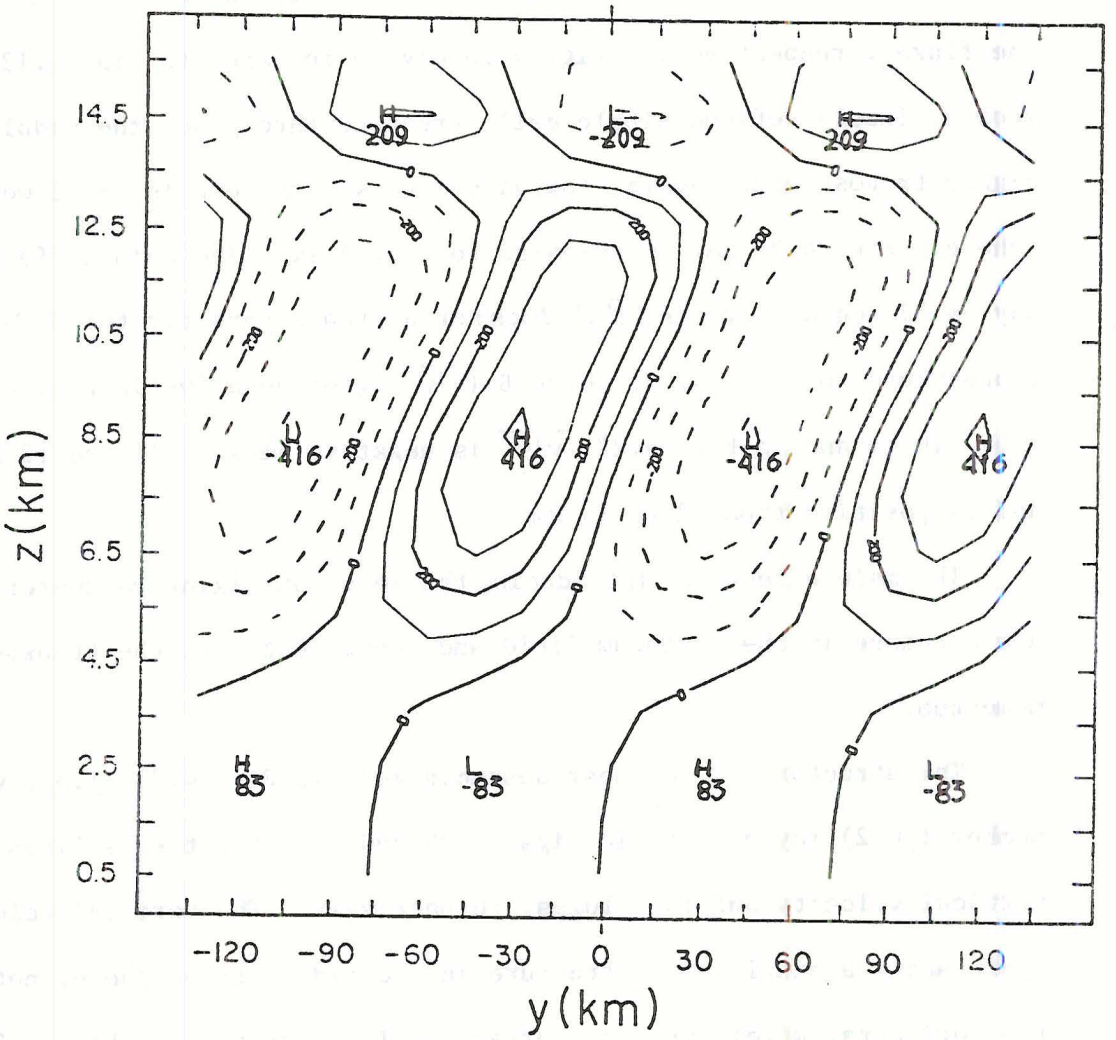

Figure 4.26. Isolines of mesoscale vertical velocity in the meridional plane at x = 0; wavenumber (2,1.3) (cf. Fig. 4.23) for cumulus heating parameters in Table 1 and momentum mixing parameterization (Fig. 4.20). (cf. Fig. 4.13).

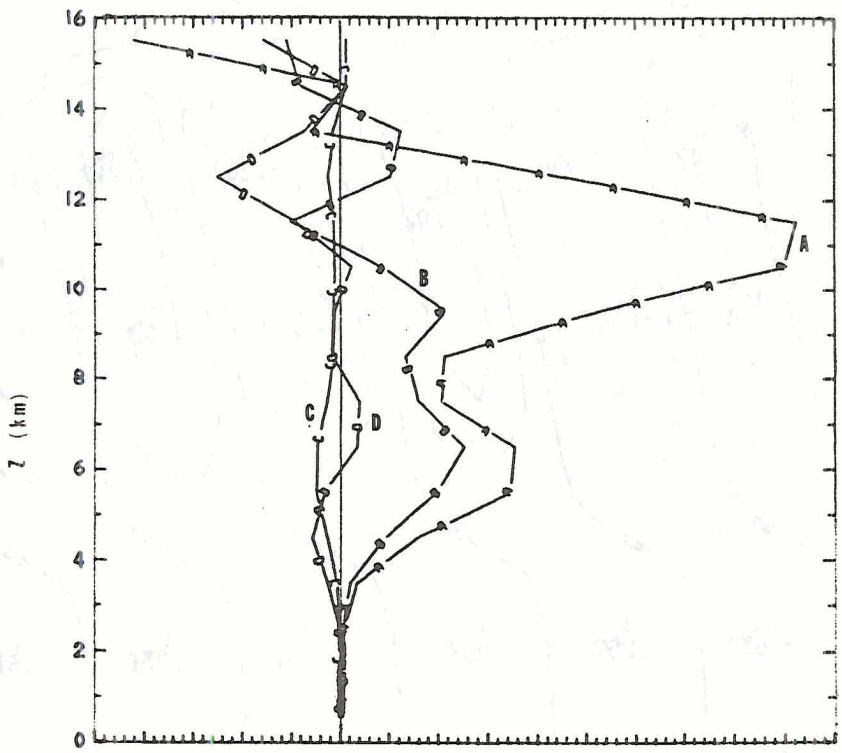

Figure 4.27. Vertical structure of (A) $\overline{u'w'}$; (B) $\overline{v'w'}$; (C) $\overline{p'w'}$; (D) $\overline{\theta'w'}$. For wavenumber (2,1.3) and with cumulus heating (Table 1) and momentum mixing parameterizations (Fig. 4.20) (cf. Fig. 4.14).

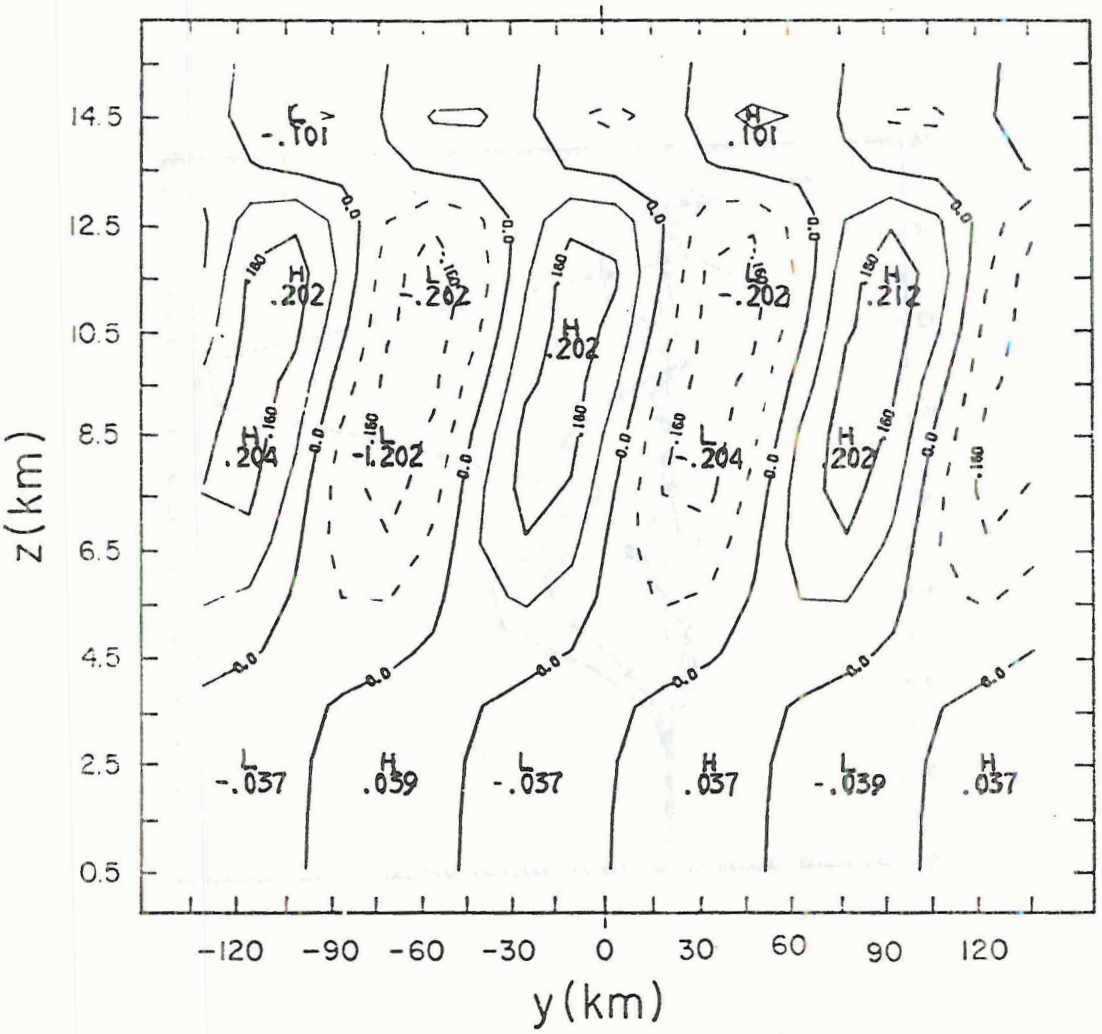

Figure 4.28. Isolines of mesoscale vertical velocity in the meridional plane at x = 0; wavenumber (10,2) (cf. Fig. 4.23). Cumulus heating parameters in Table 1 and momentum mixing parameter profiles in Fig. 4.20. (cf. Fig. 4.26).

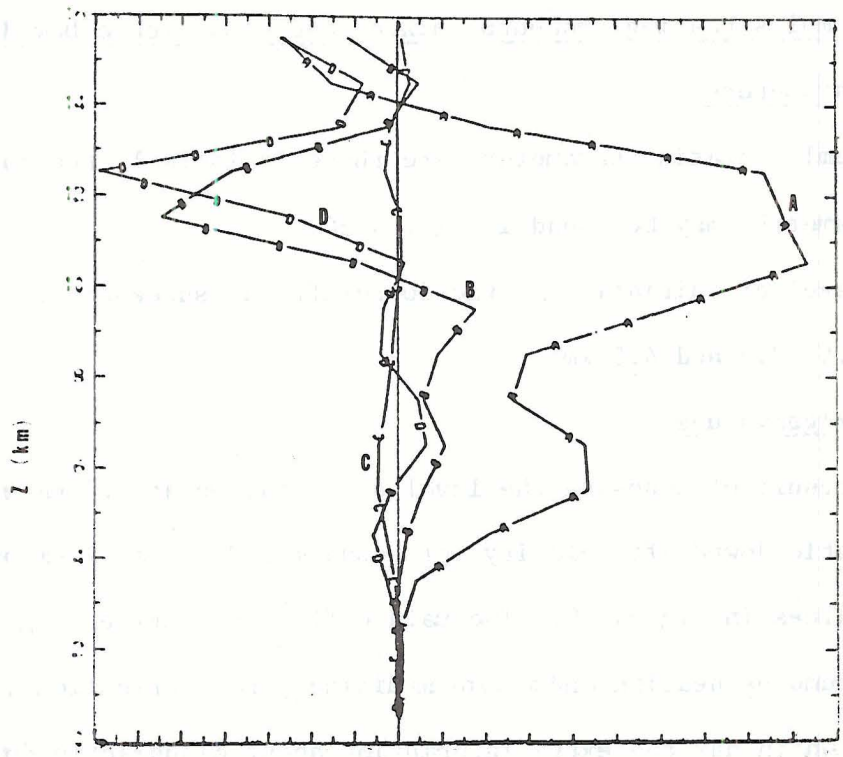

Figure 4.29. Vertical structure of (A) $\overline{u'w'}$; (B) $\overline{v'w'}$; (C) $\overline{p'w'}$; (D) $\overline{\theta'w'}$. For wavenumber (10,2). Cumulus heating parameters in Table 1 and momentum mixing parameter profiles in Fig. 4.20. (cf. Fig. 4.27).

4.1.3 Sensitivity with Respect to Cloud-scale Downdraft Parameters

The parameters involved in the cloud scale downdraft parameterization may be found in section 3.3.3, and are basically the level of initiation and the equivalent potential temperature inside the downdraft. The value of θ_E characteristic of cloud scale downdraft, according to Zipser (1969) is about 341°K, but effect of variations upon this parameter will not be investigated here.

a) Cumulus Heating, Momentum Mixing and Cloud-scale Downdraft Parameters

The cumlus heating parameters are those in Table 1; the momentum mixing parameters may be found in Fig. 4.20.

The level of initiation of the downdraft was successively imposed at 2.5, 3.5 and 4.5 km.

b) Eigenvalues

As a result of imposing the level of initation at 2.5 km with characteristic downdraft velocity (cf. equation 3.59) at 2 km produced the eigenvalues in Fig. 4.30. The main difference between Fig. 4.23, which has cumulus heating and momentum mixing parameterizations, and Fig. 4.30, which has the extra information about cloud-scale downdraft effects, is in smaller values of growth rate for high wavenumbers, and in larger values of growth rate for low wavenumbers. The most unstable mode is still for wavenumber (10,2) with growth rate of (23 min)$^{-1}$ and phase speed -19.8 m.s^{-1}.

Imposing the level of initation of the downdraft at 3.5 km (Fig. 4.31) and 4.5 km (not shown) had the drastic effect of wiping out any preferred mode for low wavenumbers, and increasing the values of growth rate by a factor of 1.5 and 2, respectively.

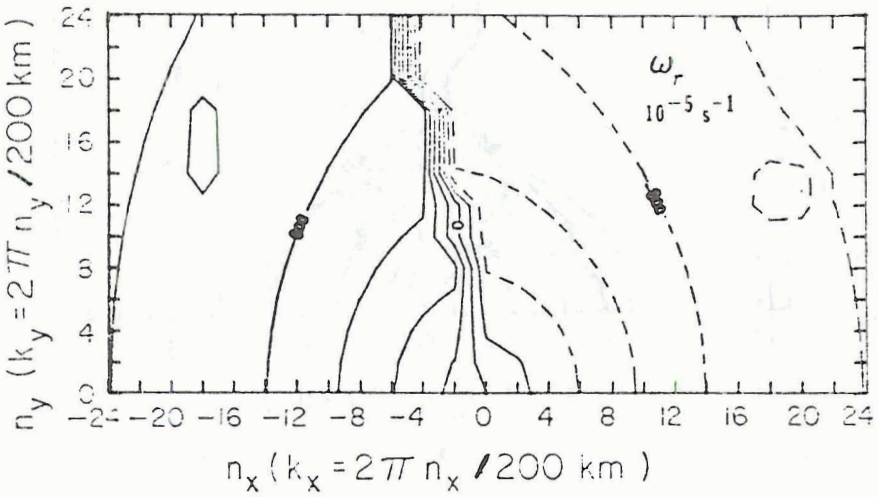

(a)

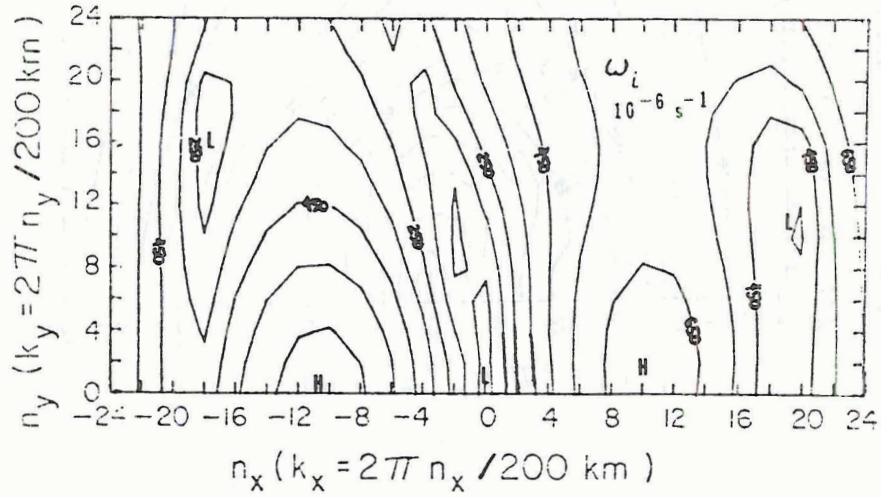

(b)

Figure 4.30. Eigenvalues for model run with cumulus heating (Table 1), momentum mixing (Fig. 4.20) and cloud-scale downdraft (downdraft initiation at 2.5 km) parameterizations.

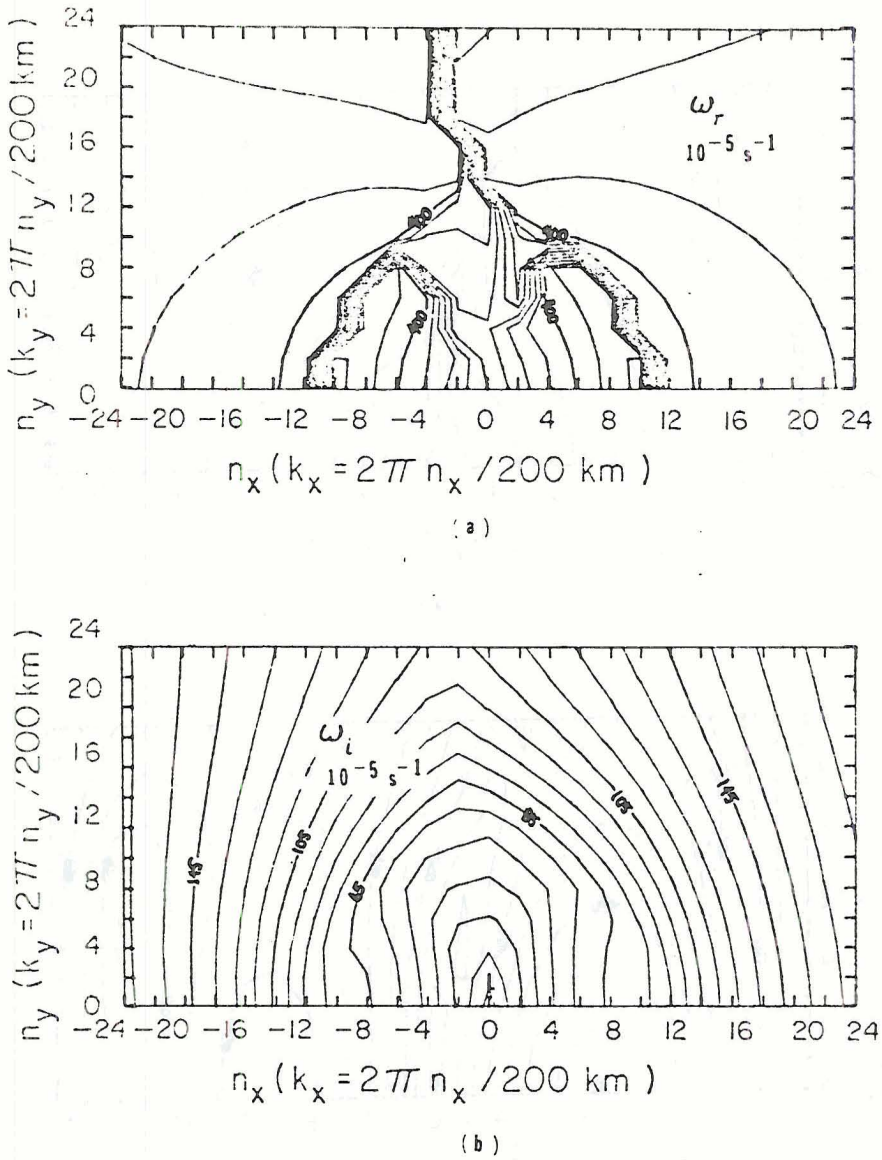

Figure 4.31. Eigenvalues for model run with cumulus heating (Table 1), momentum mixing (Fig. 4.20) and cloud scale downdraft (downdraft initiation at 3.5 km) parameterizations.

The strong dependence on the level of initiation of the downdraft is a serious problem concerning the parameterization scheme defined in section 3.3.3. However, the presentation of these results should be regarded as a first attempt to include the effect of cloud scale downdraft in a model. This parameterization will not be used in the computations to be described in following sections.

c) Vertical Structure

The vertical structure of mode (10,2) for level of initiation of the downdraft at 2.5 km is very similar to the one depicted in Figs. 4.28, 4.29 which do not contain the cloud scale downdraft parameterization, and so will not be shown.

4.1.4 Summary of Recommended Parameters

The values in Table 1 and Fig. 4.20 for the cumulus heating and momentum mixing parameterizations, respectively, may be regarded as appropriate parameters for any further computations. Variations for these values do not have significant effect on phase speed and on wavenumber of maximum instability. The value of growth rate should not, however, be regarded as accurate, since it is highly sensitive to the values of top of moist layer, mean mixing ratio in moist layer and level of maximum heating rate. Since very little is known from the observational point of view on the specification of these parameters, the values of growth rate should be regarded with caution. The vertical structure of the eigenmodes is mainly dependent on the level of maximum heating rate.

4.2 Sensitivity with Respect to Basic State

One of the objectives of the present research is to understand the

the dependence of mesoscale features on large-scale characteristics. To achieve this goal, a preliminary step, to be discussed in the following subsections, will be to present the sensitivity of the eigenvalues of equation 3.30 to basic state profiles of wind speed (4.2.1), potential temperature (4.2.2) and wind direction (4.2.3).

It should be kept in mind that the basic state profiles to be used are variations about tropical soundings. The winds, for example, do not show speeds with magnitude greater than 20 $m.s^{-1}$ as opposed to the environment of mid-latitude mesoscale systems. The study of mid-latitude as well as subtropical mesoscale systems should be the subject of future research.

Besides testing the response of the model to different basic state characterisitics, the sections that follow may be regarded as the basis for future development of parameterization schemes. In cooperation with observational work, ideas on how environmental properties affect speed and direction of propagation of mesoscale systems may be tested.

Although neither a parameterization scheme nor a detailed comparison with data will be attempted, it is hoped that the following sections will provide some understanding on the mesoscale response to basic state features.

a) Model Structure and Small-scale Parameters

The model structure is the same as in the first part of this chapter: the top boundary is at 16 km, the tropopause; there are 16 levels in the vertical with spacing of 1 km between levels. Fig. 3.1 shows a display of model structure.

The parameterizations to be used are the cumulus heating parameterization (parameters in Table 1) and the momentum mixing by cumulus clouds (parameters in Fig. 4.20) parameterization.

4.2.1 Effect of Wind Speed

The mean wind profile over the GATE, as may be seen in Fig. 4.1 (E. Atlantic) shows a low level jet around 600 mb and an upper level jet at 175 mb. For the W. Pacific (also in Fig. 4.1) the low level jet is almost non existent in the mean obtained by Reed and Recker (1971); the upper level jet, however, is very pronounced. This section investigates the sensitivity of the eigenvalues of equation 3.30 to the level and intensity of upper and lower jets in parallel flow, (i.e., no directional wind shear).

a) Basic State Wind and Temperature

The basic state wind profiles may be seen in Fig. 4.32. Profiles 1A, 1B and 1C have different intensities of upper level jet (ULJ) of 3.5 $m.s^{-1}$, 7.5 $m.s^{-1}$ and 15 $m.s^{-1}$, respectively; the level of the ULJ is 11.5 km; the lower level jet (LLJ) is at 2.5 km with an intensity of 7.5 $m.s^{-1}$; profile 1A, indeed, does not show an ULJ at all. Profiles 2A and 2B have ULJ at 13.5 km with a speed of 15 $m.s^{-1}$; 2A does not have a LLJ; 2B has a LLJ at 2.5 km with intensity of 7.5 $m.s^{-1}$. Profiles 3A and 3B have an LLJ at 2.5 km with intensity 7.5 $m.s^{-1}$; the ULJ has speed of 3.5 $m.s^{-1}$ for 3A and 15 $m.s^{-1}$ for 3B at the height of 13.5 km. Profile 4A has some shear up to 3 km but is otherwise a constant profile of 7.5 $m.s^{-1}$. 4B and 4C have LLJ at 4.5 km with intensities of 7.5 $m.s^{-1}$ and 15 $m.s^{-1}$, respectively; 4B has ULJ of 15 $m.s^{-1}$ at 13.5 km, 4C does not have ULJ.

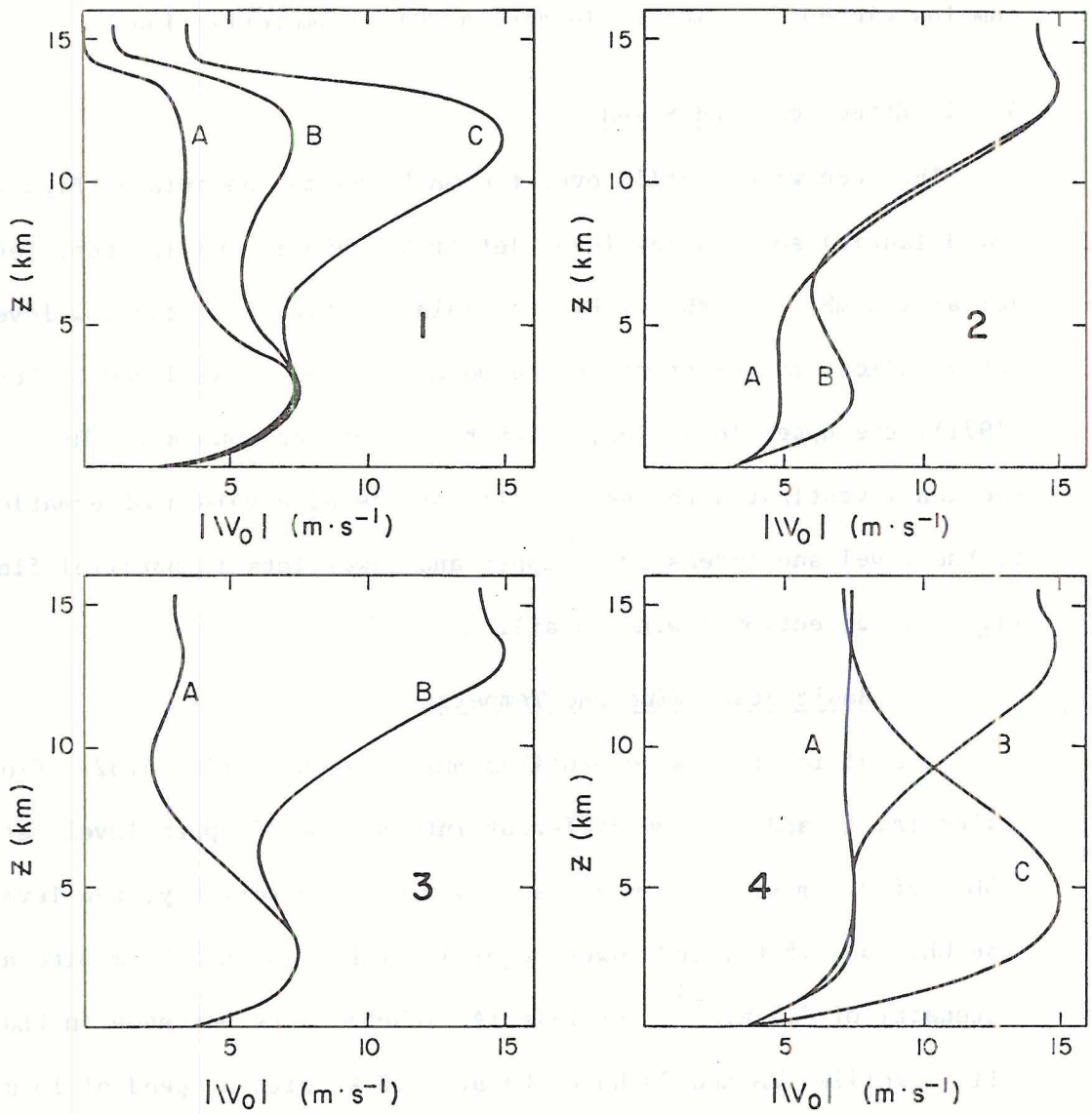

Figure 4.32, Wind speed for different levels and intensities of upper and lower level jets.

The basic state temperature used in the present section is the one labeled Day 248 in Fig. 4.2.

b) Eigenvalues

The effect of the speed of the ULJ may be seen by comparing Figs. 4.33, 4.34 and 4.35 which have basic state wind profiles 1A, 1B and 1C, respectively. Figs. 4.33 and 4.34 do not show a preferred mode except for high wavenumbers. Fig. 4.35, on the other hand, shows a mode with higher growth rate for wavenumber (14,0) and (-14,0), with wavelength of 14 km in the x-direction (east-west direction) and no structure in the y-direction or infinite wavelength in the north-south direction. The ULJ then, has to be of a certain intensity to provoke the selection of a most unstable wave.

The effect of the height of the upper-level jet may be seen by comparing Figs. 4.36 (3B) with Fig. 4.35 (1C). Comparing Figs. 4.35 and 4.36 it may be seen that the effect of raising the ULJ from 11.5 km to 13.5 km almost wipes out the selectivity encountered in Fig. 4.35 and the growth rates are somewhat lower. The fact that profile 3B shows a narrower jet than profile 1C may also be of significance.

Profile 3A shows a slight increase of wind speed at about 13.5 km while profile 1A shows constant wind from 8 km to 14 km and then a sharp decrease to zero. Fig. 4.37 shows the eigenvalues for profile 3A and may be compared to Fig. 4.33 for profile 1A. Fig. 4.33 and 4.37 are very similar except for somewhat higher values of growth rate in Fig. 4.37 for profile 3A.

The effect of the speed of the LLJ may be seen by comparing Figs. 4.38 (2A) and Fig. 4.36 (2B or 3B). Profile 2A does not really have a LLJ and profile 2B has a pronounced LLJ; Fig. 4.38 (2A) shows a

Table 2 . Summary of sensitivity with respect to basic state wind speed.

wind profile	speed of ULJ	height of ULJ	speed of LLJ	height of LLJ	(n_x, n_y) of max. growth	$(w_i)^-$	c_r	Fig.
	$m.s^{-1}$	km	$m.s^{-1}$	km		min	$m.s^{-1}$	
1A	3.5	11.5	7.5	2.5	———	—	———	4.33
1B	7.5	11.5	7.5	2.5	———	—	———	4.34
1C	15.0	11.5	7.5	2.5	(±14,0)	15	∓24.0	4.35
2B,3B	15.0	13.5	7.5	2.5	(±12,0)	22	∓24.4	4.36
3A	3.5	13.5	7.5	2.5	———	—	———	4.37
2A	15.0	13.5	5.0	2.5	(±12,0)	20	∓23.7	4.38
4B	15.0	13.5	7.5	4.5	(±14,0)	22	∓24.0	4.39
4A	7.5	13.5	7.5	4.5	———	—	———	———
4C	7.5	13.5	15.0	4.5	———	—	———	———

maximum growth rate for wavenumber (12,0) and (-12,0) while Fig. 4.36 (2B) only shows a slight tendency to the selectivity process at the same wavenumbers.

Increasing the height of the LLJ by imposing profiles 4C rather than 3A (Fig. 4.37) has the effect of increasing the growth rate, but does not affect the selection mechanism (eigenvalues for 4C are not shown).

Profiles 2A and 4B are very similar except for the speed below 5 km which is 5 $m.s^{-1}$ and 7.5 $m.s^{-1}$, respectively. Fig. 4.39 shows the eigenvalues for profile 4B with maximum growth rate at (14,0) and (-14,0) while Fig. 4.38 shows maximum growth rate at (12,0) and (-12,0). The value of growth rate is 10% higher for an atmosphere with low-level winds of smaller magnitude.

Table 2 summarizes the results described above.

In summary, the feature of the basic state wind speed that most significantly affects the selectivity process is the speed and height of the upper level jet; the presence of the lower level jet or of high speeds in the lower troposphere seem to prevent the selectivity process or to displace the mode of higher instability to a higher wavenumber with smaller values of growth rate. The height of the lower level jet does not seem to affect the eigenvalues.

4.2.2 Effect of Potential Temperature

The features in the potential temperature profiles that will be considered are the stability in the lower troposphere and upper troposphere, below the isothermal layer corresponding to the lower stratosphere.

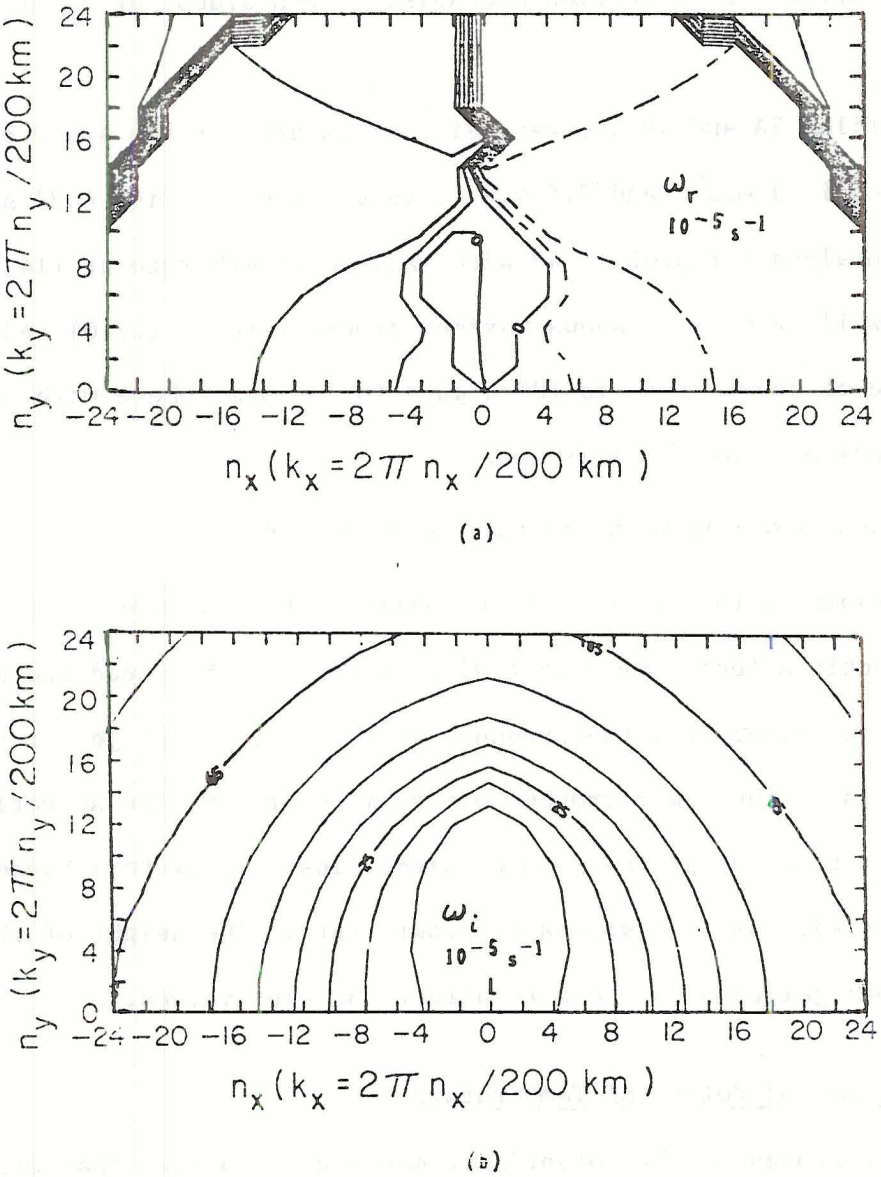

Figure 4.33. Eigenvalues for basic state wind 1A and temperature "Day 248".

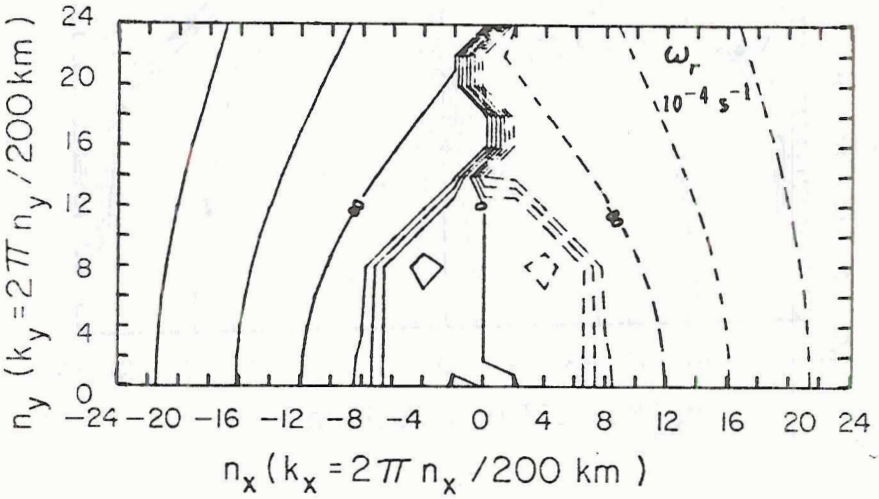

(a)

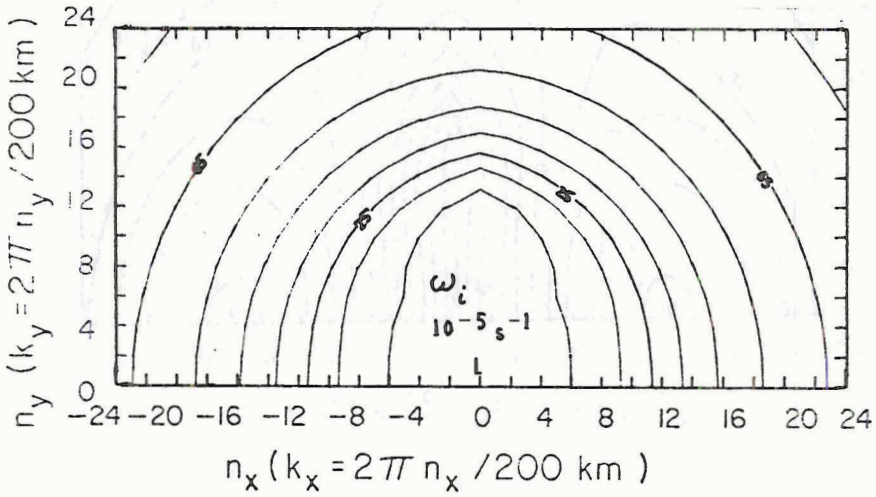

(b)

Figure 4.34. Eigenvalues for basic state wind 1B and temperature "Day 248".

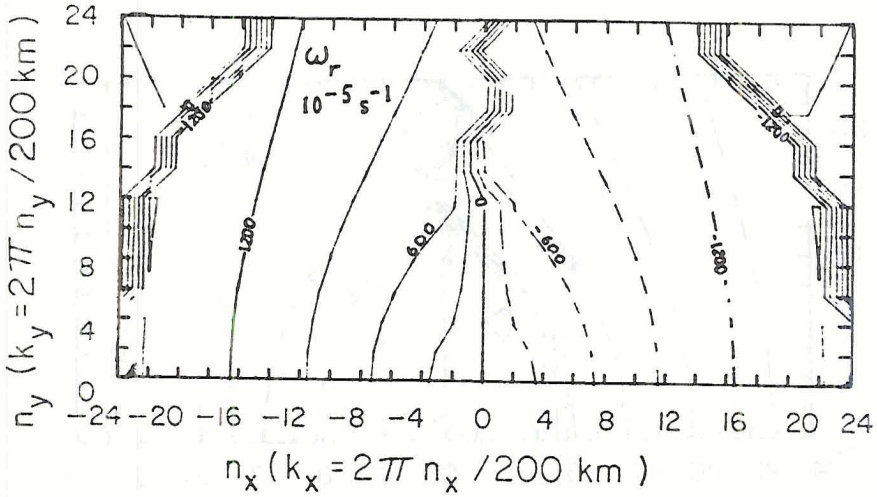

(a)

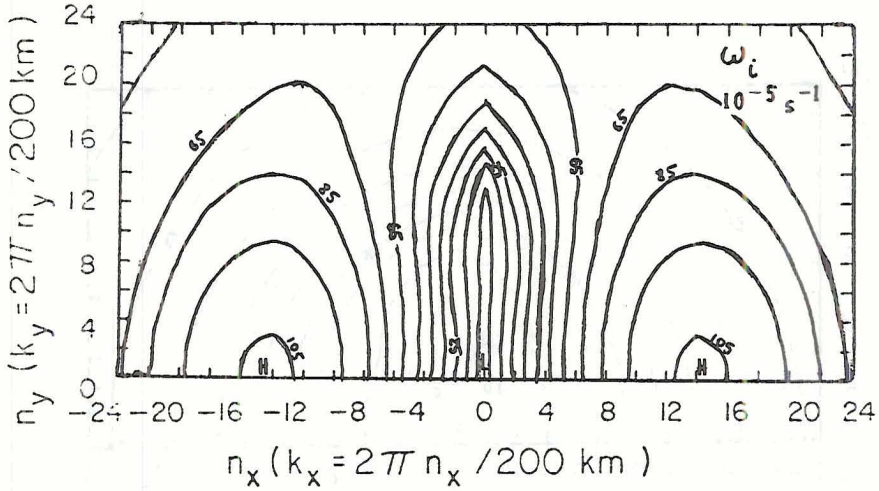

(b)

Figure 4.35. Eigenvalues for basic state wind 1C and temperature "Day 248".

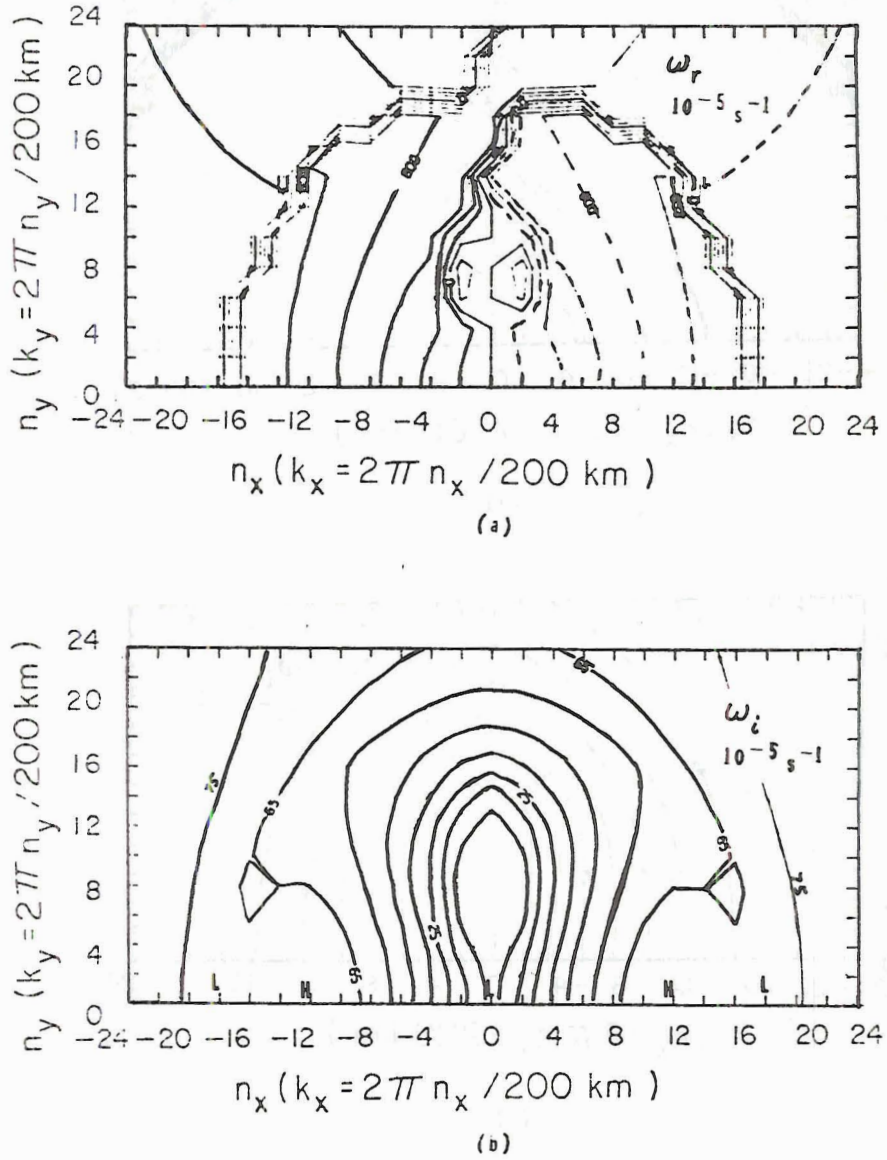

Figure 4.36. Eigenvalues for basic state wind 3B (or 2B) and temperature "Day 248".

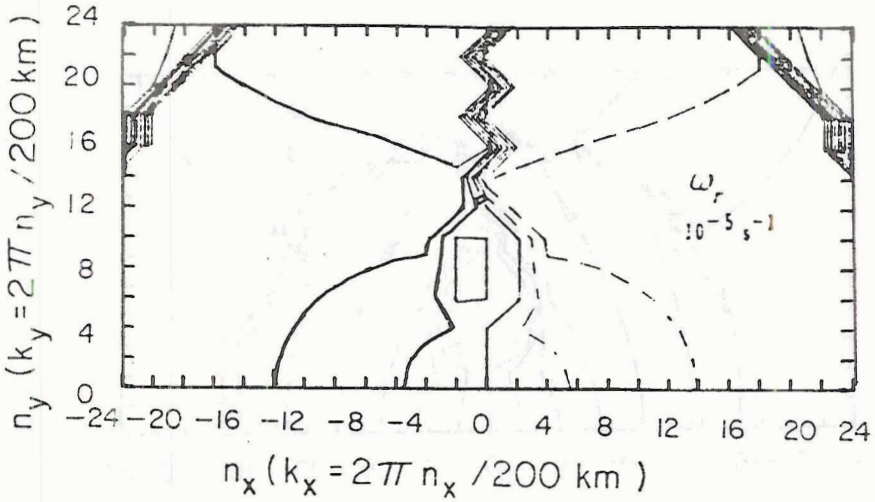

(a)

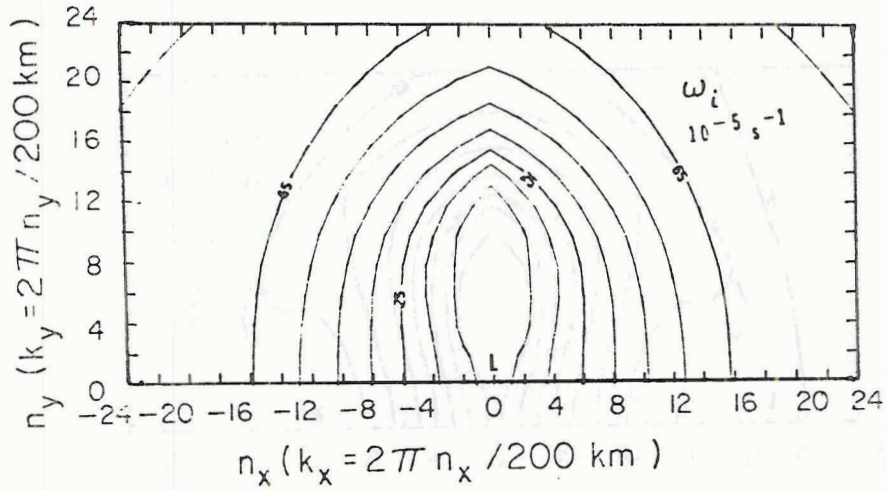

(b)

Figure 4.37. Eigenvalues for basic state wind 3A and temperature "Day 248".

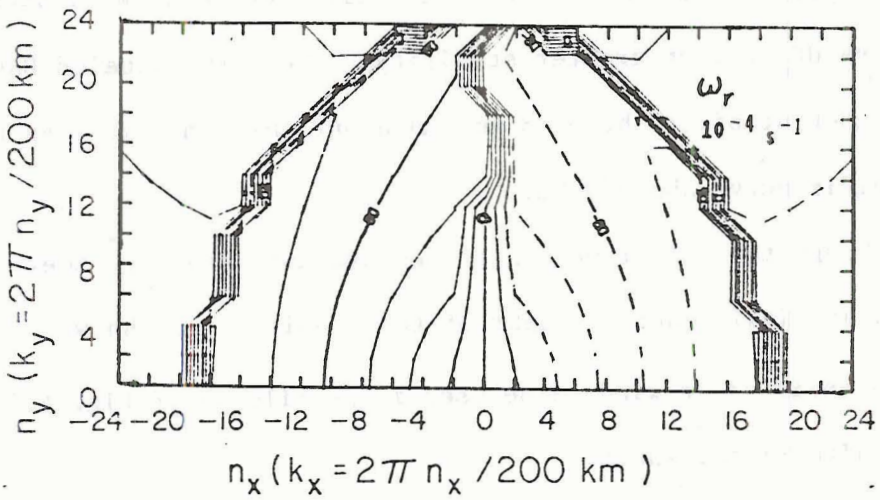

(a)

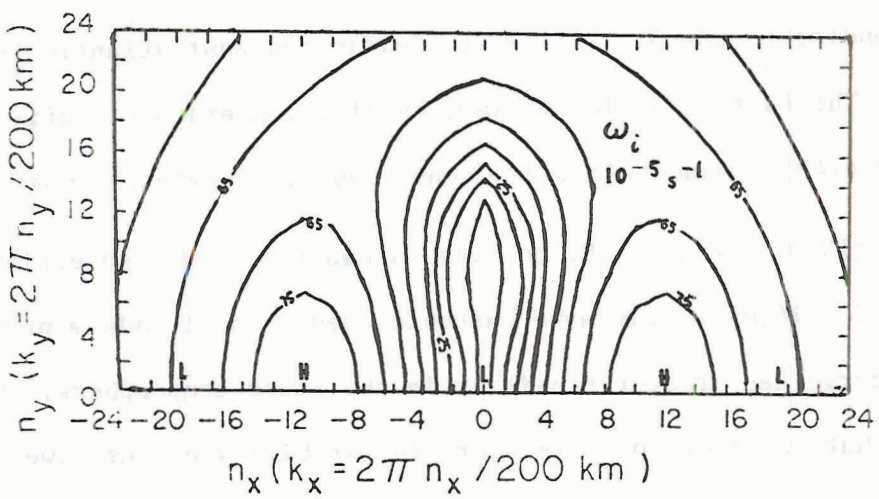

(b)

Figure 4.38. Eigenvalues for basic state wind 2A and temperature "Day 248".

a) Basic State Wind and Temperature

The potential temperature profiles in Fig. 4.2 show the East Atlantic and West Pacific curves having the same slope from the surface up to 8 km although the East Atlantic curve shows lower temperatures. Above 8 km and below 13 km, the West Pacific curve shows a higher derivative $d\theta_o/dz$, or greater stability. The curve labeled Day 248 shows higher stability below 8 km and about the same slope as the West Pacific curve above 8 km.

Although the difference in slopes are not very big, they may be regarded as significant in light of the results to be shown.

The basic state wind to be used is profile 4B of Fig. 4.32, without directional shear.

b) Eigenvalues

Fig. 4.39, 4.40 and 4.41 show the eigenvalues for temperatures corresponding to the Day 248, West Pacific and East Atlantic, respectively. The East Atlantic and West Pacific temperature profiles (Figs. 4.41 and 4.40) produce similar eigenvalues with preferred mode at (-10,0), (10,0). Fig. 4.39, however, shows a distinct selection of modes (14,0) and (-14,0) as the more unstable ones. As already mentioned, the Day 248 curve has greater stability in the lower troposphere. This may suggest that in order to break a greater stability of the lower tropopause, it is necessary for the mesoscale motions to get organized as a wave packet with enhanced and predominant growth rate. The phase speed curves are not very affected by small variations in stability.

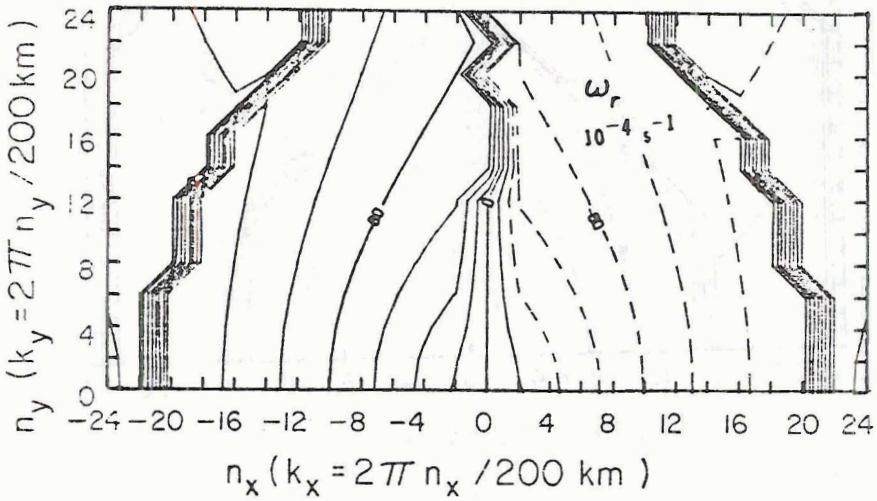

(a)

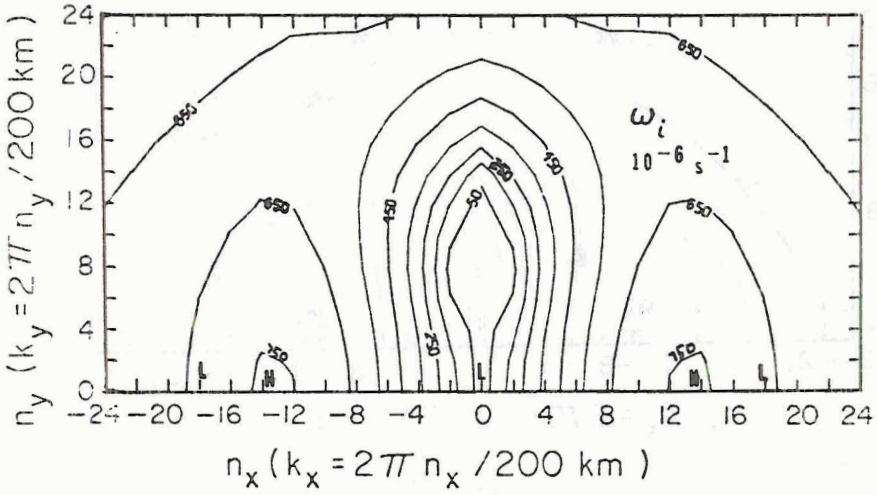

(b)

Figure 4.39. Eigenvalues for basic state wind 4B and temperature "Day 248".

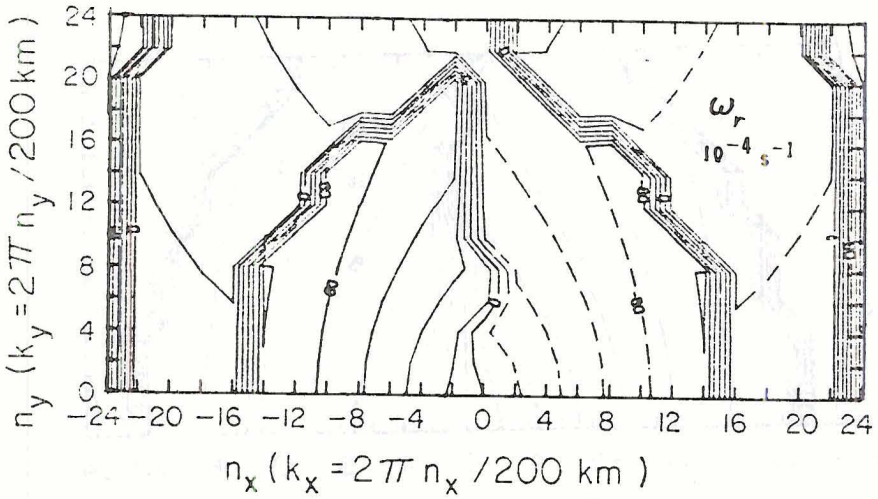

(a)

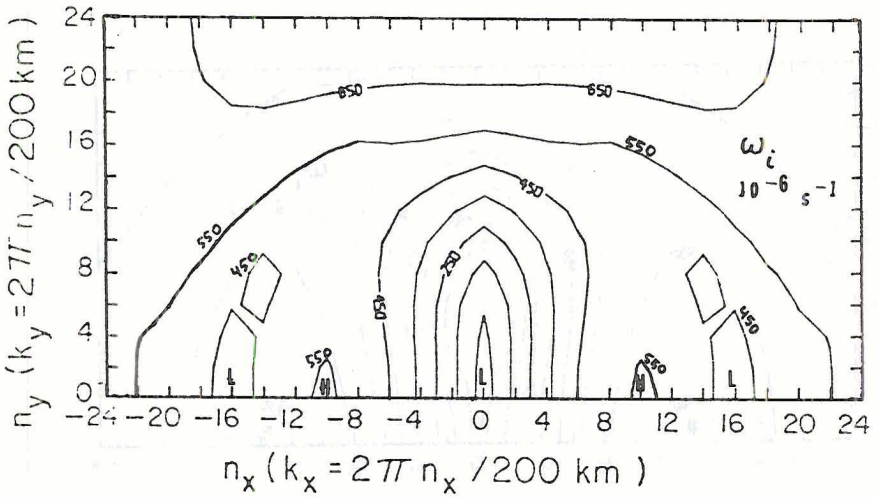

(b)

Figure 4.40. Eigenvalues for basic state wind 4B and temperature "West Pacific".

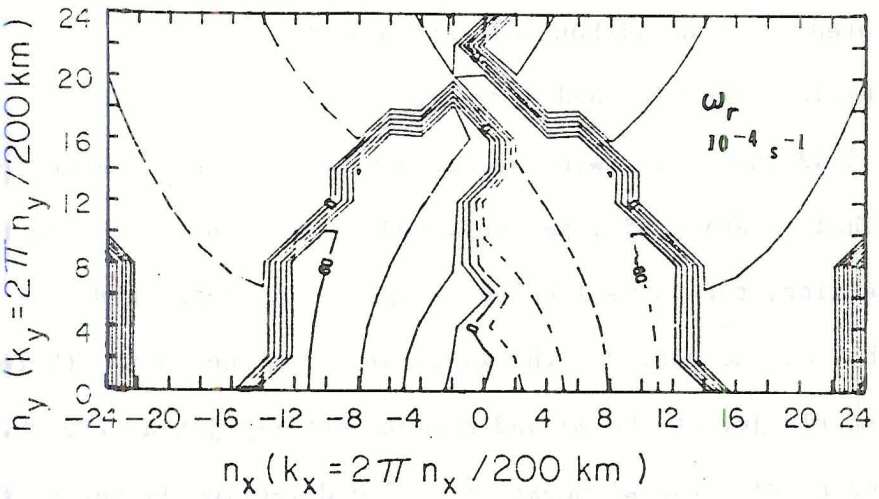

(a)

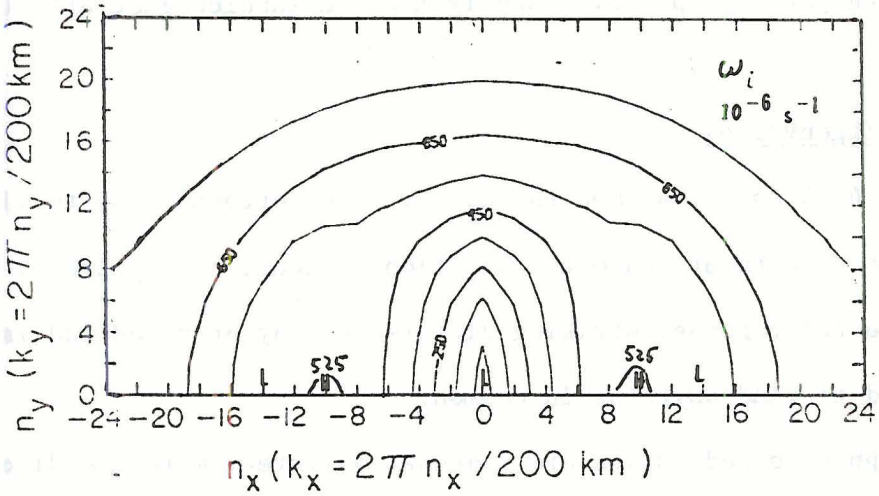

(b)

Figure 4.41. Eigenvalues for basic state wind 4B and temperature "East Atlantic".

4.2.3 Effect of Directional Shear of the Wind

This section will concentrate on a single example of how crucial the directional shear of the wind can be to the eigenvalues of equation 3.30. To illustrate the role of directional shear an observed profile has been used with and without directional shear.

a) Basic State Wind and Temperature

Fig. 4.42 shows four wind hodographs obtained by Thompson et al., (1979). Their meaning will be explained in section 5.1.2. In the present section, the curve labeled Category 1 will be used. It may be seen that at the surface, the winds are from the west; there is a northeasterly jet at 600 mb and a southeasterly jet at 200 mb. In the case of no directional shear, the wind direction is set to be from the east at all levels.

The temperature profile used is the one labeled East Atlantic in Fig. 4.2.

b) Eigenvalues

Fig. 4.43 and 4.44 show the eigenvalues corresponding to wind "Category 1" without and with directional shear, respectively. Comparing the two figures, striking differences may be noted and indeed it is hard to find anything in common.

The phase speed curves are somewhat different with the discontinuities occurring for different sets of wavenumbers.

The growth rate isolines show a greater selectivity with directional shear. The growth rate is about 50% different with directional shear than without. Some modes have higher values of growth rate and some have lower values of growth rate with directional shear than without.

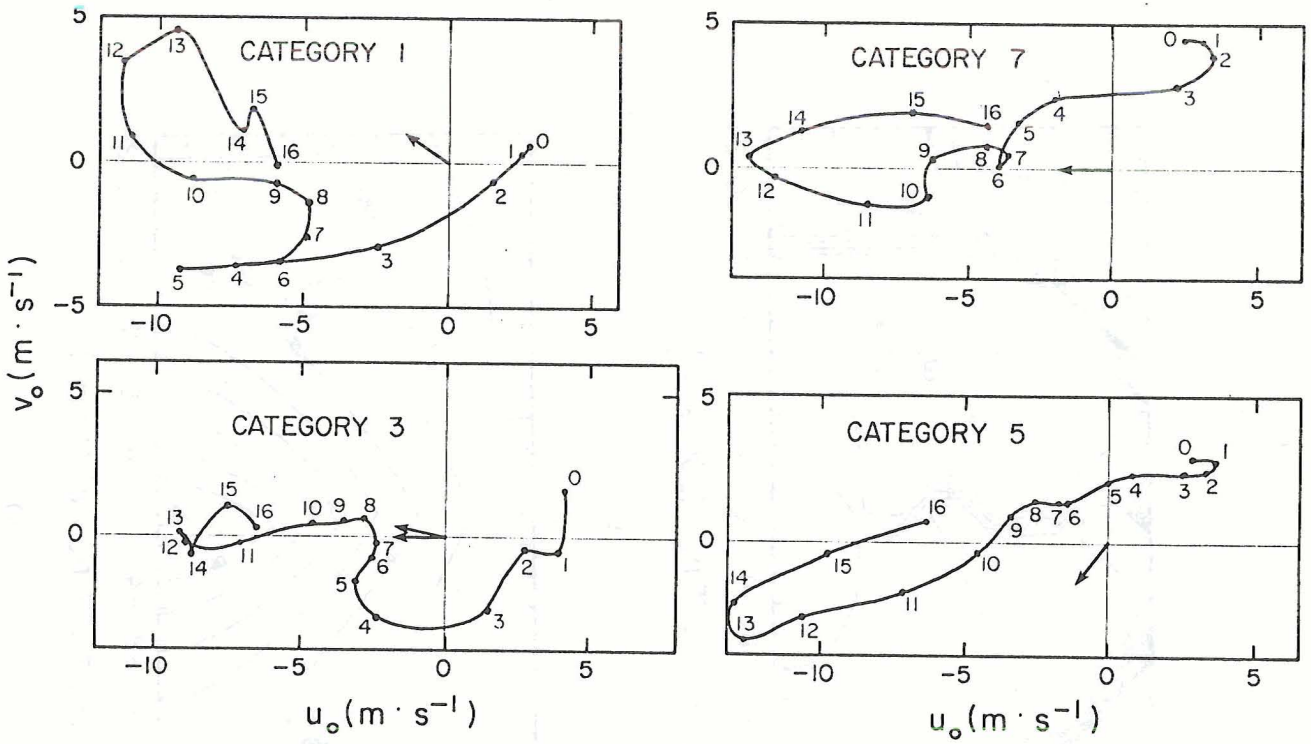

#	0	1	2	3	4	5	6	7	8	9	10	11	12	13	14	15	16
(100 mb)	SFC	95	9	8	7	6	5	4.5	4	3.5	3	2.5	2	1.75	1.5	1.25	1

Figure 4.42. Wind hodographs for categories 1, 3, 5 and 7 in Thompson et al. (1979) composited large scale easterly wave.

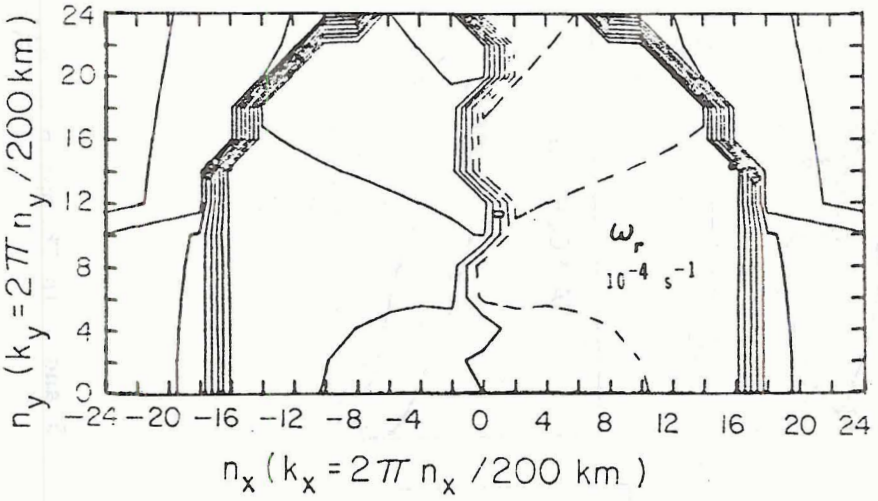

(a)

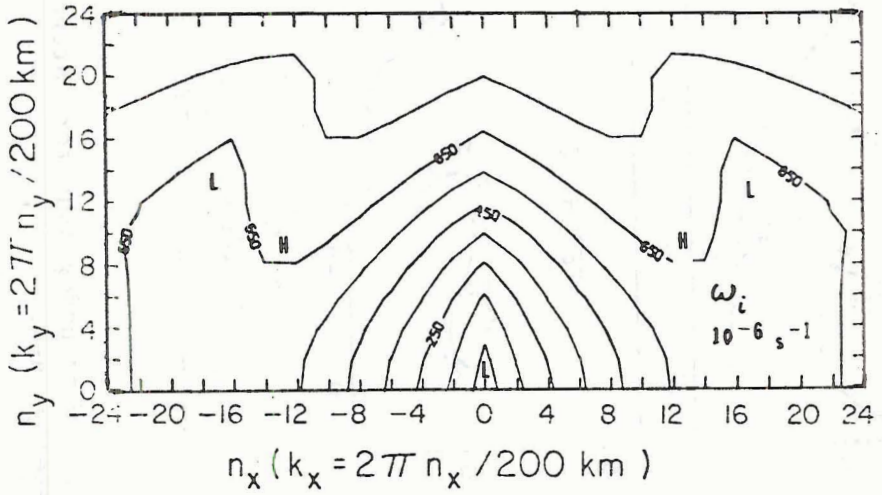

(b)

Figure 4.43. Eigenvalues for basic state wind speeds of "Category 1" <u>without</u> directional shear and basic state temperature "East Atlantic".

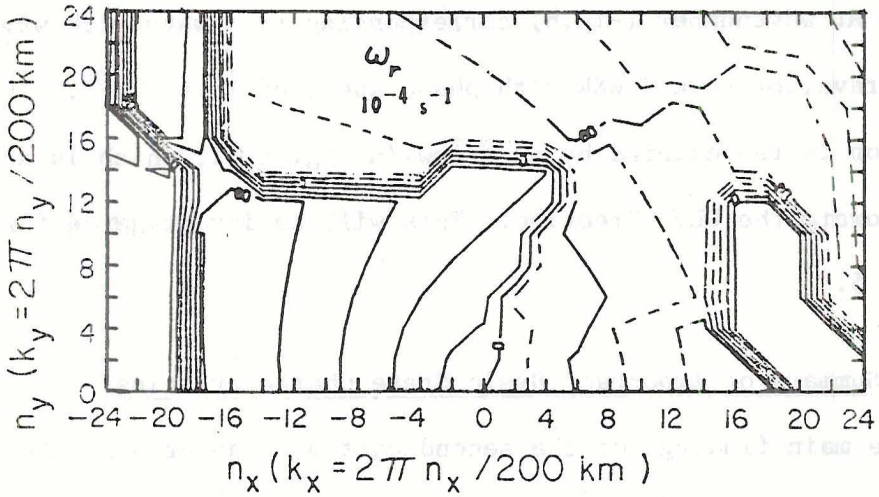

(a)

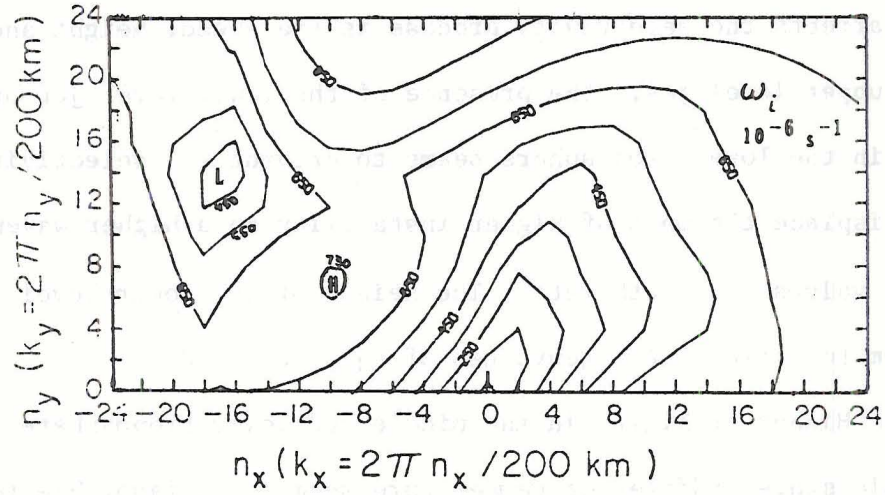

(b)

Figure 4.44. Eigenvalues for basic state wind speeds of "Category 1" with directional shear and basic state temperature "East Atlantic".

The wavelength of maximum instability is not well defined in Fig. 4.43. Fig. 4.44, on the other hand, shows a clearly defined maximum at wavenumber (-10,6) corresponding to a wave with wavelength 17 km traveling toward WNW with phase speed of 18.6 $m.s^{-1}$. This direction is represented by an arrow in Fig. 4.42, which is seen to point toward the ULJ direction. This will be investigated further in Chapter 5.

4.2.4 Summary of Important Basic State Characteristics

The main findings of the second part of Chapter 4 may be summarized as follows:

a) The feature of the basic state wind speed that most significantly affects the selectivity process is the speed, height and direction of the upper level jet; the presence of the lower level jet or of high speeds in the lower troposphere seems to prevent the selectivity process or to displace the mode of higher instability to a higher wavenumber with smaller values of growth rate. The height of the lower level jet does not seem to affect the eigenvalues of equation 3.30.

b) Higher stability in the middle and lower troposphere in the basic state profiles of temperature seem to be favorable to the selectivity of a particular mode as the most unstable. This may suggest that in order to break a greater stability of the lower troposphere, it is necessary for the mesoscale motions to get organized as a wave packet with enhanced and predominant growth rate. The phase speed is not very affected by small variations in stability.

c) The directional shear of the basic state wind profile seems to have the most crucial influence in selecting a most unstable mode.

A complete study on the sensitivity of the most unstable mode to particular characteristics of the directional shear should be undertaken in the future.

V. MODEL RESULTS

The first part of Chapter 5 is dedicated to discussing the differences and similarities found in the eigenvalues of equation 3.30 using as basic state different observed profiles of wind and temperature. The interpretation of the results is based on the discussion carried out in the previous chapter.

The second part of Chapter 5 shows the evolution of a few initial conditions and discusses the significance of the resulting mesoscale fields of wind and temperature.

The small scale processes included are the cumulus heating (Table 1) and momentum mixing by cumulus clouds (Fig. 4.20).

5.1 Differences in Tropical Regimes

The results of Chapter 4 show that the speed of the upper level jet and stability of the lower atmosphere are important in the definition of the wavenumber corresponding to the most unstable mode. The directional shear of the wind is, however, the most important factor in determining the mode of maximum growth rate.

The following subsections will use these ideas with the objective of understanding the differences between the basic state at the East Atlantic tropical region and the West Pacific tropical region (5.1.1); the basic state for different sections of an easterly wave as composited by Thompson et al. (1979); the definition of "basic state" for a particular day (5 Sept., 1974) during the GATE and the consequences of choosing a particular sounding.

5.1.1 East Atlantic vs. West Pacific

The basic state representative of the East Atlantic and West Pacific may be seen in Figs. 4.1 and 4.2 for the wind and potential temperature fields, respectively.

The East Atlantic curves are the ones obtained by Thompson et al. (1979) by a linear fit in both horizontal space dimensions and time to the data observed during Phase III of the GATE (August 30-Spetember 18, 1974). The East Atlantic curves of Figs. 4.1 and 4.2 correspond to the mean in time, at the center of the ship array which is located at 8.5^{o} N, 23.5^{o}W.

The basic state curves representative of the West Pacific tropical region were obtained by Reed and Recker (1971) by averaging the soundings obtained at three stations, Kwajalein, Eniwetok and Ponape (KEP triangle), which form a triangle centered at 10°N, 162.5^{o}W, during the period July-September, 1967.

The profiles of potential temperature in Fig. 4.2 are similar for the two regions. The wind profiles, as shown in Fig. 4.1, are quite different. The East Atlantic wind hodograph shows southwesterly winds at the surface turning to easterlies above 800 mb. The West Pacific wind profile shows southeasterlies at the surface gradually turning to easterlies, and to northeasterlies at the top. The direction of the wind in the East Atlantic curve above 800 mb does not depart more than 8° from an east wind while in the West Pacific the wind directions vary by as much as 30° north of east.

a) Eigenvalues

The eigenvalues obtained with the East Atlantic basic state have

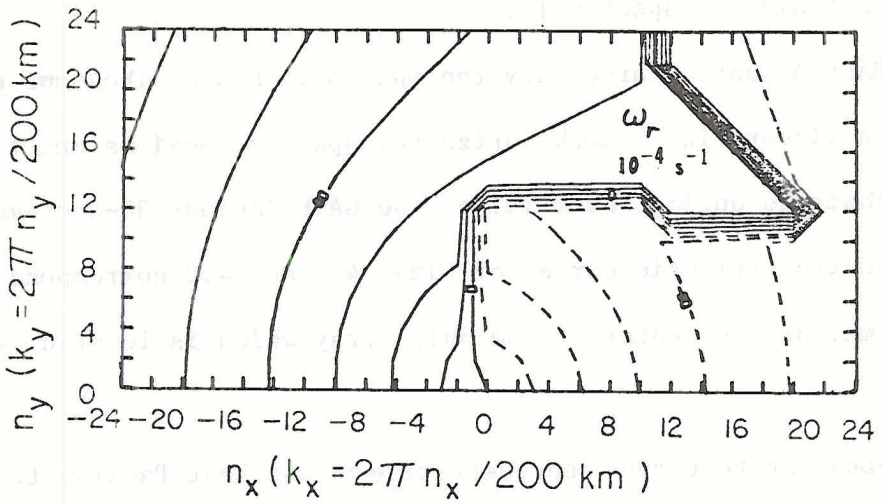

(a)

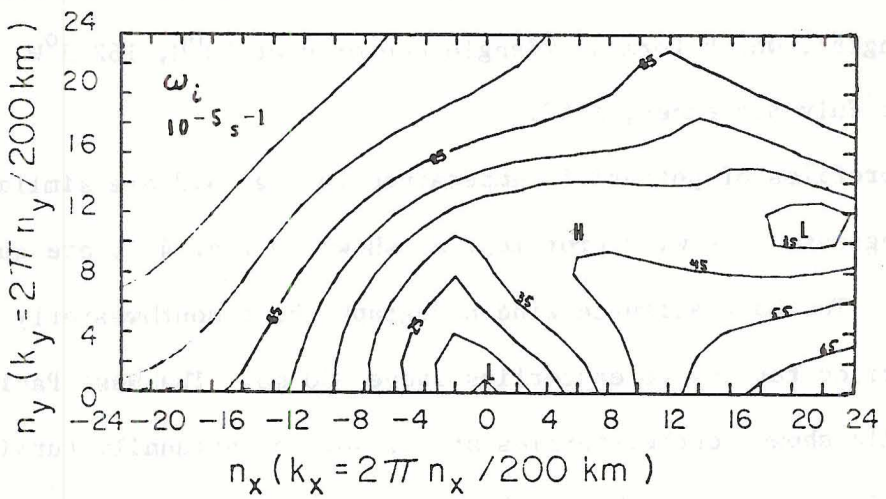

(b)

Figure 5.1 Eigenvalues for basic state wind speeds of "West Pacific" and basic state temperature "West Pacific".

already been discussed and may be seen in Fig. 4.23. The eigenvalues corresponding to the West Pacific basic state may be seen in Fig. 5.1. Comparing Figs. 4.23 and 5.1, it may be seen that the East Atlantic basic state produces higher values of growth rate and a more clearly defined mode of maximum growth than the West Pacific basic state. The growth rate isolines in Fig. 5.1 b corresponding to the West Pacific basic state show a local maximum around wavenumber (6,11), but no preferred mode can be defined. The growth rate isolines in Fig. 4.23b, for the East Atlantic basic state, shows a clearly preferred mode at the wavenumbers (10,2) and (-10,0).

The basic state temperature profiles for the East Atlantic and the West Pacific shown in Fig. 4.2 are very similar and the discussion in section 4.2.2 showed that the resulting eigenvalues are not very sensitive to the small differences between the two potential temperature profiles.

The wind hodographs in Fig. 4.1, however, show considerable differences. Above 700 mb, the East Atlantic wind hodograph shows considerable shear in the wind speed, but little directional shear; the West Pacific hodograph, on the other hand, shows little variation in speed above 700 mb, but considerable directional shear. The upper level jet has a higher speed (11.3 $m.s^{-1}$ at 175 mb) in the East Atlantic than in the West Pacific (9.2 $m.s^{-1}$ at 150 mb). The upper level jet is about 1 km lower in the East Atlantic than in the West Pacific. The speed of the upper level jet was seen in section 4.2.1 to influence the selectivity process. The higher the speed of the upper level jet, the higher the selectivity. Also, the lower the upper level

jet, the higher the selectivity. Both factors point toward the East Atlantic basic state as most likely to produce eigenvalues with a preferred mode.

The East Atlantic basic state produces growth rate isolines almost symmetrical about $n_x = 0$, while the West Pacific basic state produces totally asymmetric growth rate isolines. As seen in section 4.2.3, this is a direct result of a more complex profile of directional shear. The direction of propagation of the modes with maximum growth rates in Figs. 4.23b and 5.1b have been plotted as arrows in the wind hodograph in Fig. 4.1. In both cases, the direction of propagation of the most unstable modes corresponds to the direction of the upper level jet. This seems to indicate that the propagation of gravity waves in shear flow is dictated by the direction of the jet. This finding is confirmed in the next two subsections.

5.1.2 Easterly Wave Categories

Reed and Recker (1971) defined eight categories in a large-scale easterly wave by analyzing the meridional wind component averaged from the surface to 500 mb for each observation. Categories 2, 4, 6 and 8 were centered, respectively, on the maximum northerly wind, the trough axis, the maximum southerly winds, and the ridge axis of the waves. Categories 1, 3, 5 and 7 occupy intermediate positions. Thompson et al. (1979) followed the same procedure except that the wave categories were defined in terms of the meridional wind at 700 mb. Fig. 4.42 shows the composited winds for categories 1, 3, 5 and 7 as presented by Thompson et al.(1979) for the East Atlantic large-scale easterly wave. Both studies mentioned above show that the strongest upward

vertical motion and heaviest precipitation generally occur in or slightly in advance of the trough. Category 3 precedes the trough.

Examining Fig. 4.42, it may be seen that Category 1 shows a strong low-level jet while Category 5 shows the strongest upper-level jet. Categories 5 and 7 do not show a low-level jet at all, and the latter appears only slightly in Category 3. The wind turns clockwise (backs) with height from the surface up to 600 mb in Categories 1 and 3, and turns counterclockwise (veers) with height from 900 mb up to 250 mb in Categories 5 and 7. Above 250 mb, all four categories show winds veering with height. Above 500 mb, Category 3 shows less, and Category 1 more directional shear than the other categories in in Fig. 4.42.

The temperature profiles, according to Thompson et al.(1979), do not change significantly from one category to another, so that the mean temperature profile for the East Atlantic (Fig. 4.2) is used in all computations of this section.

a) Eigenvalues

The eigenvalues corresponding to the basic state characteristic of Categories 1, 3, 5 and 7 may be seen in Figs. 4.44, 5.2, 5.3 and 5.4, respectively.

Information concerning the most unstable mode for each category is summarized in Table 3.

A general statement that can be made is that Categories 1 and 3, which precede the 700 mb trough, are more selective than Categories 5 and 7. It is clear that Figs. 4.44 and 5.2 (for Categories 1 and 3, respectively) are highly selective. Category 5 has wavemode of higher growth rate for wavenumber (12,16) and wavelength of 10 km which may

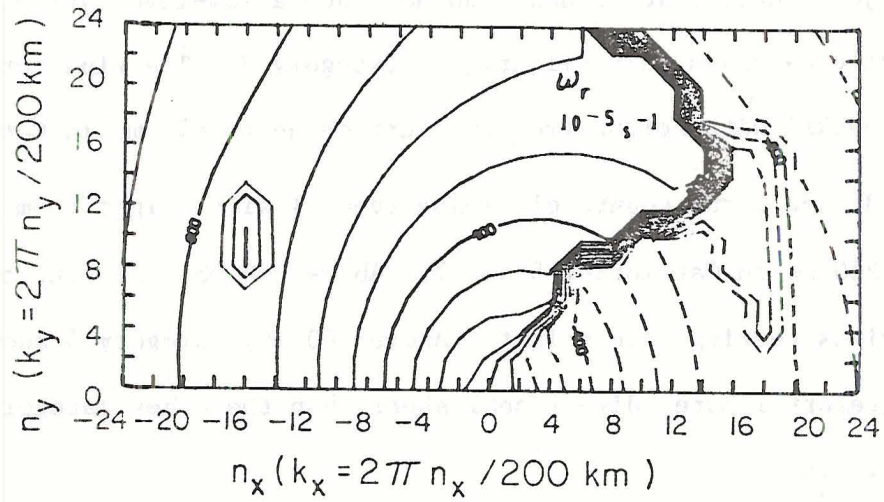

(a)

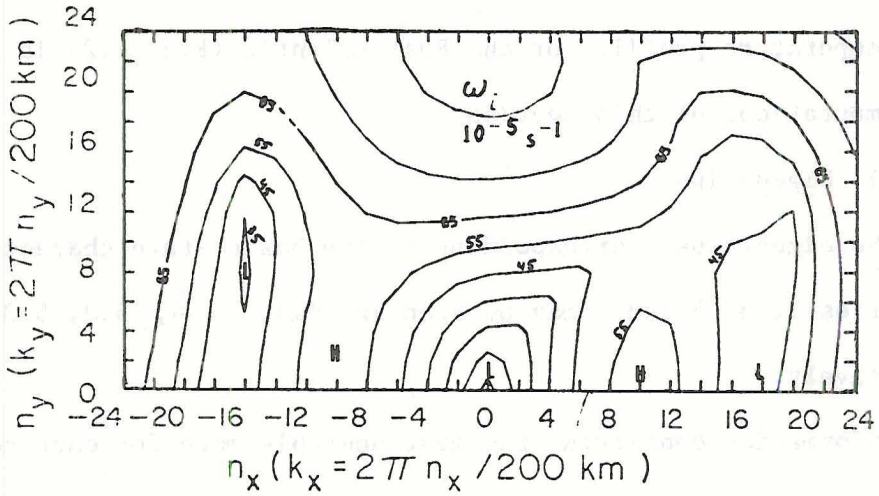

(b)

Figure 5.2. Eigenvalues for basic state wind speeds of "Category 3" and basic state temperature "East Atlantic".

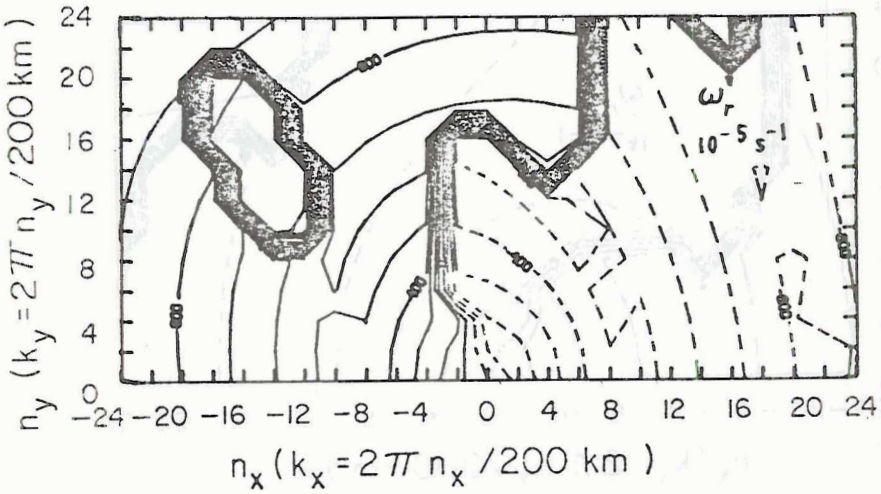

(a)

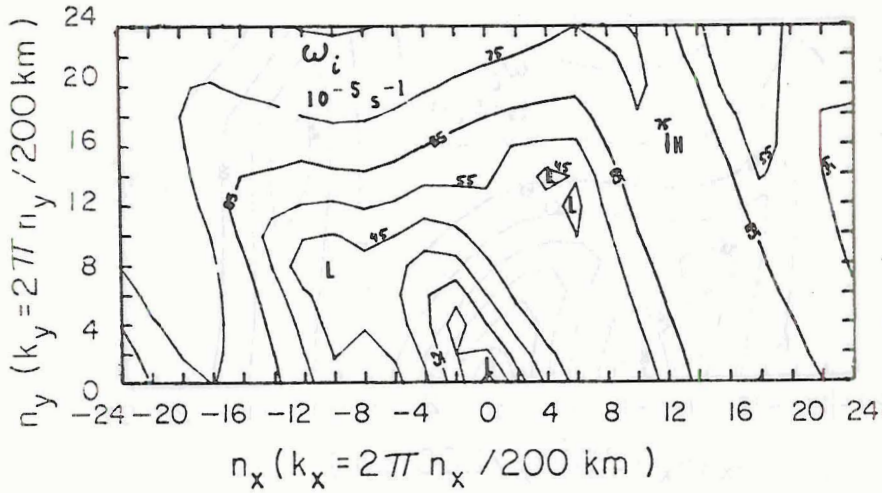

(b)

Figure 5.3. Eigenvalues for basic state wind speeds of "Category 5" and basic state temperature "East Atlantic".

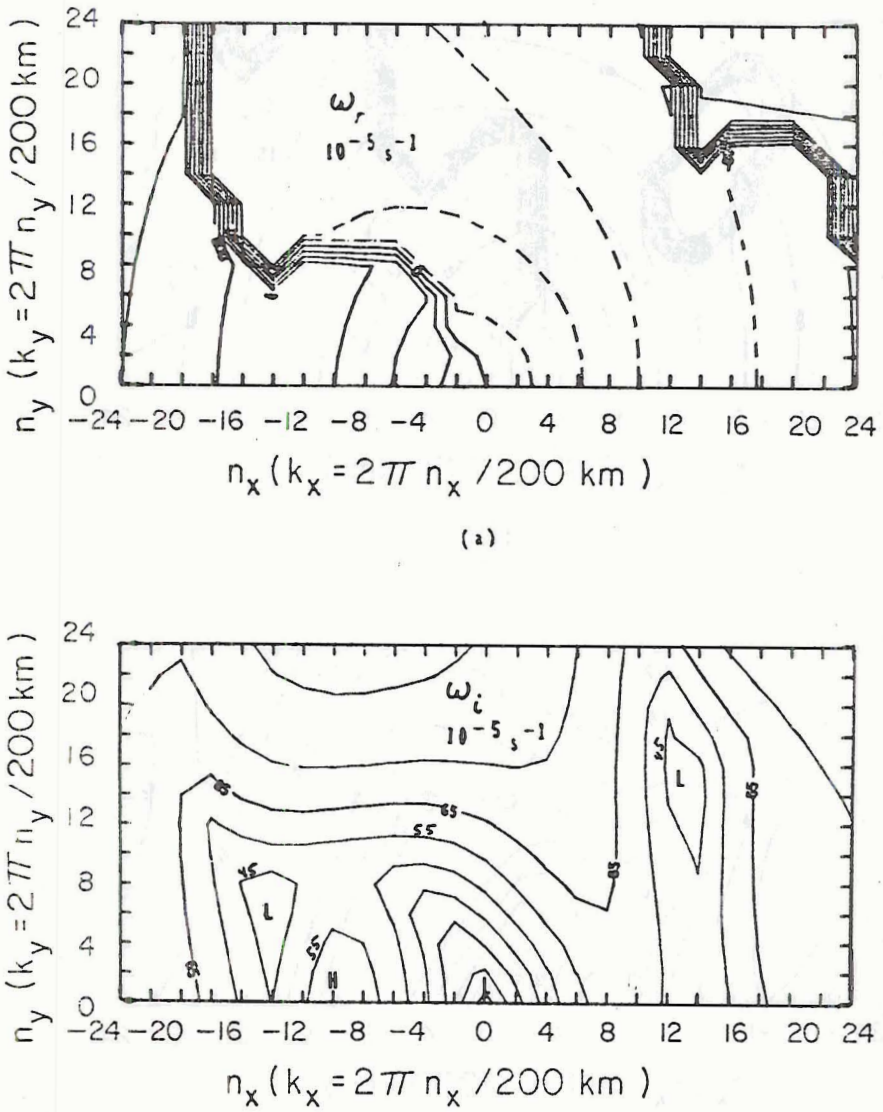

Figure 5.4. Eigenvalues for basic state wind speeds of "Category 7" and basic state temperature "East Atlantic".

be considered to lie in the boundary between mesoscale and small scale processes. The region for which there was a maximum growth rate for Categories 1 and 3 (along $n_x = -10$) shows a minimum in growth rate in Fig. 5.3 for Category 5. Fig. 5.4 shows a local maximum at wavenumber (-10,0), but it is not well defined since wavenumber (10,0) has a higher value of growth rate, without being a local maximum.

The actual value of growth rate may be affected by different characteristics in the small scale processes of each category which are not being taken into account in the prsent discussion. The differences encountered in the eigenvalues are due only to differences in wind profiles.

Although a high speed of the upper level jet was shown in section 4.1.1 to produce highly selective growth rate isolines, this feature does not seem to predominate here: Categories 5 and 7 have the stronger upper level jets. The amount of directional shear does not seem to matter greatly also, since, as already mentioned, Category 1 shows greater variability in the wind direction and Category 3 has less variability in the wind direction than the other categories in Fig. 4.42.

There is a strong low-level jet in the wind profile of Category 1 and a slight maximum in the low-level winds in Category 3 and 7. Category 5 does not show a low-level jet at all. The existence or not of the low-level jet cannot be used to explain the differences encountered.

As mentioned in the introduction of this chapter, the low-level winds in Categories 1 and 3 turn clockwise with height, while in Categories 5 and 7 they turn counterclockwise with height. Is this

Table 3. Summary of Figs. 4.44, 5.2, 5.3 and 5.4

Basic state represents category #	Wavenumber for local maximum growth rate (n_x, n_y)	$(\text{Growth rate})^{-1}$ min	Phase speed $m.s^{-1}$	Wavelength km	Maximum well defined for wave-numbers less than $(\lvert n_x \rvert . \lvert n_y \rvert)$
1	(-10, 7)	22	18	16	(18, 14)
3	(-10, 2)	28	17	20	(18, 10)
5	(12, 16)	22	-11	10	(16, 18)
7	(-10, 10)	27	19	20	not well defined

feature what determines the degree of selectivity found in the growth rate isolines? If so, what is physically happening?

There is again the confirmation that the directional characteristics of the wind are the most important factor in determining the selectivity of the growth rate curves. The direction of propagation of the most unstable modes corresponding to categories 1,3,5 and 7 have been plotted as arrows on the wind hodographs in Fig. 4.42. Again, the direction of propagation of the most unstable modes corresponds to the direction of the upper level jet.

5.1.3 Day 248

The main objective of this subsection is to show the difficulties encountered when trying to model specific atmospheric situations with the objective of comparing the model results with observations. The main difficulty in the case of a mesoscale model, as the one used for the present work, is the definition of the basic state. The better choice would probably be to choose Category 3, described in the previous section, as in the case of modelling the GATE mesoscale convection. Another approach would be the one followed by Raymond (1975, 1976) which consists of picking up a particular sounding in the vicinity of the initiating disturbance and say that it represents the basic state. Here we consider the differences that may be found following the two approaches.

Day 248, or 5 September, 1974 during the GATE has been chosen as an example. The radar composites previous to the one in Fig. 1.2 show that at about 600 GMT, the GATE array was free of precipitation if not of cloudiness, and so the observations taken at this hour would, according to Raymond's approach, represent the basic state of an

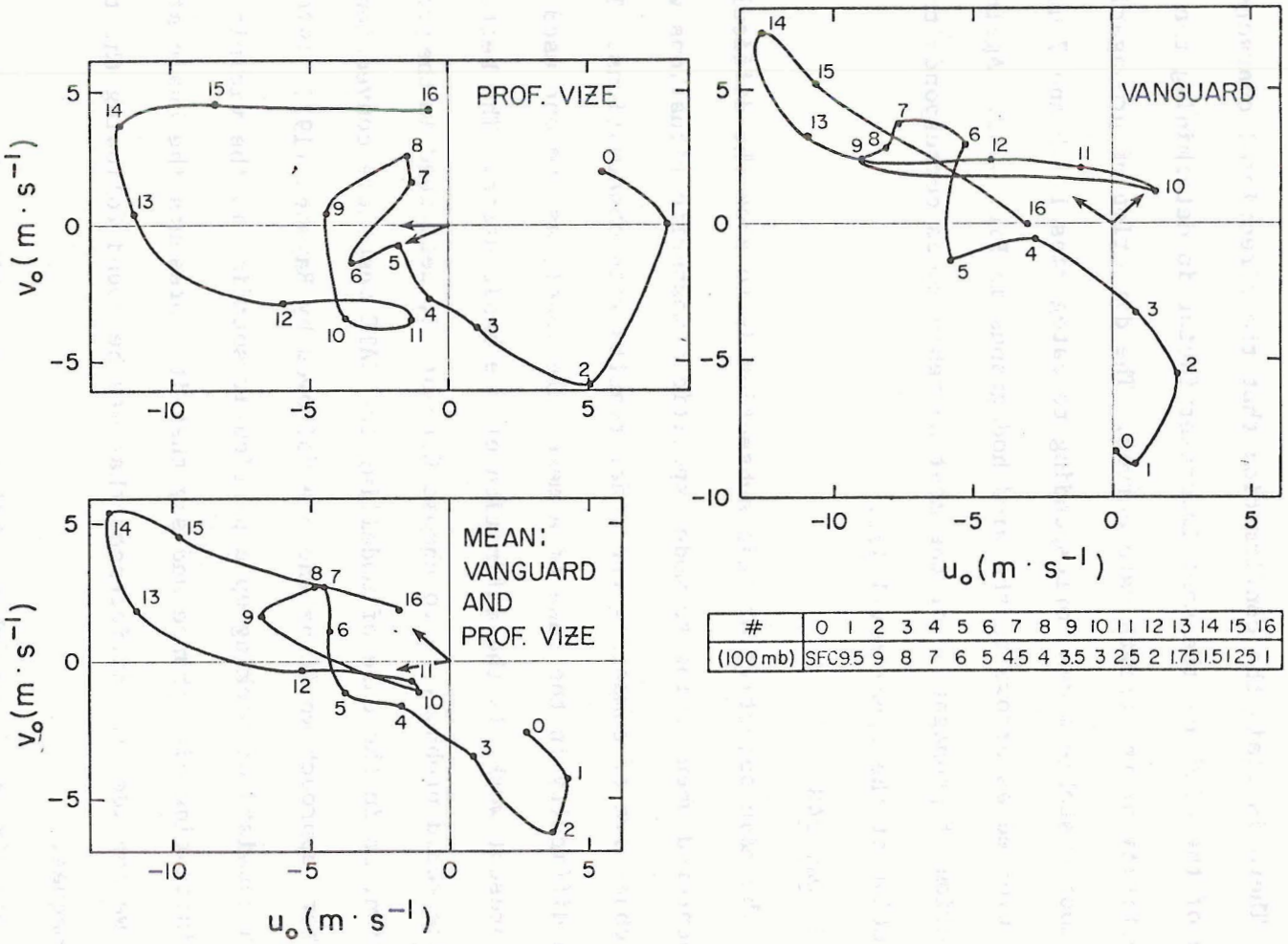

#	0	1	2	3	4	5	6	7	8	9	10	11	12	13	14	15	16
(100 mb)	SFC	9.5	9	8	7	6	5	4.5	4	3.5	3	2.5	2	1.75	1.5	1.25	1

Figure 5.5. Wind hodographs for soundings in ships Prof.Vize (8,5°N,23,5°W) and Vanguard (10°N,23.5°W) and for the mean between the two soundings. This data corresponds to 600 GMT on % Sept. 1974 (Day 248) during GATE.

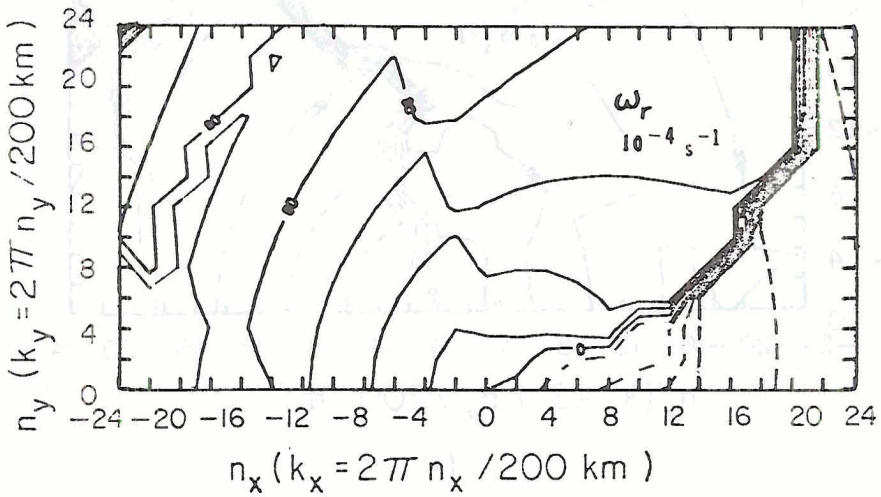

(a)

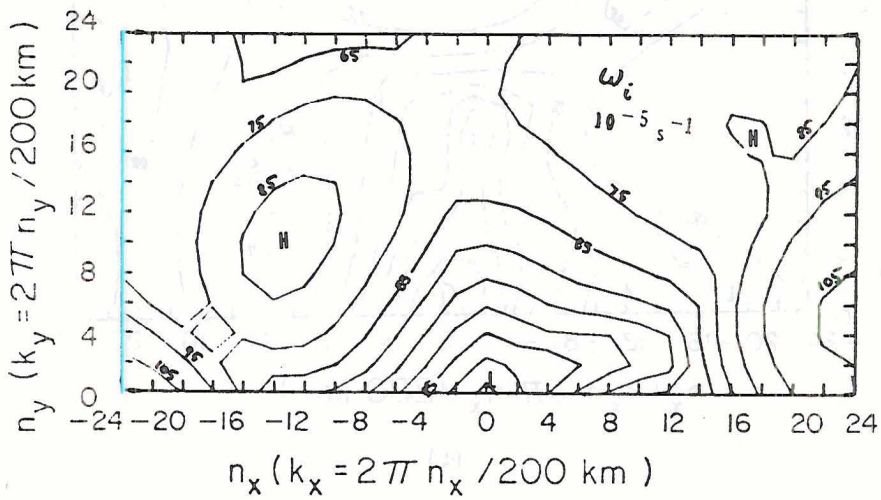

(b)

Figure 5.6. Eigenvalues for basic state winds from ship Vanguard and basic state temperature of "Day 248".

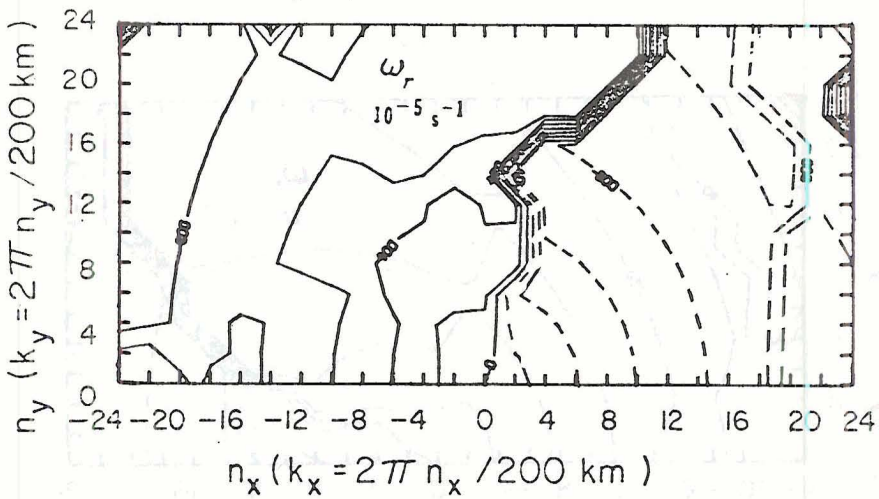

(a)

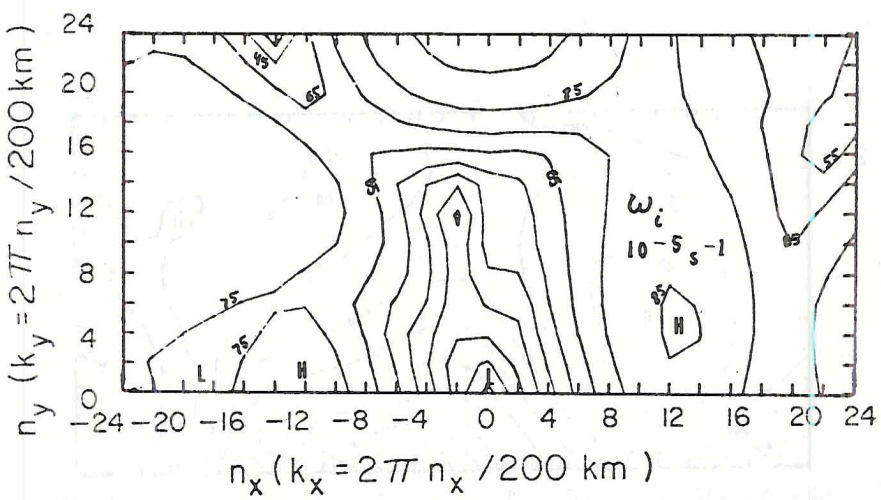

(b)

Figure 5.7. Eigenvalues for basic state winds from ship Prof. Vize and basic state temperature of "Day 248".

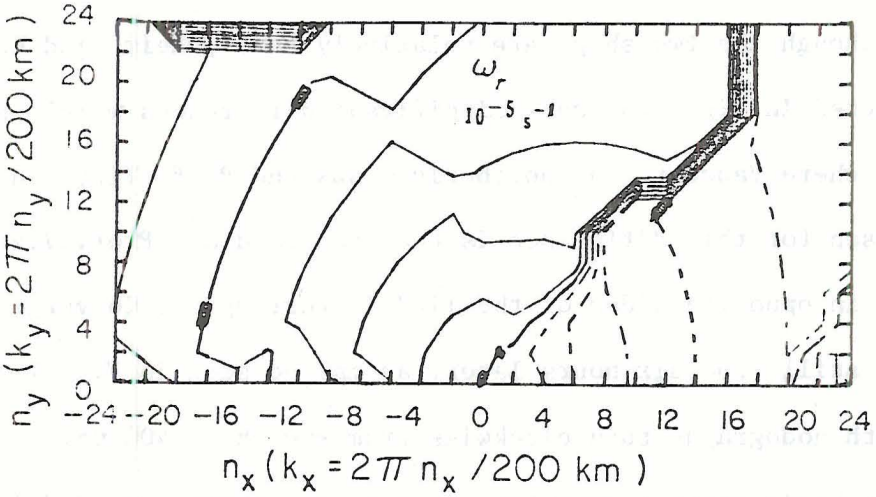

(a)

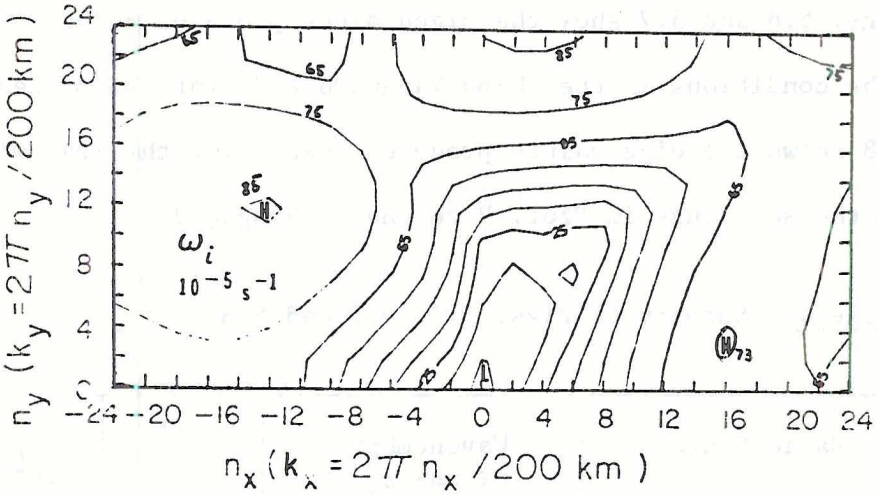

(b)

Figure 5.8. Eigenvalues for basic state winds which are a mean between the winds at Vanguard and Prof. Vize; basic state temperature of "Day 248".

initiating disturbance. Among all the ships involved in the GATE, two have been chosen, namely Vanguard (10°N, 23.5°W) and Prof. Vize (8.5°N, 23.5°W). Fig. 5.5 shows the wind hodographs for each of these ships and the mean between the two (these observations were included in Category 3 in Thompson et al., (1979) composite).

Although the two ships are relatively close, their wind hodographs, as depicted in Fig. 5.5, show significant differences mainly at the surface where Vanguard had northerly winds and Prof. Vize southwesterly. The reason for this difference is that Vanguard and Prof. Vize are located in opposite sides of the ITCZ (Intertropical Convergence Zone). This is still true six hours later, as may be seen in Fig. 1.3.

Both hodographs turn clockwise from 900 mb to 400 mb.

The basic state temperature is the one labeled Day 248 in Fig. 4.2.

a) Eigenvalues

Figs. 5.6 and 5.7 show the eigenvalues produced using as basic state the conditions in the ships Vanguard and Prof. Vize, respectively. Fig. 5.8 shows the eigenvalues produced when using the mean winds between the soundings in Prof. Vize and in Vanguard.

Table 4. Summary of Figs. 5.6, 5.7 and 5.8

Basic State	Wavenumber of max ω_i	ω_i^{-1} min	c_r $m.s^{-1}$
Vanguard	(-14,10)	19	15.0
Prof. Vize	(12,5)	19	-17.9
Mean	(-14,12)	19	15.8

Table 4 summarizes the information about the most unstable mode in Figs. 5.6, 5.7 and 5.8. Using the basic state as depicted in Vanguard the most unstable mode travels toward the WNW at 15 $m.s^{-1}$. There is about 60° difference in direction and 20% difference in phase speed from the two cases.

Using the mean wind as basic state produced eigenvalues that have some similarities with the ones obtained with the individual soundings. The most unstable mode is about the same as the one obtained with the winds in Vanguard. There is, however, a secondary maximum at wavelength (16,4) at about the same region as the most unstable mode obtained with the winds at Prof. Vize. The difference between Figs. 5.6, 5.7, 5.8 and Fig. 5.2 corresponding to the basic state in Category 3 is also striking.

This should remain as an example of how delicate is the problem of choosing a basic state. In fact, the approach of choosing a particular sounding as representative of the basic state leaves too much margin for variability since the particular sounding may already include mesoscale effects, thus invalidating the results.

The wind hodographs in Fig. 5.5 show considerable variation in wind direction. However, the direction of propagation of the most unstable modes, denoted by the arrows on the hodographs, still have about the same direction as the upper level jet. In the case of Vanguard, one of the arrows points to the direction of the upper level jet, while the other arrow points to the wind at 300 mb, which corresponds to a local minimum. Clearly, the upper level jet in this case does not determine uniquely the direction of propagation of most unstable modes;

the wind structure below the upper level jet must certainly play a role in modifying the instability characteristics.

Observational work should be done in this subject to try to determine the validity of our conclusion that the upper level jet speed and direction are very important in determining the mode of maximum instability and its direction of propagation.

5.1.4 Summary

The main conclusions related to the differences in tropical regimes may be summarized as

a) The speed and direction of the upper level jet seem to be very important in determining the mode of maximum instability and its direction of propagation.

b) The West Pacific basic state does not produce a preferred mode in the mesoscale, while the East Atlantic basic state does.

c) The large-scale easterly wave categories that precede the trough produce highly selective eigenvalues while the categories after the trough do not.

d) The definition of the basic state in a particular case study is a delicate problem since it involves a complete separation between basic state and mesoscale features.

5.2 Evolution of Initial Disturbance

The validity of the conclusions drawn in Chapter 4, concerning the sensitivity of the eigenvalues of equation (3.30) with respect to basic state characterisitics, may undergo a final test by the actual Fourier summation defined in equations (3.32) and (3.36). The coefficient C(k,m) in equation (3.36) depends essentially on the initial

condition through equation (3.35). The implication of this dependence is that different weight is given to different modes in the Fourier summation so that the predominance of the most unstable mode in equation (3.36) is not instantaneous. The initial condition may be defined as a function of a horizontal length scale l_H. Variations in l_H may provide initial conditions ranging from a concentrated area of convergence to a relatively broad large-scale feature. It is known from the theory of Fourier transforms (e.g., Butkov, 1961) that a relatively peaked function has a relatively flat Fourier transform and vice versa. Accordingly, a concentrated area of convergence has a flat Fourier transform $\hat{\underset{\sim}{Z}}(|k,0)$ (cf. equation 3.35). This means that after a relatively short time, the most unstable mode predominates in the Fourier summation. An initial condition with very large horizontal scale has Fourier transform a narrow half width; if the maximum in the Fourier transform does not happen to occur in the vicinity of the mode of maximum instability, it may take a very long time for the most unstable mode to predominate.

The objective of this section is to present the mesoscale fields obtained with different horizontal scale of the initial condition. For each case, the speed and direction of propagation will be examined, as well as the vertical and horizontal structure of the disturbance.

The fact that the present model does not include non-linear terms, particularly non-linear advection, and has no effect of Coriolis force, makes the modelling of a mesoscale vortex a questionable venture. No success has been obtained as yet in the reproduction of an imposed

initial condition of rotation. A convergence line oriented in the east-west direction has still not been reproduced with success. More work is being done on this subject. In this section, the structure and propagation of a north-south convergence line will be examined.

a) Basic State and Small Scale Parameters

The basic state used is the one representing the East Atlantic in Figs. 4.1 and 4.2. The small scale parameterizations are the momentum mixing by cumulus clouds (Fig. 4.30) and cumulus heating with parameters in Table 1, except for the top of the moist layer which is set at 3 km. The eigenvalues have already been presented in Fig. 4.24. As discussed previously, Fig. 4.24 shows a preferred mode for scales larger than individual cumulus elements. The growth rate of maximum instability has wavelengths (100 km, 20 km) with growth rate of $(27\ \mathrm{min})^{-1}$ and phase speed of $-18.7\ \mathrm{m.s}^{-1}$.

b) Truncation in the Fourier Summation

In section 3.1.3, the set of wavenumbers over which the Fourier summation is performed, was presented. L_x and L_y are set to 300 km (as opposed to 200 km in the figures of Chapter 4 and first half of Chapter 5) and $n_x = n_y = -25,\ldots,-1, 0, 1,\ldots 25$, so that the highest mode (25, 25) has wavelength of 8.5 km. This corresponds to retaining $|n_x|, |n_y| \leq 16$ in Fig. 4.24.

c) Analytical Expression for the Initial Condition and its Fourier Transform

The choice of a particular initial condition is a somewhat arbitrary task. The desirability of having an initial condition with

an analytical Fourier transform makes the choice easier. This requirement is not essential; the need of computer storage, however, is considerably diminished, if the initial condition, as well as its Fourier transform, does not have to be stored at every single grid point and for every variable.

The representation of areas of convergence or divergence may be done by defining the fields of horizontal mesoscale velocity by

$$u'(x,y,z,0) = g(z)\,\frac{x}{a}\exp\left(-\frac{x^2}{a^2}-\frac{y^2}{b^2}\right) \tag{5.1}$$

$$v'(x,y,z,0) = g(z)\,\frac{y}{b}\exp\left(-\frac{x^2}{a^2}-\frac{y^2}{b^2}\right) \tag{5.2}$$

where a and b are horizontal length scales in the x and y direction, respectively. The vertical velocity is obtained by introducing equations (5.1) and (5.2) in the continuity equation (3.7).

The Fourier transform of equations (5.1) and (5.2) may be found in any book of mathematical physics (e.g., Butkov, 1961) to be

$$F(u') = -g(z)\; ia^2bk_x \exp\left(-k_x^2\, a^2/4 - k_y^2\, b^2/4\right) / 8\pi \tag{5.3}$$

$$F(v') = -g(z)\; iab^2k_y \exp\left(-k_x^2\, a^2/4 - k_y^2\, b^2/4\right) / 8\pi \tag{5.4}$$

The Fourier transform of the vertical velocity is

$$F(w') = \frac{1}{\rho_o}\int_o^z i\rho_o\left[k_x\, F(u') + k_y\, F(v')\right] dz \tag{5.5}$$

(5.6)

or

$$F(w') = (a^2b\ k_x^2 + a\ b^2k_y^2)\ \exp\ (-k_x^2\ a^2/4\ -k_y^2\ b^2/4)\ \frac{1}{8\pi\rho_o}\int_o^z \rho_o(z)g(z)dz$$

The sign of g(z) at a particular level denotes convergence or divergence. Negative sign corresponds to convergence and positive sign to divergence. Fig. 5.9 shows a plot of the coefficient of equation (5.6), for different values of a, b, as a function of k_x and k_y. It may be seen that the greater the scale of the initial condition, the more peaked the Fourier transform. Clearly, different functions of height may be used in the definition of u' and v' in equations (5.1) and (5.2), respectively. Different combinations of height dependences and signs of u' and v' provide a wide variety of initial conditions that will not be considered here.

The choice of g(z) is a delicate one, however. The fact of having a discrete set of eigenvalues and eigenfunctions makes the reproduction of an arbitrary initial condition depend on how well this particular initial condition can be described by the existing set of eigenmodes. The closer g(z) is to one of the eigenfunctions, the greater the chance of accurate reproduction. As defined in equation (3.37), only the projection of the initial condition on the given set of eigenfunctions is obtained. It has been found that the function

$$g(z) = \alpha\ \sin\left(\pi\ \frac{9km-z}{8km}\right) \tag{5.7}$$

is satisfactorily reproduced. This function corresponds to a profile of mesoscale vertical velocity of upward motion up to 3 km and downward

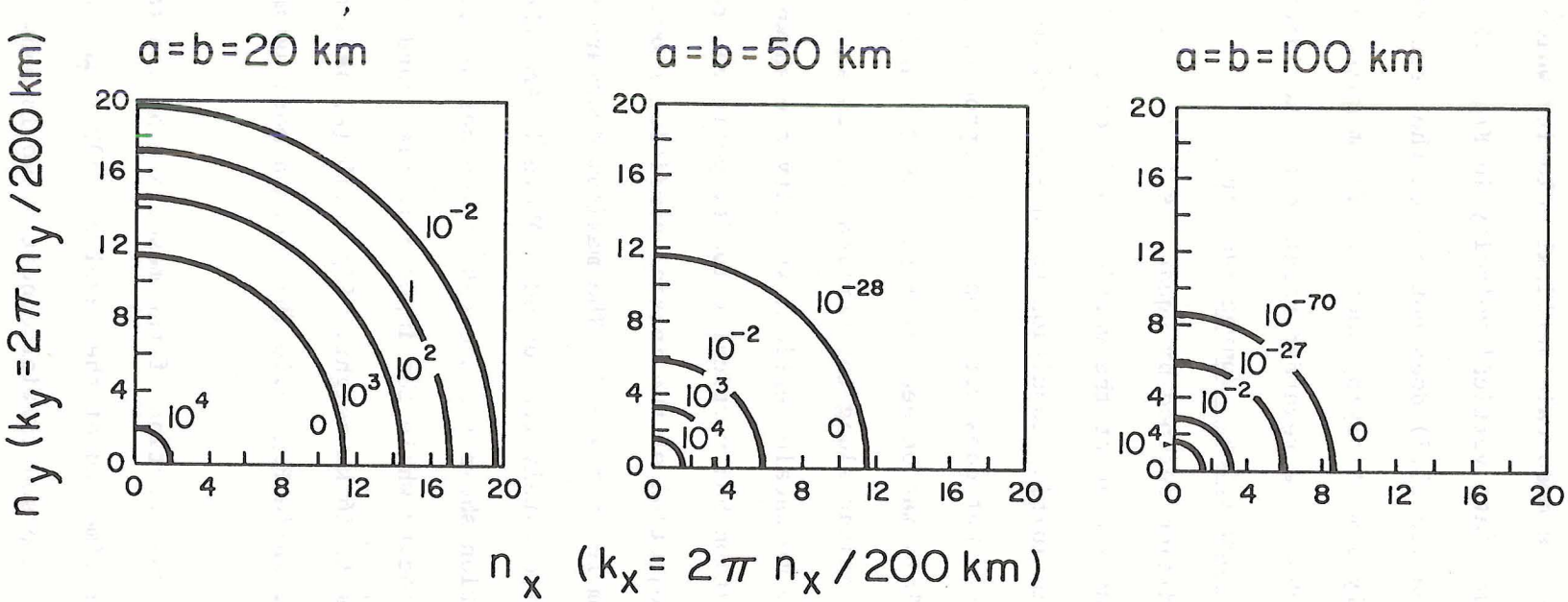

Figure 5.9. Isolines of $(a^2bk_x^2 + ab^2k_y^2)\exp(-k_x^2a^2/4 - k_y^2b^2/4)$ for different values of a,b. The circle denotes the most unstable mode in Fig. 4.24.

motion above, with that maximum downward velocity at 9 km. It must be remembered that this is the mesoscale vertical velocity which is a perturbation of the basic state vertical velocity in Fig. 4.21. Clearly, the value of α in equation (5.7) does not affect the results of a linear model since it is only a multiplying factor. The magnitude of the mesoscale variables should be regarded relative to the initial value.

5.2.1 Narrow Initial Condition: Convective Line

The initial condition defined by equations (5.1), (5.2) and (5.7) is cylindrically symmetric about the vertical axis centered at $x = y = 0$. The projection of this initial condition for $a = b = 20$ km, however, has a tendency to symmetry, but does not completely reproduce the imposed initial condition. This may be seen in Fig. 5.10 (a) and (b), where the vertical cross sections along the vertical planes at $x = 0$ and $y = 0$, respectively, for the mesoscale vertical velocity are shown. The imposed initial condition had vertical velocity positive from the surface to 3 km; the projection of the initial condition shows the zero isoline at about 4 km for $x = y = 0$. The maximum downward vertical velocity at 9 km is accurately reproduced. Above 12 km, the projection of the initial condition shows two successive regions of upward and downward vertical velocity while the imposed initial condition did not change sign from 3 km to 16 km height. Fig. 5.10 (a) is almost symmetrical about $y = 0$, while Fig. 5.10 (b) shows a more asymmetric pattern.

The horizontal cross section of the mesoscale horizontal wind vector at the initial time and at the level $z = 500$ m may be seen in Fig. 5.10. While the imposed initial condition would show a point of convergence, the projection of this inital condition shows more of

a line format oriented in the north-south direction and so perpendicular to the middle and upper tropospheric basic state winds (cf. Fig. 4.1, East Atlantic wind hodograph).

We may speculate at this point what kind of phenomena would produce an initial disturbance in the form of a line oriented in the north-south direction. According to observations (Kuettner, 1971, LeMone, 1976), when the winds in the planetary boundary layer are sufficiently high and the surface heat flux not too strong, longitudinal rolls, aligned approximately parallel to the mean lower tropospheric wind appear in the lower troposphere. Looking at the hodograph for the basic state characteristic of the GATE area in Fig. 4.1, it may be seen that the lower level winds have a strong component in the north-south direction. Numerical and theoretical studies (Asai, 1970; Howard, 1961, among others) have tried to account for the formation of the longitudinal rolls based on instability of stratified shear flows. Some success has been obtained in defining the preferred direction of rolls based on wind shear profiles; however, the shear of the winds used for example by Asai (1970) is only in the speed, i.e., the direction of the horizontal wind vector does not change with height. The effect of directional shear of the wind in the instability characteristics of a stratified flow is not known.

Considering again the initial disturbance in Fig. 5.11, we may assume that when there is sufficient moisture supply, a cloud line will form in the region of surface convergence and upward vertical velocity. In this way, the initial disturbance displayed in Figs. 5.10 and 5.11 may be viewed as a line of shallow convection. Its evolution

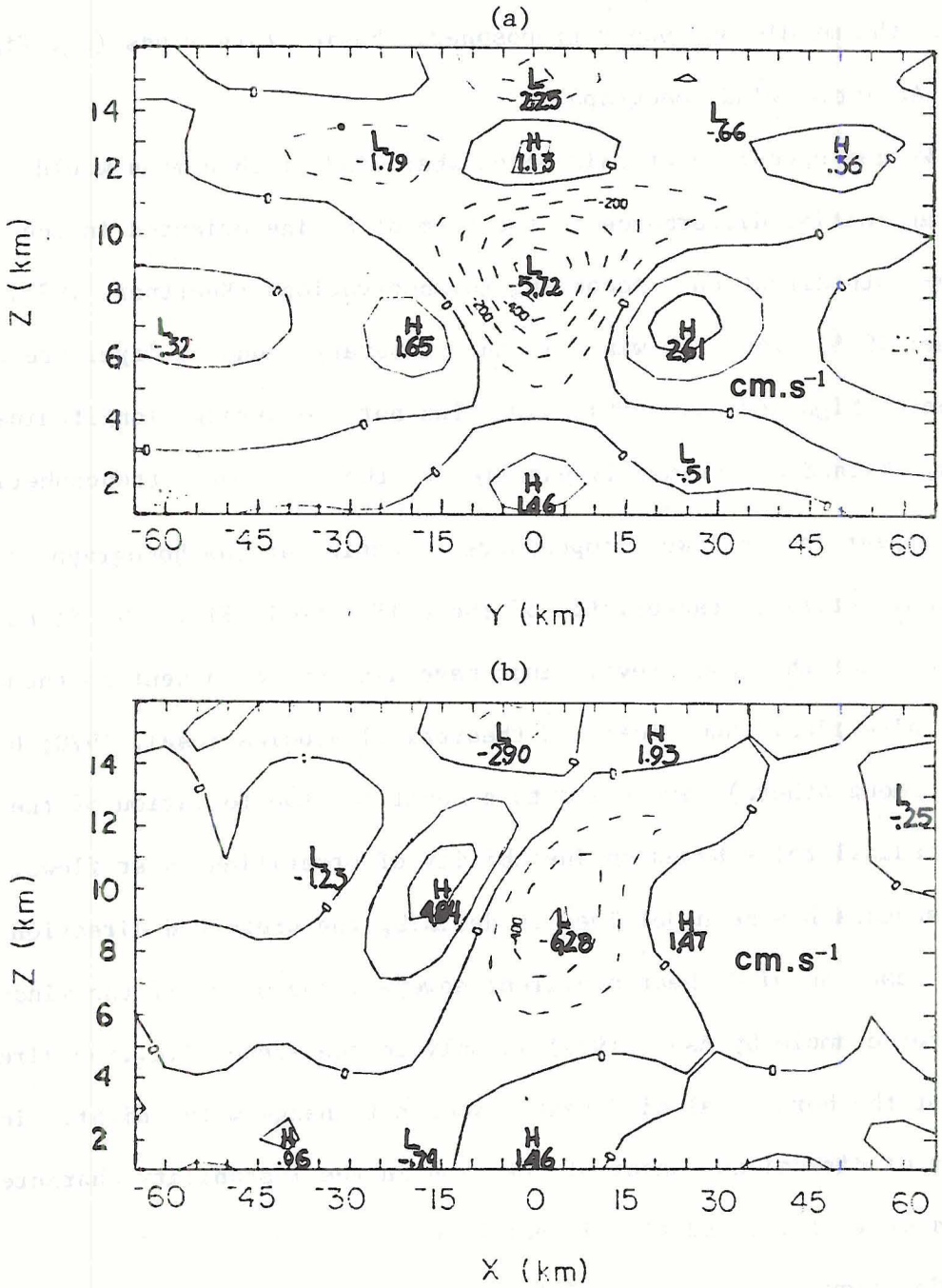

Figure 5.10. Vertical cross sections of mesoscale vertical velocity (a) along z = 0 (east-west plane); (b) along y = 0 (north-south plane) at time t = 0. (Initial condition: a = b = 20 km).

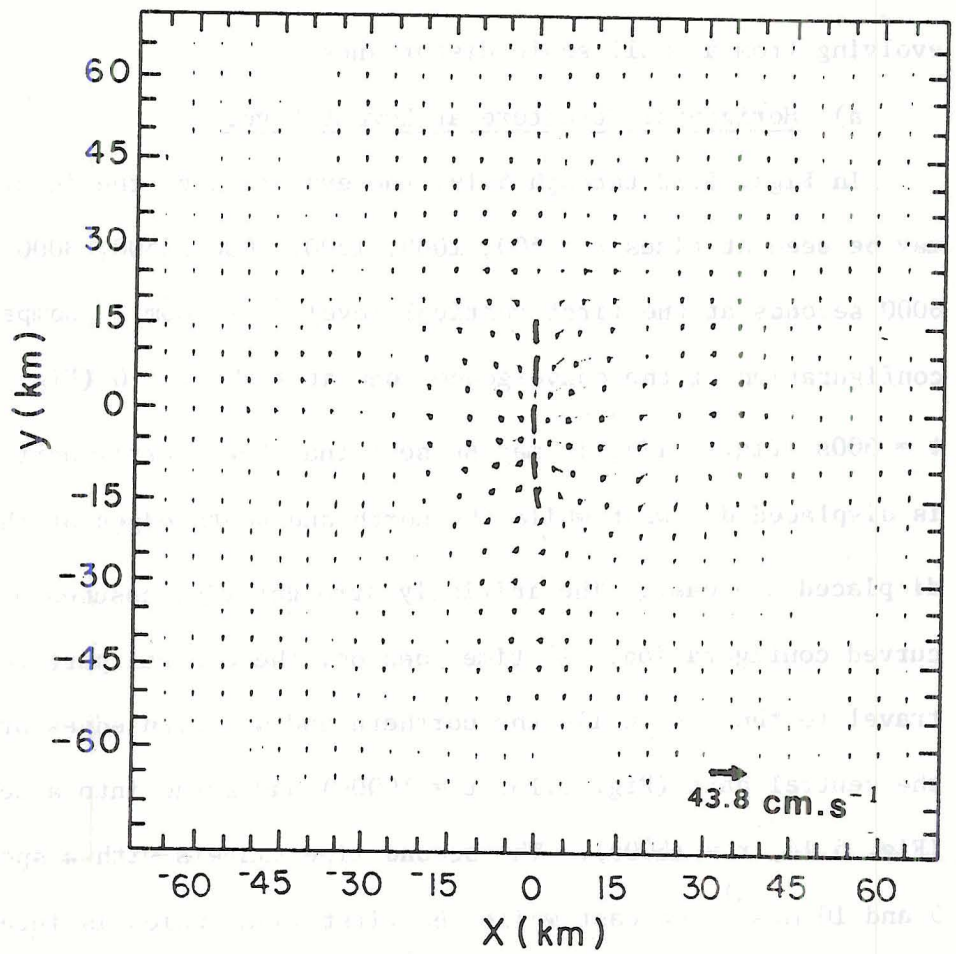

Figure 5.11. Horizontal cross-section of the mesoscale horizontal wind vector (u',v') at z = 500 m and t = 0. Dashed lines denote axis of convergence (Initial condition: a = b = 20 km).

into a full size convective line or even squall line may now be investigated.

We may also speculate that the initial line of convergence may be produced by the downdraft outflow of a small scale line of cumulonimbus clouds. In both cases, we may regard the mesoscale system as evolving from a small scale disturbance.

a) Horizontal Structure at Lowest Level

In Figs. 5.12 through 5.19, the evolution of the initial line may be seen at times t = 500, 1000, 1500, 2000, 2500, 3000, 4500 and 6000 seconds at the first vertical level (z = 500m). Comparing the configuration of the convergence zone at times t = 0 (Fig. 5.11) and t = 500s (Fig. 5.12), it may be seen that the central part of the line is displaced due west while the north and south edges of the line are displaced due east. The initially straight line assumes a rather curved configuration. As time goes on, the central part continues to travel to the west while the northern and southern edges break from the central part (Fig. 5.13, t = 1000s) and merge into a second line (Fig. 5.14, t = 1500s). The second line travels with a speed between 5 and 10 $m.s^{-1}$ due east while the first line, which is intensifying rapidly, travels at about 20 $m.s^{-1}$ due west. At t = 2500 seconds (Fig. 5.16), the lines have approximately the same intensity. From t = 3000 sec (Fig. 5.17) onward (Figs. 5.18, 5.19), it may be seen that the intensification of the first line is greater, so that in a relative sense, the second line appears progressively weaker. It is interesting to note that the initially straight line assumes a rather curved format. Observations of squall line during the 4-5 September

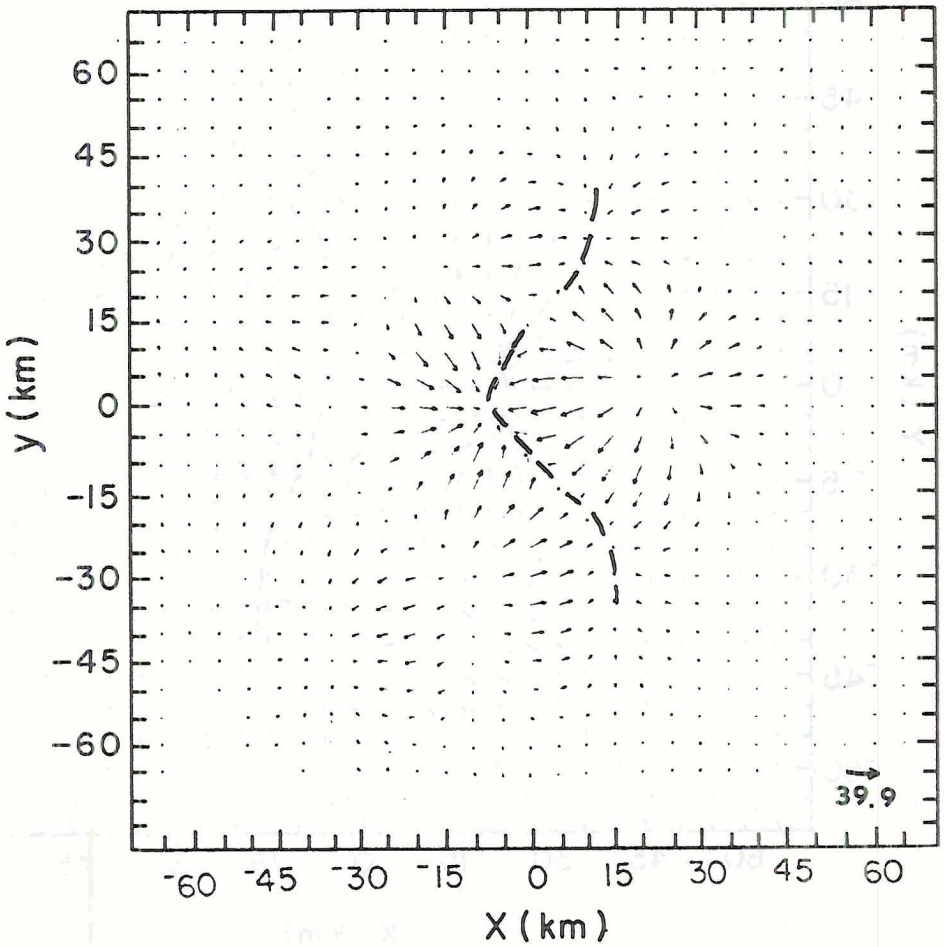

Figure 5.12. Horizontal cross section of the mesoscale horizontal wind vector (u',v') at z = 500 m and t = 500 seconds. (Initial condition: a = b = 20 km).

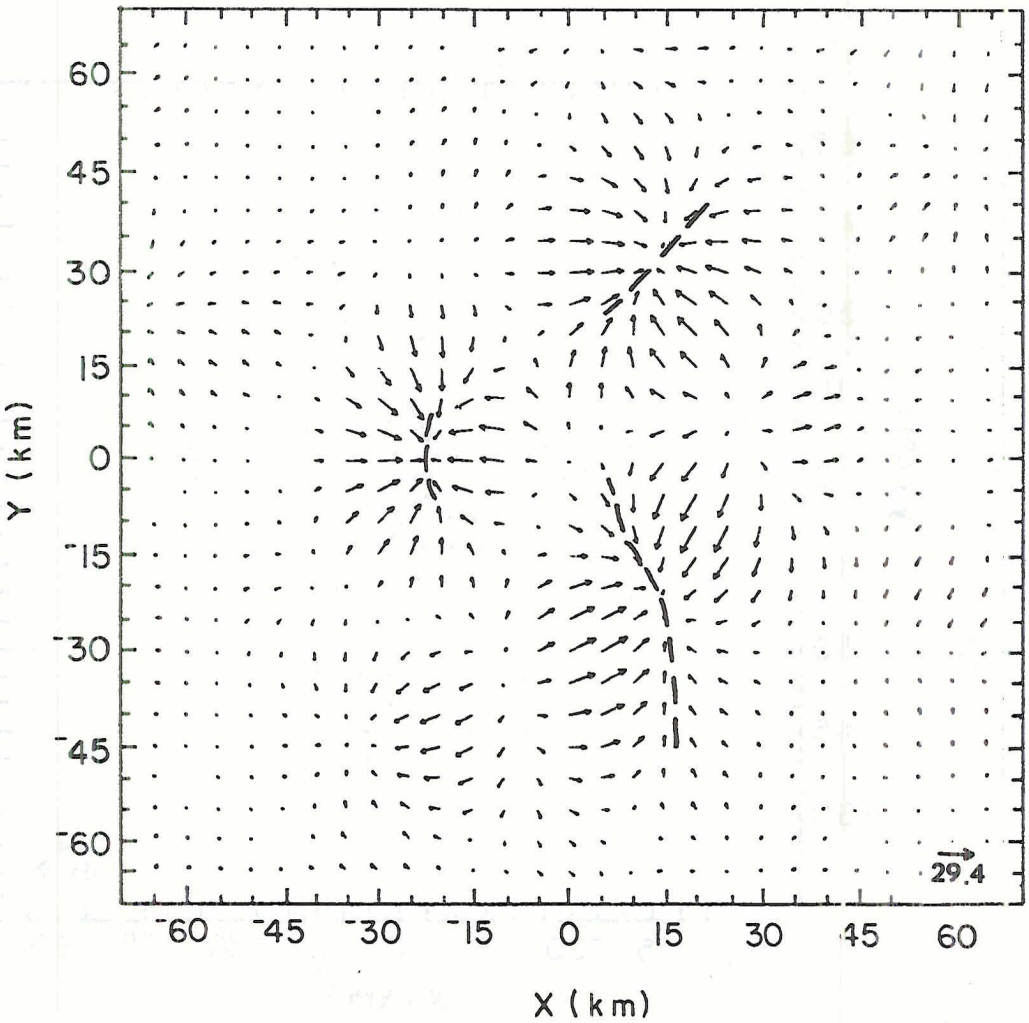

Figure 5.13. Horizontal cross section of the mesoscale horizontal wind vector (u',v') at z = 500 m and t = 1000 seconds. (Initial condition: a = b = 20 km).

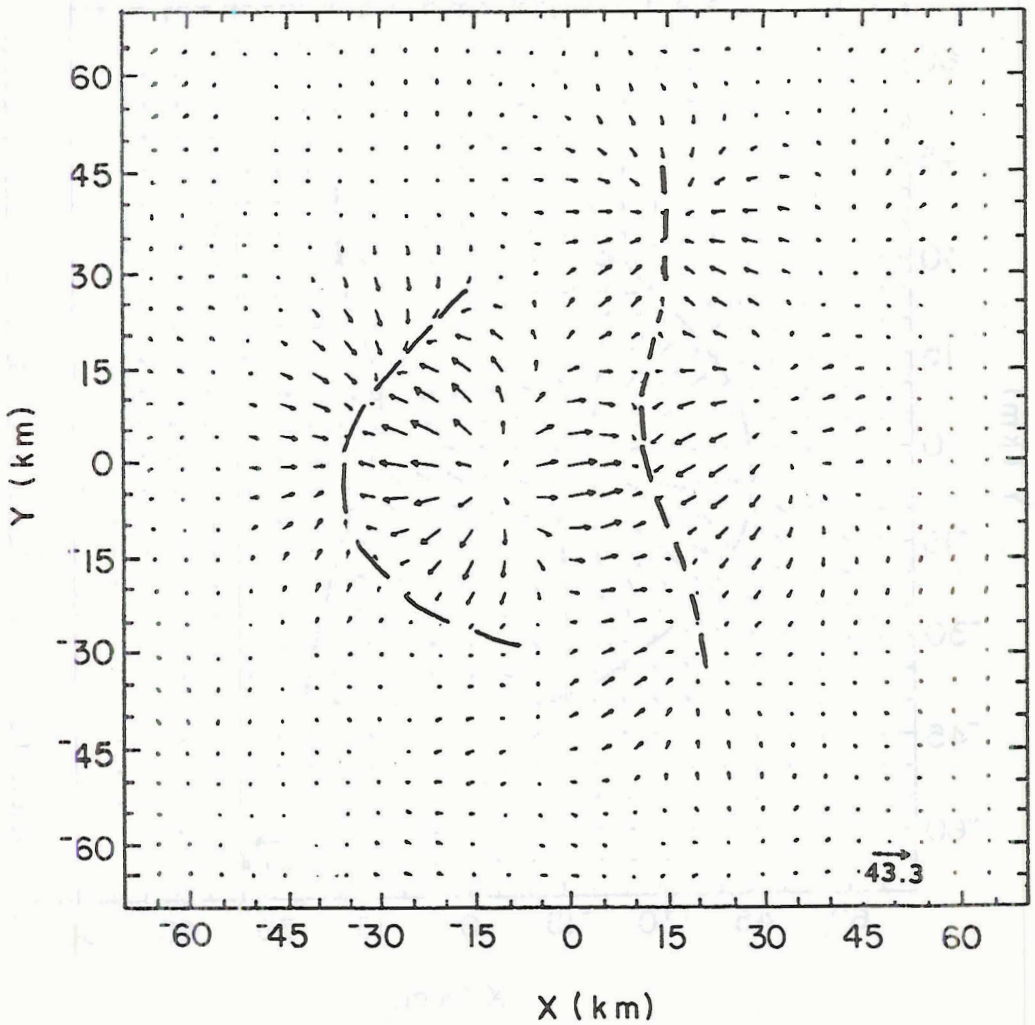

Figure 5.14. Horizontal cross section of the mesoscale horizontal wind vector (u',v') at z = 500 m and t = 1500 seconds (Initial condition: a = b = 20 km).

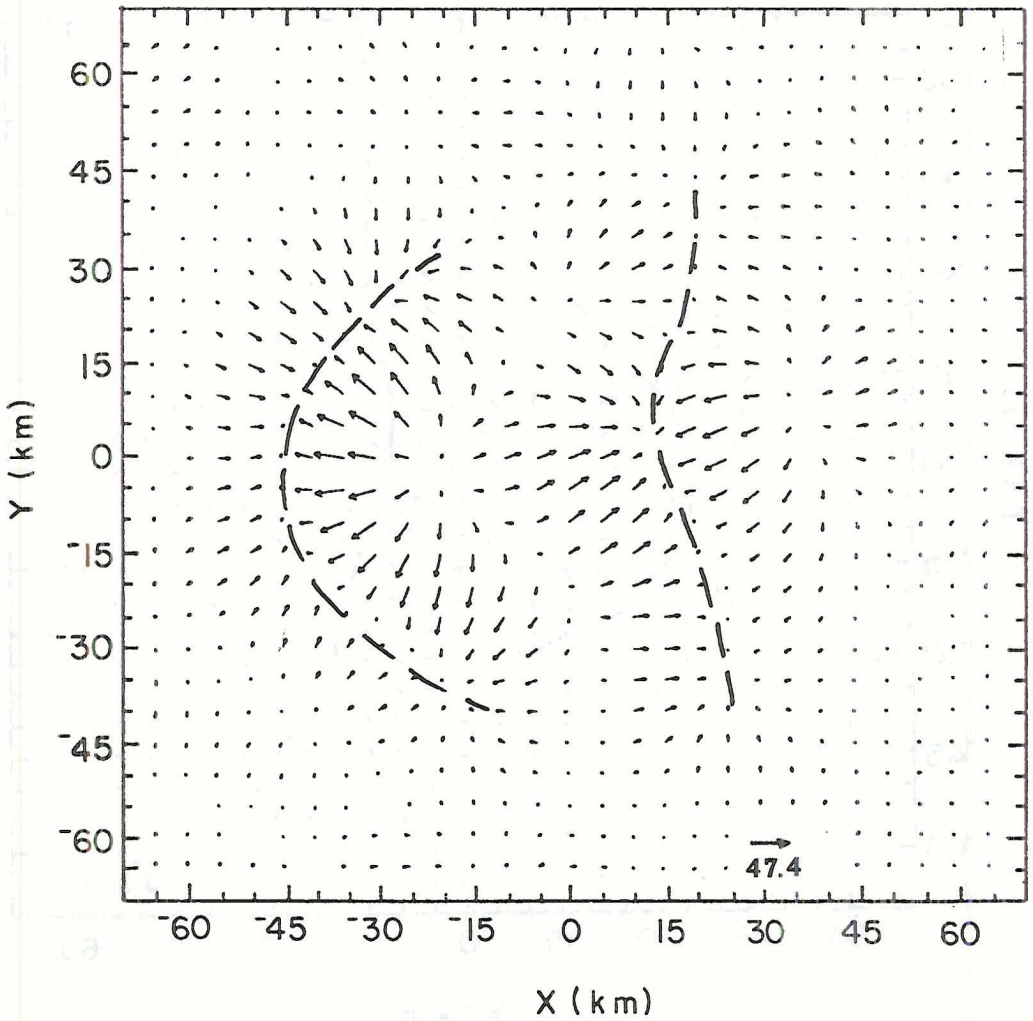

Figure 5.15. Horizontal cross section of the mesoscale horizontal wind vector (u',v') at z = 500 m and t = 2000 seconds. (Initial condition: a = b = 20 km).

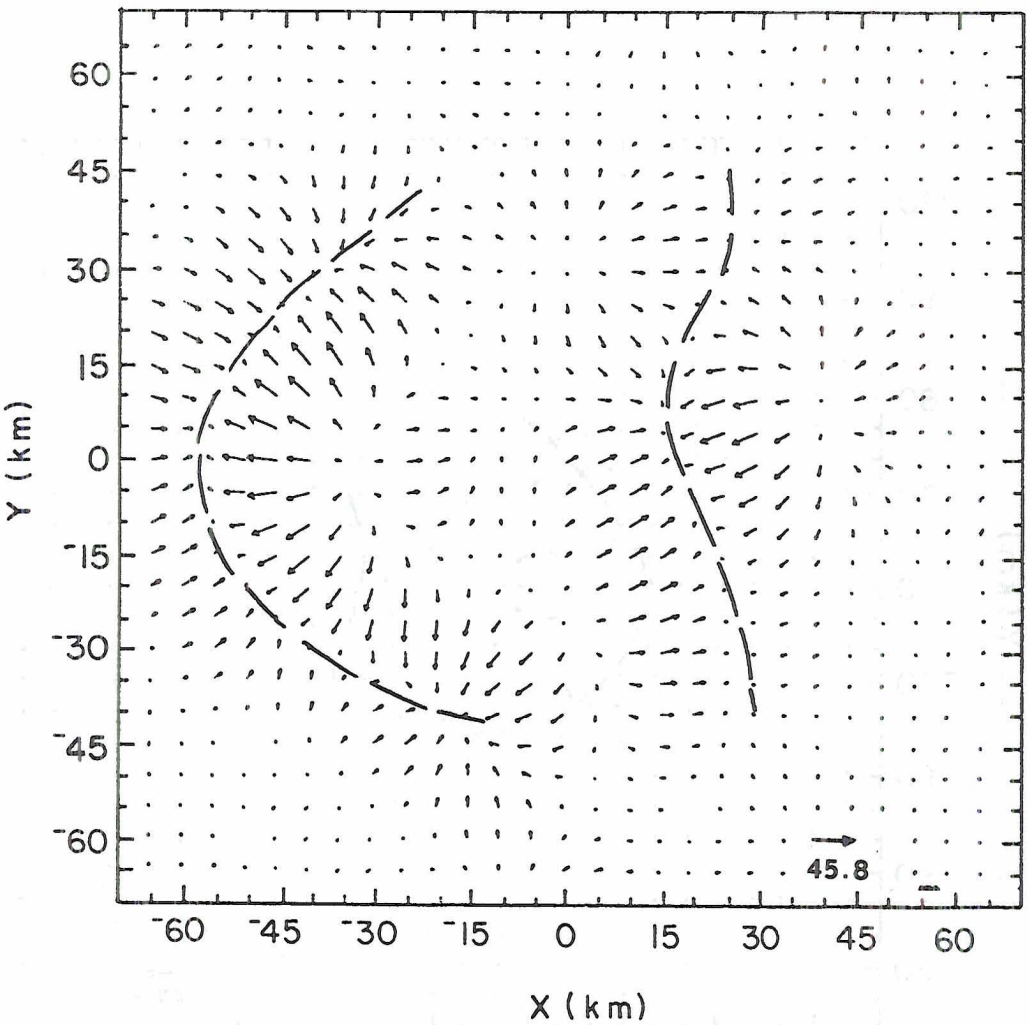

Figure 5.16. Horizontal cross section of the mesoscale horizontal wind vector (u',v') at z = 500 m and t = 2500 second. (Initial condition: a = b = 20 km).

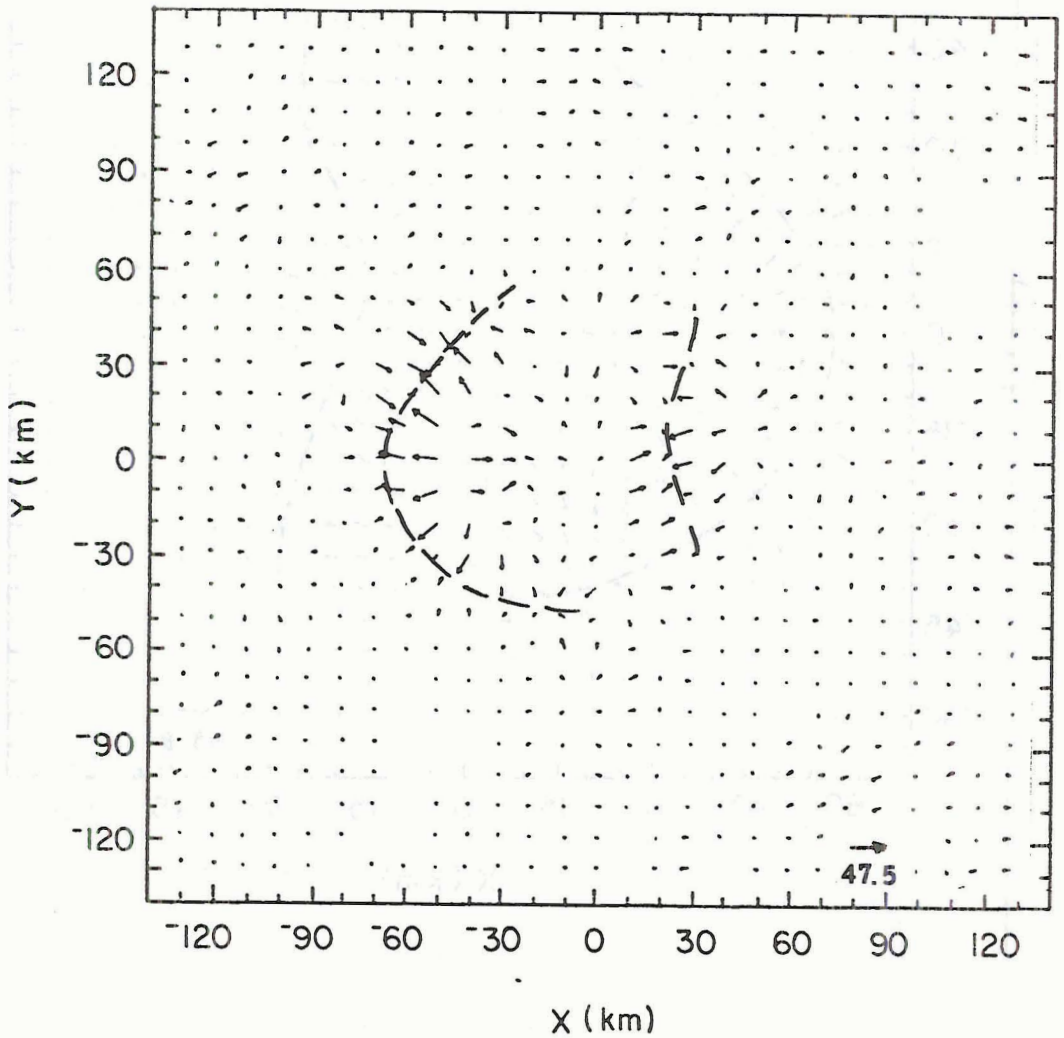

Figure 5.17. Horizontal cross section of the mesoscale horizontal wind vector (u',v') at z = 500 and t = 3000 seconds. Note the change in scale from previous figures. (Initial condition: a = b = 20 km).

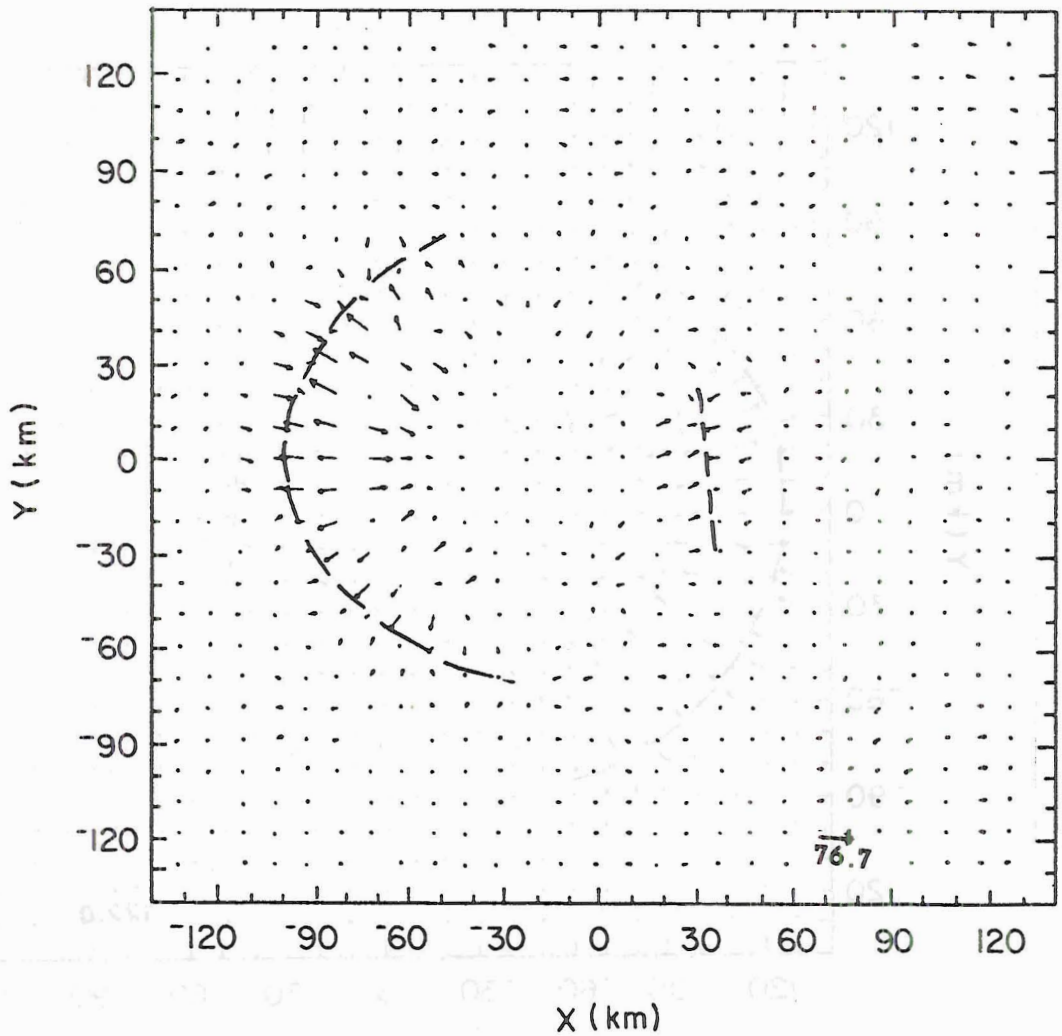

Figure 5.18. Horizontal cross section of the mesoscale horizontal wind vector (u',v') at z = 500 m and t = 4500 seconds. (Initial condition: a = b = 20 km).

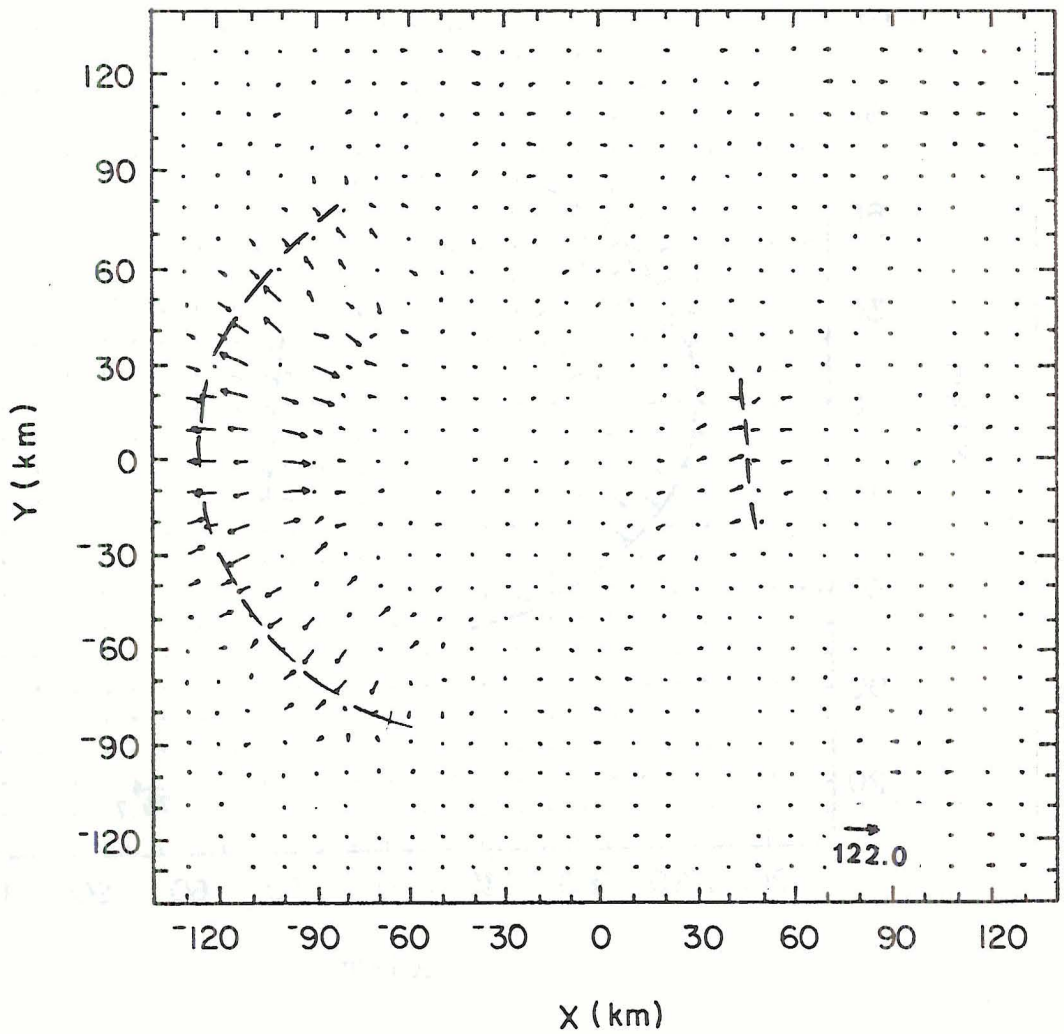

Figure 5.19. Horizontal cross section of the mesoscale horizontal wind vector (u',v') at z = 500 m and t = 6000 second. (Initial condition: a = b = 20 km).

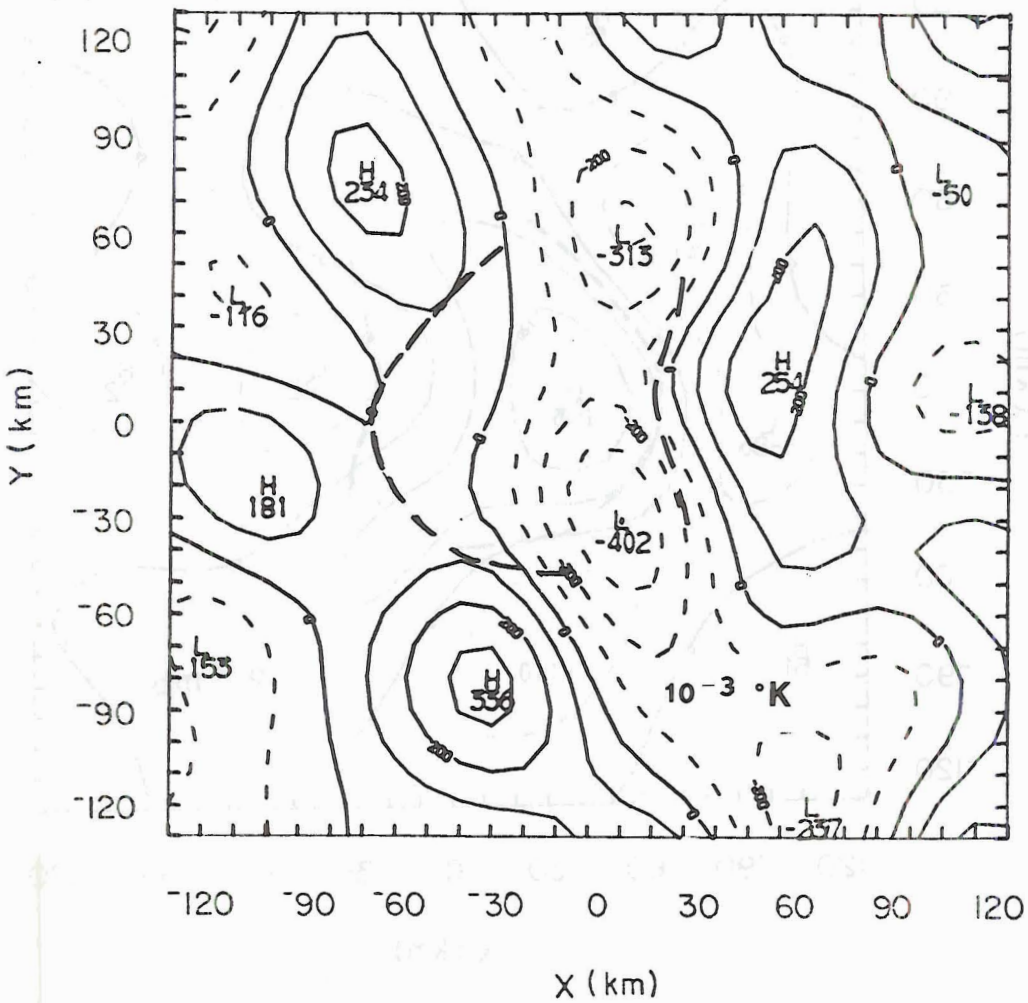

Figure 5.20. Isolines of mesoscale potential temperature θ' at z = 500m and t = 3000 seconds. (Initial condition: a = b = 20 km).

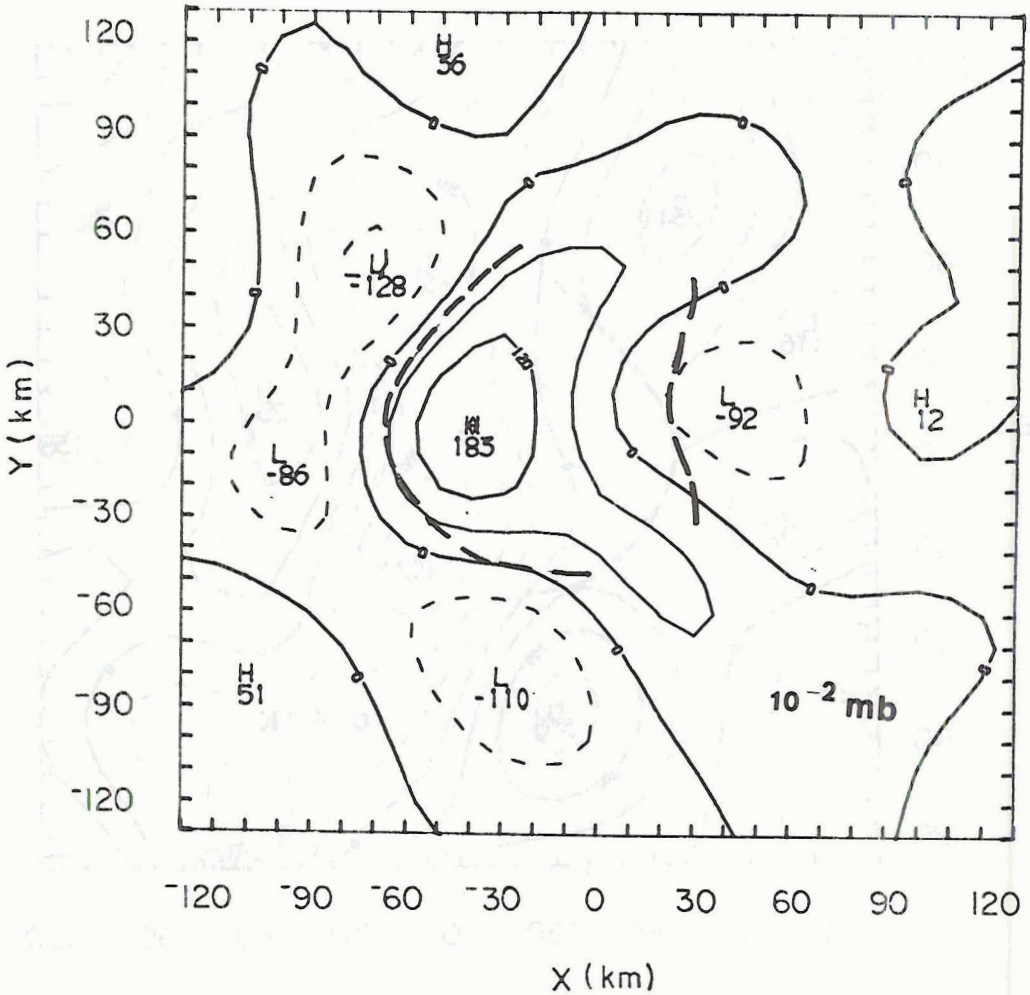

Figure 5.21. Isolines of mesoscale pressure p' at $z = 500$ m and $t = 3000$ seconds.(Initial condition: $a = b = 20$ km).

1974 mesoscale events during the GATE (houze, 1977) show squall lines with strong curvature traveling towards the WSW with great resemblance to the convergence lines of Figs. 5.17 and 5.18.

We may speculate on the reasons for the observed curvature of squall lines. In previous Wave-CISK studies by Hayashi (1970) and Lindzen (1974), for each wavenumber there were Rossby and Kelvin modes and eastward and westward propagating gravity waves. The above mentioned studies were made in rotating planes with no basic state wind; hence, for small scales, the eastward and westward propagating gravity modes have the same phase speed (with opposite signs) and same growth rate. Furthermore, they are nearly non-dispersive in the sense that the group velocity is a constant. In this case, an initial condition of a point of convergence (like throwing a stone in a tank filled with still water) would evolve into a circular, non-dispersive front of convergence that would propagate away from the initial position. A line of convergence (like throwing a stick in a tank) would evolve into an oval front.

The dynamics of gravity waves may then be used to explain the curvature observed in Figs. 5.12 - 5.19. In the present study, the wind profile in the basic state destroys the symmetry between the eastward and the westward gravity waves: the westward gravity wave has higher growth rate and phase speed than the eastward gravity wave; hence, the most unstable, i.e., the westward gravity wave, predominates. Consequently, only the westward propagating part of the front of convergence is seen. The eastward propagating part of the front may barely be seen in Fig. 5.12 at x = 40 km.

The spreading of a gravity wave front may be used to explain the curvature of the convergence zone through the whole atmosphere.

Previous explanations for the observed curvature of squall lines were based on the spreading of a density current generated by evaporation of rain in a mesoscale downdraft. The effect of evaporation of rain in the mesoscale is not included in the present model and furthermore, the mesoscale temperature structure shown in Fig. 5.20 at t = 3000 sec does not show a cooler region right after the convergence zone. The mesoscale pressure field at t = 3000 sec is shown in Fig. 5.21 and it shows a mesohigh right behind the convergence zone and mesolows in front of the convergence zone. The same structure was obtained by Fritsch (1978).

This model can thus separate the essentially dynamic effect of propagation of gravity wave front from the essentially thermodynamic effect of propagation of a density current. Certainly there must be, in nature, a coupling between the density current and the gravity front; Moncrieff and Miller (1976) mention that inequality in speeds between the two phenomena results in either impulsive behaviour or decay of the main convection.

It may be noted that the speed of propagation of the main line after time t = 3000 sec is the phase speed of the most unstable mode mentioned earlier (19-20 $m.s^{-1}$). Fig. 5.22 shows the time sequence of the position of the leading edge of the two convective lines. The main line travelling due west is accelerated and decelerated in

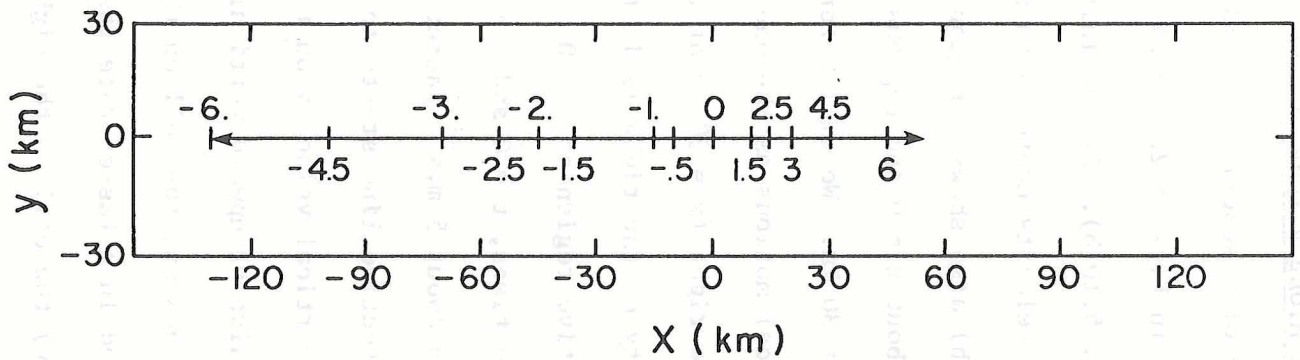

Figure 5.22. Time sequence of the position of the leading edge of the two convective lines shown in Figures 5.11 to 5.19. The numbers denote time steps in 1000 seconds.

successive time steps until a constant speed is obtained after t = 3000 seconds. The group velocity calculated through equation (4.1) at the most unstable mode is 18 $m.s^{-1}$ towards the SSW.

b) Vertical Structure Along a Zonal Plane

The vertical structure of mesoscale vertical velocity for the same time steps may be seen in Figs. 5.22 - 5.24. The initial disturbance may be seen in Fig. 5.10(b). At the initial time, there was a region of upward vertical velocity centered in x = y = 0 up to the height of 4 km. Fig. 5.10(b) also shows a region of strong sinking in the middle troposphere at about x = 0 and regions of weaker upward motion at x = -15 km and x = 30 km. We will refer to these two regions of middle troposphere vertical motions as the one on the left (x = -15 km at t = 0) and the one on the right (x = 30 km at t = 0). The region of positive vertical velocity on the right is initially disconnected from the lower level convective region at x = 0. The evolution in time and space shows that between times, t = 0 and t = 1500 sec the middle tropospheric pattern travels about 5 $m.s^{-1}$ faster than the surface disturbance so that the convective line starts to feed the region of middle tropospheric upward vertical velocity on the right. This region had, initially, a smaller value of upward vertical velocity than the cell on the left. As time goes on, the cell on the right has its vertical velocity intensified in a faster rate than the one on the left; by t = 1000 sec (Fig. 5.22 b) the cell on the right has greater vertical velocity than the cell on the left. From t = 2000 sec (Fig. 5.24 b) onward the region of upward vertical velocity reaches the height of the upper level jet on the basic state field (cf. Fig. 4.1). From

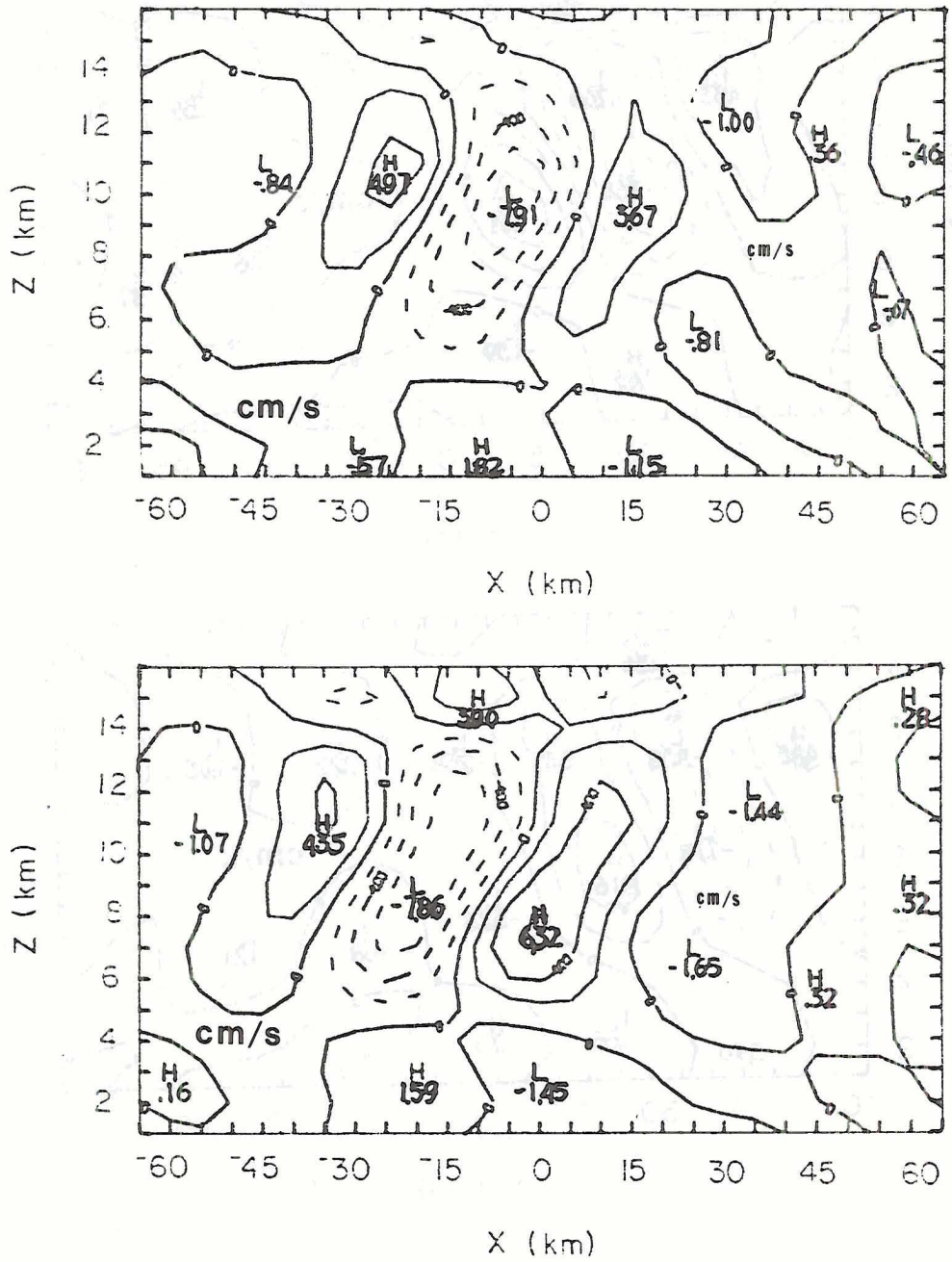

Figure 5.23. Vertical cross sections along y = 0 (zonal plane) of mesoscale vertical velocity (a) at t = 500 seconds; (b) at t = 1000 sec. (Initial condition: a = b = 20 km).

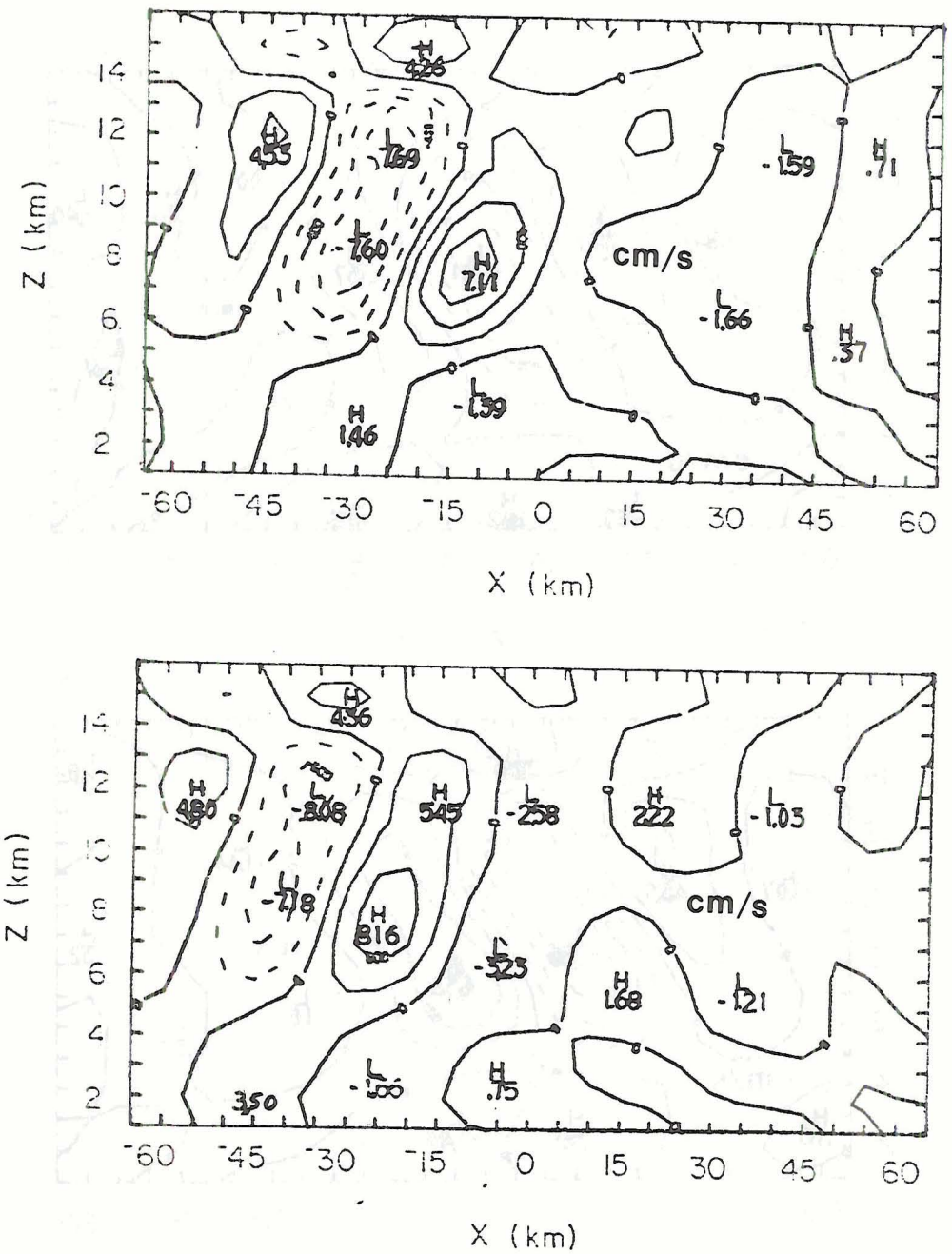

Figure 5.24. Vertical cross sections along y = 0 (zonal plane) of mesoscale vertical velocity. (z) at t = 1500 seconds; (b) at t = 2000 sec. (Initial condition: a = b = 20 km).

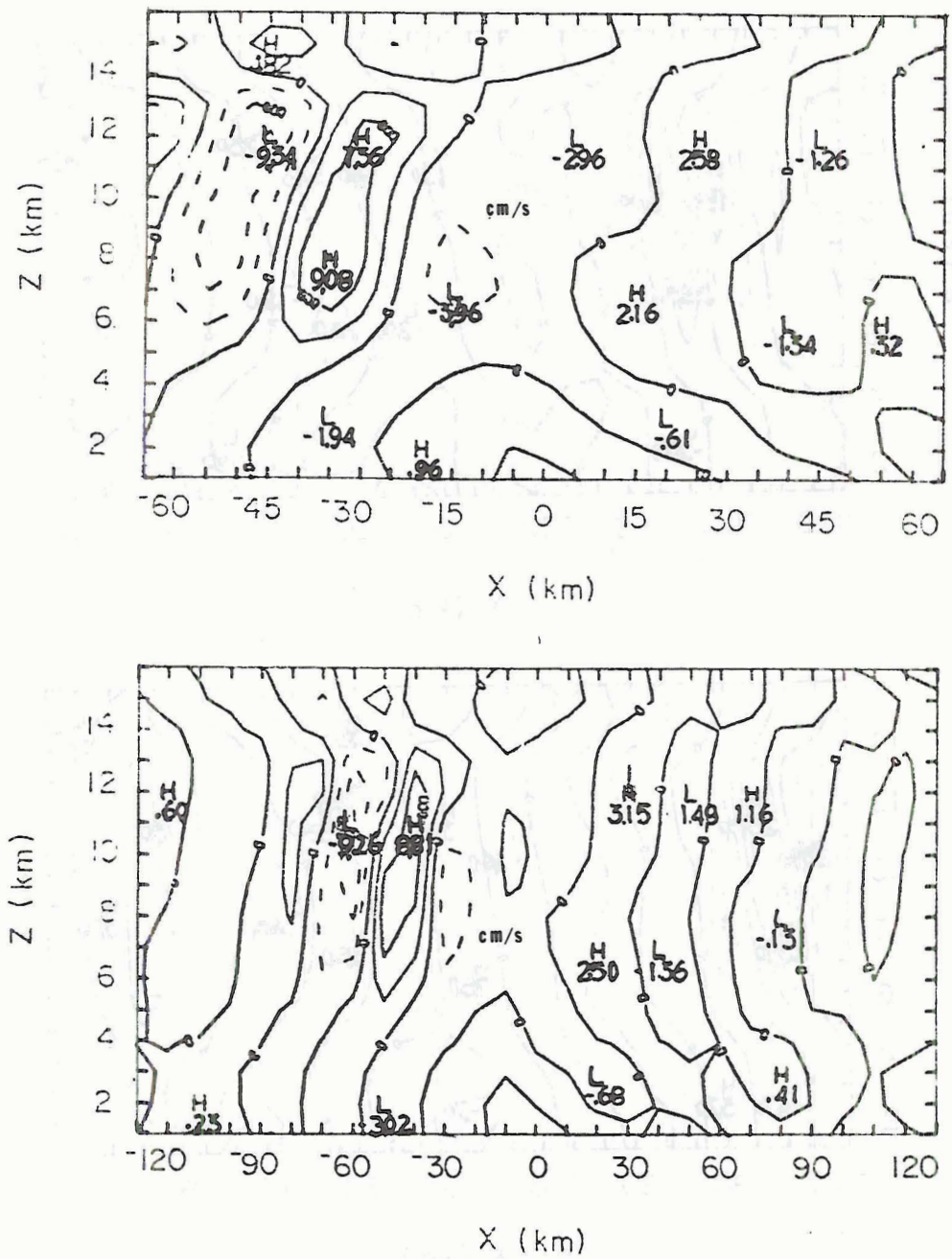

Figure 5.25. Vertical cross sections along y = 0 (zonal plane) of mesoscale vertical velocity. (a) at t = 2500 seconds; (b) at t = 3000 sec. Note difference in scales between (a) and (b). (Initial condition: a = b = 20 km).

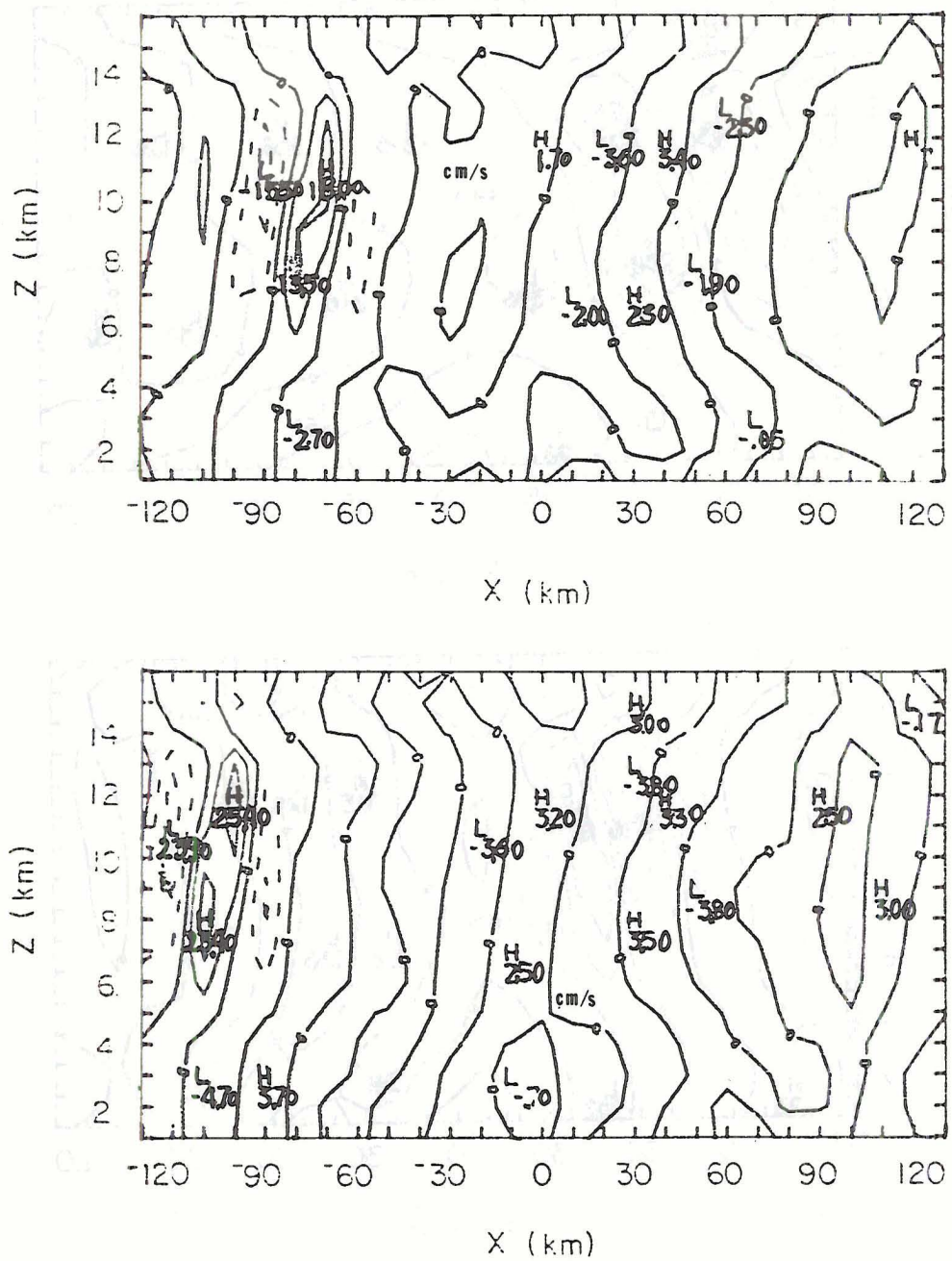

Figure 5.26. Vertical cross sections along y = 0 (zonal plane) of mesoscale vertical velocity. (a) at t = 4500 seconds; at t = 6000 sec. (Initial condition: a = b = 20 km).

then on, it may be considered that the initial disturbance has developed into a convergence line that extends through the whole troposphere.

The secondary line of surface convergence observed in Figs. 5.14 - 5.19 can also be followed in Figs. 5.22 - 5.24. At time t = 1500 sec, the position of the secondary line was x = 15 km. Fig. 5.22(a) shows that the lower region of upward vertical velocity at x = 15 km barely reaches the 2 km level. Not until k = 6000 sec does the secondary line, which has moved to x = 45 km (Fig. 5.23a), begin to extend through the whole troposphere. By this time, however, its intensity is only a seventh of the main line now located at x= -110 km (Fig. 5.23b). It may be noted that the maximum magnitude of upward vertical velocity at t = 4500 sec is about 4 times its initial value.

The tilting of the main line after t = 2500 sec is comparable to the tilting reported by Houze (1977) and by Sanders and Emanuel (1977), i.e., the middle tropospheric region of upward motion lags between 20 and 30 km behind the surface region of upward motion.

At time t = 2500 sec (Fig. 5.24b) and in subsequent figures, it may be noted that on both sides of the convergence line there are broad regions of downward motion. This may be identified with compensating subsidence. The compensating subsidence in front of the line is stronger than behind; this is in accordance again with Fritsch (1978) results.

c) Horizontal Structure at Higher Levels

The horizontal structure of the mesoscale winds at time t = 2500 sec at z = 6.5 km may be seen in Fig. 5.25 and at z = 13.5 km in Fig. 5.24. Referring back to Fig. 5.23(b), we see that Fig. 5.25 is a

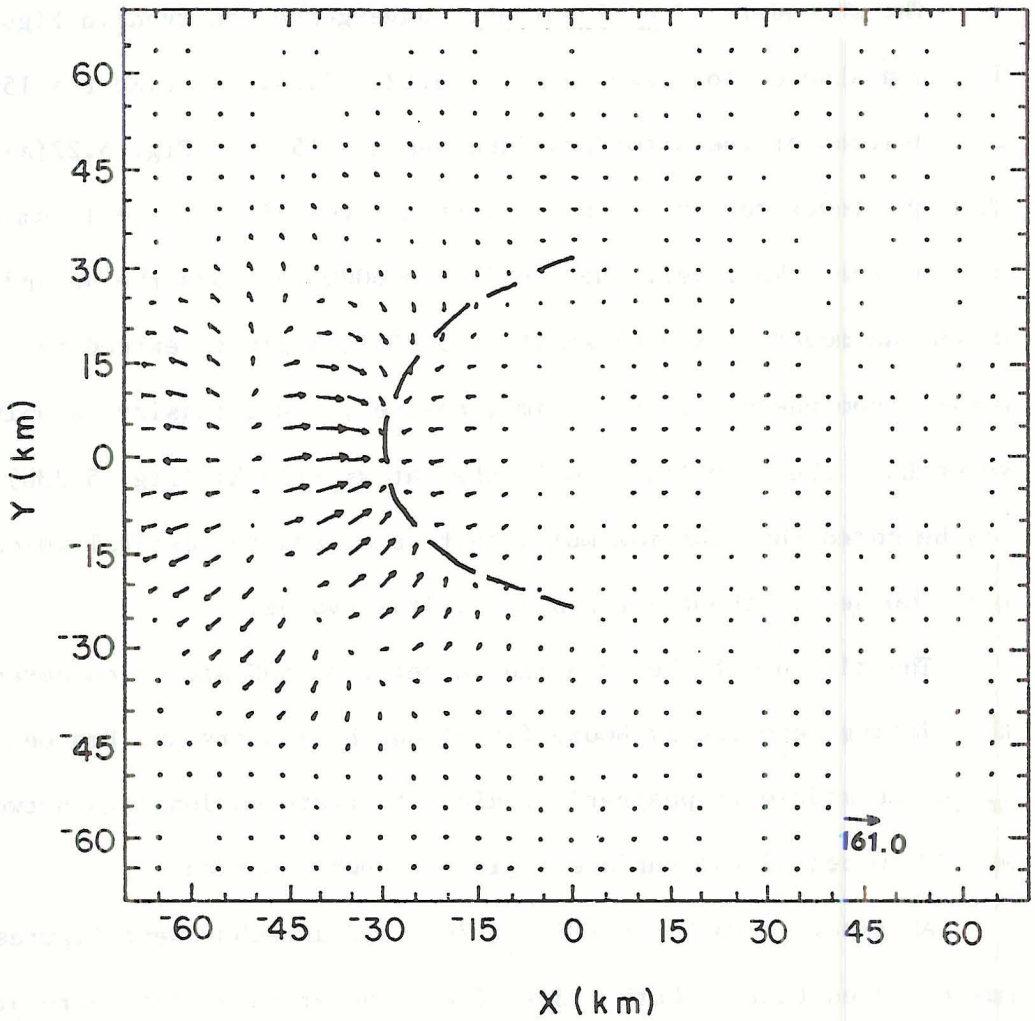

Figure 5.27. Horizontal cross section of the mesoscale horizontal wind vector (u',v') at z = 6.5 km and t = 2500 sec. (cf. Figure 5.15). Initial condition: a = b = 20 km).

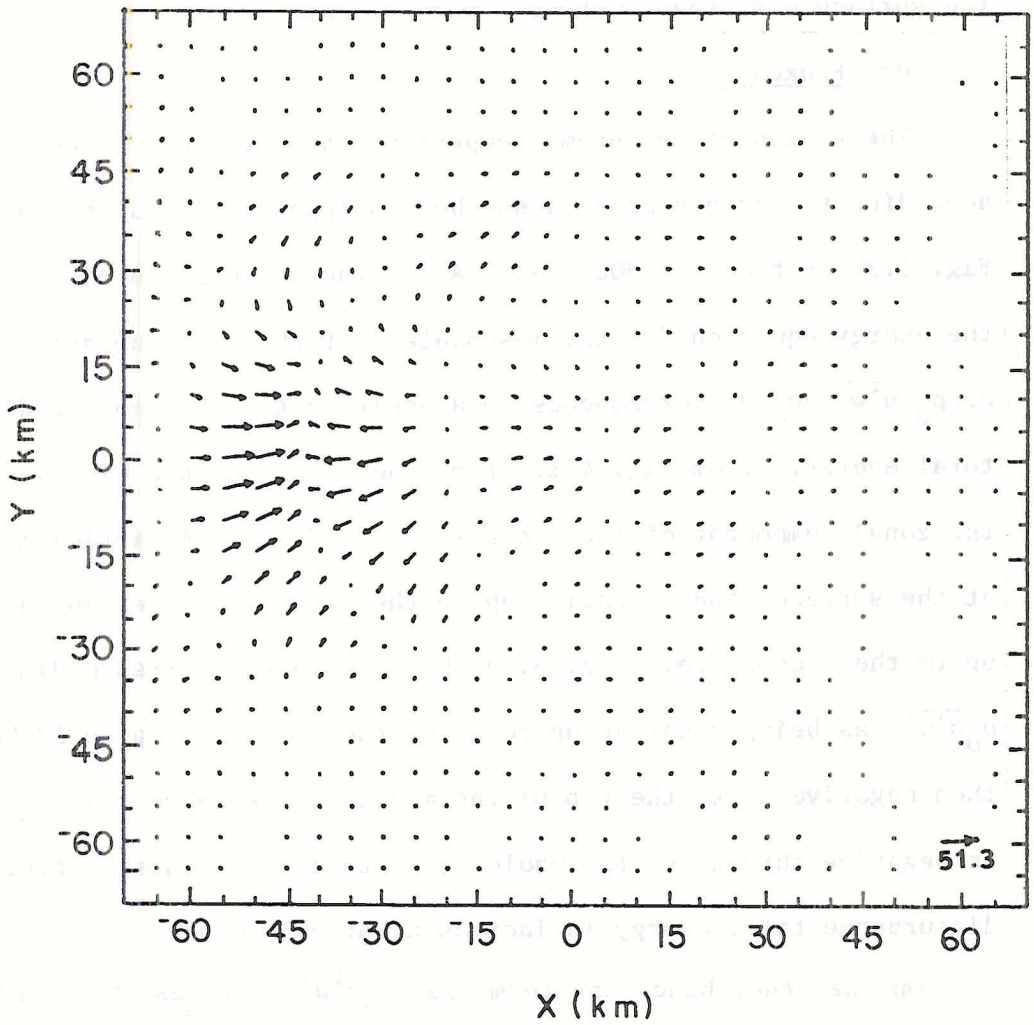

Figure 5.28 Horizontal cross section of the mesoscale horizontal wind vector (u',v') at z = 13.5 km at t = 2500 sec. (cf. Figures 5.15 and 5.23). (Initial condition: a = b = 20 km).

horizontal cross section through a region of high upward vertical velocity at x = 30 to 40 km. Fig. 5.25 can be compared to Fig. 5.16 which shows the horizontal structure at the lowest level. The middle tropospheric line of convergence, besides being located to the east of the surface disturbance shows a more concave curvature.

d) Fluxes

The fluxes of momentum, temperature and pressure calculated according to the procedure described in Appendix A2 may be seen in Fig. 5.29 at time t = 3000 sec. According to equation(A1.8), defining the energy equation for the mesoscale disturbance, a negative value of $\rho_o \overline{u'w'}\, du_o/dz$ corresponds to a positive tendency on the disturbance total energy. From Fig. 4.1, it may be seen that the wind shear in the zonal component of the basic state wind (East Atlantic) is positive at the surface, then negative up to the upper level jet and positive up to the tropopause. Fig. 5.29 shows curve (A) corresponding to $\rho_o \overline{u'w'}$ as being negative up to 2 km, then positive up to 13 km and then negative up to the top of the model. This means that $\rho_o \overline{u'w'}\, du_o/dz$ is negative throughout the whole troposphere and consequently, the disturbance total energy is increasing at all levels.

On the other hand, the term $d/dz\ \rho_o \overline{u'w'}$ denotes the effect of the mesoscale wind field on the basic state wind. Fig. 5.29(A) shows that there is an upward transport of westerly momentum; hence, the mesoscale convergence line would be reducing the intensity of the upper level easterly jet. This conclusion should be checked against observations. It should be noted, however, that the three-dimensional character of the wind fields during mesoscale events makes the comparison of the above conclusion with observations a rather difficult task.

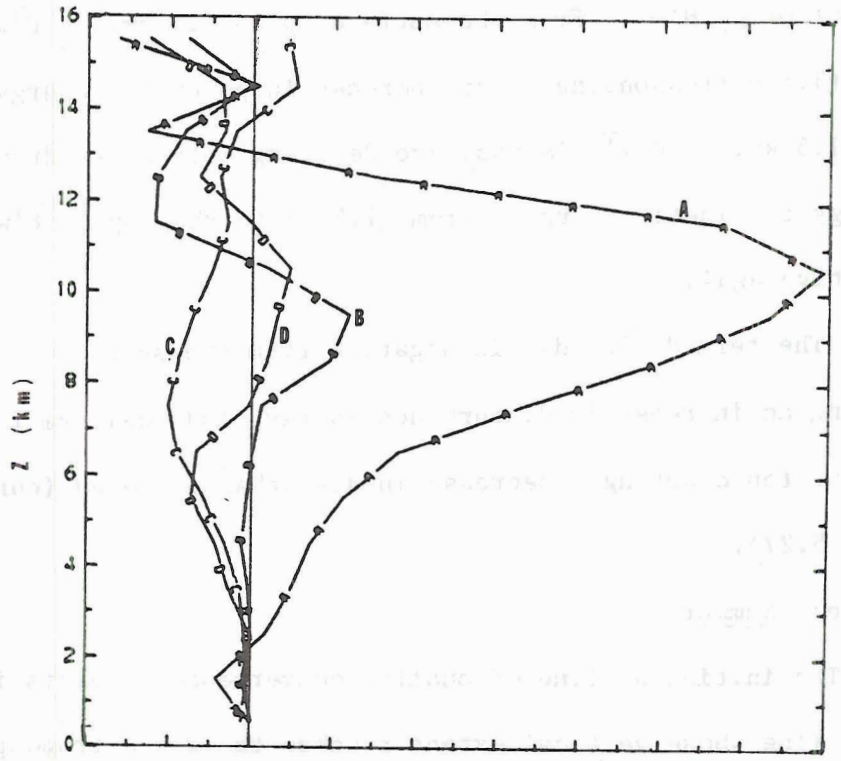

Figure 5.29. Vertical structure of: (A) $\rho_o \overline{u'w'}$; (B) $\rho_o \overline{v'w'}$; (C) $\overline{p'w'}$; (D) $\rho_o \overline{\theta'w'}$ at time t = 3000 seconds; (Initial condition: a = b = 20 km).

The conversion between potential energy and kinetic energy is done through the term $\rho_o \overline{w'\theta'}/\theta_o$ (cf. equation A1.3 and A1.4). A negative correlation between vertical velocity and temperature perturbation (up-cold, down-warm) increases the potential energy and decreases the kinetic energy of vertical motions. Curve (D) in Fig. 5.29 shows a plot of $\rho_o \overline{\theta'w'}$. From the surface up to 7.5 km, $\rho_o \overline{\theta'w'}$ is negative corresponding to an increase in potential energy. From 7.5 km to 11.5 km, $\rho_o \overline{\theta'w'}$ is positive denoting a transfer from potential energy to kinetic energy. From 11.5 km to the top, $\rho_o \overline{\theta'w'}$ is negative again.

The term $d\,\overline{p'w'}/dz$ is negative from the surface to 7.5 km, denoting an increase in disturbance energy, and positive from 7.5 km to the top denoting a decrease in disturbance energy (curve (C) in Fig. 5.27).

e) Summary

The initiating line of shallow convergence develops into a convergence line whose vertical extent reaches the whole troposphere. The structure of this line compares fairly well with observations of squall lines: it develops curvature and vertical tilting comparable with observations by Houze (1977) and Sanders and Emanuel (1977). A mesohigh also develops behind the systems in accordance with the descriptions by Zipser (1977). Compensating subsidence is stronger in front of the line, downwind from the upper level easterly jet, in accordance with the numerical results obtained by Fritsch (1978). The flux of momentum is such as to produce an upward transport of westerly momentum; the mesoscale line may be viewed as reducing the intensity of the upper level easterly jet.

5.2.2 Wide Initial Disturbance: a = b = 50 km

With a horizontal scale of 50 km in the initial condition, the ratio of the Fourier transform of w' (equation 5.6) at wavelengths (50 km, 50 km) and (100 km, 20 km) corresponding to the most unstable mode is 10^{21} (cf. Fig. 5.9), so that the time for the most unstable mode to predominate is about a month ... In the mean time, the peak in the initial condition still provides a solution that very much resembles a convective line. Fig. 5.30 shows the projection of the initial condition on the eigenfunctions at level z = 500 m. This figure may be compared with Fig. 5.11 where the initial condition had scale of 20 km (note the difference in scale between the two figures). While Fig. 5.11 shows a line of about 50 km length, Fig. 5.28 shows a line about 100 km long.

a) Horizontal Structure at Lowest Level

The evolution of the initial disturbance may be seen in Figs. 5.31, 5.32, 5,33 for times t = 1500, 3000 and 4500 sec, respectively. At t = 1500 sec, the original line presents a strong curvature, but its central part has barely moved from the initial location at x = 10 km. At t = 3000 sec (Fig. 5.32), another line appears well ahead of the initial one, at x = -80 km. The initial line is displaced to x = 30 km at about 13 $m.s^{-1}$. Looking into the interval between t = 1500 sec and t = 3000 sec with a small time step (not shown), it is seen that the line that appears at x = -80 km is formed from the convergence generated by compensating subsidence related to the first line. It may be noted that on the 2 September, disturbance during the GATE (Mower, 1977), several lines were observed with spacing of about 60 km.

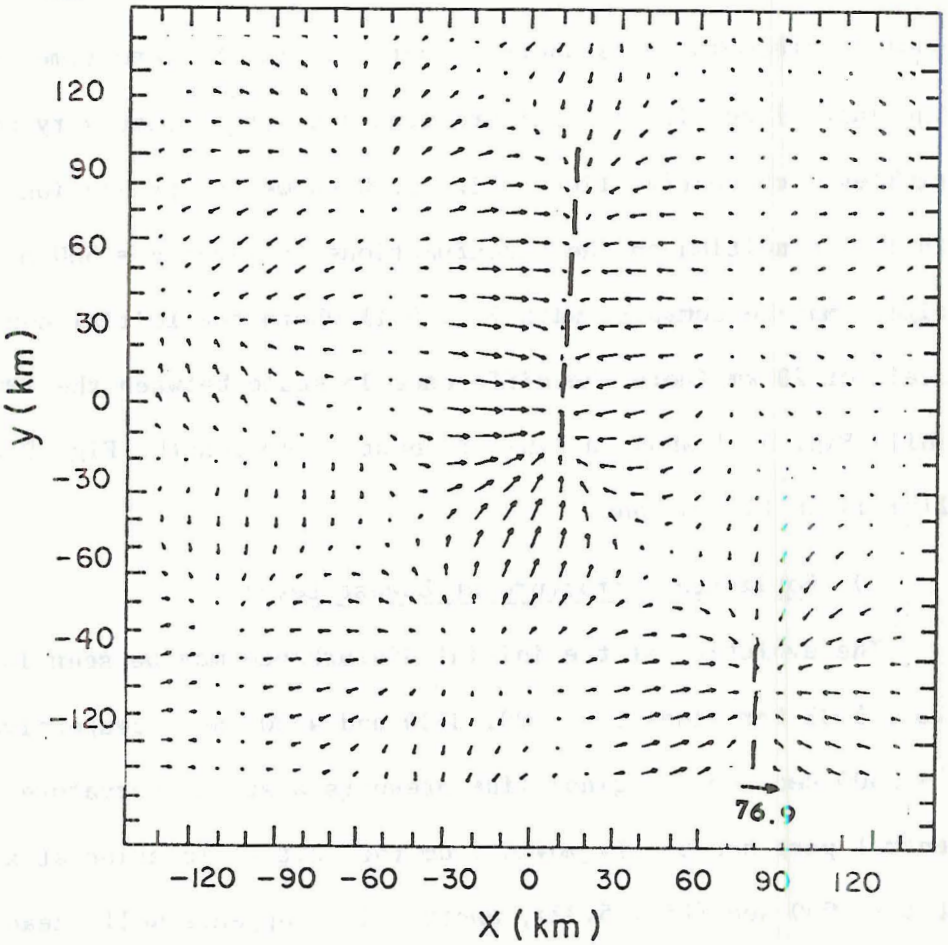

Figure 5.30. Horizontal cross section of mesoscale horizontal wind vector (u',v') at z = 500 m and t = 0. (Initial condition: a = b = 50 km).

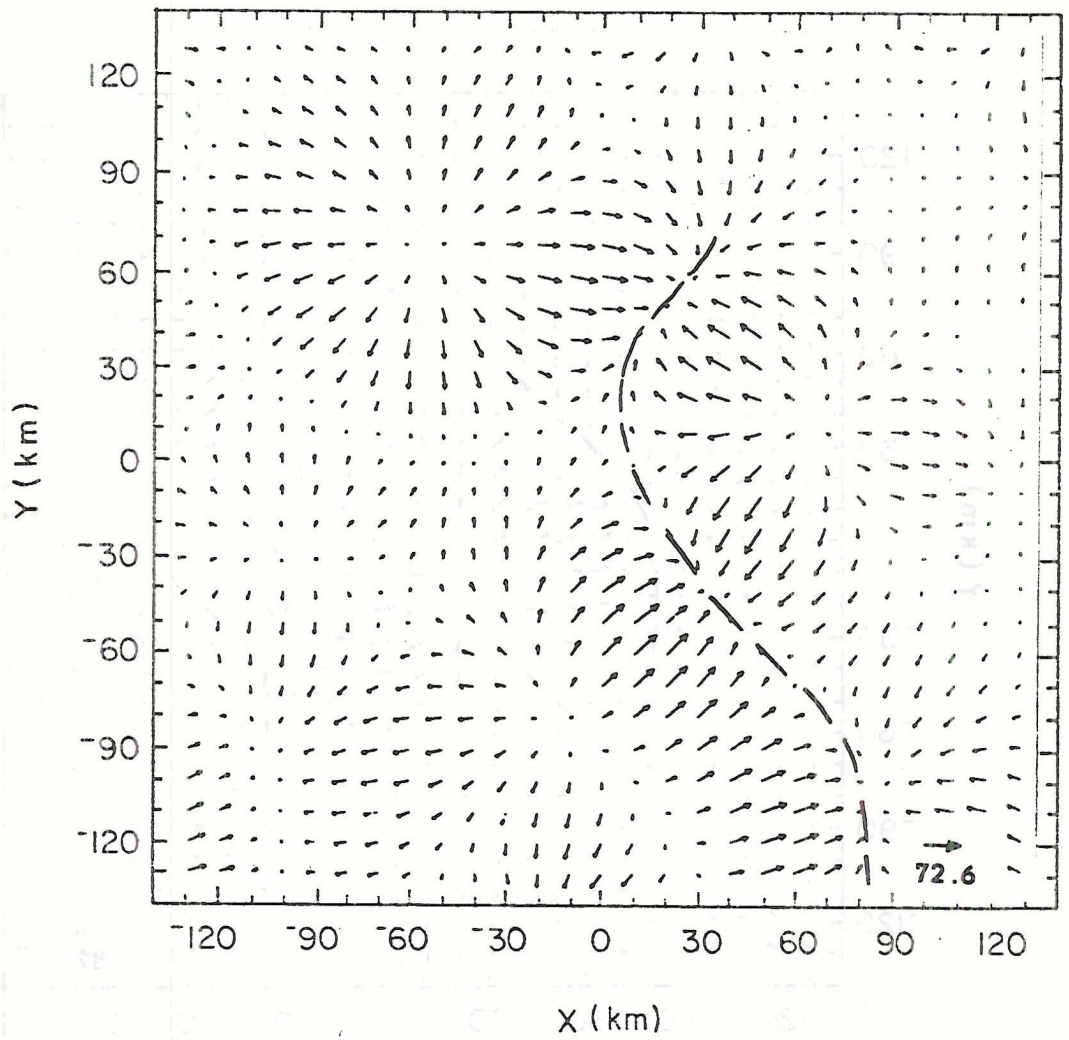

Figure 5.31. Horizontal cross section of mesoscale horizontal wind vector (u',v') at z = 500 m and t = 1500 seconds. (Initial condition: a = b = 50 km).

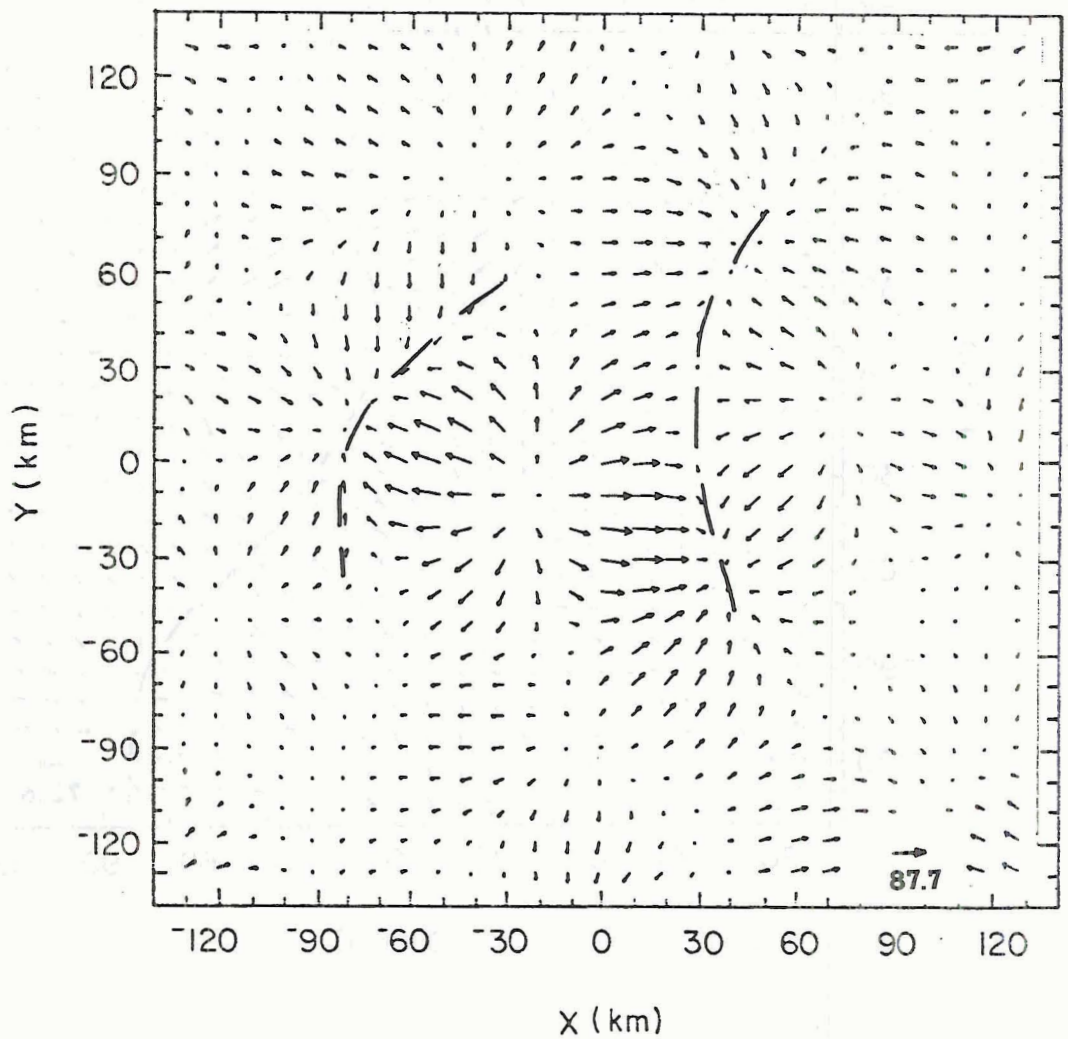

Figure 5.32. Horizontal cross section of mesoscale horizontal wind vector (u',v') at z = 500 m and t = 3000 sec. (Initial condition: a = b = 50 km).

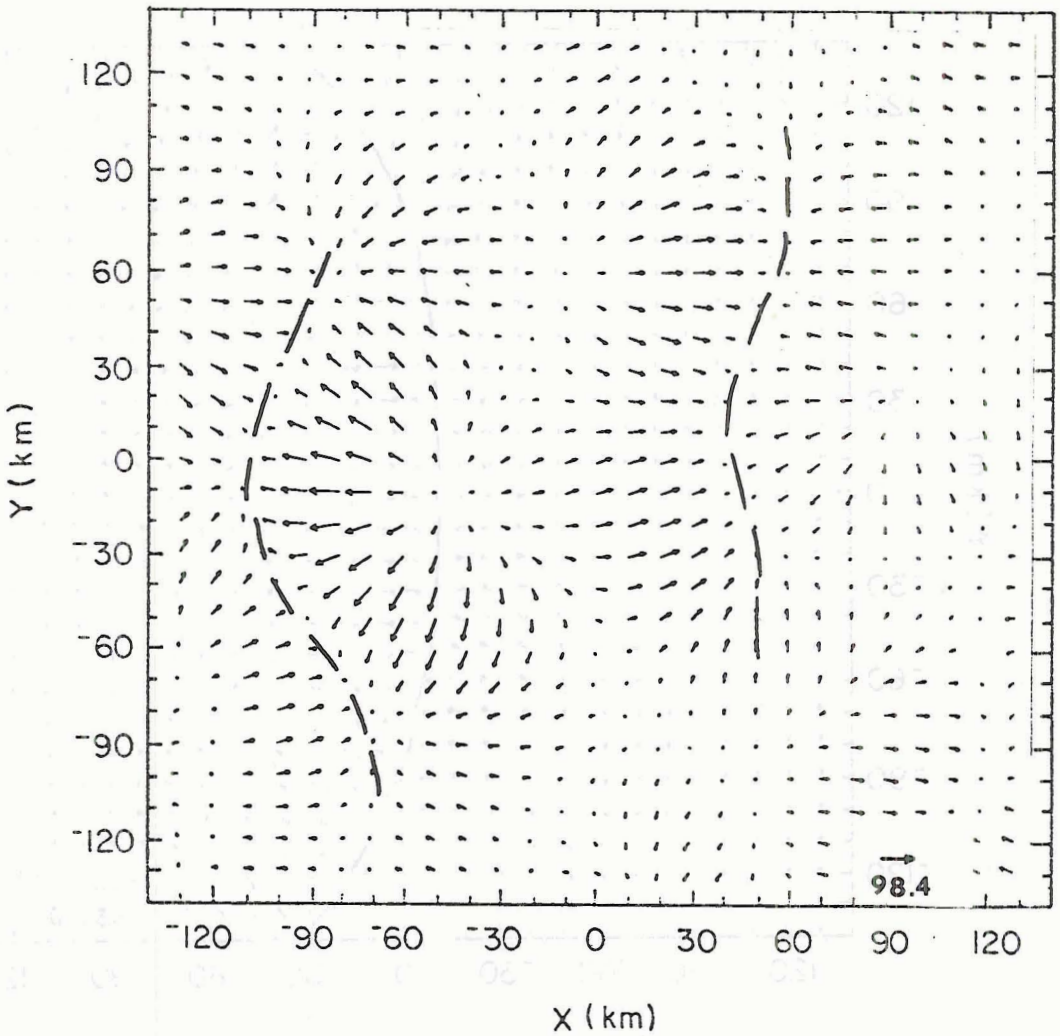

Figure 5.33. Horizontal cross section of mesoscale horizontal wind vector (u',v') at z = 500 m and t = 4500 sec. (Initial condition: a = b = 50 km).

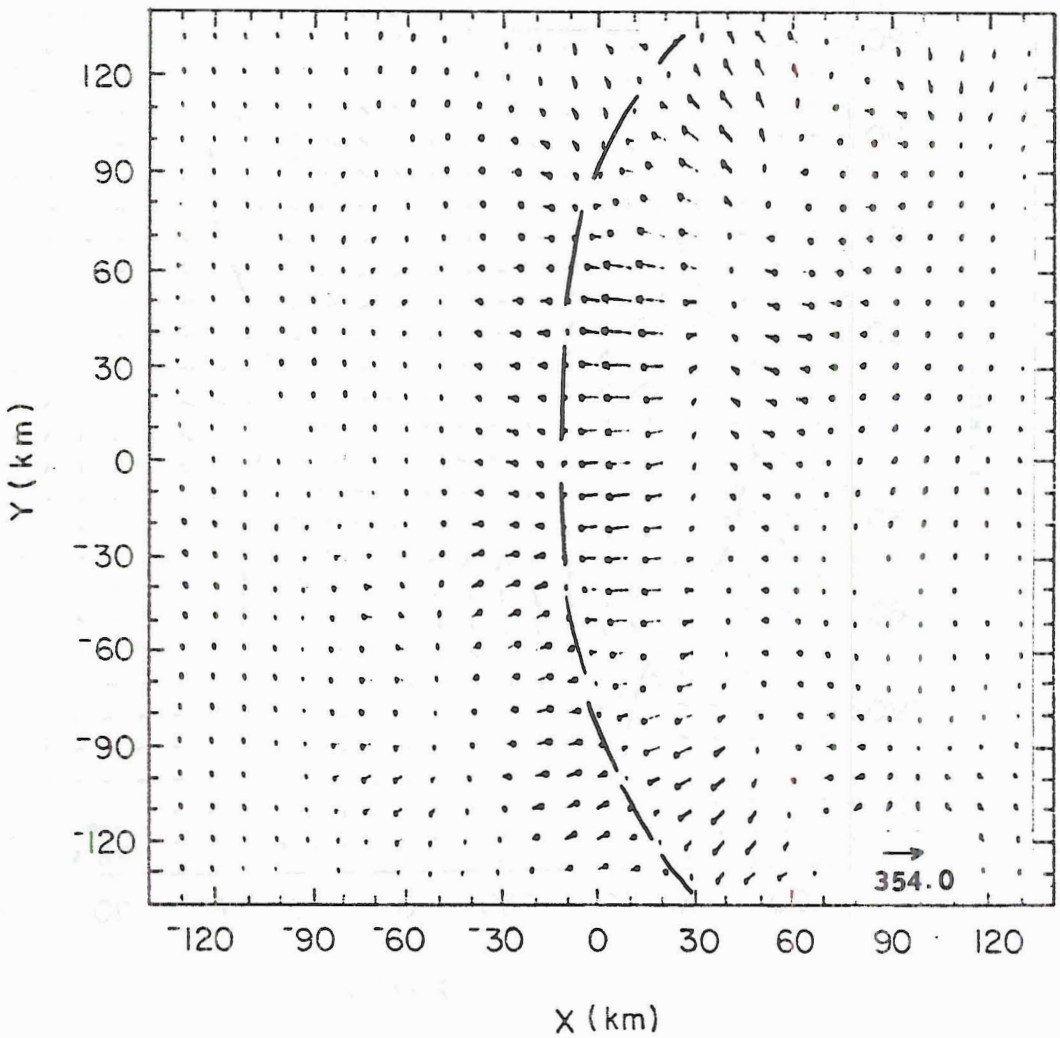

Figure 5.34. Horizontal cross section of mesoscale horizontal wind vector (u',v') at z = 500 m and t = 14400 sec. (Initial condition: a = b = 50 km).

At t = 4500 sec (Fig. 5.32), the line on the left traveled due west at about 20 $m.s^{-1}$ while the one on the right is still traveling due east, but with a speed of 7 $m.s^{-1}$, The line on the left is already more intense than the one on the right. However, the magnitude of the maximum wind vector is only 1.3 times the initial value.

As time goes on, the disturbances leave the grid on one side and reenter again on the other side due to the periodic boundary condition. By t = 14400 sec (4 hrs), there is only one line left (Fig. 5.34) with slight curvature, extending over the whole meridional dimension of the background, i.e., about 300 km long, traveling due west at 20 $m.s^{-1}$. A region of divergence is trailing behind the line of convergence. The maximum wind vector has only now reached a value 5 times larger than the initial value.

b) Vertical Structure in a Zonal Plane

The same evolution in the vertical structure discussed in the case of a = b = 20 km may be observed for a = b = 50km. Fig. 5.35(a,b) shows the mesoscale vertical velocity vector for y = 0, at t = 0 and t = 4500 sec. There are a few differences between these figures and the corresponding ones for a narrow initial disturbance (Fig. 5.10 b and Fig. 5.26 a). First of all, the inclination of the region of upward vertical velocity is quite different: the narrow initial condition has a more upright region of positive vertical velocity than the wider initial condition. Besides that, in Fig. 5.26 a region of upward vertical velocity is 20 km wide, while in Fig. 5.3(b), it is 50 km wide and remains like that in following times.

The region of gentle downward motion is still present trailing

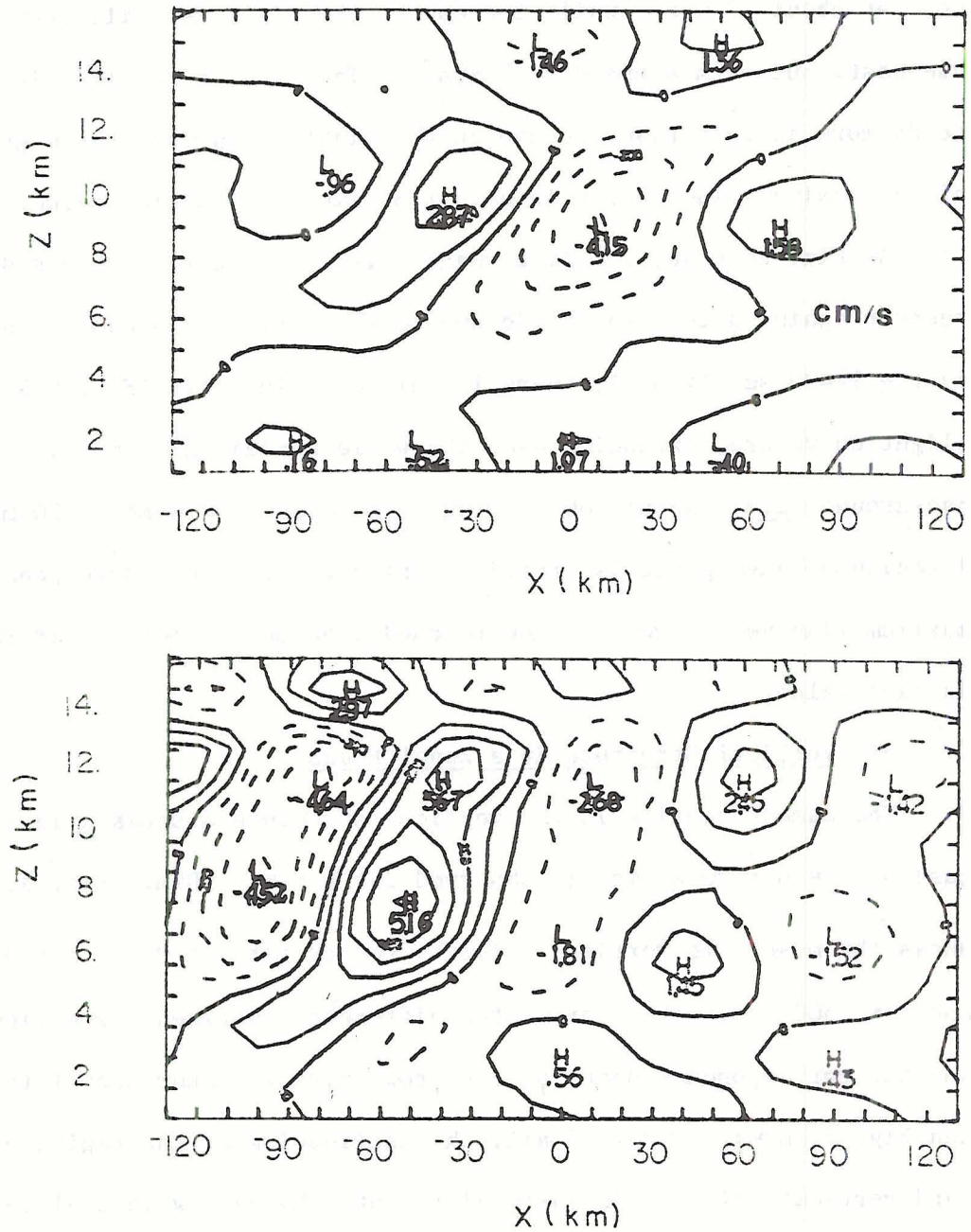

Figure 5.35. Vertical cross sections of mesoscale vertical velocity along a zonal plane at y = 0. (a) at time t = 0; (b) at time t = 4500 sec. (Initial condition: a = b = 50 km).

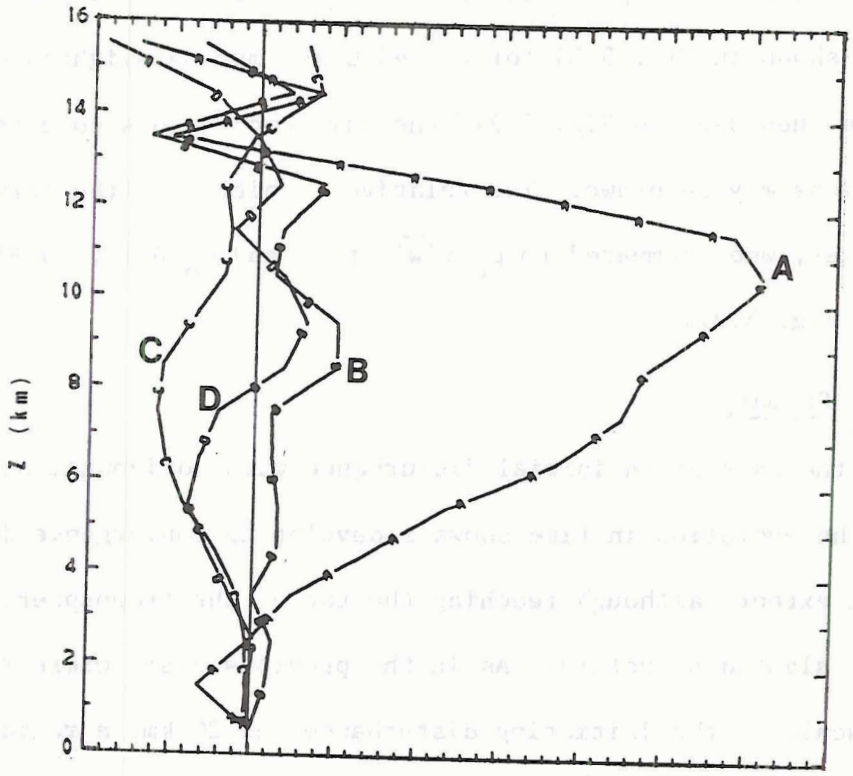

Figure 5.36. Vertical structure of: (A) $\rho_o \overline{u'w'}$; (B) $\rho_o \overline{v'w'}$; (C) $\overline{p'w'}$; (D) $\rho_o \overline{\theta'w'}$; at time t = 4500 sec. (Initial condition: a = b = 50 km).

right behind the line of convergence, with stronger compensating subsidence downwind from the upper level jet.

c) Fluxes

Although the shape of the fluxes $\rho_o \overline{u'w'}$, $\rho_o \overline{v'w'}$, $\overline{p'w'}$ and $\rho_o \overline{\theta'w'}$ shown in Fig. 5.34 for t = 4500 sec may be slightly different from the ones seen in Fig. 5.27, the same conclusions concerning energy conversions may be drawn. The relative magnitude of the term $\rho_o \overline{u'w'}$ is smaller, when compared to $\rho_o \overline{v'w'}$, $\overline{p'w'}$ and $\rho_o \overline{\theta'w'}$, in Fig. 5.34 than in Fig. 5.27.

d) Summary

In the case of an initial disturbance with horizontal scale of 50 km, the evolution in time shows a developing convergence line whose vertical extent, although reaching the top of the troposphere, shows a rather slanted structure. As in the previous case, where the horizontal scale of the initiating disturbance was 20 km, a region of sinking develops behind and in front of the convergence line. Again, the mesoscale disturbance draws energy from the basic state flow at all levels.

5.2.3 Still Wider Initial Condition: a = b = 100 km

The case a = b = 100 km shows results totally different from the previous ones. The projection of the initial condition, to begin with, is somewhat different. The two previous cases initiated with meridional lines (Fig. 5.11 and Fig. 5.30) while the present case shows a line of convergence inclined in the NW-SE direction, as may be seen in Fig. 5.37.

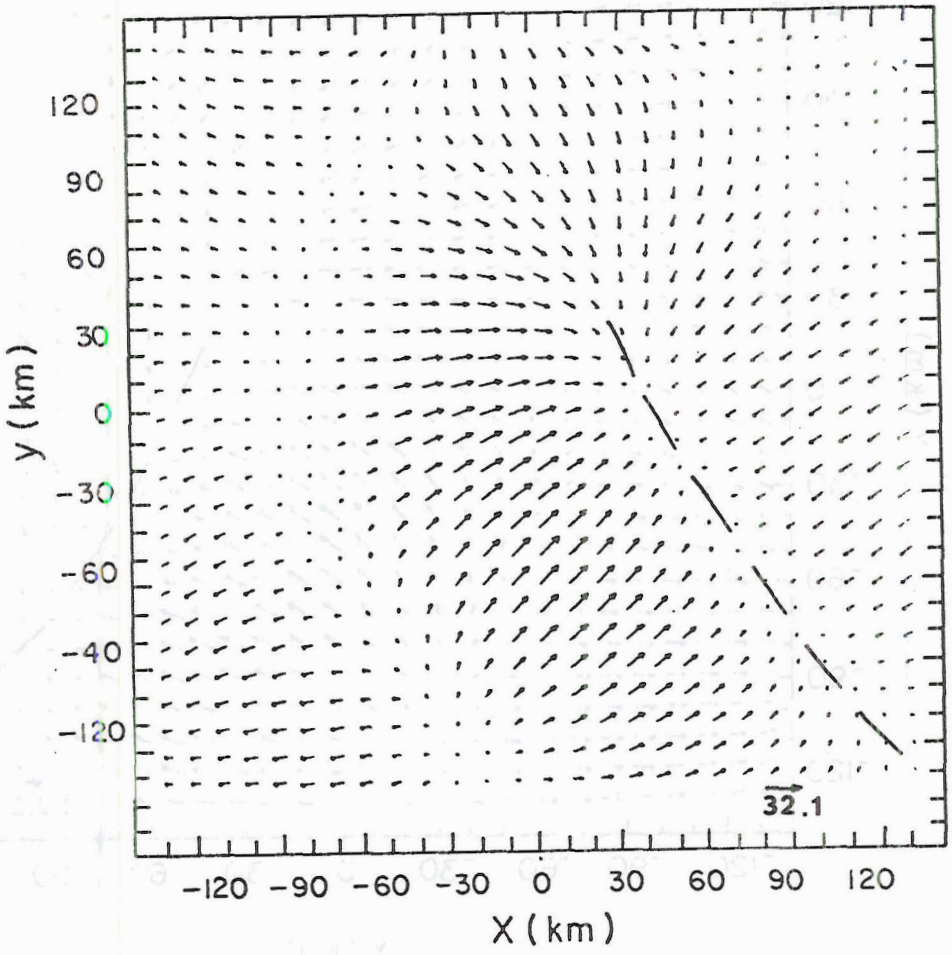

Figure 5.37. Horizontal cross section of mesoscale horizontal wind vector (u',v') at z = 500 m and t = 0. (Initial condition: a = b = 100 km).

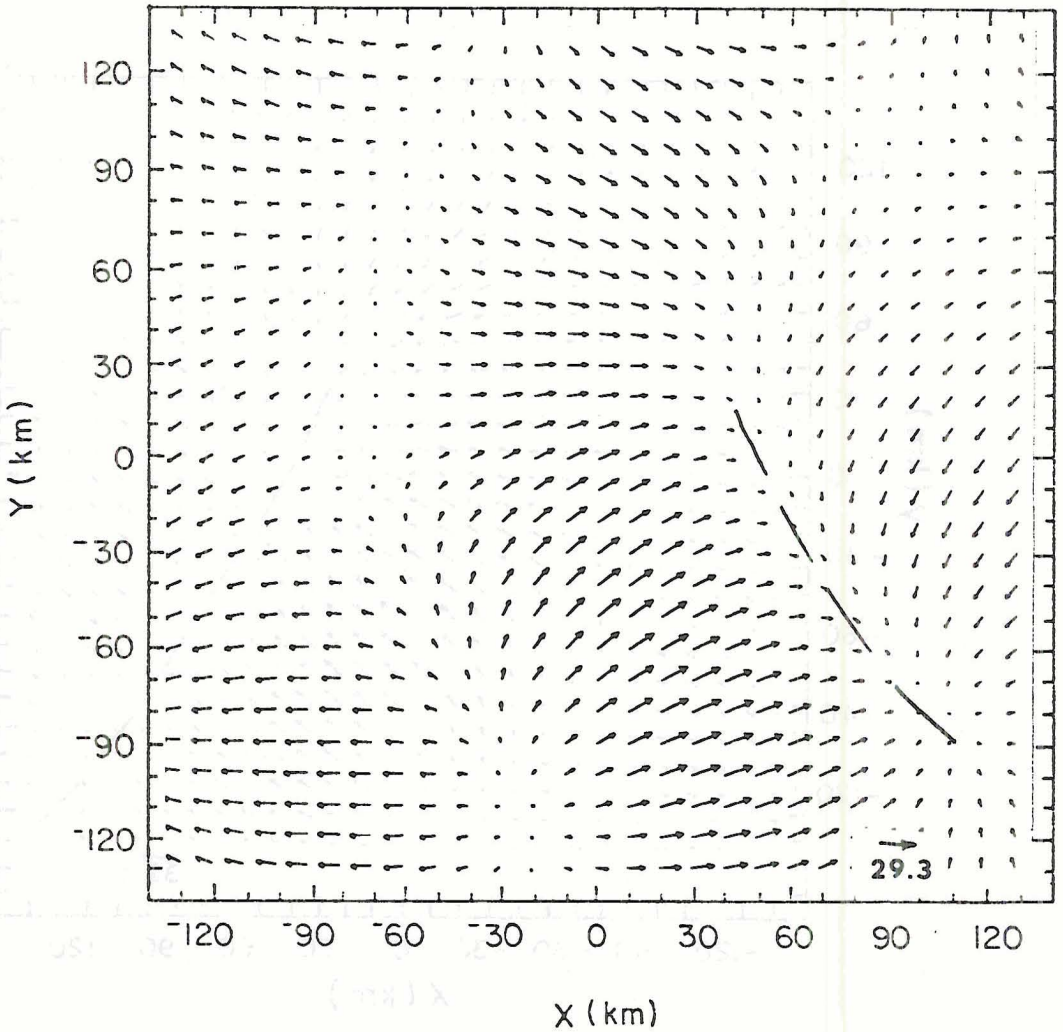

Figure 5.38. Horizontal cross section of mesoscale horizontal wind vector (u',v') at z = 500 m and t = 1500 seconds. (Initial condition: a = b = 100 km).

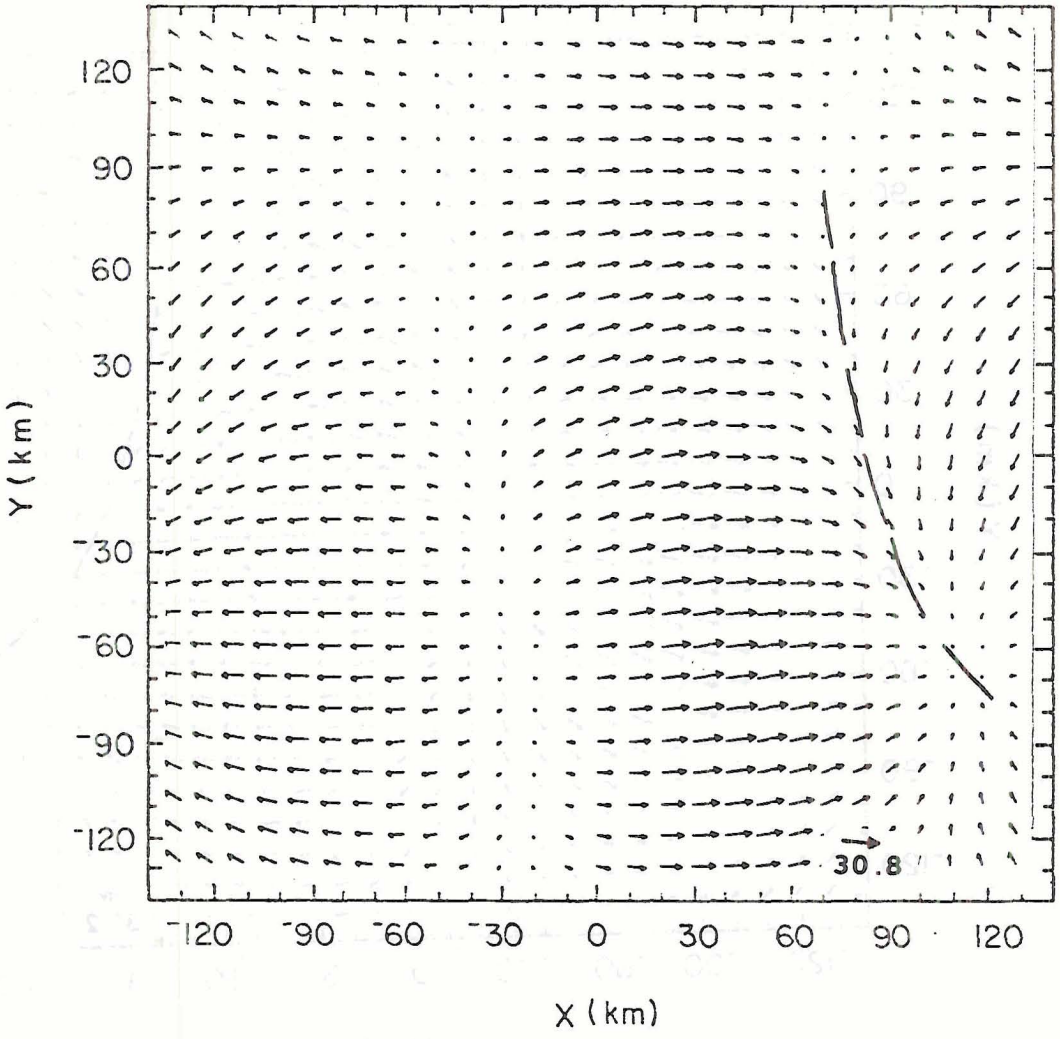

Figure 5.39. Horizontal cross section of mesoscale horizontal wind vector (u',v') at z = 500 m and t = 3000 seconds. (Initial condition: a = b = 100 km).

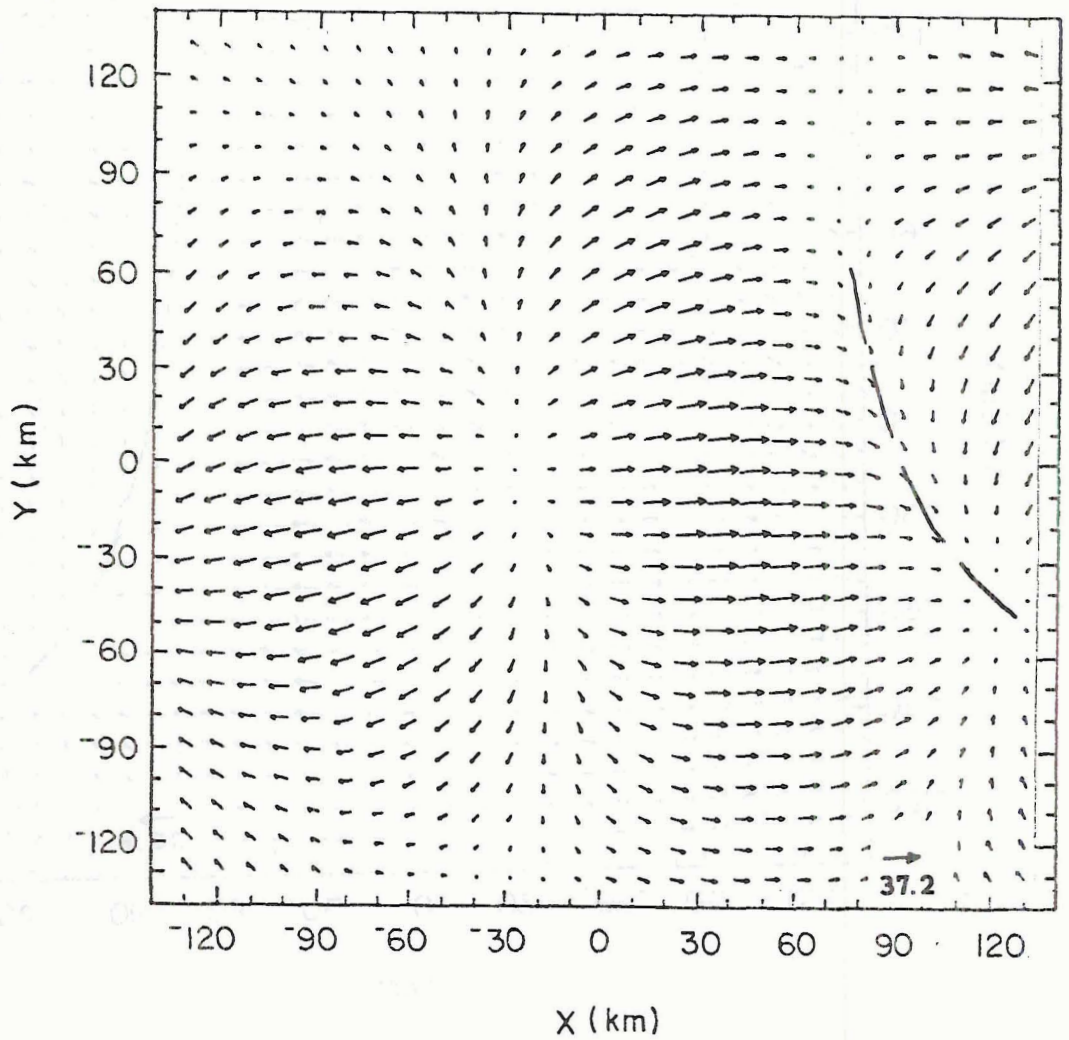

Figure 5.40. Horizontal cross section of mesoscale horizontal wind vector (u',v') at z = 500 m and t = 4500 seconds. (Initial condition: a = b = 100 km).

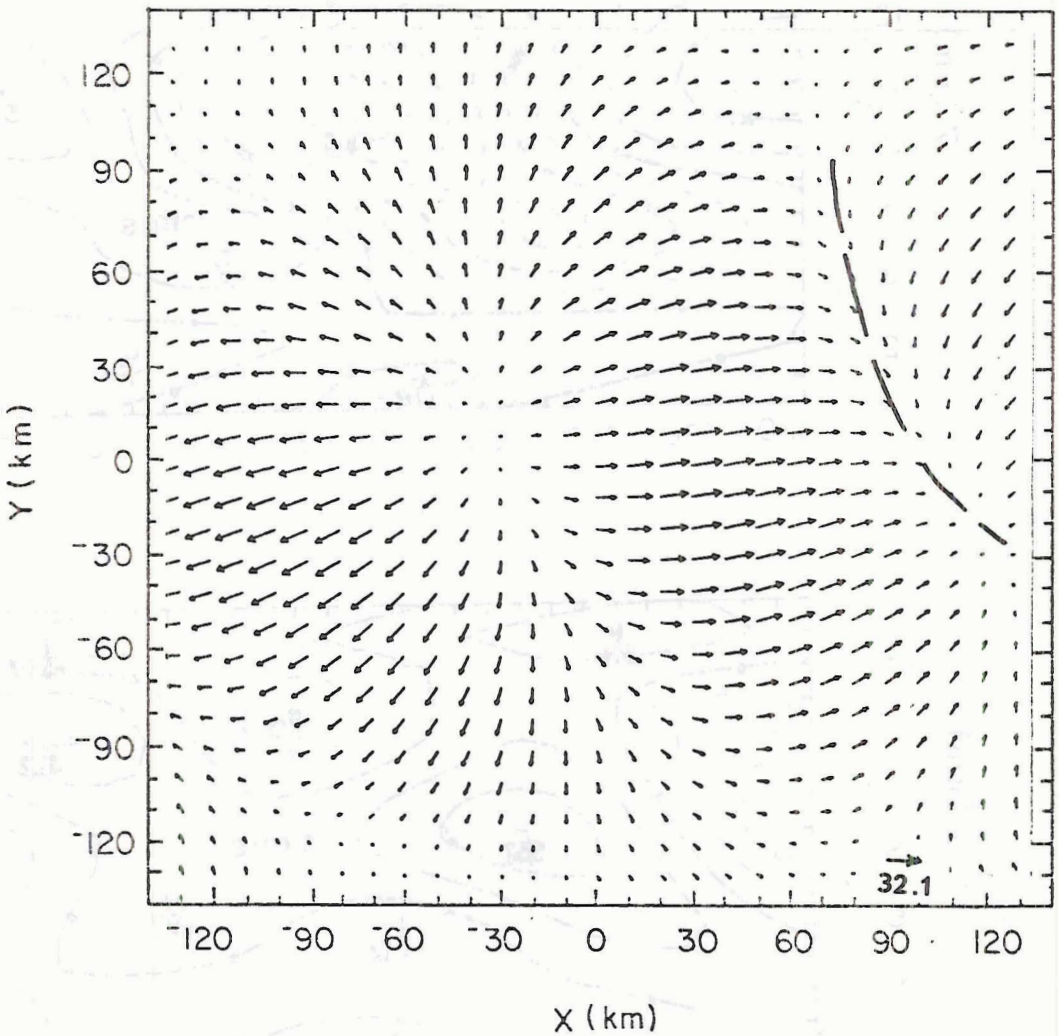

Figure 5.41. Horizontal cross section of mesoscale horizontal wind vector (u',v') at z = 500 m and t = 6000 seconds. (Initial condition: a = b = 100 km).

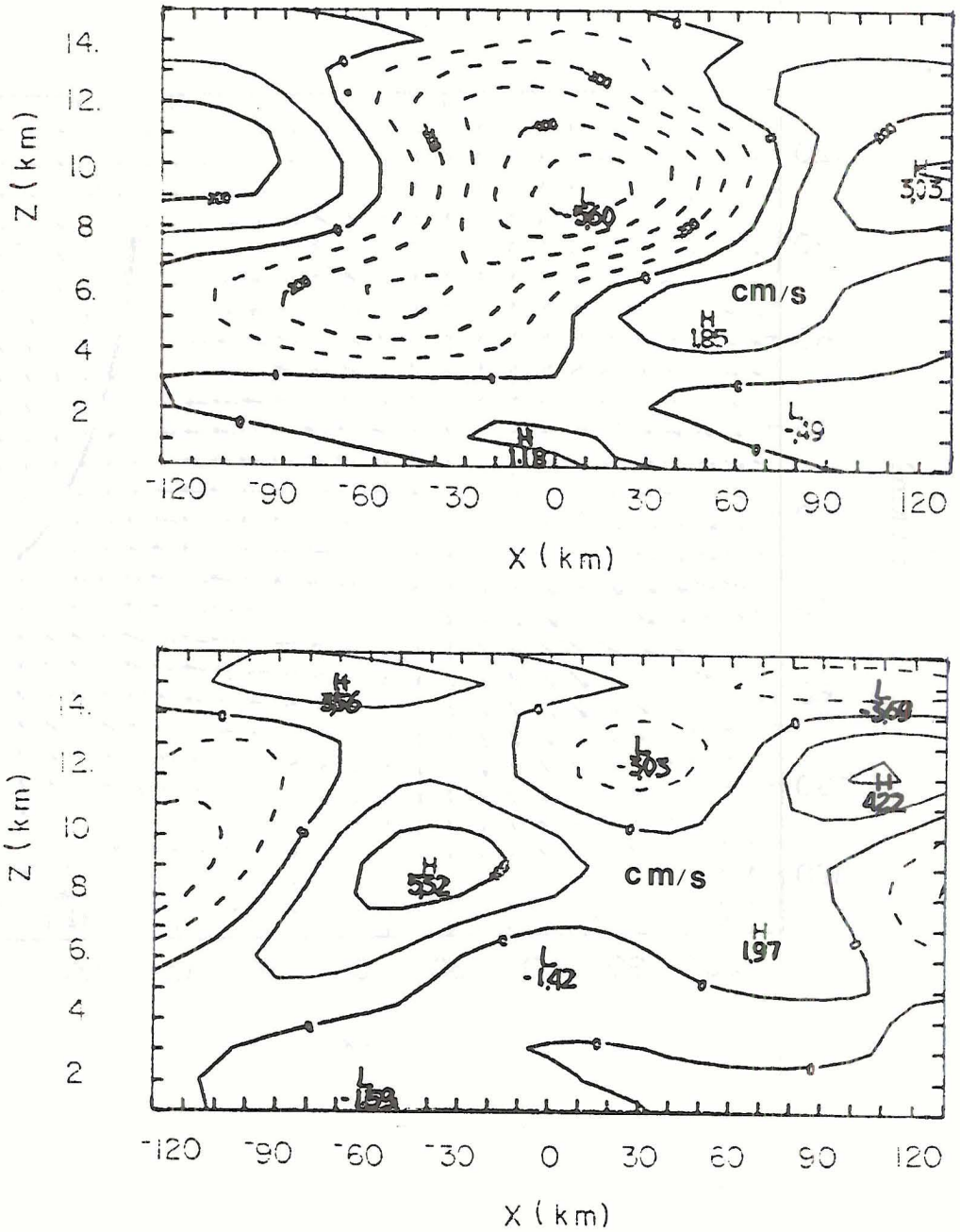

Figure 5.42. Vertical cross sections of mesoscale vertical velocity in a zonal plane at y = 0. (a) at time t = 0; (b) at time t = 6000 seconds. (Initial condition: a = b = 100 km).

a) Horizontal Structure at Lowest Level

The evolution in time at z = 500 m may be seen in Figs. 5.38, 5.39, 5.40, and 5.41 for t = 1500, 3000, 4500 and 6000 seconds, respectively. It may be observed that the line of convergence is displaced towards the northeast without much change in structure, with a speed of about 10 $m.s^{-1}$. There is no noticeable intensification from t = 0 to t = 6000 sec in the magnitude of the maximum wind vector. By t = 14400 sec or 4 hrs (not shown), the maximum wind vector has barely doubled its initial value.

b) Vertical Structure in a Zonal Plane

The vertical structure is very confused in this case. At time t = 0 and at y = 0, the mesoscale vertical velocity in Fig. 5.42(a) shows a region of sinking in the middle and upper troposphere about 150 km wide with regions of upward vertical motion in the lower troposphere and around the sinking region. At time t = 6000 sec, there is no clear structure,and regions of up and down motion succeed each other in the vertical. This structure does not resemble a squall line at all.

c) Summary

The initial line of convergence remains shallow throughout at at least 6 hours without any extension of the upward motion region to upper levels. No similarity with convective lines can be drawn in this case. The growth rate is very low and nothing seems to develop.

5.2.3 Summary of Main Points

The main points of this chapter may be summarized as follows

a) The scale of the initial disturbance is very important in determining which mode is going to predominate as time evolves.

b) Initial lines of shallow convergence with scales of 20 km and 50 km develop to convergence lines with regions of upward vertical motion extending from the surface to the tropopause.

c) The evolution of the small scale line compares fairly well with observations of squall lines: it develops curvature and vertical tilting comparable to observations by Houze (1977) and Sanders and Emanuel (1977).

d) A mesohigh develops behind the convergence line in accordance with observations by Zipser (1977).

e) Compensating subsidence is stronger downwind from the upper level easterly jet.

f) The 50 km line has about the same structure as the 20 km line except that its vertical structure is more tilted.

g) The curvature of the convergence lines is related to the spreading of a gravity wave front; there is no effect of cold density current in the present model.

h) A wider initial disturbance with scale of 100 km does not produce any meaningful development.

VI. CONCLUSIONS AND RECOMMENDATIONS FOR FUTURE WORK

The achievements of the model described in the previous chapters may be divided in two parts: technical and conceptual. The technical improvements with respect to previous versions of this model (e.g. Raymond, 1975, 1976) are:

a) Any general linear parameterization may be used; in the present case, momentum mixing by cumulus clouds has been included through the scheme proposed by Schneider and Lindzen (1978). The cumulus heating parameterization is the so-called Wave-CISK, with the magnitude of the heating given by an idealized moisture budget (Stevens and Lindzen,1978).

b) For each wavenumber, all unstable modes may be used in the Fourier summation; Raymond (1976) used only the most unstable mode for each wavenumber.

c) The initial condition may have vertical structure as opposed to being constrained to only one level.

The main conceptual achievements may be listed as:

a) With the inclusion of momentum mixing, there are unstable modes in the mesoscale length scale.

b) The model gives growth rates of order of 1/2 hour.

c) The direction and intensity of the upper level jet are very important in determining a mode of maximum instability in the mesoscale length scale and its direction of propagation.

d) An initial zone of shallow convergence develops into convergence lines with regions of upward vertical motion extending from the surface to the tropopause. It develops curvature, vertical tilting and mesohighs and mesolows comparable to observations (Houze, 1977; Sanders and Emanuel, 1977; Zipser, 1977).

e) The curvature of the convergence lines is related to the spreading of a gravity wave front; there is no effect of cold density current in the present model.

We should also mention the following conclusions.

Thorpe and Miller (1978) claim that a model that does not include both components of the horizontal wind and its variation with height is unable to properly model severe storms. We would go a step further and say that even in the case where the two components of the basic state wind are used, the greatest care should be exercised in choosing what particular observation or set of observations is used to represent the larger scale basic state. Horizontal variations in vertical structure of the horizontal wind vector are likely to be present, especially around an incipient mesoscale disturbance. As seen in subsection 5.1.3, the selection of a preferred mode is very sensitive to the definition of the basic state in a particular case study making the comparison with observed data a difficult task.

Features in the basic state wind field can effectively determine, for example, that the East Atlantic region has, in the mean, a preferred mode which falls in the mesoscale length scale, while the West Pacific shows no preferred mode in the mesoscale length scale. Differences in wind hodographs between different categories of a composited easterly wave in the East Atlantic lead to the conclusion that the categories which precede the trough clearly define a preferred mode in the mesoscale, while the categories after the trough do not. Observations show that mesoscale organization is more likely to occur ahead of the easterly wave trough (e.g., Thompson et al., 1979).

The actual development of a mesoscale disturbance depends also on the scale of the initial condition. For an initial line of surface convergence with characteristic horizontal length scale between 20 and 50 km, the evolution may be clearly identified to lead to a convergence line with structure comparable with observed squall lines. A horizontal scale, of the initial convergence zone, of 100 km does not produce any meaningful result.

The research described in the previous chapter has been devoted mainly to identify the controls of mesoscale organization. Apart from the details of the parameterization scheme, it may be said that the main controls are the basic state wind field and features of the initial disturbance. And it is hard to say which is more important. The model used for the purposes described above is relatively simple, however, and can certainly be improved. It is recommended that future revision of the linear model include the Coriolis parameter as well as mesoscale moisture. A subsequent version should certainly include topography. A more complex basic state might also be important especially in the vicinity of the ITCZ where the horizontal shear of the wind is not negligible. This would allow the inclusion of vorticity and/or divergence in the basic state.

But before all these models improvements are made, several questions should be answered. First of all, can the parameterization of small scale processes be improved? Are these parameterization schemes really representing what cumulus clouds do? More basic than that is the question of scale separation: how far can we go improving small scale parameterizations and basic state characteristics and still keep

the modeled mesoscale in between as a separate entity? All these questions will probably remain unanswered for years to come.

Supposing that some consensus is reached on the questions raised above, the next step should be to compare model results with a few case studies. How to define the basic state is a question that should receive close attention in this case. The data required to evaluate the model performance in terms of speed and direction of propagation may be simply a time sequence of satellite pictures, or depending on availability, radar scans which locate areas of precipitation. Both resources are easily available for several mesoscale events during the GATE.

Finally, the last and ultimate goal of mesoscale modeling is the development of a parameterization scheme suitable for inclusion of mesoscale effects in large-scale and general circulation models. The mesoscale energy fluxes and conversions should be studied carefully for that purpose. Probably a non-linear model should be considered as a future option after the basic relationships are understood. However, even if some sort of parameterization scheme is developed in the next few years, it is our belief that the understanding of the physical processes that govern the scale interactions may lag, at least, another 10 years. When this is achieved, if it is, we will be able to say that the goals of this work have been attained.

REFERENCES

Arakawa, A., and V. R. Lamb, 1977: Methods in computational physics, Vol. 17: General Circulation Models of the Atmosphere, ed. by Julius Chang. Academic Press, 357 pp.

Arakawa, A., and W. H. Schubert, 1974: Interaction of a cumulus cloud ensemble with the large-scale environment, Part I. J. Atmos. Sci., 31, 674-701.

Aspliden, G. A., Y. Tourre, and J. B. Sabine, 1976: Some climatological aspects of West African disturbance lines during GATE. Mon. Wea. Rev., 104, 1029-1035.

Betts, A. K., R. W. Grover, and M. W. Moncrieff, 1976: Structure and motion of tropical squall-lines over Venzuela. Quart. J. R. Met. Soc., 102, 395-404.

Betts, A. K., and M. F. Silva Dias, 1979: Unsaturated downdraft thermodynamics in cumulonimbus. J. Atmos. Sci., 36, (in press, June 1979).

Bretherton, F. P., 1969: Momentum transport by gravity waves. Quart. J. R. Met. Soc., 95, 213-243.

Brown, J. M., 1979: Mesoscale unsaturated downdrafts driven by rainfall evaporation: A numerical study. J. Atmos. Sci., 36, 313-338.

Burpee, R. W., 1972: The origin and structure of easterly waves in the lower troposphere of North Africa. J. Atmos. Sci., 29, 77-90.

Byers, H. R., and R. R. Braham, 1949: The thunderstorm. U. S. Department of Commerce, 287 pp.

Chang, C.-P., 1976: Vertical structure of tropical waves maintained by internally-induced cumulus heating. J. Atmos. Sci., 33, 729-739.

Charney, J. G., and A. Eliassen, 1964: On the growth of the hurricane depression. J. Atmos. Sci., 21, 68-75.

Charney, J. G., and J. Pedlosky, 1963: On the trapping of unstable planetary waves in the atmosphere. J. Geophys. Res., 68, 6441-6442.

Cotton, W. R., 1975: On parameterization of turbulent transport in cumulus clouds. J. Atmos. Sci., 32, 548-564.

Cotton, W. R., and G. J. Tripoli, 1978: Cumulus convection in shear flow - Three-dimensional numerical experiments. J. Atmos. Sci., 35, 1503-1521.

Dean, G., and C. Smith, 1977: A study of synoptic and mesoscale interaction over the GATE ship network: 4-5-6 September 1974. Technical Note NCAR/TN-122+STR, NCAR, Boulder, Colo., 95pp.

Dutton, J. A., 1976: The Ceaseless Wind. An introduction to the theory of atmospheric motion. McGraw-Hill, 579 pp.

Dutton, J. A., and G. H. Fichtl, 1969: Approximate equations of motion for gases and liquids. J. Atmos. Sci., 26, 241-254.

Eliassen, A., and E. Palm, 1960: On the transfer of energy in stationary mountain waves. Geofys. Publ., 22, 1-23.

Frank, W. M., 1977: The life-cycle of GATE convective systems. J. Atmos. Sci., 35, 1256-1264.

Fritsch, J. M., 1978: Parameterization of mid latitude organized convection. Ph.D. thesis, Colorado State University, 143 pp. [Available from author, APCL, ERL, NOAA, Boulder, Co.]

Fujita, T., 1963: Analytical mesometeorology:a review. Meteor. Mongr., No. 27, 77-125.

Gray, W. M., 1973: Cumulus convection and large scale circulations I. Broadscale and mesoscale considerations. Mon. Wea. Rev., 101, 839-855.

Gray, W. M., 1977: Report of the U.S. GATE central program workshop. NCAR, Boulder, Co. 723 pp.

Gray, W. M., and R. W. Jacobson, Jr., 1977: Diurnal variation of deep cumulus convection. Mon. Wea. Rev., 105, 1171-1188.

Haltiner, G. J., 1971: Numerical Weather Prediction. John Wiley & Sons. 317 pp.

Hayashi, Y., 1970: A theory of large-scale equatorial waves generated by condensation heat and accelerating the zonal wind. J. Meteor. Soc. Japan, 48, 140-160.

Hazel, P., 1971: Numerical studies of the stability of inviscid stratified shear flows. J. Fluid. Mech., 51, 39-61.

Holton, J. R., 1973: A one-dimensional model including pressure perturbation. Mon. Wea. Rev., 101, 201-205.

Holton, J. R., 1975: The dynamic meteorology of the stratosphere and mesosphere. Meteorological Monographs, 15, No. 37, American Meteorological Society.

Houze, R. A., 1973: A climatological study of vertical transports by cumulus-scale convection. J. Atmos. Sci., 30, 1112-1123.

Houze, R., 1977: Structure and dynamics of a tropical squall-line system. Mon. Wea. Rev., 105, 1540-1567.

Howard, L. N., 1963: Neutral curves and stability boundaries in stratified flow. J. Fluid Mech., 16, 333-342.

Johnson (1978): Cumulus transports in a tropical wave composite for Phase III of GATE, J. Atmos. Sci., 35, 484-494.

Kelley, J., 1977: Report of the U. S. GATE central program workshop. NCAR, Boulder, Colo. 723 pp.

Klemp, J. B., and D. K. Lilly, 1978: The dynamics of wave-induced downslope winds. J. Atmos. Sci., 32, 320-339.

Klemp, J. B., and R. B. Wilhelmson, 1978a: The simulation of three-dimensional convective storm dynamics. J. Atmos. Sci., 35, 1070-1096.

Klemp, J. B., and R. B. Wilhelmson, 1978b: Simulation of right-and left-moving storms produced through storm splitting. J. Atmos. Sci., 35, 1097-1110.

Koss, W. J., 1976: Linear stability of CISK-induced disturbances: Fourier component eigenvalue analysis. J. Atmos. Sci., 33, 1195-1222.

Kreitzberg, C. W., and O. J. Perkey, 1976: Release of potential instability: Part I. A sequential plume model within a hydrostatic primitive equation model. J. Atmos. Sci., 33, 456-475.

Kreitzberg, C. W., and D. J. Perkey, 1977: Release of potential instability: Part II. The mechanism of convective mesoscale interaction. J. Atmos. Sci., 34, 1569-1595.

Lenshow, D. H., 1974: Model of the height variation of the turbulence kinetic energy budget in the unstable planetary boundary layer. J. Atmos. Sci., 31, 465-474.

Lindzen, R. S., 1974: Wave-CISK in the tropics. J. Atmos. Sci., 31, 156-179.

Liu, J. V., and H. D. Orville, 1969: Numerical modelling of precipitation and cloud shadow effects on mountain-induced cumuli. J. Atmos. Sci., 26, 1283-1298.

Miller, M. H., and A. K. Betts, 1977: Travelling convective storms over Venezuela. Mon. Wea. Rev., 105, 833-848.

Miller, M. J., and R. P. Pearce, 1974: A three-dimensional primitive equation model of cumulonimbus convection. Quart. J. R. Met. Soc., 100, 133-154.

Moncrieff, M. W., and M. J. Miller, 1976: The dynamics and simulation of tropical cumulonimbus and squall lines. Quart. J. R. Met. Soc., 102, 373-394.

Mower, R. N., 1977: Case study of convection lines during GATE. Atmospheric Science Paper No. 271, Colorado State University, Fort Collins, 92 pp.

Murakami, M., 1973: Response of the tropical atmosphere to the initial forcing on the equator and the middle latitude boundary. J. Met. Soc. Japan, 51, 252-262.

Nitta, T., 1977: Response of cumulus updraft and downdraft to GATE A/B - scale motion system. J. Atmos. Sci., 32,

Ogura, Y., and N. A. Phillips, 1962: Scale analysis of deep and shallow convection in the atmosphere. J. Atmos. Sci., 19, 173-179.

Ooyama, K., 1963: A dynamical model for the study of tropical cyclone development. III Technical Conference on Hurricanes and Tropical Meteorology. Geofisica International, 186-198.

Ooyama, K., 1969: Numerical simulation of the life cycle of tropical cyclones. J. Atmos. Sci., 26, 3-40.

Payne, S. W., and M. M. McGarry, 1977; The relationship of satellite inferred convective activity to easterly waves over West Africa and the adjacent ocean during Phase III of GATE. Mon. Wea. Rev., 105, 413-420.

Pedlosky, J., 1964: An initial value problem in the theory of barotropic instability. Tellus, 16, 12-17.

Pennel, W. T., and M. A. LeMone, 1974: An experimental study of turbulence structure in the fair weather trade wind boundary layer. J. Atmos. Sci., 31, 1308-1323.

Pielke, R. A., 1974: A three-dimensional numerical model of the sea breezes over south Florida. Mon. Wea. Rev., 102, 115-139.

Pielke, R. A., and Y. Mahrer, 1978: Verification analysis of the University of Virginia three-dimensional mesoscale model prediction over South Florida for 1 July 1973. Mon. Wea. Rev., 106, 1568-1589.

Raymond, D. J., 1975: A model for predicting the movement of continuously propagating convective storms. J. Atmos. Sci., 32, 1308-1317.

Raymond, D. J., 1976: Wave-CISK and convective mesosystems. J. Atmos. Sci., 33, 2392-2398.

Reed, R. J., and E. E. Recker, 1971: Structure and properties of synoptic scale wave disturbances in the equatorial western Pacific. J. Atmos. Sci., 28, 1117-1133.

Reed, R. J., D. C. Norquist and E. E. Recker, 1977: The structure and properties of African wave disturbances as observed during Phase III of GATE. Mon. Wea. Rev., 105, 317-333.

Sanders, F., and K. A. Emanuel, 1977: The momentum budget and temporal evolution of a mesoscale convective system. J. Atmos. Sci., 34, 322-330.

Schneider, E. K., and R. S. Lindzen, 1976: A discussion of the parameterization of momentum exchange by cumulus convection. J. Geophys. Res., 81, 3158-3160.

Smith, C. L., E. J. Zipser, S. M. Daggupaty, and L. Sapp, 1975a: An experiment in tropical mesoscale analysis: Part 1. Mon. Wea. Rev., 103, 878-892.

Smith, C. L., E. J. Zipser, S. M. Daggupaty, and L. Sapp, 1975b: An experiment in tropical mesoscale analysis: Part 2. Mon. Wea. Rev., 103, 893-903.

Stevens, D. E., and R. S. Lindzen, 1978: Tropical Wave-CISK with a moisture budget and cumulus friction. J. Atmos. Sci., 35, 940-961.

Stevens, D. E., R. S. Lindzen and L. J. Shapiro, 1977: A new model of tropical waves incorporating momentum mixing by cumulus convection. Dyn. Atmos. Oceans, 1, 365-425.

Takeda, T., 1971: Numerical simulation of a precipitating convective cloud: the formation of a "long-lasting" cloud. J. Atmos. Sci., 28, 350-376.

Thompson, R. M., Jr., S. W. Payne, E. E. Recker, and R. J. Reed, 1979: Structure and properties of synoptic-scale wave disturbances in the intertropical convergence zone of the Eastern Atlantic. J. Atmos. Sci., 36, 53-72.

Thorpe, A. J., and M. J. Miller, 1978: Numerical simulations showing the role of the downdraught in cumulonimbu motion and splitting. Quart. J. R. Met. Soc., 104, 873-893.

Williams, D. T., 1963: The thunderstorm wake of May 4, 1961. Nat. Severe Storms Project Rep. No. 18, U. S. Dept. of Commerce, Washington, D. C., 23 pp.

Yamasaki, M., 1969: Large-scale disturbances in a conditional unstable atmosphere in low latitudes. Papers in Meteor. Geophys., 20, 289-336.

Yanai, M., W. Esbensen and J. H. Chu, 1973: Determination of bulk properties of tropical cloud clusters from large scale heat and moisture budgets. J. Atmos. Sci., 30, 611-627.

Zipser, E. J., 1969: The role of organized unsaturated convective downdrafts in the structure and rapid decay of an equatorial disturbance. J. Appl. Meteor., 8, 799-814.

Zipser, E. J., 1977: Mesoscale and convective-scale downdrafts as distinct components of squall line circulation. Mon. Wea. Rev., 105, 1568-1589.

Zipser, E. J., and C. Gautier, 1978: Mesoscale events within a GATE tropical depression. Mon. Wea. Rev., 106, 789-805.

APPENDIX A1. DISTURBANCE ENERGETICS

The total energy equation for the disturbance may be obtained by multiplying equations (3.5) and (3.6) by $\rho_o \backslash v'$ and by $\rho_o \theta'/(\theta_o d\theta_o/dz)$ and using the continuity equation (3.7) to get

$$\left(\frac{\partial}{\partial t} + u_o \frac{\partial}{dx} + v_o \frac{\partial}{\partial y} + w_o \frac{\partial}{\partial z}\right) \rho_o \frac{u'^2}{2} + \rho_o u'w' \frac{du_o}{dz} + u' \frac{dp'}{dx}$$

$$= \rho_o u' \psi_x \qquad \text{(A1.1)}$$

$$\left(\frac{\partial}{\partial t} + u_o \frac{\partial}{\partial x} + v_o \frac{\partial}{\partial y} + w_o \frac{\partial}{\partial z}\right) \rho_o \frac{v'^2}{2} + \rho_o v'w' \frac{dv_o}{dz} + v' \frac{\partial p'}{\partial y}$$

$$= \rho_o v' \psi_x \qquad \text{(A1.2)}$$

$$\left(\frac{\partial}{\partial t} + u_o \frac{\partial}{\partial x} + v_o \frac{\partial}{\partial y} + w_o \frac{\partial}{\partial z}\right) \rho_o w'^2 + \rho_o w'w' \frac{dw_o}{dz} +$$

$$\rho_o w' \frac{d}{dz}\left(\frac{p'}{\rho_o}\right) - \rho_o \frac{\theta' w'}{\theta_o} g = \rho_o w' \psi_z \qquad \text{(A1.3)}$$

$$\left(\frac{\partial}{\partial t} + u_o \frac{\partial}{\partial x} + v_o \frac{\partial}{\partial y} + w_o \frac{\partial}{\partial z}\right)\left(\frac{\rho_o}{2s}\left(g\,\frac{\theta'}{\theta_o}\right)\right)^2 +$$

$$\rho_o\, w_o \frac{1}{s}\left(g\,\frac{\theta'}{\theta_o}\right)^2\left[\frac{d}{dz}\ln s(z) + \frac{s}{g}\right] + g\rho_o \frac{w'\theta'}{\theta_o}$$

$$= g\,\frac{\rho_o \theta' \psi_\theta}{\theta_o \dfrac{d_o}{dz}} \qquad \text{(A1.4)}$$

where

$$s(z) = \frac{g}{\theta_o}\frac{d\theta_o}{dz} \qquad \text{(A1.5)}$$

Adding equations A1.1, A1.2, A1.3 and A1.4, and defining

$$E' = \rho_o\left(\frac{u'^2}{2} + \frac{v'^2}{2} + \frac{w'^2}{2} + \frac{1}{2s}\left(g\,\frac{\theta'}{\theta_o}\right)^2\right) \qquad \text{(A1.6)}$$

and

$$\frac{d}{dt} = \frac{\partial}{\partial t} + u_o\frac{\partial}{\partial x} + v_o\frac{\partial}{\partial y} + w_o\frac{\partial}{\partial z} \qquad \text{(A1.7)}$$

we may write

$$\frac{dE'}{dt} + \rho_o\, w_o\left(g\,\frac{\theta'}{\theta_o}\right)^2\left(\frac{1}{g} + \frac{1}{s}\,\frac{d}{dz}\ln s\right) +$$

$$\rho_o\, u'w'\,\frac{du_o}{dz} + \rho_o\, v'w'\,\frac{dv_o}{dz} + \rho_o\, w'w'\,\frac{dw_o}{dz} +$$

$$\rho_o\,\nabla\cdot\left(\mathbf{w}'p'\right) = \rho_o\,\mathbf{w}'\cdot\underset{\sim}{\psi} + g\,\frac{\rho_o}{\theta_o\dfrac{d\theta_o}{dz}}\,\theta'\psi_\theta \qquad \text{(A1.8)}$$

where the continuity equation (3.7) has been used in the term containing the pressure perturbation.

It may be noted that the term in $\theta'w'$ is cancelled between equations (A1.3) and (A1.4) denoting a conversion of potential energy into kinetic energy of vertical motions. A positive correlation between θ' and w' corresponds to a decrease in potential energy and an increase in kinetic energy.

The energy equation (A1.8) is discussed by Dutton (1976). According to Dutton, the most important terms in the energy equation are ($\rho_o u'w' \, du_o/dz$, $\rho_o v'w' \, dv_o/dz$) which correspond to the transfer of energy from the basic state to the perturbations through the Reynolds stress acting on the shear of the mean flow. The term $\partial(\rho'w')/\partial z$ is related to the convergence of wave energy (cf. Eliassen and Palm, 1960; Holton, 1975).

APPENDIX A2. PROCEDURE TO CALCULATE HORIZONTAL AVERAGES OF VERTICAL FLUXES.

The horizontal averages of vertical fluxes may be computed numerically from the values obtained in grid points, but a more accurate result may be obtained by using the eigenvalues and eigenvectors of equation (3.30) and the Fourier transform of the initial condition represented by $C(k_x, k_y, m)$ in equation (3.37). The procedure to be presented here has been previously used by Murakami (1973).

Consider, for example, the vertical flux of zonal momentum. The field of u' may be written, in a discretized version of equation 3.32 and 3.36, as

$$u'(x,y,z,t) = \sum_{n_x} \sum_{n_y} \sum_{m} c(n_x, n_y, m)\ \hat{u}(n_x,n_y,m)$$

$$\exp\left(i\left(k_x\ x + k_y\ y - \omega\ (k_x,k_y,m)\ t\right)\right)\frac{4\pi^2}{L_x L_y} \qquad \text{(A2.1)}$$

where

$$k_x = \frac{2\pi}{L_x} n_x \quad \text{and} \quad k_y = \frac{2\pi}{L_y} n_y \qquad \text{(A2.2)}$$

and analogously for w' .

Now define

$$a = a_r + i\ a_i = \sum_m c(n_x,n_y,m)\ \hat{u}(\omega_x,n_y,m)$$

$$\exp\left(-i\ \omega\ (k_x,k_y,m)\ t\right) . \qquad \text{(A2.3)}$$

and

$$b = b_r + i\, b_i = \sum_m c(n_x,n_y,m)\ \hat{w}(n_x,n_y,m)$$

$$\exp\left(-i\ \omega\left(k_x,k_y,m\right)\ t\right) \qquad \text{(A2.4)}$$

The horizontal mean corresponding to the fundamental ($n_x = n_y = 1$) wavelengths L_x, L_y of u'w' will be denoted by a bar; the only part that has physical meaning is the product of the real part of u' and w' which may be written as (A2.5)

$$\mathrm{Re}\ [u'] = \sum_{n_x}\sum_{n_y}\left(a_r \cos\left(k_x\ x + k_y\ y\right) - a_i \sin\left(k_x\ x + k_y\ y\right)\right)\frac{4\pi^2}{L_x L_y}$$

(A2.6)

$$\mathrm{Re}\ [w'] = \sum_{n_x}\sum_{n_y}\left(b_r \cos\left(k_x\ x + k_y\ y\right) - b_i \sin\left(k_x\ x + k_y\ y\right)\right)\frac{4\pi^2}{L_x L_y}$$

Defining

$$\overline{\mathrm{Re}\ [u']\ \mathrm{Re}\ [w']} = \frac{1}{L_x L_y}\int_0^{L_y}\int_0^{L_x} \mathrm{Re}\ [u']\ \mathrm{Re}\ [w']\ dx\ dy$$

it may be seen that

$$\overline{\mathrm{Re}\ [u']\ \mathrm{Re}\ [w']} = \sum_{n_x}\sum_{n_y}\left(a_r\ b_r + a_i\ b_i\right)\frac{2\pi^2}{L_x L_y} \qquad \text{(A2.7)}$$

or

$$\overline{\mathrm{Re}\ [u']\ \mathrm{Re}\ [w']} = \sum_{n_x}\sum_{n_y}\left(a^*\ b + ab^*\right)\frac{\pi^2}{L_x L_y} \qquad \text{(A2.8)}$$

And analogously with the other fluxes.

BIBLIOGRAPHIC DATA SHEET	1. Report No. CSU - ATS - 311	2.	3. Recipient's Accession No.

4. Title and Subtitle

Linear Spectral Model of Tropical Mesoscale Systems

5. Report Date: August, 1979

6.

7. Author(s)

Maria F. Silva Dias

8. Performing Organization Rept. No. CSU - ATS - 311

9. Performing Organization Name and Address

Department of Atmospheric Science
Colorado State University
Fort Collins, CO. 80523

10. Project/Task/Work Unit No.

11. Contract/Grant No.

NSF ATM-78-05743
NSF ATM-77-15369

12. Sponsoring Organization Name and Address

Global Atmospheric Research Program
National Science Foundation
Washington, D.C. 20550

13. Type of Report & Period Covered

Ph.D. Thesis

14.

15. Supplementary Notes

16. Abstracts The sensitivity of mesoscale features with respect to large scale tropical profiles of wind and temperature and to small scale parameterizations is investigated through a linear, spectral, non-hydrostatic model. The cumulus heating parameterization is the so-called Wave-CISK parameterization, defined by an idealized moisture budget. The momentum mixing parameterization is as developed by Schneider and Lindzen (1976). The speed of propagation and the mode of maximum growth rate are not very sensitive to small scale parameterization. The feature of the basic state wind that most seriously influences the selection of a most unstable mode is the direction and the speed of the upper level jet. An initial small scale (20-50 km) line of shallow convergence evolves into a convergence line whose vertical extent reaches the whole troposphere. The convergence line assumes curvature and vertical tilting comparable to squall lines studied by Houze (1977).

17. Key Words and Document Analysis. 17a. Descriptors

Squall lines
Tropical systems
Spectral model

17b. Identifiers/Open-Ended Terms

17c. COSATI Field/Group

18. Availability Statement	19. Security Class (This Report) UNCLASSIFIED	21. No. of Pages 213
	20. Security Class (This Page) UNCLASSIFIED	22. Price